U.PORTO

FEUP FACULDADE DE ENGENHARIA
UNIVERSIDADE DO PORTO

Hybrid CFRP/Titanium bolted joints

Cláudia Cardoso

Supervisors:
Prof. Dr. Pedro P. Camanho
Prof. Dr. Francisco Pires

A Thesis submitted in partial fulfillment of the requirements for the degree of Doctor of Philosophy in Mechanical Engineering

Porto, Junho 2016

Abstract

Nowadays the increasing use of composite materials in aeronautical industry poses new challenges in terms of design optimization and development costs. One of the main advantages of composite design is the possibility to apply a high integral design strategy but, even though the need for structural coupling is reduced, it still remains unavoidable due to size, design and logistic limitations on one side and maintenance, repair and inspection requirements on the other. Advanced joining techniques have been currently developed in order to minimize the weight penalties and increase the efficiencies in composite joints, particularly in mechanically fastened joints. A number of reinforcement techniques have been proposed to increase the load capacity of composite bolted joints namely the local reinforcement with titanium foils. This local hybridization technique was extensively tested under several experimental conditions having demonstrated promising results.

In this work, a contribution towards advanced simulation methods of hybrid titanium/CFRP joints is given, particularly through the use and development of adequate material models for the composite and titanium plies. For the CFRP plies fully three dimensional damage models that can accurately account for the impact of the through-thickness effects on the strength of the joint are used whereas for the titanium plies adequate material models accounting for plastic deformation and damage were developed.

As an hexagonal closed packed metal, the accurate modelling and simulation of the titanium plies poses new challenges. The specifics of the mechanical response of hcp metals demand for adequate macroscopic plasticity models as classic formulations fail to capture simultaneously the anisotropy and the strength differential effect characteristic of titanium alloys and other hcp metals. In this work, two new macroscopic elasto-plastic models, one proposed by Cazacu, Barlat and Plunkett commonly known as CPB06 and other, more recent, proposed by Nixon, were numerically implemented on an Abaqus VUMAT subroutine and validated for the Ti6Al4V alloy.

The constitutive models like the ones proposed by Nixon or Cazacu have proven to be adequate not only for titanium and its alloys but also for other hexagonal closed packed metals like magnesium or zinc. However, the reliability of these advanced models is strongly dependent on the accurate identification of their parameters. The number of parameters tends to increase with the sophistication of the models, which demands for more elaborate and robust optimization techniques. In this work, a mixed optimization procedure based on local and global search techniques was used for the determination of the parameters of the Nixon and CPB06 constitutive models for the Ti6Al4V alloy.

Although significant progress has been made in the modelling of the plastic deformation of hcp metals, modelling damage and failure in titanium and its alloys is still under development as the influence of the asymmetry in yielding on the damage evolution is not fully understood. In this work, following an uncoupled approach for damage modelling, several relevant failure criteria were incorporated into the subroutine of the CPB06 elasto-plastic model. The capability of the different criteria to capture the fracture initiation for two tensile specimens (smooth and notched) of Ti6Al4V alloy was studied. The main advantage in the use of fracture criteria is their simplicity regarding the computational implementation. However, difficulties were found in the correct assessment of the fracture initiation site in the notched specimen for the majority of the criteria tested. Alternatively, a coupled approach based on the continuum ductile damage model proposed by Lemaitre was used. In this way, by establishing a relationship between damage evolution and plasticity, more realistic solutions can be obtained. For an adequate description of the deformation and damage behaviour of hcp materials an improvement of the Lemaitre damage model is proposed by replacing the original von Mises criterion by the Cazacu's CPB06 criterion. The proposed model was implemented in a VUMAT subroutine and validated for the Ti6Al4V titanium alloy.

With the development and implementation of adequate material models, full three dimensional hybrid joints were then modelled considering different titanium contents. The bearing test was simulated using the adequate constitutive models for the titanium and CFRP plies and the results were compared with the results obtained using the material models available in Abaqus. Furthermore, the effect of the titanium content, the titanium sheets orientation and the clamping pressure on the bearing strength of the joint was also assessed. Overall, the full three-dimensional models have proven to be adequate in the modelling of the bearing failure mode of hybrid joints. Additionally, the increase in bearing strength of the hybrid joint with increasing titanium content and the impact of the clamping pressure and the orientation of the titanium plies was demonstrated.

Resumo

Atualmente, com o aumento da utilização de materiais compósitos na indústria aeronáutica surgem novos desafios, quer ao nível da otimização de design quer em termos de custos de desenvolvimento de novos produtos. Uma das principais vantagens na utilização de compósitos advém da possibilidade de utilizar estratégias de design que permitem a redução do número de ligações. O recurso a ligações estruturais é no entanto um requisito muitas vezes incontornável, por limitações associadas à dimensão, limitações de design ou logísticas por um lado e por outro por questões relacionadas com a manutenção, reparação e inspeção das estruturas. Neste contexto, têm sido desenvolvidas e aperfeiçoadas novas técnicas de ligação que procuram otimizar o peso e ao mesmo tempo melhorar a eficiência de juntas em compósito, particularmente de juntas aparafusadas. Uma das técnicas proposta visa reforçar a junta localmente com recurso a camadas de metal incorporadas nas camadas em compósito. Esta técnica de hibridação local na zona da junta tem demonstrado resultados promissores em testes experimentais tendo sido utilizada com sucesso em aplicações espaciais.

Este trabalho procura ser uma importante contribuição no sentido do desenvolvimento de métodos avançados de simulação de juntas hibridas titânio/CFRP através do uso e desenvolvimento de modelos constitutivos adequados tanto para os compósitos como para o titânio. Nas camadas em compósito, modelos de dano tridimensionais capazes de captar o efeitos na direção da espessura do laminado foram considerados enquanto que para as camadas de titânio é necessário o desenvolvimento de modelos capazes de prever corretamente a deformação plástica e o dano.

Sendo um material de estrutura hexagonal compacta, o titânio coloca novos desafios relativamente à sua modelação e simulação. A especificidade do comportamento mecânico de metais de estrutura hexagonal compacta requer modelos macroscópicos de plasticidade adequados, capazes de prever simultaneamente a anisotropia e a assimetria tração/compressão. Neste trabalho dois critérios de plasticidade, um proposto por Cazacu, Barlat e Plunkett denominado por CPB06 e outro mais recente proposto por Nixon, foram implementados numericamente, com recurso a uma subrotina VUMAT e validados para a liga de titânio Ti6Al4V.

Os modelos constitutivos, como os propostos por Nixon ou Cazacu, demonstraram ser adequados não só para ligas de titânio como também para outros metais de estrutura hexagonal compacta como o magnésio ou o zinco. Contudo, a fiabilidade destes modelos está intrinsecamente dependente da correta determinação dos seus parâmetros. Uma vez que o número de parâmetros tende a aumentar com o grau de complexidade dos modelos, são frequentemente necessárias técnicas de identificação de parâmetros mais avançadas e robustas.

Neste trabalho foi utilizado um procedimento de otimizaçao misto baseado na utilização de técnicas de pesquisa globais e locais para a determinação dos parâmetros dos modelos de Nixon e CPB06 para a liga de titânio Ti6Al4V.

Embora significativos progressos tenham sido alcançados no que diz respeito à modelação da deformação plástica de metais de estrutura hexagonal compacta, a modelação dos mecanismos de dano e fratura está ainda em desenvolvimento e a influência da assimetria tração/compressão na evolução do dano interno não está ainda inteiramente compreendida. Neste trabalho, diversos critérios de fratura foram implementados juntamente com o modelo de plasticidade CPB06. A capacidade dos diferentes critérios em prever a localização de início da fratura foi analisada para dois provetes axissimétricos em tração uniaxial, com e sem entalhe, para a liga de titânio Ti6Al4V. A principal vantagem do uso de critérios de fratura reside na sua facilidade de implementação, no entanto, para o provete com entalhe a grande maioria dos critérios não foi capaz de prever corretamente o local de início de fratura. Alternativamente, foi proposto um modelo de dano acoplado baseado nos conceitos da mecânica de dano contínuo desenvolvidos por Lemaitre e recorrendo ao modelo de plasticidade proposto por Cazacu. O modelo proposto foi implementado computacionalmente e aplicado na modelação numérica de dano dúctil em dois provetes de titânio axissimétricos, com e sem entalhe, e demonstrou ser capaz de captar corretamente a iniciação e evolução do dano e a sua influência no fluxo plástico do material.

Modelos tridimensionais da junta híbrida foram desenvolvidos considerando diferentes laminados com diferentes percentagens de titânio. A rutura por esmagamento do laminado devido à presença do parafuso foi simulada com recurso aos modelos constitutivos adequados quer para as camadas de titânio quer para as camadas de compósito e os resultados foram comparados com os obtidos com recurso aos modelos disponíveis no Abaqus. Para além disso, foi possível avaliar o efeito da orientação das camadas de titânio na resistência da junta bem como o impacto da força de aperto. No geral, os modelos implementados demonstraram ser adequados para a simulação de juntas híbridas. Os resultados demonstraram um aumento da resistência da junta híbrida com o aumento da percentagem de titânio e o impacto da orientação das camadas de titânio bem como da variação da força de aperto foram demonstrados.

Acknowledgements

I wish to thank my supervisors, Prof. Dr. Pedro P. Camanho and Prof. Dr. Francisco Pires, for giving me the opportunity to work in such an extraordinary research field, and for the support and guidance throughout the execution of this work.

I would like to express my gratitude towards *Fundação para a Ciência e Tecnologia* for the doctoral degree grant SFRH/BD/79641/2011 within the *QREN-POPH-Tipologia 4.1-Formação Avançada* and funded by *FSE* and *MEC*.

I wish to thank also all the colleagues with whom I shared this journey for the support, motivation and friendly environment.

A very special thanks to my family for the encouragement and support and for always believing in me.

Contents

List of Acronyms

2D	Two-dimensional
3D	Three-dimensional
ARALL	Aramide Reinforced Aluminium Laminate
bcc	Body Centered Cubic
CDM	Continuum Damage Mechanics
CFRP	Carbon Fibre Reinforced Plastic
CPB06	Cazacu, Plunkett and Barlat 2006 yield criterion
CRES	Corrosion Resistant Steel
CRSS	Critical Resolved Shear Stress
CTE	Coefficient of Thermal Expansion
DIC	Digital Image Correlation
GA	Genetic Algorithm
GLARE	Glass Reinforced Aluminium Laminate
hcp	Hexagonal Closed Packed
HTCL	Hybrid Titanium Composite Laminate
LD	Longitudinal Direction
M-C	Mohr-Coulomb criterion
NM	Nelder-Mead Algortihm
RVE	Representative Volume Element
SD	Strength Differential
SSH	Simple Shear
ST	Small Transverse Direction

TD Transverse Direction

TiGr Titanium Graphite

TT Through thickness direction

VTP Vertical Tail Plane

XRD X-Ray Diffraction

List of Symbols

$\mathbf{A}$	Set of hardening thermodynamical forces
$\boldsymbol{\alpha}$	Set of internal variables associated with hardening
α_{11}, α_{22}	CTE in longitudinal and transverse directions
$\mathbf{B}$	Strain-displacement matrix
$\mathcal{B}$	Generic body
$\boldsymbol{\beta}$	Back-stress tensor
β_{11},β_{22}	Coefficients of hygroscopic expansion in the longitudinal and transverse directions
$\mathbf{D}^e$	Isotropic elasticity tensor
D	Damage variable
d_1,d_2,d_6	Damage variables for the CDM model (Maimí et al.)
E	Young modulus
$\boldsymbol{\varepsilon}$	Strain tensor
$\boldsymbol{\varepsilon^e}$	Elastic strain tensor
$\boldsymbol{\varepsilon^p}$	Plastic strain tensor
$\bar{\varepsilon}_p$	Accumulated Plastic strain
η	Stress triaxiality
$\mathbf{f}_e^{int}$	Element internal force vector
$\dot{\gamma}$	Plastic multiplier
$\mathbf{H}$	Generalised hardening modulus
$\mathbf{I}$	Identity tensor
I	Fracture indicator
I_1, I_2, I_3	First, second and third principal invariants

j	Jacobian determinant
J_2, J_3	Second and third invariants of the deviatoric stress
J_2^0, J_3^0	Second and Third invariants of the transformed deviatoric stress
$\mathbf{N}$	Flow vector
ν	Poisson ratio
Φ	Yield function
$\phi_{N,N=1\pm,2\pm}$	Failure criteria
ψ	Specific free energy potential
$\bar{\rho}$	Average mass density
$\mathbf{S}$	Deviatoric stress tensor
$\mathrm{S^L}$, $\mathrm{S^T}$	Longitudinal and transverse compressive strength
$\boldsymbol{\sigma}$	Cauchy stress tensor
$\bar{\sigma}$	Equivalent stress
σ_y	Yield stress
σ_T	Yield stress in tension
σ_C	Yield stress in compression
σ^{th}	Theoretical or predicted yield stress
σ^{exp}	Experimental yield stress
σ_H	Hydrostatic stress
σ_m	Average of the three normal stress components
σ_n	Normal stress component in fracture plane
τ_y	Yield stress in pure shear
τ^T, τ^L	Transverse and longitudinal shear components in fracture plane
Υ	Dissipation function
w	Gaussian quadrature weights
$\mathrm{X^T}$, $\mathrm{X^C}$	Longitudinal tensile and compressive strength
$\mathrm{Y^T}$, $\mathrm{Y^C}$	Transverse tensile and compressive strength
ζ	Lode angle

List of Figures

List of Tables

List of Boxes

Chapter 1

Introduction

1.1 Context and Objectives

The use of composite materials in primary (load carrying) structural components is evermore present in the aeronautical industry including civil aircrafts, not only because of their weight to strength ratio but also because of their superior fatigue behaviour and corrosion resistance. To maintain a competitive advantage, the aeronautical industry continuously seeks more optimized designs with a reduced development cost and weight that can lead to an increase in the aircraft operating efficiency.

One of the advantages of using composite materials and their associated manufacturing technologies is the possibility of having integrated design concepts that allow the minimization of the number of structural parts and consequently the reduction of the number of joints. But the existence of joints still remains unavoidable due to production limitations, maintenance and handling and transportation requirements. Mechanical fastening techniques specifically, are an important joining method for composite structures. They have the advantage of not requiring special surface preparations, allow simple disassemble of parts and are a well-known method from the metallic structural design. However, the joining of composite parts either to other composite parts or to traditional metallic parts is not straightforward since structural coupling in composite materials is significantly less efficient than it is for metals. Composites have higher notch sensitivity, lower shear and bearing strength and a dependence on laminate configuration which hinder the achievement of a satisfactory structural coupling. Moreover, composites are today present in highly loaded joints that play a crucial role in the distribution and sharing of loads and the failure of these joints may lead to catastrophic situations.

In single fastener joints the possible laminate failure modes are: net-section failure, shear-out failure, cleavage (results from the combination of the first two modes) and pure bearing (see Figure 1.1). The net-section and cleavage modes are abrupt with a well defined failure load whereas bearing and shear-out are usually more ductile. The bearing failure mode is the less catastrophic one hence it is the most desirable, although it is not the most efficient [1]. The lower mechanical characteristics of composites require that highly loaded joints include local reinforcement. Various reinforcement techniques have been proposed that aim to overcome the composite materials deficiencies in view of the joint strength increase. Some examples of

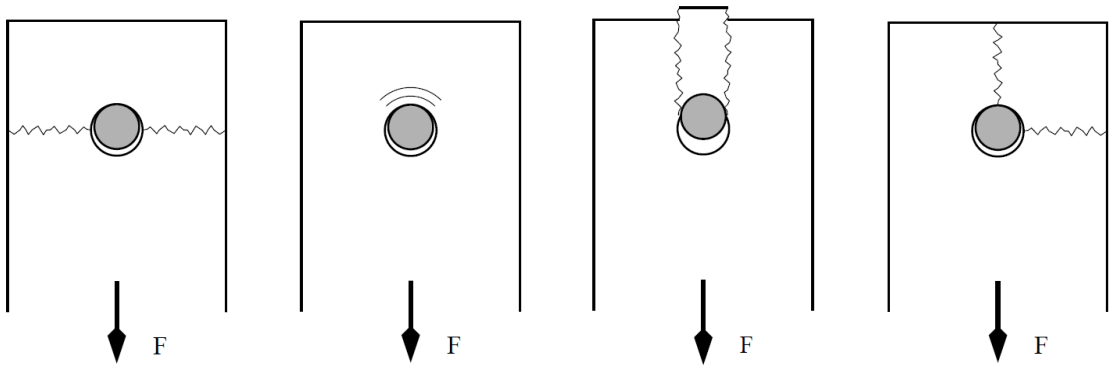

(a) Net-section (b) Bearing (c) Shear-out (d) Cleavage

Figure 1.1: Failure modes of composite joints.

these technologies are the fibre steering technique [2] and the use of bonded metallic inserts [3] as illustrated in Figure 1.2.

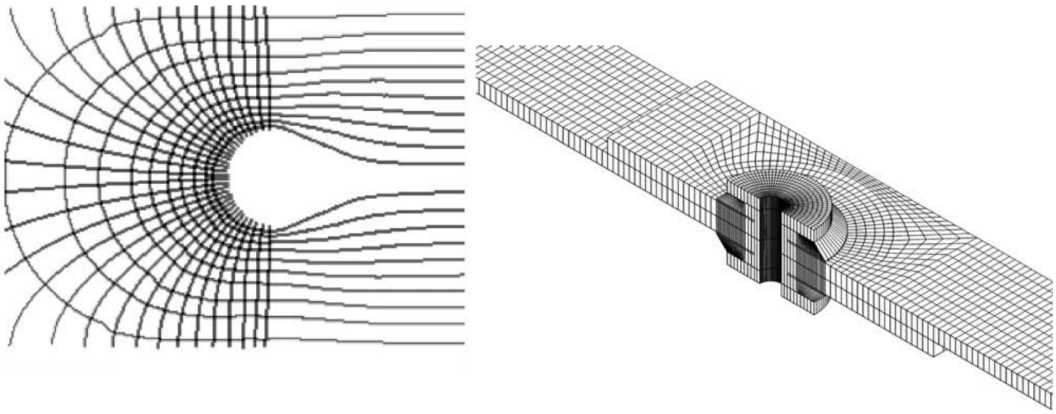

(a) Fibre steering (b) Bonded metallic inserts

Figure 1.2: Reinforcement techniques [2, 3].

Another usual practice to improve the load capacity of composite bolted joints is by means of a local laminate built up at the structure coupling area. However many disadvantages can be pointed out for the use of local thickening techniques. Joint parts are increased in size to accommodate the additional material thickness which will imply weight increase and more space to fit the joints. Additionally, the manufacturing of thickened joints adds complexity to the overall component manufacture as well as to the surrounding parts which have to take into account the thickened part from the dimensional and assembly point of view. In Figure 1.3 two examples of local thickening are illustrated.

One of the most effective ways to improve the load capacity of composite bolted joints resulted from the research activities conducted at the German Aerospace Centre and consists of using a local fibre metal laminate, i. e., a reinforcement of the composite laminate with high strength metal layers. The special feature of this reinforcement technique consists of

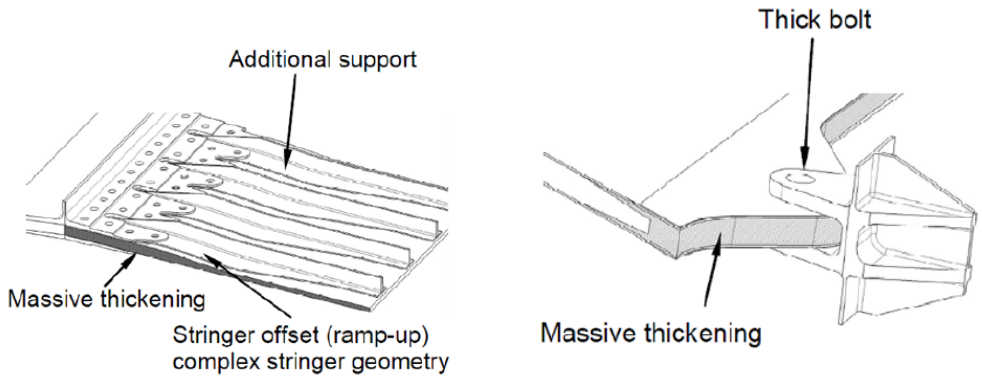

(a) Wing root attachment (b) VTP fuselage attachment

Figure 1.3: Design difficulties due to massive thickening.

embedding the metal layers locally into the bolted joining area as schematically represented in Figure 1.4.

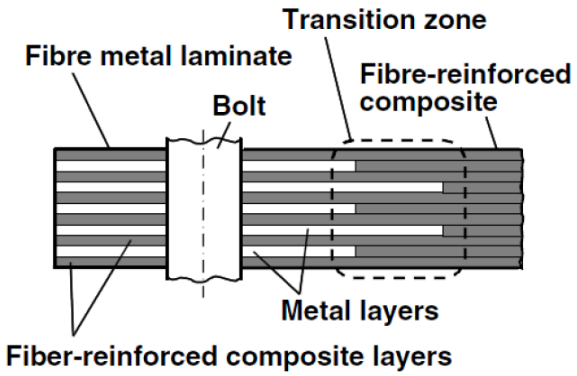

Figure 1.4: Schematic view of a composite bolted joint locally reinforced by metal layer embedding [4].

The local hybridization concept has been investigated mainly for its use in spacecraft applications. The most relevant project is BOJO which dealt with the local reinforcement of highly loaded joints of Ariane 5 boosters [5], payload adapters [6] and distancing modules. It was demonstrated that with local hybridization with titanium the local thickening could be completely eliminated and consequently a simplification of the geometry of the joint and peripheral elements such as ribs, stringers and fittings could be achieved. As a result of the larger bearing capabilities, important weight savings were obtained through the reduction of the overall size of the metallic fittings and the reduction of the number of mechanical fasteners. Although good results were obtained in the frame of BOJO project, the use of this concept in commercial aircraft is not straightforward. Many issues arise when considering the application of hybrid laminate joints in commercial aircraft mainly related with long term requirements. Nevertheless the potential for aeronautical applications is tremendous. By improving the mechanical properties of the composite material locally, joint design will be

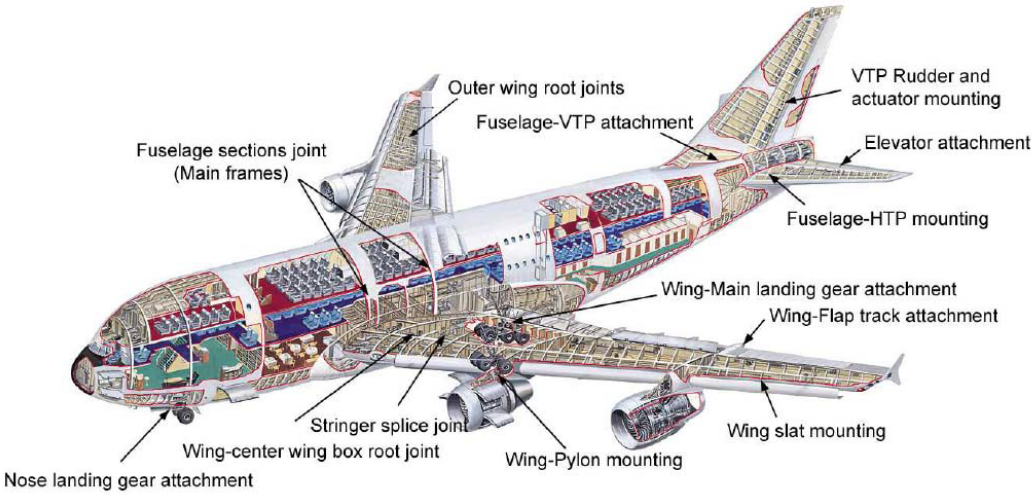

Figure 1.5: Examples of typical highly loaded joints in an aircraft.

lighter and simpler to integrate into aero-structures with special emphasis in highly loaded joints. In Figure 1.5 typical highly loaded joints in a current aircraft are shown.

In this context, the objective of this work is to develop simulation methods capable of predicting the behaviour of hybrid laminate joints allowing a significant reduction in testing and hence time and development costs, and at the same time contribute to the development of design methodologies of hybrid joints that can be used in an industrial environment. The existing analysis methods implemented in finite element codes are based on plane stress formulations that cannot account for the pressure dependent response of the materials used in the joints and the corresponding effect of clamping pressure. For the CFRP plies fully three-dimensional damage models that can accurately account for the effect of clamping pressure on the strength of the joint and the correct simulation of the failure mechanisms have to be considered. For the metal plies, adequate constitutive models that account for plastic deformation, damage initiation and evolution will have to be identified and developed. The use of titanium sheets as reinforcement material poses specific challenges as it requires appropriate plasticity models that are able to predict both the anisotropy and the tension/compression asymmetry.

This work aims to be an important contribution towards the development of advanced reinforcement and joining techniques which enable a considerable improvement of the compatibility of mechanical fastening with the physical properties of composite materials. The purpose is to promote the continued integration of composites into the primary structures with optimal weight savings, accomplishing the maximum potential benefits of composites.

1.2 Thesis Layout

In light of the context and objectives previously outlined, the present thesis is organized as follows. In **Chapter 2** a detailed overview of the state-of-the-art regarding the hybrid joints in terms of the concept, successfully accomplished applications, materials used, common

manufacturing processes and numerical and experimental analysis performed is given.

Chapter 3 is devoted to a detailed description and overview of the importance and challenges regarding the application and modelling of titanium and titanium alloys. The main properties and experimental characterization of the Ti6Al4V alloy is given as well as a review of the current constitutive models developed for the description of materials with hexagonal closed packed crystal structures.

In **Chapter 4** the material parameters of two models applied to the description of Ti6Al4V alloy were determined. The optimization methods used are described and a mixed technique is proposed for the determination of the material parameters of the yield criteria studied.

In **Chapter 5** the numerical and computational procedures for the implementation of the constitutive models for the titanium alloy Ti6Al4V in the finite element framework is presented and the validation of the models is performed through comparison with experimentally obtained data.

Chapter 6 deals with the application of damage models to hexagonal closed packed materials, namely the Ti6Al4V alloy. A number of fracture criteria were implemented and tested. Additionally, a coupled continuum ductile damage model based on the continuum damage mechanics concepts and with plastic flow governed by the CPB06 model was proposed. The proposed model was numerically implemented and its predictive capabilities were tested on axisymmetric Ti6Al4V specimens.

In **Chapter 7** an overview of the numerical modelling of damage onset and evolution of fibre reinforced composites is given. The damage mechanisms are reviewed and the continuum damage model proposed by Maimí et al. [7] is presented.

In **Chapter 8** the numerical modelling of hybrid titanium/CFRP joints is performed. Advanced numerical models for the titanium and composite plies are used for the simulation of bearing in three specimens with different titanium contents. The use of full three-dimensional models as opposed to the Abaqus built-in models was assessed. The impact of the titanium content, clamping pressure and orientation of the titanium plies on the bearing response of the hybrid joints was evaluated.

Finally in **Chapter 9** the main conclusions regarding the several topics addressed in this thesis are presented. The main research topics still under development concerning the improvement of composite joints by means of local hybridization are outlined.

Chapter 2

State-of-the-art

2.1 Concept

The reinforcement of composite bolted joints by means of local hybridization was first suggested for the design of boron reinforced struts of spacecraft applications by Nadler et al. [8]. Nadler proposed a local reinforcement of single-row bolted joints with thin metal sheets at the metallic fitting attachment region. The local hybrid laminate was accomplished through the insertion of adhesive coated and segmented steel sheets between the continuous composite plies. Althof and Muller [9] also proposed a local reinforcement but with all composite plies being replaced by thin metal sheets adhesively bonded to each other in a similar manner to the use of a massive local metallic fitting. Like the massive local metallic fitting, the Althof and Muller's solution also implies that the entire load has to be transferred through the adhesive bond. Although the fatigue performance of the bolted joint was improved, the bonded laminated solution had lower static strength of both the bolted joint and the transition region between the metal laminate and the composite laminate when compared to the monolithic metal arrangement.

The reinforcement of bolted joints by means of the insertion of metal sheets in the composite laminate in the joining area can be achieved either by a ply addition technique or a ply substitution technique. The total load capability of this reinforcement approach depends not only on the load capability of the bolted joint, but also on the strength of the transition zone between the pure fibre composite material and the hybrid laminate zone.

The ply insertion technique consists of interleaving the metal sheets between the continuous composite plies without interrupting them as schematically represented in Figure 2.1. This technique avoids ply interruption and allows the free choice of the metal insert thickness but generates a local thickening. The thickening is however less pronounced when compared to a pure composite built-up with a quasi-isotropic pattern due to the larger bearing load capability of metal in terms of bearing and shear strength. In aircraft structures where concentrated loads are transferred to thin structures like the attachment points of stabilizers, fuselage skin splice joints or the attachment of vertical tail planes, the ply insertion technique is more suitable.

Ply substitution consists of interrupted composite plies and its local replacement by a

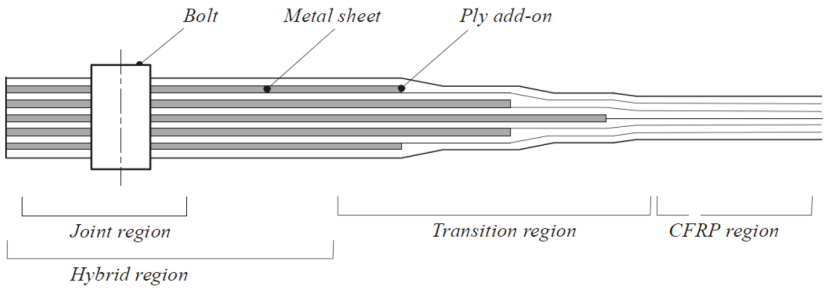

Figure 2.1: Local reinforcement using the ply insertion technique.

metal sheet of corresponding thickness. In Figure 2.2 a local reinforcement based on ply substitution is schematically represented. The composite ply and the metal sheet abut against each other in the ply substitution point. Composite plies adjacent to the interrupted plies and to the embedded metal sheets are continuous and act as adhesive interlayers between the metal foils. The continuous plies should preferably contribute most to the total load carrying of the laminate. When the metal sheet thickness is equal to the nominal single ply thickness a total elimination of local thickening can be achieved. Prepreg laminates with thick sections are particularly flexible in terms of hybridization implementation. Initially an adhesive film coating was used in combination with the metal sheets, however for a given ply thickness the effective metal content gets reduced and can become especially low for thin sheets and highly discretized laminate built-up.

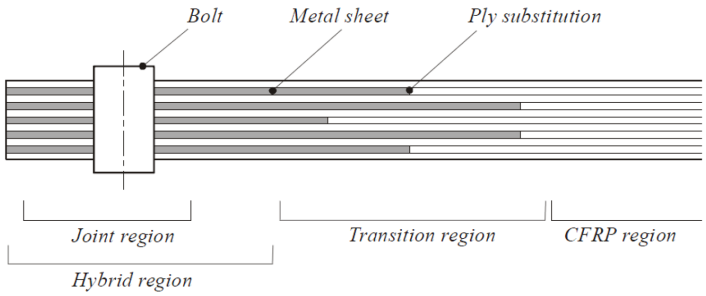

Figure 2.2: Local reinforcement using the ply substitution technique.

In both configurations, three main regions can be identified:

- Hybrid region: is constituted by the joint region where the laminate is purely hybrid. Includes the bolt loaded region and a portion of undisturbed hybrid laminate whose extension depends on the overall structural behaviour, manufacturing restrictions and structural integration aspects. The bolt loaded region is subjected to notch effects, bearing and shear stressing as result of the bolt load transfer.
- Transition region: is the region that contains the composite ply drop-offs and the corresponding metal sheet add-ons. In the ply substitution technique the interrupted composite ply and the inserted metal sheet abut against each other in the ply substitution point. Because a material discontinuity exists, in this case, ply overstressing and delaminations are prone to occur.

- Basis laminate: is the full CFRP region.

The use of adhesive coatings is deemed dispensable in view of the progresses achieved not only in the fields of resins (aiming for higher toughness and strains) but also in the surface treatments for metals. Thus the research activities conducted have mainly focused on ply substitution techniques without the use of additional adhesive coatings.

2.2 Current applications

Hybrid laminates are known as a structural skin material for aerospace applications for more than 40 years. The combination of metal and fibre reinforced plastics at the ply level emerged as a way to improve the performance of the individual constituents. The metal/composite laminated structure stands out due to its excellent specific strength and stiffness and its superior fatigue performance in comparison to pure metal structures. The metal constituent improves the composite properties in terms of impact and damage tolerance behaviour, bearing strength, creep and conductivity. Well known examples are ARALL (Aramid Reinforced ALuminum Laminates) and GLARE (GLAss Reinforced) which were the first and second hybrid laminates to be developed. Arall has been developed for the lower wing skin panels of the former Fokker 27 aircraft and the cargo door of the Boeing C-17 [10]. GLARE laminates are currently applied, for example, in the upper fuselage and leading edges of the tail planes of the Airbus A380 [11]. Other variants have been successfully developed namely the carbon fibre reinforced plastic and titanium laminates, known as HTCL (Hybrid Titanium Composite Laminates) or TiGr (Titanium Graphite) for supersonic applications.

The use of the hybrid laminate concept for the reinforcement of joints is more recent and can be found within the BOJO project in the payload adaptor [6], booster case [5] and distancing modules. The payload adaptor is represented in Figure 2.3.

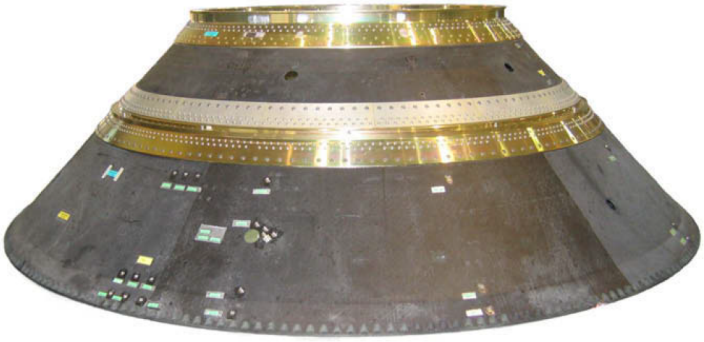

Figure 2.3: Ariane 5 payload adaptor (EADS CASA Espacio) [6].

The baseline structure is a conical monolithic shell with 3mm thick laminate designed as shown in Figure 2.4 and manufactured by a conventional automatic fibre placement process using 0.25mm prepreg tows.

Composite payload adaptors are typical composite structures in spacecraft applications where the aluminium joints and fasteners easily amount to a quarter of the total structural

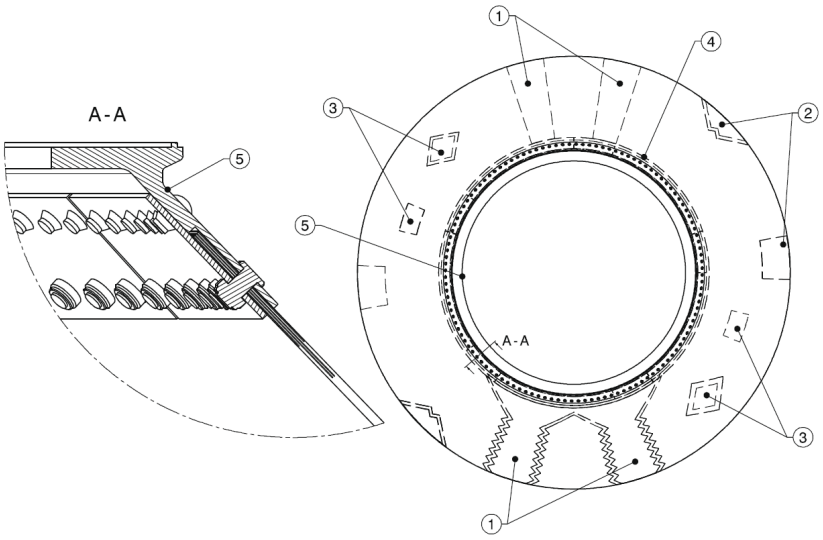

Figure 2.4: Payload adaptor with multiple hybridized zones: circumferential upper root joint reinforcement (4), discrete lower root joint reinforcement (2), line reinforcement along generatrix (1), local reinforcements(3), detail of the aluminium fitting (5) [6].

mass and are hence deemed a potential source of weight savings. With the local reinforcement of the bolted joints with titanium, significant improvements of the bearing, shear and pull-out strength capabilities were achieved. Also, by reducing the bolt rows, fasteners, edge and pitch distances and overlap lengths significant weight savings were accomplished. The simplification of the joint geometry with the consequent simplification of the peripheral elements contributed for the reduction of design, manufacturing and maintenance costs [6].

The intersegment joint of the composite booster case is characterized by a massive local thickening in order to provide enough bearing and shear capabilities and a two bolt row in staggered configuration. The conventional monolithic design and the alternative hybrid design are shown in Figure 2.5. The local hybridization with high strength steel or titanium allowed the total elimination of the laminate thickening and a single-row design yielding a reduction in weight of about 36%, the elimination of secondary stresses and lower bolt bending and through-the-thickness stress gradients. Apart from the weight reduction, the lower number of fasteners also implied a reduction of the assembly work. Also the use of a single bolt row design resulted in smaller and lighter steel connecting rings.

Despite its demonstrated high efficiency, this local reinforcement technique did not found widespread use mainly due to difficulties associated with the surface preparation, bond durability and manufacturing complexity. However, currently, as a result of the increasing requirements for weight reduction together with recent advances in surface preparation techniques, as well as new metal alloys, the local hybridization with metal sheets was put into focus.

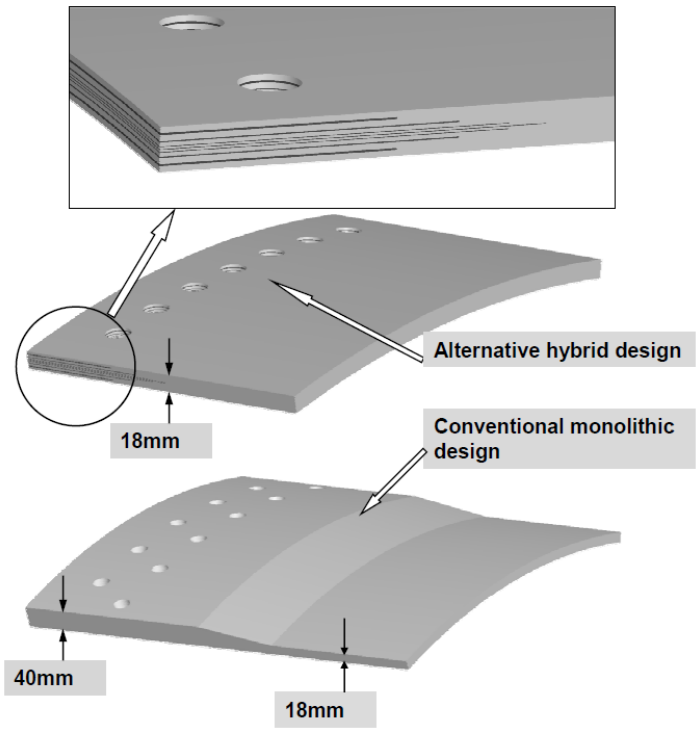

Figure 2.5: Hybrid material application on the intersegment joint of the booster case [5].

2.3 Reinforcement materials

The properties of both the metal and the composite constituent of a hybrid laminate have a crucial effect in the reinforcement efficiency. In general terms, the higher the stiffness and strength of the metallic constituent the more predominant it becomes in the mechanical response of the hybrid laminate. However, the overload of the stiffer constituent may result in the early failure of the other constituent and so having a significantly higher metal stiffness does not necessarily implies a higher joint strength.

For all types of loading conditions, the reinforcement metal has to simultaneously feature higher bearing stiffness and strength than the composite constituent in order to provide a certain extent of reinforcement [1]. Moreover, it is required that the metallic constituent features sufficient ductility to allow the formation of the plastic zone at the notch root and avoid premature shear cracks that reduce the ultimate bearing strength. An adequate ductility also promotes impact behaviour as well as the sheet forming capabilities necessary to tailor the foils geometry. Thus, on a loaded bolted joint, a balance between the ductility and strength properties is essential to promote an optimal damage and strength behaviour. With larger metal stiffness the bearing strength at the damage onset increases and the hole elongation decreases. But, a larger effective stiffness of the metal sheet aggravates the stiffness discontinuity at each ply substitution point and hence leads to the occurrence of metal sheet delamination which affects both fatigue resistance and the static strength of the transition region. In view of the lay-up of the metal sheets, especially on curved surfaces, a larger effective stiffness may be disadvantageous once it requires better bonding capabilities between the composite plies

and the metal sheets in order to avoid spring back or peeling during the lamination process.

Another important issue that needs to be considered especially for the stable long term behaviour in aircraft applications is the corrosion resistance of the metallic constituent and the galvanic compatibility between the metal and the composite. The mismatch of the coefficient of the thermal expansion (CTE) together with the electrochemical properties mismatch, affects the compatibility of the composite and the metal at the material and structural level. Large thermomechanical discrepancies lead to intralaminar and interlaminar stresses that reduce the hybrid material yield stress, deteriorate the fatigue resistance and aggravate the delamination. Also, in terms of dimensional tolerances and assembly, important drawbacks may be generated due to structural distortions after curing. Secondary stresses arise as a result of the constrictions of adjacent structural parts in the assembled components.

Although the first research work on local hybrid laminates has focused mainly on titanium sheets as reinforcement on carbon fibre reinforced plastics [5], high strength steels represent also a promising candidate as reinforcement material. Both feature higher bearing strength and stiffness than optimal CFRP laminates which make them suitable reinforcement materials. Titanium alloys stand out due to their high specific strength, excellent galvanic compatibility to carbon and their low CTE. On the other hand, corrosion resistance steels (CRES) are characterized by a high absolute stiffness (twice as large as titanium alloys), high absolute strengths (reached by inexpensive cold work operations) and excellent fatigue behaviour. The particular advantage of CRES over titanium alloys lies in the specific raw material cost (defined as ratio of cost per strength) that is 20 times lower for steel than it is for titanium [1]. However steels show larger incompatibilities in terms of CTE and galvanic corrosion when compared to titanium.

The bond between the metal and the resin of the composite layers represents another critical aspect that affects the functionality of the hybridization technique. For aeronautical applications, strong requirements regarding the durability and bond strength are imposed. Metals like titanium and CRES are considered difficult to bond, but there exists a wide variety of physical, chemical and electrochemical techniques that are usually combined with previous mechanical processes that promote an improved bonding surface by modifying both the surface topology at macro and microlevels as well as the chemical condition of the metallic surface. Wet chemical etching, anodizing and sol-gel technologies are some of the approaches used for structural bonding [1]. Wet chemical etching and anodizing have good bonding strength and durability, but have the disadvantage of using hazardous materials and are complex processes that demand the development of advanced techniques. Sol-gel technologies have demonstrated good initial and long term durability for titanium and steel bonding [12] with the advantage of being an environmentally friendly, cost-effective, simple and automatable process [13].

2.4 Manufacturing processes

The hybrid composite material can be manufactured using different technologies. The manufacturability aspect is indeed a key issue regarding the industrial acceptance and widespread use of the hybrid reinforcement technology.

The most appropriate manufacturing technology is the prepreg technique in which metal sheets and pre impregnated fibres are stacked and cured in an autoclave. Prepreg technology is widely used for highly loaded structures in a great variety of applications and offers a high flexibility considering the design of the multilayered hybrid material. During the lay-up process, alternate layers of metal foils and prepreg plies are stacked without the addition of any adhesive. The use of adhesive films not only compromises the effective metal content on a hybrid laminate, particularly for thin and highly discretized laminates, but also became dispensable in view of the developments achieved in the surface treatment field. Regarding the surface preparation of titanium for bonding the current industry standard is the Boing Sol-Gel process. The Sol-Gel process is easy to control, is chromate and solvent free and additionally is suited to continuous coil to coil processing of thin gage foil for use in titanium/graphite laminates. In conjunction with bond primer is also an excellent preparation for bonding of 300 series stainless steel [13]. Other surface preparation techniques include grit blasting and subsequent pre-treatment by chemical cleaning and etching [5].

Resin infusion techniques have also shown to be adequate for the local hybrid laminates. Nevertheless, the use of tailored non crimped fabrics does not offer the high design flexibility of prepreg techniques and complicates the achievement of optimal ply substitution arrangements. A reasonable infusion strategy ensures the complete impregnation of the reinforced area without voids [5].

2.5 Experimental Analysis

2.5.1 Bearing Strength

The bearing strength is a crucial parameter that governs the load capability of a bolted joint. In composite materials a minimum edge-to-diameter and width-to-diameter must be met to exploit the bearing strength capabilities and attain a pure bearing failure mode. The lay-up configuration also plays an important role in the bearing strength. By promoting a nearly quasi-isotropic pattern an improvement of the bearing strength can be achieved although it leads to a reduction in the maximum joint efficiency. Thus the exploitation of the isotropic behaviour of metal through the local introduction of metallic plies in the joint area can improve the bearing strength capabilities of a hybrid joint. However, due to higher specific weight of metal the joint's weight efficiency tend to reduce. Many studies were conducted for the experimental evaluation of the bearing strength of hybrid bolted joints under various conditions [1, 14, 15].

Influence of the metal content

The influence of the metal content on the bearing strength of hybrid laminate joints was studied by Kolesnikov et al. [4], P. Camanho et al. [15] and A. Fink et al. [6]. The metal content within the hybrid laminate can be changed by varying the number of metal foils thus influencing the mechanical properties. The first experimental study regarding the impact of the metal content on the load capability of hybrid bolted joints was conducted by Kolesnikov et al. [4] where single-row and three-row bolted joints were tested with titanium contents of

0%, 13%, 23%, 34% and 54%.

P. Camanho et al. [15] conducted an experimental and numerical investigation of the mechanical response of bolted joints with local hybridization. Tests regarding the analysis of the bearing strength were made with several specimens featuring different titanium contents. The stacking sequence and geometric details of the specimens manufactured are shown in Tables 2.1 and 2.2 and in Figure 2.6. The two B7 specimens have the same stacking sequence but differ in the length of the titanium plies.

Table 2.1: Stacking sequence of the test specimens [15].

Reference	Lay-up
B1/TT0	$[0/+45/0/90/-45/0]_s$
B6/TT1	$[0/+45/0/Ti90/-45/0]_s$
B7/TT2	$[0/Ti+45/0/90/Ti-45/0]_s$
B7/TT3	$[0/Ti+45/0/90/Ti-45/0]_s$
B8/TT4	$[0/Ti+45/0/Ti90/Ti-45/0]_s$

Table 2.2: Geometric details of the bearing test specimens [15].

Reference	Geometry	Observations
B1/TT0	w/d=7, e/d=4	Reference
B6/TT1	w/d=7,e/d=4	Hybrid
B7/TT2	w/d=7,e/d=4	Hybrid
B8/TT4	w/d=7,e/d=4	Hybrid

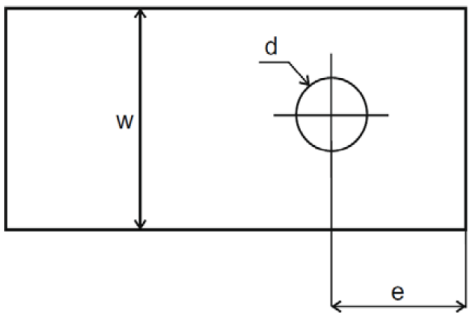

Figure 2.6: Geometry of the bearing test specimen (e-end distance, d-hole diameter, w-width).

The experimental results demonstrated the relation between the bearing stress and the cross head displacement for different titanium contents (Figure 2.7).

It was concluded that the bearing strength increases with the titanium content: by increasing the titanium content from 0 to 50% the bearing strength increased 154%. Also the specific bearing strength, defined as the ratio between the bearing strength and the mass of the joint, increased 29% when compared to a monolithic CFRP joint.

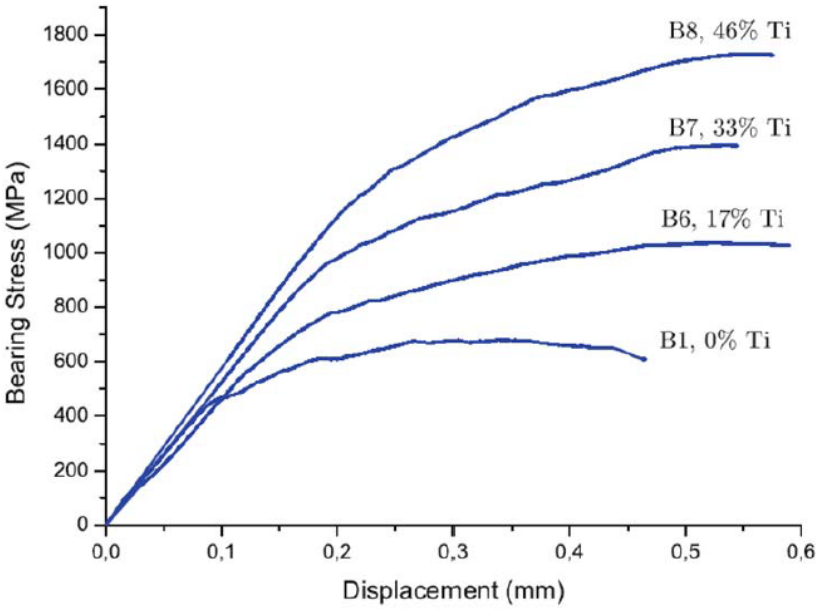

Figure 2.7: Experimental relation between the bearing stress and the cross-head displacement [15].

The experimental study of the bearing strength of various titanium hybrid laminate configurations (16.7%, 33.3% and 50% titanium content) was also performed by A. Fink et al. [6] according to the standards [16] for on-axis and off-axis loadings. The results were presented in terms of ultimate bearing strength (Figure 2.8) and 0.5% offset bearing strength (assumed as a representative value for the onset of damage)(Figure 2.9).

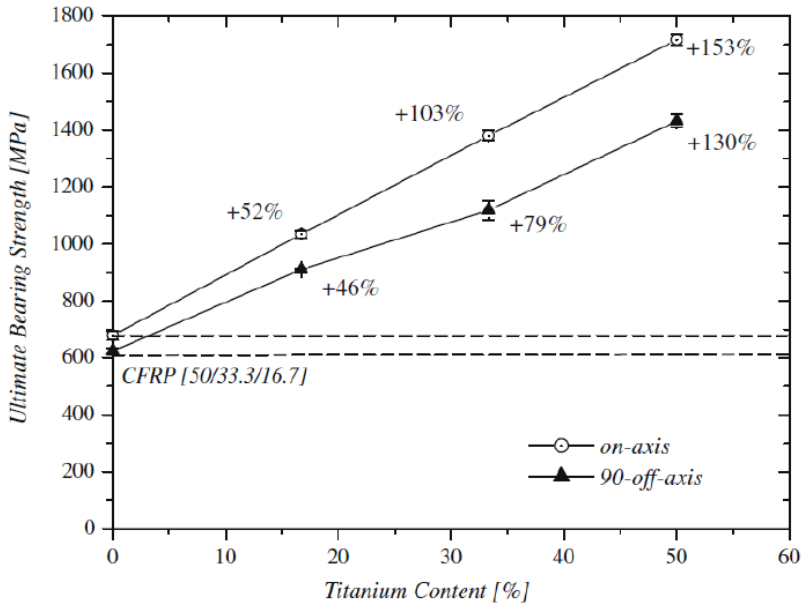

Figure 2.8: Ultimate bearing strength vs. titanium content [6].

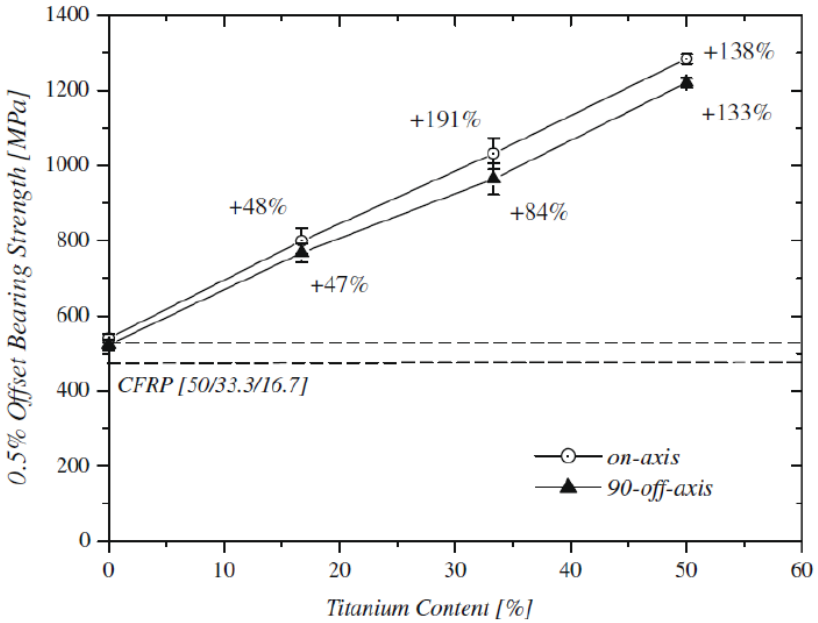

Figure 2.9: 0.5% offset bearing strength vs. titanium content [6].

The bearing performance showed an almost linear behaviour with increasing metal content leading to improvements of 153% of the ultimate bearing strength. Regarding the offset bearing strength, only slightly lower improvements were obtained denoting similar efficiencies if taking the ultimate bearing strength or the permanent hole deformation as the bearing design criteria. The experimental bearing response for the on-axis configurations was obtained as a function of the relative hole elongation. Similarly to the previous results a linear elastic region and a degradation region triggered by damage onset and accumulation could be identified.

The on-axis and 90° off-axis bearing strengths of unidirectional CFRP prepreg laminates hybridized with a varying content of titanium (Ti-15-3-3-3 with 0.25mm thickness) and steel (type 301 with 0.3mm thickness) were presented in [1]. A comparison with three different composite laminates ([50/50/10] on-axis, [70/20/10] on-axis and quasi-isotropic) was made. The study demonstrated the rapid increase of the bearing strength with the rising metal content. The results are shown in Figure 2.10.

The results obtained demonstrated that at very low metal contents, between 10% and 20% and for both on-axis and off-axis loading, the bearing strength of the hybrid laminate exceeded the bearing strength of optimal pure composite laminates. The superior strength behaviour of the steel reinforced laminates in comparison to titanium was also noticeable. Furthermore, the on-axis strength was generally larger than the 90° off-axis bearing strength but with rising metal content the difference decreased due to the predominant role of the metal constituent. For steel hybrid laminates, slightly larger off-axis strength was observed for higher metal content.

The bearing stress curves for titanium hybrid laminates with metal contents of 20%, 36.4% and 50% were also presented and compared to the [50/40/10] composite laminate. Figure 2.11 depicts the on-axis bearing stress curves against the hole elongation for the hybrid laminates

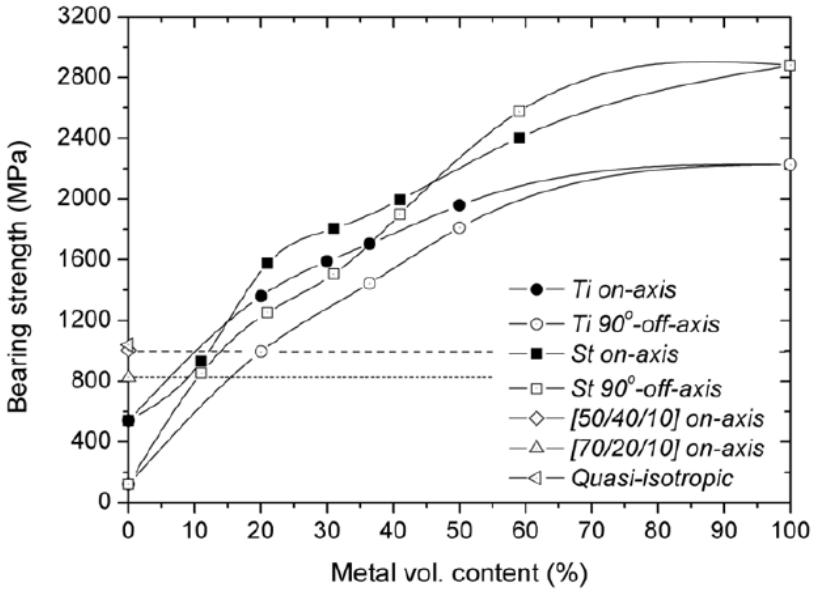

Figure 2.10: Bearing strength of CFRP/steel (0^o+St) and CFRP/titanium(0^o+Ti)laminates against the metal volume content in comparison to pure CFRP laminates [1].

and the [50/40/10] composite laminate.

The onset of the nonlinear response for the hybrid laminates and for the composite laminate took place at a hole elongation of about 4%. However, the maximum bearing strength for the hybrid laminates was reached at higher hole elongations than for the composite laminate. The bearing curves evidenced an apparent metal-like hardening effect for the hybrid laminates while the pure composite showed a moderate and irregular increase of the load bearing capabilities once the yield point was exceeded. The hybrid laminates also showed a clear maximum bearing load capability followed by a drastic drop of strength typical of laminated materials subjected to standard bolt bearing testing.

The bearing curves for the steel reinforced unidirectional composite laminates were also presented in [1] and are depicted in Figure 2.12. The results for hybrid laminates with five different metal contents (11%, 21%, 31%, 41% and 59%) were compared with a [50/40/10] pure composite laminate. The bearing curves present similarities with the ones obtained for the hybrid titanium laminates. However, for the steel hybrid laminates the yield point was reached at lower elongations. This evidenced the stronger role played by steel at the onset of the inelastic response.

A fractographic analysis of the bearing plane allows the visualization of the failure mechanisms leading to the bearing damage. Through-thickness fractographys of the bearing plane for the titanium and the steel hybrid laminates are presented respectively in [15] and [1]. The intra-ply failure mechanisms like kink band formation and transverse matrix shear for the composite plies as well as the metal sheets plastic deformation and fracture and also inter-ply failure mechanisms (delamination) can be seen. Figure 2.13 and 2.14 show the damage evolution at different percentages of the maximum bearing strength. Both in the titanium hybrid laminate and in the steel hybrid laminate, the formation of kink bands in the 0^o plies is vis-

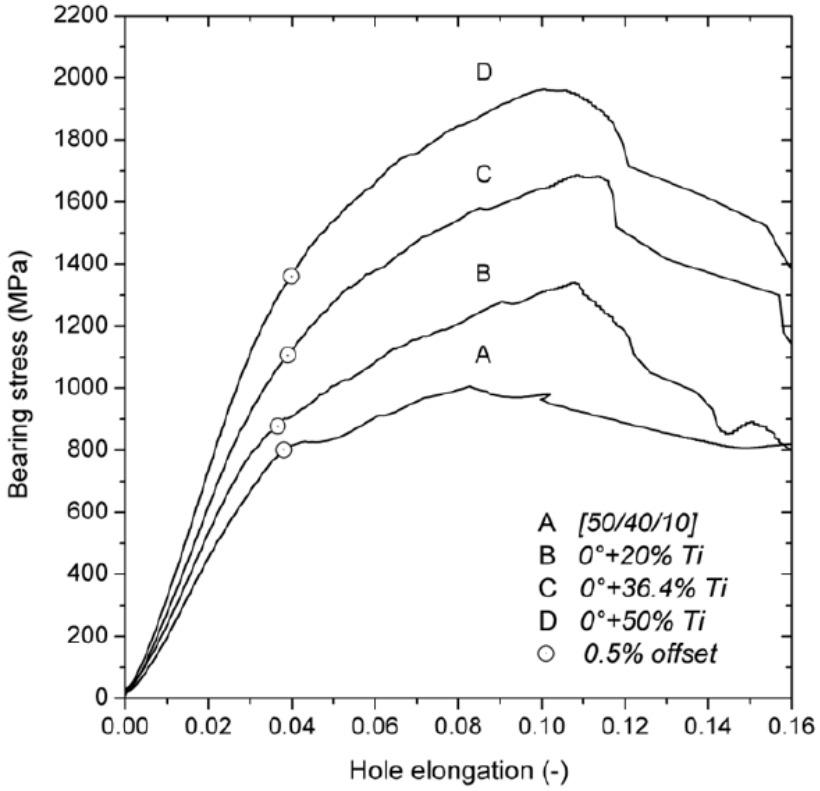

Figure 2.11: Bearing stress curves for three CFRP/titanium hybrid laminates (0^o-Ti) with different titanium content in comparison to a reference composite laminate [1].

ible, and delaminations and plastic deformation of the metal sheets are present at 80% of the maximum bearing strength. The titanium sheets shear fractures are deemed a consequence of its relatively low ductility as a result of the high hardening level and evidenced the limited reinforcement effect of extremely maximized titanium strengths [6].

It is evident that the onset of the damage behaviour at the hybrid laminate is driven by the damage of both the metal and the composite plies and their interaction. The damage onset at the metal plies is mainly related to the plastic zone at the notch root while the bearing damage onset at the composite plies is associated with the kink band formation. Thus, the bearing damage onset is attributed to the damage onset of the composite as long as this is the weakest constituent and the metal the reinforcing one. It was finally concluded that a higher effective stiffness of the reinforcing constituent, higher modulus and volume content relives the composite plies and allows for larger stresses at the onset of damage. Moreover, a larger metal stiffness allows for a better distribution of stresses around the loaded hole, reducing the out-of-plane deformation of the metal sheets once the delamination and the loss of lateral support are initiated. Hence larger stiffness shows greater potential for developing higher ultimate bearing strengths.

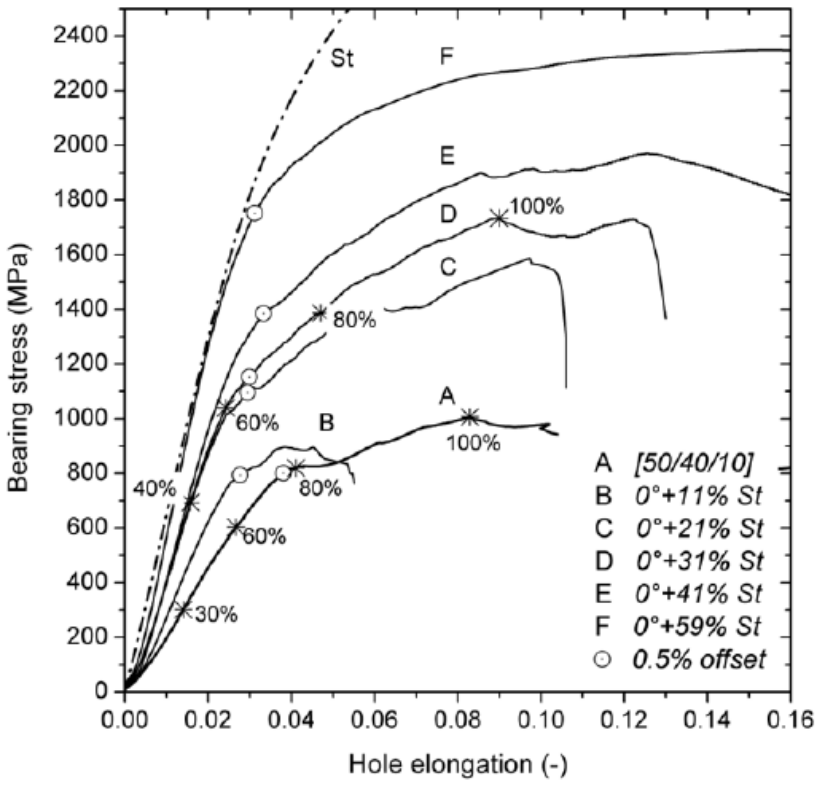

Figure 2.12: Bearing stress curves for five CFRP/steel hybrid laminates (0°+St) with different steel content in comparison to a reference composite laminate [1].

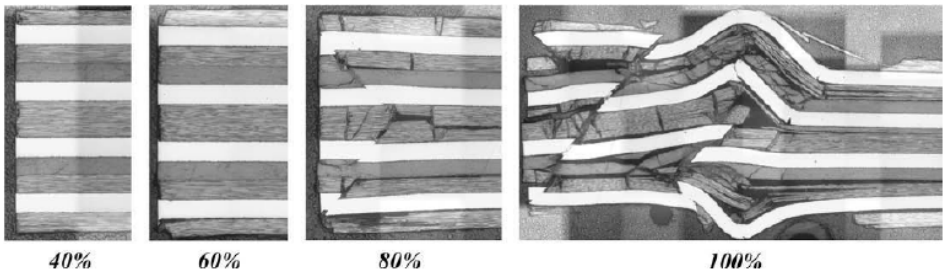

Figure 2.13: Damage evolution at the bearing plane of a hybrid CFRP/Ti laminate under bolt-bearing loading for different percentages of maximum bearing strength [15].

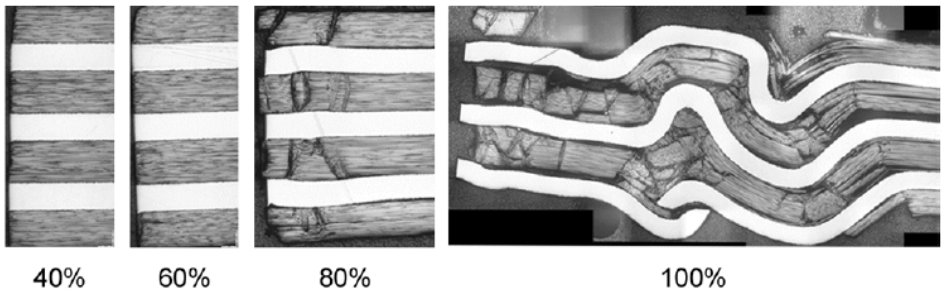

Figure 2.14: Damage evolution at the bearing plane of a hybrid CFRP/steel laminate under bolt-bearing loading for different percentages of maximum bearing strength [1].

Influence of metal strength and stiffness

The effect of the metal strength and stiffness was experimentally analysed by A. Fink [1]. Hybrid laminates reinforced with titanium with three different tensile strengths (980MPa, 1370MPa and 1630MPa) and two for the steel (1612MPa, 2000MPa) have been used and compared to two reference CFRP laminates ([50/40/10] and [70/20/10]). The impact of rising metal strength on the laminates bearing behaviour is depicted in Figure 2.15. It was demonstrated that larger tensile strengths of the reinforcing metal resulted in higher reinforcement effects.

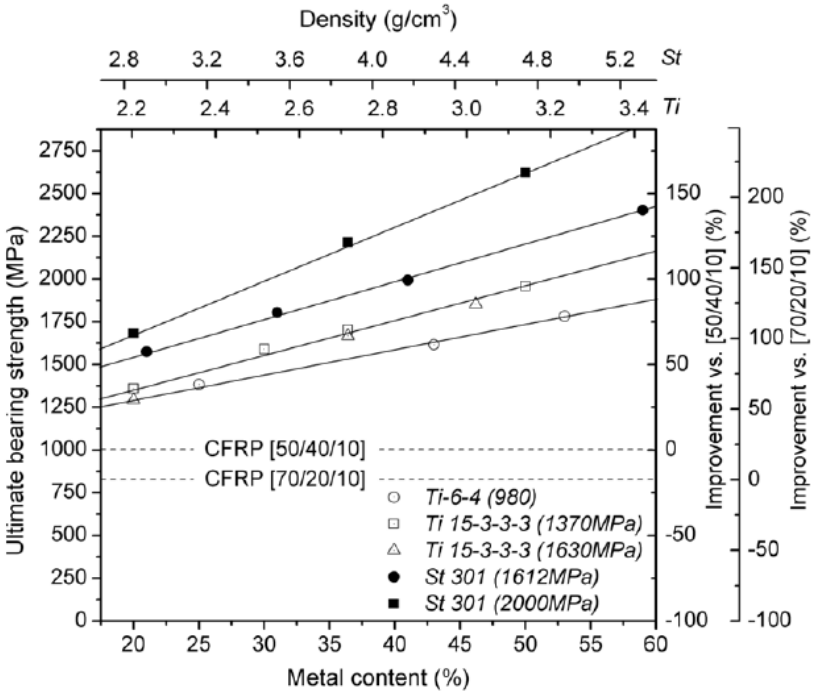

Figure 2.15: Ultimate bearing strength of CFRP/steel (0°+St) and CFRP/titanium (0°+Ti) laminates for different metal content and metal strengths in comparison to two reference CFRP laminates [1].

The use of greater strengths has however a limited impact. As it was demonstrated for the titanium, no improvements were obtained beyond 1370MPa. The limited effect of further strength increase is associated with the damage accumulation on the composite constituent, which will lower the bearing strength capability and induce overstressing of the metal sheets that will undergo plastification and deform laterally and buckle. Thus, despite the titanium strength, the damage onset on the composite plies remains unavoidable and consequently the failure of the hybrid laminate will take place. The increase in the metal strength will only have a positive impact if it is accompanied by an increase of the metal modulus. This is achieved by the steel hybrid laminates. It was showed that the strength increase is twice as efficient for steel as for titanium, i.e., an increase of 400MPa leads to an improvement of the bearing strength by a factor of two. For a metal content of 50%, titanium hybrid laminates report an improvement of 100% while the steel laminates register an increase of 160% of the

bearing strength with reference to a composite [50/40/10] laminate.

The analysis of the specific ultimate bearing strengths (ratio of ultimate bearing strength to laminate density) was also reported in [1]. The experimental results obtained for the specific ultimate bearing strength as a function of the metal content and the metal strength were given (Figure 2.16). It was concluded that due to the specific weight of steel, the steel hybrid laminates have higher densities, however less volume content is needed to attain a specific bearing strength. This would imply less additional laminate mass, less sheets, less manufacturing complexity and lower material and process costs. Thus, to achieve a bearing strength of 1750MPa with a titanium hybrid laminate, a 40% metal content would be necessary. On the other hand, with a steel hybrid laminate, only 23% metal content is necessary. The resulting specific weight of the steel hybrid laminate is only 7% higher than its titanium counterpart.

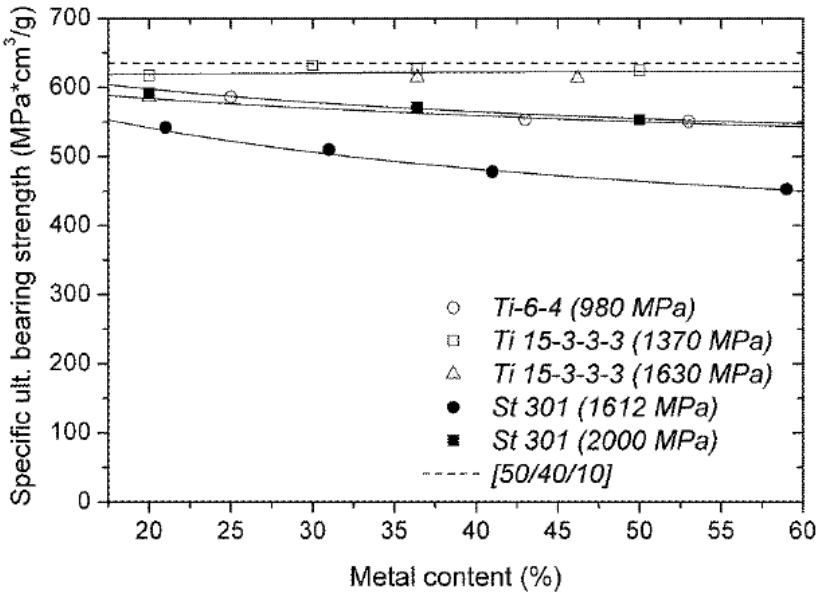

Figure 2.16: Specific ultimate bearing strength of CFRP/steel (0^o+St) and CFRP/titanium (0^o+Ti) laminates for different metal content and metal strengths in comparison to a reference CFRP laminate [1].

Concerning bolted joints the specific values with reference to the laminates density alone do not provide a proper mass efficiency evaluation. Additional mass of fasteners, overlaps, fittings, straps, laminate ramps for pad-ups and peripheral elements need to be considered. Thus, the absolute values are the determining factor in the assessment of the joints weight efficiency. With larger absolute strength a reduction or even elimination of local pad-up, consequent reduction of ramps, eccentricities and fastener grip lengths could be achieved.

Influence of edge distances

The edge distance is an important aspect in the design of single row or lug joints since it represents an influencing factor on the bearing strength and consequently on the joint efficiency.

Bearing failure is the preferred failure mode due to its less catastrophic characteristics. Although for composite laminates the maximum joint efficiency can be obtained at net tension failure modes, the difference over the maximum joint efficiency at bearing failure is small [1]. The effect of varying the edge-to-diameter and width-to-diameter ratios for a titanium hybrid laminate composed of 70% 0º plies and 30% titanium sheets was studied by A. Fink [6]. Standard bearing specimens featuring an edge-to-diameter ratio of e/d=4 and a width-to-diameter ratio of w/d=7. By reducing the edge and width distance, an increase in the joints weight efficiency can be achieved. However, large reductions of both the width and edge distances result in catastrophic and inefficient net-tension and shear-out failures respectively. The effect of varying edge-to-diameter and width-to-diameter ratios is presented in Figure 2.17. Even for low metal contents the hybrid laminate reaches its maximum bearing strength at edge-to-diameter and width-to-diameter ratios of three [1].

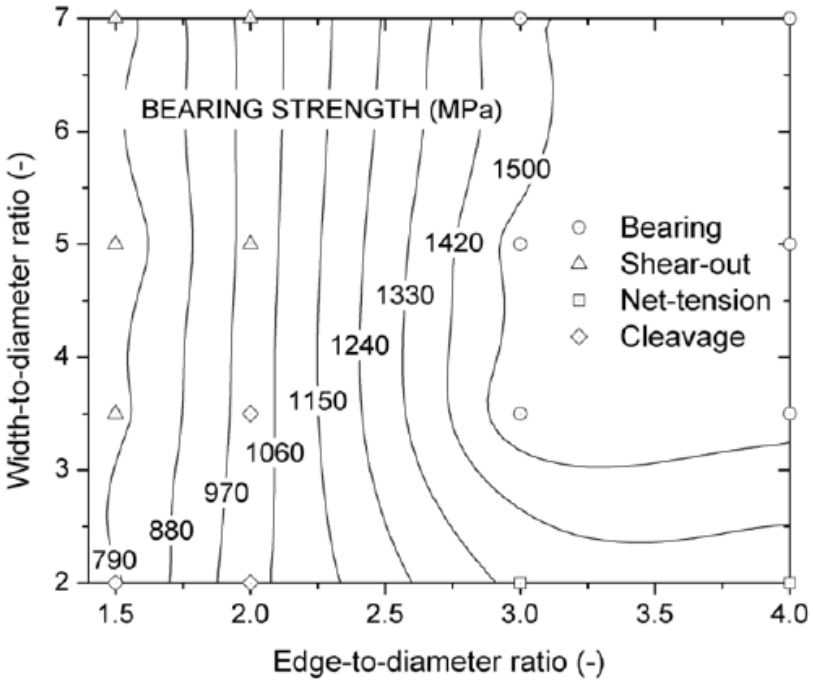

Figure 2.17: Impact of width-to-diameter and edge-to-diameter ratios on the bearing strength of a hybrid laminate (0º+30% Ti) [1].

The effect of the diameter-to-width variation in the bearing strength for a titanium hybrid laminate and a steel hybrid laminate both with 30% metal content and 0º composite plies was compared with typical composite laminates [1]. It was observed that higher bearing strengths were obtained for lower width-to-diameter ratios and that after reaching the bearing failure, despite the diameter-to-width ratio, the laminate bearing strength remained constant (Figure 2.18).

Considering the bearing capabilities it was shown that the titanium and steel hybrid laminates offered an improvement of around 40% and 60% respectively on the joint efficiency. Due to larger diameter-to-width ratios for the hybrid laminates, the mechanical efficiency increased by an additional factor of 1.8 for the titanium and 1.4 for the steel resulting in

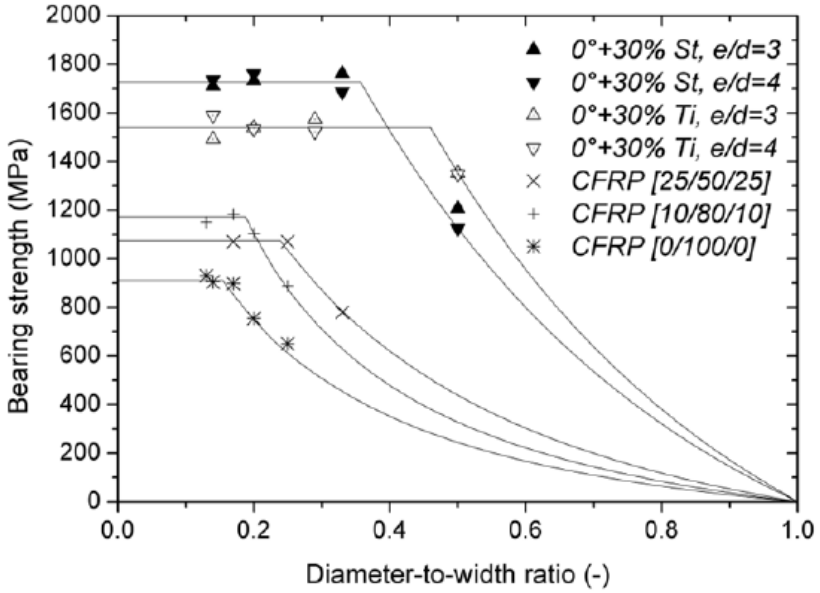

Figure 2.18: Impact of diameter-to-width ratios on the bearing strength of hybird laminates in comparison to typical composite laminates [1].

reinforcement efficiencies of 2.6 and 2.2 times larger when compared to a quasi-isotropic laminate. However, given that the reduction of the number of fasteners is a primary objective of the use of local hybrid laminates, the narrowing of bolt spacing has no practical meaning and thus the additional increase of joint efficiency for large diameter-to-width ratios was presented has an academic approach.

2.5.2 Transition region

Together with the mechanical behaviour of the bolt loaded hole, the mechanical response of the transition region in locally reinforced laminates also influences the joint efficiency. The ply substitution points, or ply addition points represent material discontinuities prone to induce delaminations and stresses. To exploit the full reinforcement capabilities within the bolted joint region it is imperative to ensure that the transition region has larger joint efficiencies than the bolted joint itself [1]. Experimental investigations concerning the transition region were conducted by A. Fink et al. [6] and P. Camanho et al. [15].

In [15] a number of test specimens representing the transition region with various configurations and stacking sequences were used. The relation between the remote stress, defined as the ratio between the applied load and the cross-section of the test specimen, and the cross-head displacement was obtained. It was verified that this relation is linear and that the hybrid laminate has only marginally lower strength than the full composite specimen (Figure 2.19).

A C-Scan of one of the specimens was also performed evidencing a delamination propagating from the end of the titanium plies just before the specimen failed (Figure 2.20).

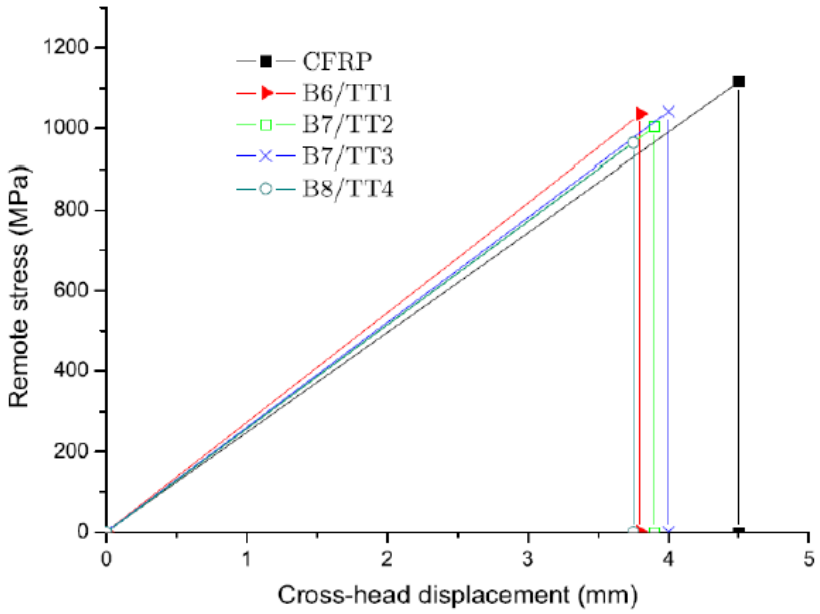

Figure 2.19: Relation between the remote stress and the displacement for the transition specimens [15].

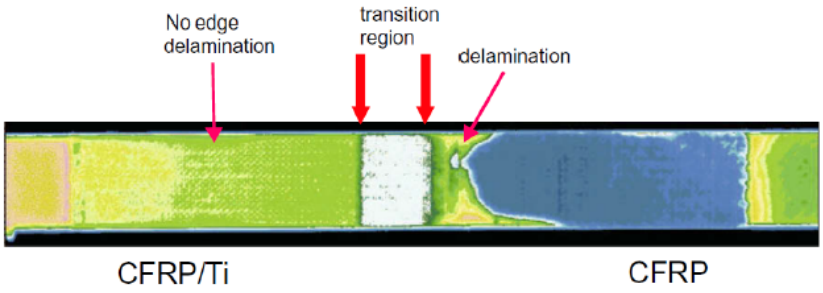

Figure 2.20: C-scan of a CFRP/titanium specimen [15].

In the experimental work conducted by A. Fink et al. [6] the coupling efficiency (the ratio of the transition strength to the basis composite strength) under tensile loading was determined. The results showed that very high values of the coupling efficiency (between 90% and almost 100%) are reached (Figure 2.21). To evaluate the effect of closely placed substitution points a reduced step distance was considered in one of the specimens. No negative impact was detected for small step distances. The fracture of all specimens was located within the transition region in the composite and involved light delaminations which are mainly associated with laminate stacking induced edge-effects.

The compressive performance was also evaluated. The higher compressive strength obtained for the pure hybrid specimen resulted of the substitution of the weaker composite plies by stiffer and stronger titanium sheets. The transition specimen evidenced a higher compressive strength than the pure composite due to the higher hybrid laminate stiffness and possible differences in load introduction. Thus, even with large titanium sheet thicknesses the higher performance and robustness of the transition region was demonstrated for tension

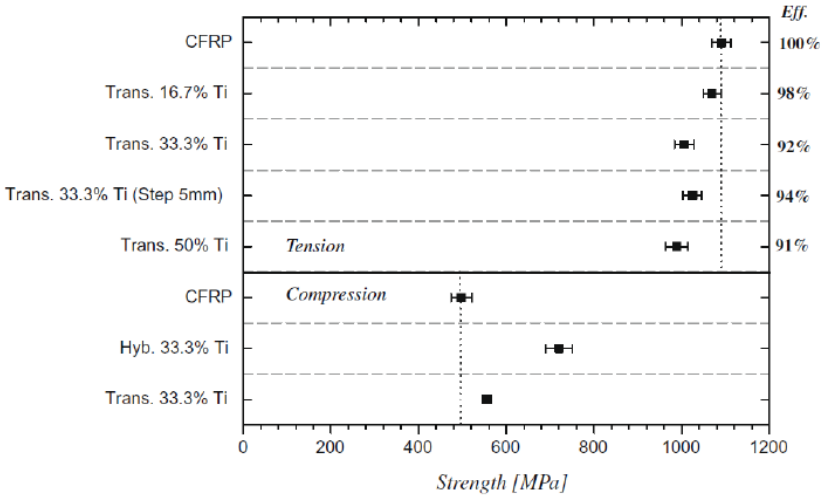

Figure 2.21: Tensile and compressive strength of different transition region configurations [6].

and compression loading.

2.6 Numerical Modelling

Numerical techniques such as the finite element method are currently available to effectively examine complex structures and provide detailed information throughout the entire loading history avoiding the need for extensive experimental work. Nevertheless, experimental results have a crucial role in the calibration and validation of numerical models. A numerical investigation on the mechanical response and damage behaviour of a bolted joint manufactured using hybrid composite laminates was conducted by P. Camanho et al. [15]. The local hybridization consisted of the substitution of CFRP with titanium plies and two regions were considered in the analysis: the bolt bearing region and the transition region. Abaqus finite element code was used for the numerical analysis performed.

The simulation of the bolt bearing region was performed using a three-dimensional model that accounts for ply failure mechanisms and a plasticity model for the simulation of the inelastic response of the titanium plies. The failure mechanisms that occur in the composite plies were simulated using the progressive damage model available in Abaqus. The Abaqus progressive damage model uses the Hashin failure criteria for the prediction of the onset of the different types of intralaminar damage: fibre tensile fracture, fibre kinking, matrix tensile cracking and matrix compressive failure. In addition, the model used, also predicts the propagation of the different ply damage mechanisms by defining a linear damage evolution law that uses the material toughness for each failure mechanism, ensuring a mesh-independent result. For the titanium plies and the bolt an elastic-plastic material model was used. The onset of plastic flow was determined by the von Mises yield criteria and the plastic deformation was simulated using an isotropic hardening behaviour and an associated flow rule.

The specimen was meshed using eight-node continuum shell elements with two levels of refinement: a finer mesh that was used in the neighbourhood of the hole and a coarser mesh approximately four times less refined. On the coarser mesh a linear elastic response was imposed. In the thickness direction one element per ply was considered. The bolt was modelled by a titanium cylinder meshed with fully integrated three-dimensional linear hexahedral elements. The frictional contact between the bolt and the laminate was taken into account in the analysis following a Coulomb's friction law with a coefficient of 0.3. For the simulation of ply damage and non-uniform contact through the thickness of the hole of the laminate, plane stress elements were used that represent the free-edge of the specimens. For the simulation of delamination and fracture in the transition region plane-stress and cohesive elements were used. The numerical models were validated by comparison of the experimental data with the predicted results. For all specimens simulated a non-catastrophic bearing failure mode, characterized by a progressive elongation of the hole, was predicted by the numerical model. In Figure 2.22 the predicted region where fibre kinking takes place in the 0^o ply at 40%, 60% and 80% of the maximum predicted bearing stress is presented.

The predicted bearing strengths and the bearing stresses at the onset of damage were compared with the corresponding values obtained experimentally. It was demonstrated that the numerical models predicted with accuracy the maximum bearing stress for the different specimens tested and that the elastic limit of the joints, i e., the bearing stress at the onset of damage, was predicted within reasonable accuracy. For the prediction of the elastic limit, higher errors were obtained. These errors are associated with the fact that Abaqus damage model is defined for plane stress conditions which means that only the in-plane components of

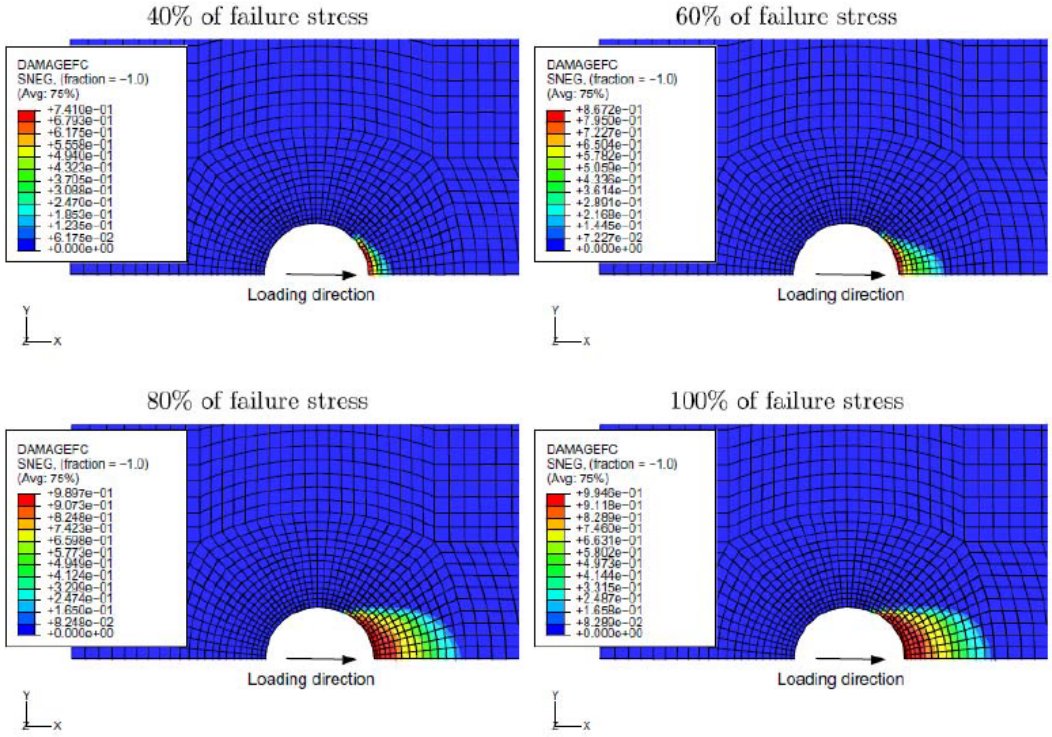

Figure 2.22: Predicted evolution of fibre kinking on top 0º ply of one CFRP/titanium test specimen [15].

the stress tensor were predicted and the out of plane components of the stress tensor that are present along the hole of the laminate were not used in the failure criteria. Also, the effect of the shear stresses on the onset of fibre kinking is not considered by the Hashin failure criteria leading to an over-prediction of the elastic limit. In Figure 2.23, the relations between the bearing stress and bolt displacement for the numerical and experimental results are compared. It was verified that the displacement at the peak value of the bearing stress is higher than the predicted by the numerical models which can be explained by the fact that the delaminations experimentally identified through C-scan were not simulated in the finite element models.

Regarding the titanium plies, despite the fact that the finite element models account for their elasto-plastic response, their fracture is not considered and so consequently after cracking the titanium plies can still transfer load under compression due to the contact between the crack planes. However, the relative movement of the fractured surfaces of the titanium plies increases the compliance of the joint leading to a higher displacement at the peak load.

The transition region is simulated using two-dimensional plane stress finite elements in the free edge of the laminate. The use of linear elasticity in the numerical analysis of the transition region created a difficulty associated with the fact that there are multi-material corners that represent singularities in the stress field. Thus the maximum stress predicted by the numerical models increases with the mesh refinement. Therefore cohesive elements were used along the titaniuum-CFRP and CFRP-CFRP interfaces and in the vertical interface between CFRP plies and the end of the titanium layers. By using cohesive elements it was possible to simulate a fracture process zone in the interfaces between the plies and a transverse

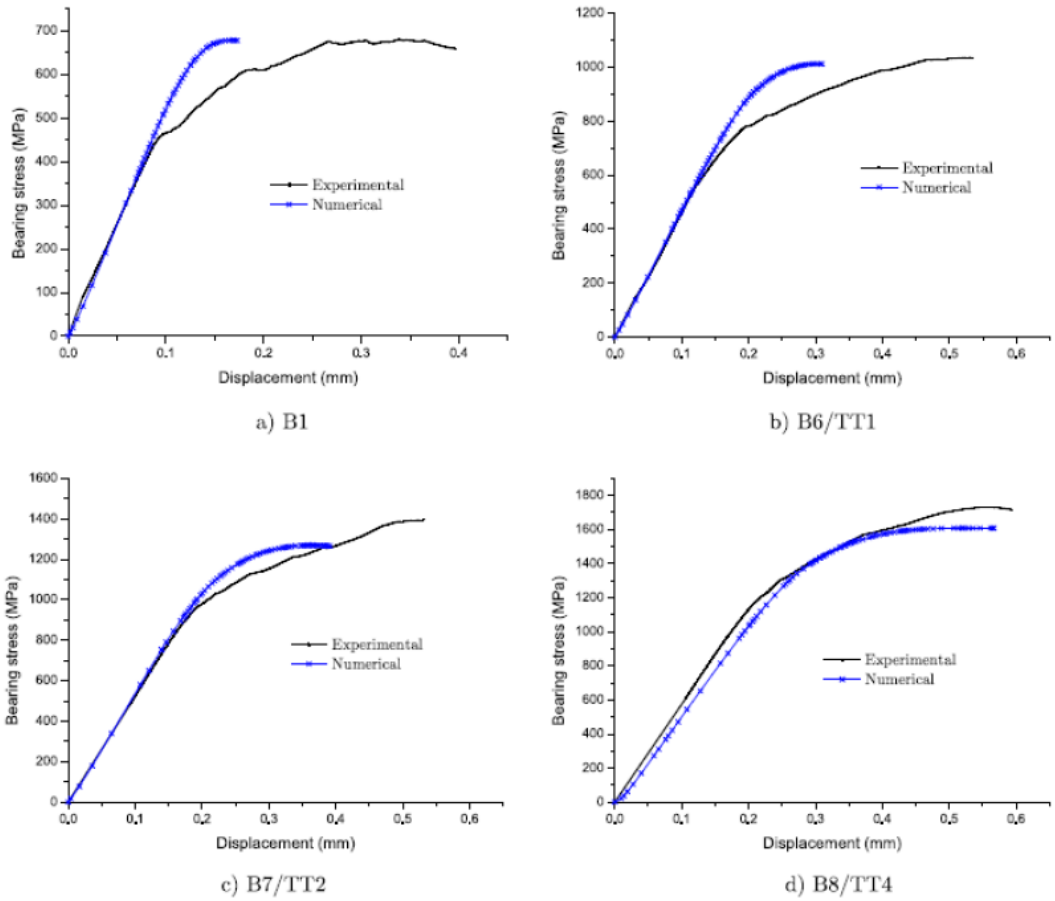

Figure 2.23: Predicted and experimental bearing stress-bolt displacement relations [15].

crack at the end of the titanium ply. The results obtained showed that the strength of the transition region could be predicted with accuracy. The numerical models predicted a linear load-displacement relation up to failure, which was consistent with the experimental results. The change in the step distance from 5mm to 15mm decreased the strength of the transition region by 1.8%. It was observed that the strength of the transition region was always higher than that of the bolt bearing region which sustains the failure mode of the hybrid laminates: the failure occurs in the bolt-bearing region and not in the transition region.

Chapter 3

Titanium and Titanium Alloys: physical aspects and constitutive modelling

3.1 Titanium and titanium alloys in aeronautics

Titanium is a fairly abundant metal in the earth's crust predominantly in the form of oxide minerals like rutile (TiO_2) and ilmenite ($FeTiO_3$). It was first discovered in 1971 but the production of ductile, high purity titanium proved to be difficult. It was not until 1936 that a commercially viable process was established and the commercial production of titanium became possible. This process, known as "Kroll process", is still the most widely used method for titanium production. As a structural material, titanium alloys gained major acceptance after the Second World War for aircraft engines. Today, the aerospace sector is still the prime consumer of titanium and its alloys as cost continues to be the major barrier to a broader application range. Aerospace is the sector where higher costs for weight savings are supported. The much lower payload capacity in aircraft legitimises the much higher payoff for weight reduction thus sustaining the importance of light metals like titanium and its alloys as materials of choice in aircraft and space industries.

The success of titanium alloys for aerospace applications is driven by the combination of outstanding properties like weight, strength, corrosion resistance and/or high temperature stability where aluminium alloys, high strength steels or nickel based superalloys are insufficient. Typical applications are heavily loaded airframe structures like wing boxes, wings and undercarriage parts, landing gear components and jet engine parts. Their compatibility with carbon fibre composites makes them particularly adequate for applications where these two materials are placed in contact and as the use of composites increases with each generation of aircraft so does the need to use titanium alloys. The use of titanium in large passenger aircraft has grown from a relatively modest 3-5% of the structural weight before 1980 to much grater percentages in modern aircraft, like A380 and B777, where titanium accounts for 9% and 10% of the structural weight respectively. In military aircraft these percentages can go up to 30% as higher airframe loads are generally present. The increase in the use of titanium

in commercial and military aircraft over recent decades is shown in Figure 3.1.

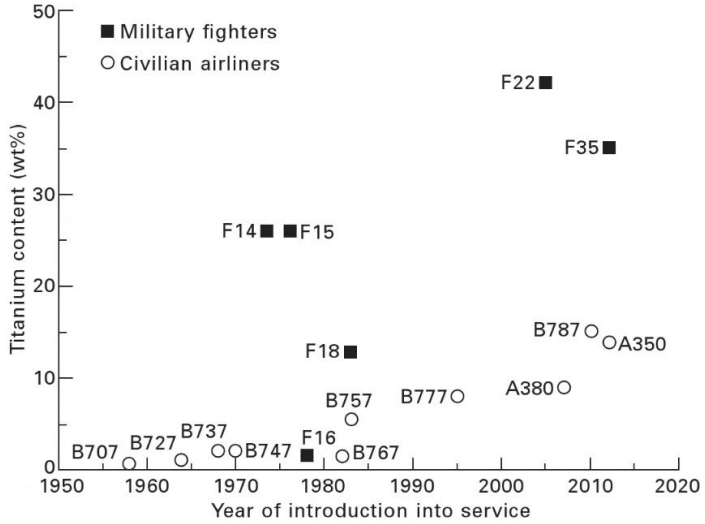

Figure 3.1: Titanium content used in aircraft [17].

The properties of titanium and its alloys derive from the metals allotropic modifications at 882°C (temperature at which one crystal structure is transformed into another) from hexagonal closed packed, hcp (α phase), occurring at low temperatures to body centred cubic, bcc (β phase), at high temperatures. The effect of alloying on the stability and physical and mechanical behaviour of these two phases allows the manipulation of these properties. Commercially pure titanium is a single-phase α alloy and is extensively used in applications that are not particularly demanding in terms of strength but require good corrosion resistance. They are used in non-structural applications, such as water supply systems for galleys and sanitary, and for ducts and piping where corrosion resistance and good formability is required [18]. Two phase $\alpha + \beta$ alloys have a range of combination of strength, toughness, and high temperature which make them attractive for applications demanding high specific properties to temperatures of around 600°C. An important $\alpha + \beta$ alloy is the Ti6Al4V alloy. Ti6Al4V is one of the most widely used titanium alloys due to its attractive properties combined with inherent workability. At room temperature this alloy consists of about 90 vol% α and thus its physical and mechanical properties are dominated by the α phase [19]. Ti6Al4V represents, in the US only, more than half of the total titanium production [20]. This alloy can be found in many airframes as a structural material and in engine parts. Due to the low allowable temperature this alloy is used for fan blades, fan cases and the intake section where temperatures are relatively low. The β alloys can satisfy requirements of very high strength with adequate toughness and fatigue resistance. These alloys have been gaining importance on the last few decades but their share of the titanium market is still small. An example of a high strength β alloy used in aerospace is the Ti10V2Fe3Al. This alloy has been selected for the landing gear of the Boing 777 over a high strength steel, not only for weight reasons, but also to eliminate the risk of hydrogen embrittlement failure. Another application of β alloys in large aircraft is for springs. By replacing steel springs with titanium springs weight savings were accomplished and the need for protection by painting was eliminated. In springs, fracture is a lesser concern and consequently β alloys with very high strength but low tensile

ductility can be used safely.

3.2 Properties

Some of the basic characteristics of titanium and other structural metallic materials based on Fe, Ni and Al are summarized in Table 3.1. Titanium has the highest strength to density ratio but has also the highest price which restricts its use to high-end applications. The high price of titanium results from its high reactivity with oxygen which requires an inert atmosphere or vacuum during the production process of titanium sponge as well as during the melting process. This high reactivity with oxygen is, on the other hand, responsible for the titanium's superior corrosion resistance. When in contact with air an immediate oxide layer is formed on the surface inhibiting the effects of aggressive environments.

The main advantage of titanium over its principal competitor, aluminium, relies on the much higher melting temperature of titanium making it the material of choice for applications where higher temperatures are present. But maximum useful temperatures for structural applications can only go up to approximately 600°C. Above this temperature the diffusion of oxygen through the oxide layer becomes too fast resulting in excessive growth of the oxide layer and embrittlement of the adjacent oxygen rich layer [20].

The coefficient of thermal expansion (CTE) is somewhat lower than that of steel and less than half of that of aluminium. Additionally, titanium alloys are chemically more compatible with carbon fibres than aluminium and are used to avoid galvanic corrosion problems.

Table 3.1: Some important characteristics of titanium and titanium based alloys as compared to other strucutral metallic materials based on Fe, Ni and Al [20].

	Ti	Fe	Ni	Al
Melting Temperature (°)	1670	1538	1455	660
Allotropic Transformation (°)	$\beta \xrightarrow{882} \alpha$	$\gamma \xrightarrow{912} \alpha$	-	-
Crystal Structure	bcc→hex	fcc→bcc	fcc	fcc
Room Temperature E (GPa)	115	215	200	72
Yield Stress Level (MPa)	1000	1000	1000	500
Density (g/cm^3)	4.5	7.9	8.9	2.7
Comparative Corrosion Resistance	Very High	Low	Medium	High
Comparative Reactivity with Oxygen	Very High	Low	Low	High
Comparative Price of Metal	Very High	Low	High	Medium

3.3 Crystallographic structure

Titanium exits in more than one crystallographic form. It exhibits an allotropic phase transformation at 882°C (β transus temperature) where one crystal structure transforms into another. The exact transformation temperature depends on the purity of the metal as it is

influenced by the interstitial and substitutional elements. Pure titanium and the majority of titanium alloys has an hexagonal closed packed (hcp) structure at low temperatures (α phase). At higher temperatures the body centred cubic (bcc) structure is found (β phase). The hexagonal unit cell of the α phase and the body centred cubic cell of the β phase are illustrated in Figure 3.2. More specifically, Figure 3.2 schematically illustrates the three most densely packed types of lattice planes: the basal plane (0001), one of the three $\{10\bar{1}0\}$ planes, also called prismatic planes and one of the six pyramidal planes $\{10\bar{1}1\}$. The three axes a_1, a_2 and a_3 are the close-packed directions with the indices $<11\bar{2}0>$. The room temperature values of the lattice parameters a and c are respectively 0.295nm and 0.468nm resulting on a c/a ratio of 1.587 for pure α titanium, smaller than the ideal 1.633 for the hcp structure. The bcc unit cell depicts the lattice parameter value of pure β titanium at 900°C (a=0.332nm) and one variant of the six most densely packed {110} lattice planes.

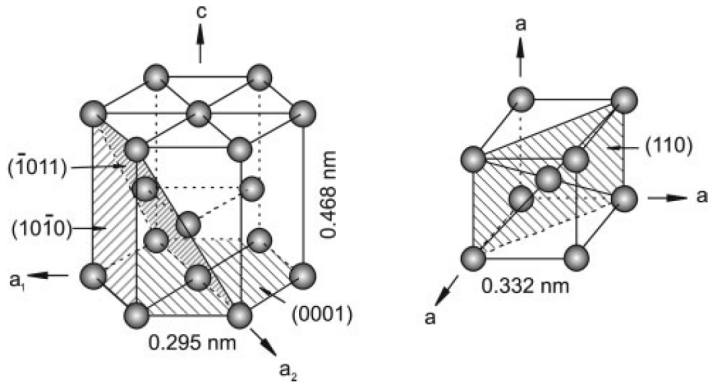

Figure 3.2: Crystal structure of hcp α and bcc β phase [21].

The crystal structures together with the corresponding transformation temperature or transus temperature play a major role in defining the large variety of titanium alloys properties.

The alloying elements of titanium can increase or decrease the α/β transformation temperature and depending on their influence they can be classified as α stabilizers, β stabilizers or neutral (Figure 3.3). The α stabilizers are elements that extend the α phase field to higher temperatures, i.e., increase the transus temperature, while β stabilizing elements shift the β phase field to lower temperatures. Neutral elements have minor effect on the transus temperature.

The alloying elements that favour the α crystal structure include Al, O, N, and C. Aluminium is the most widely used alloying element in titanium alloys because it not only raises the transformation temperature but exhibits also large solubilities in both the α and β phases. The β stabilizing elements can be divided into two groups. The β isomorphous group consists of elements that are miscible in the β phase. Examples of β isomourphous elements are V, Mo, and Nb. The other group consists of β eutectoid forming elements. The eutectoid group includes Cr, Fe and Si that are used in many titanium alloys and Ni, Cu, Mn, W, Pd and Bi that have a more limited usage. Alloying elements like Sn and Zr are considered neutral since they do not strongly promote phase stability and are used primarily to strengthen the α phase.

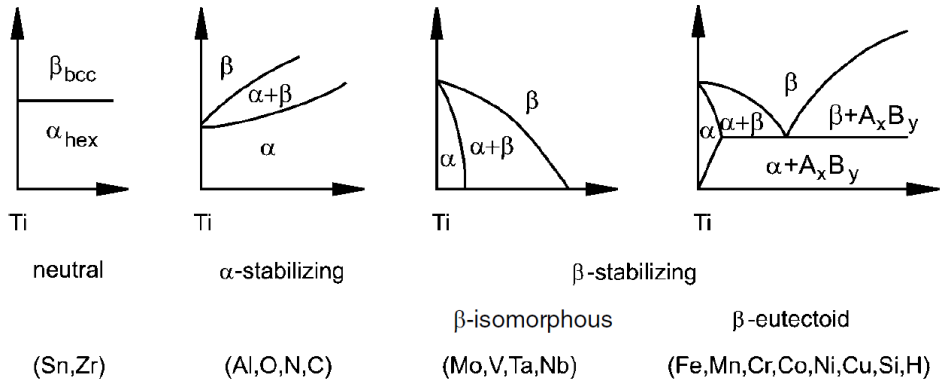

Figure 3.3: Influence of alloying elements on phase diagrams of Ti alloys [21].

Based on the α and/or β phases present, the titanium alloys are classified as: α, near-α, α-β and β. These categories describe the origin of the microstructure in terms of the basic crystal structure favored by alloying. As was seen, commercially pure (CP) titanium has an α structure. The addition of alloying elements produces a range of possible microstructures. By adding sufficient β stabilizers, β phase is produced on heating and transformed during the cooling following high processing. The resulting structures are representative of the α-β alloys. When only small amounts of beta stabilizers are added a variation of α alloys is obtained, the near-α alloys. The β alloys are generally referred to metastable β alloys and retain an essentially β structure on cooling to room temperature.

3.4 Deformation mechanisms

Plastic deformation of metals occurs essentially by either slip or twinning (Figure 3.4). Which mechanism is dominant depends on which one of the mechanisms requires the least amount of stress to initiate and sustain plastic deformation.

According to von Mises [23], to undergo an arbitrary homogeneous plastic deformation, five independent slip systems are necessary. The number of slip systems is equivalent to the number of dislocation glide opportunities in a crystal lattice and is determined by the number of slip planes multiplied by the number of slip directions [21]. These slip planes and directions are energetically more favourable for plastic deformation as the denser slip planes facilitate the dislocation glides. While for hcp structure the number of slip systems is only 3, for the bcc lattice there are 12 slip systems. Furthermore, the energy needed for plastic deformation depends directly on the length of the minimal slip path. In hcp structures this minimum slip path (that depends directly on the value of the lattice parameter, a) is higher than in bcc structures and even though the hcp lattice have higher packing densities of the atoms on the slip planes, the plastic deformation in these structures is limited when compared to the bcc structures. Thus slip is often the dominant mechanism in metals with highly symmetric cubic crystal whereas for hcp metals the deformation mechanisms involves both slip and twinning.

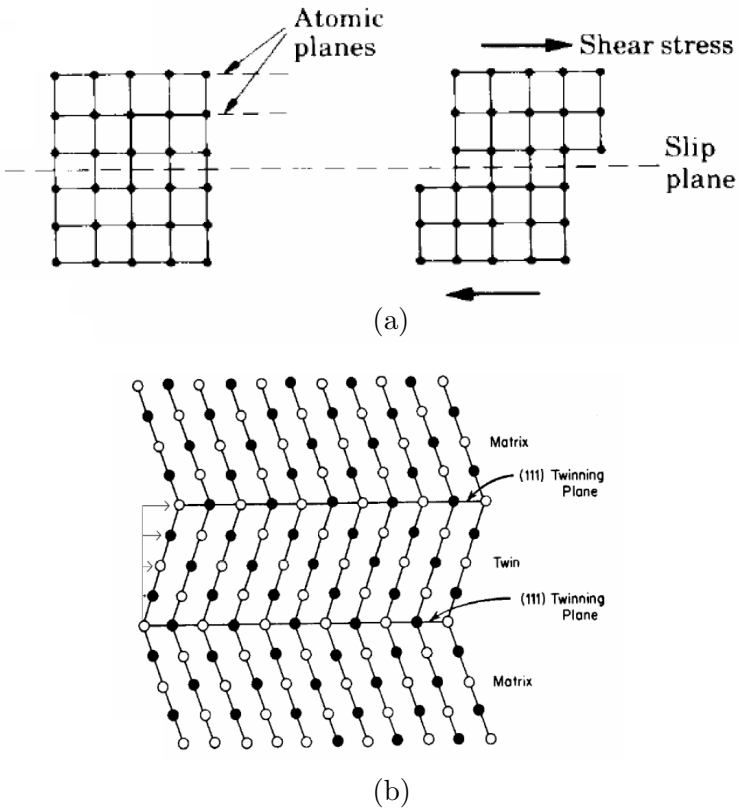

Figure 3.4: Schematic illustration of (a) slip and (b) twinning [22].

3.4.1 Slip modes for α Ti

The various slip systems present in α titanium are schematically illustrated in the hexagonal unit cell in Figure 3.5. The main slip directions are the three close-packed directions of the type $<11\bar{2}0>$. The slip planes containing this $\vec{a}$ type of Burgers vector are the basal plane, the three prismatic planes and the six pyramidal planes which consist of only 4 independent slip systems.

For a slip system to be active the resolved shear stress has to be grater than the Critical Resolved Shear Stress (CRSS) required for slip. At room temperature only basal slip is active, which corresponds to only two independent slip systems requiring the other slip systems to be provided by prismatic slip, pyramidal slip or twinning. As prismatic and pyramidal slip systems requires a much larger CRSS, these slip systems are essentially inactive at room temperature [24].

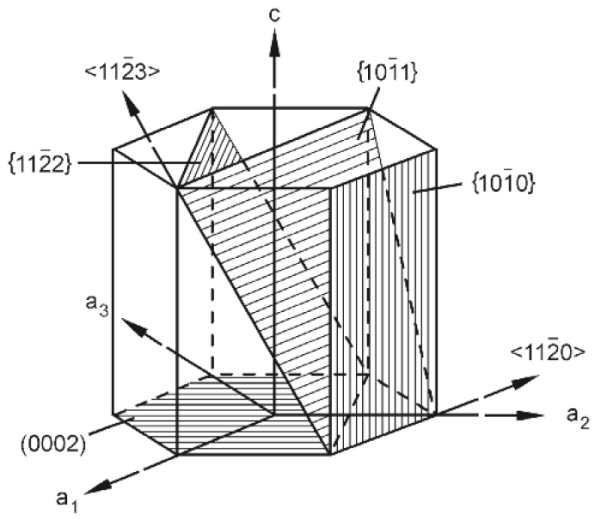

Figure 3.5: Slip planes and slip directions in the hexagonal α phase [20].

3.4.2 Deformation twinning for α Ti

Twinning is a mechanism of deformation where the lattice structure of the material changes. The atoms move only a fraction of an interatomic space which leads to a rearrangement of the lattice structure.

The most important twinning modes in pure α titanium are $\{10\bar{1}2\}$, $\{11\bar{2}1\}$ and $\{11\bar{2}2\}$. Twinning modes are particularly important for plastic deformation and ductility, at low temperatures, if the stress axis is parallel to the c-axis and the dislocation motion is not possible. Under tension the $\{10\bar{1}2\}$ and $\{11\bar{2}1\}$ is activated allowing an extension along the c-axis. In compression the $\{11\bar{2}2\}$ twins are activated leading to a contraction along the c-axis (Figure 3.6).

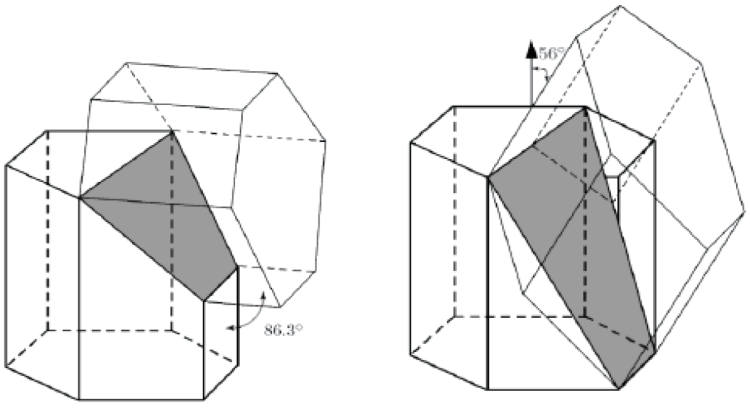

(a) Tension twinning (b) Compression twinning

Figure 3.6: Twinning modes in hcp materials [24].

Unlike slip, twinning is sensitive to the sign of the applied stress. This polar nature of

twinning is the basis of the strong asymmetry between yield in tension and compression.

3.5 Experimental characterization

Because of their extensive use in aircraft, space and other high-performance applications, titanium and its alloys have been thoroughly studied. Research on the characterization and modelling of the response of titanium alloys can be found, for example, on the work of Follansbee et al. [25], Lee and Lin [26], Nemat-Nasser et al. [27], Picu and Majorell [28] and Khan et al. [29–31] which focused mainly on the uniaxial and torsional responses at different strain rates and temperatures. Nixon et al. [32], Gilles et al. [33] and Tuninetti et al. [34] focused on the quasi-static behaviour at room temperature of high purity α-titanium and Ti6Al4V alloy.

Regarding the plastic deformation mechanisms, investigators like Meyers et al. [35], Song and Gray [36], Chichili et al. [37], Salem et al. [38] and Chun at al. [39] focused mainly on the identification of the microscopic mechanisms and its relation with the macroscopic response on pure α titanium.

In the framework of this research, the Ti6Al4V alloy was selected and the experimental results from Tuninetti [34] were used for the development and implementation of the numerical models as will be discussed in the following chapters.

Ti6Al4V is an α-β alloy, i.e, it consists of hcp α and bcc β grains. The specimens used in the experimental tests conducted by Tuninetti et al. [34] were machined from an Ti6Al4V ingot with the dimensions depicted in Figure 3.7.

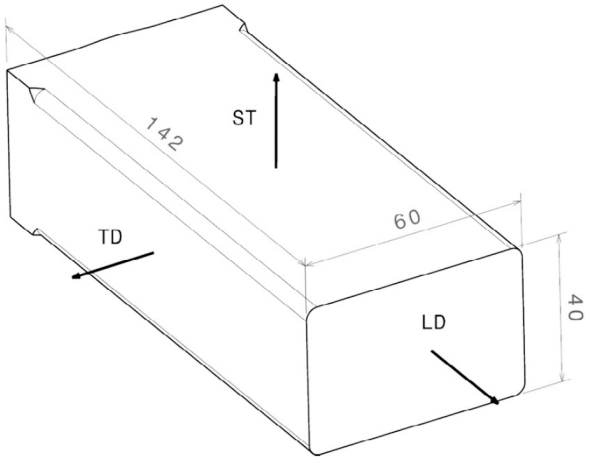

Figure 3.7: Ti6Al4V ingot with material directions (LD-longitudinal, TD-transverse and ST-short transverse) and dimensions in mm [34].

Depending on the heat treatment and interstitial content (mainly oxygen) the volume fraction of the α and β may vary. The alloy presented in [34] has 94% of the volume of α phase. Regarding the microstructure, optical microscopy showed slightly elliptic grains with a mean grain size equal to 12μ in the ST-LD plane and 9μ in ST-TD plane. The initial texture

of the material was determined by X-Ray diffraction (XRD) which showed a considerably weak initial texture. The texture refers to the non-uniform distribution of crystallographic orientations in a polycrystalline aggregate. The chemical composition and elastic properties are presented in Table 3.2 and Table 3.3.

Table 3.2: Chemical composition of the Ti6Al4V alloy [34].

Al	V	Fe	N	O	C	Ti
6.1	4.0	0.3	0.05	0.2	0.08	Bal.

Table 3.3: Elastic properties of Ti6Al4V [34].

Young modulus, E (GPa)	Poisson ratio, ν
108	0.3

Tuninetti et al. performed tensile, compression, shear and plane strain experimental tests. The tensile and compression tests were performed in the LD, TD and ST directions. Shear and plane strain were performed on the ST-LD plane. All the tests were performed at room temperature and at a constant strain rate of $10^{-3}s^{-1}$.

The geometry and dimensions of the specimens used by Tuninetti [34] for the compression tests are illustrated in Figure 3.8. The elliptical shape was chosen because this geometry is more sensitive to the materials plastic anisotropy.

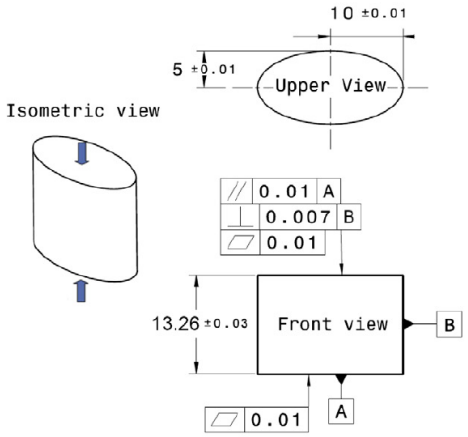

Figure 3.8: Geometry and dimensions(in mm) of the compression test specimens [34].

For tensile tests, axisymmetric specimens of 6mm diameter for the LD direction were used. For the TD and ST directions axisymmetric specimens with 4mm in diameter were used. The simple shear and plane strain tests were carried out with the biaxial machine developed and validated by Flores et al. [40] and the specimens are represented in Figure 3.9.

The experimental stress-strain curves obtained by Tuninetti et al. are represented in Figure 3.10.

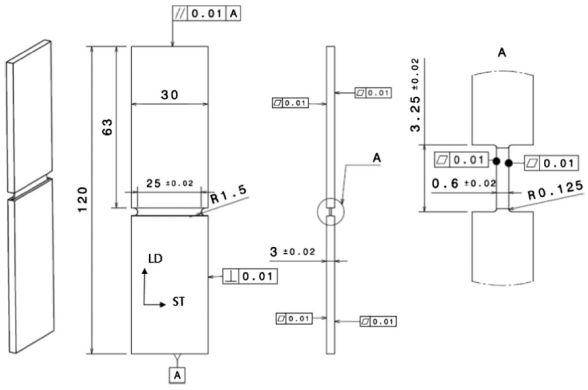

Figure 3.9: Geometry and dimensions(in mm) of the simple shear and plane strain test specimens [34].

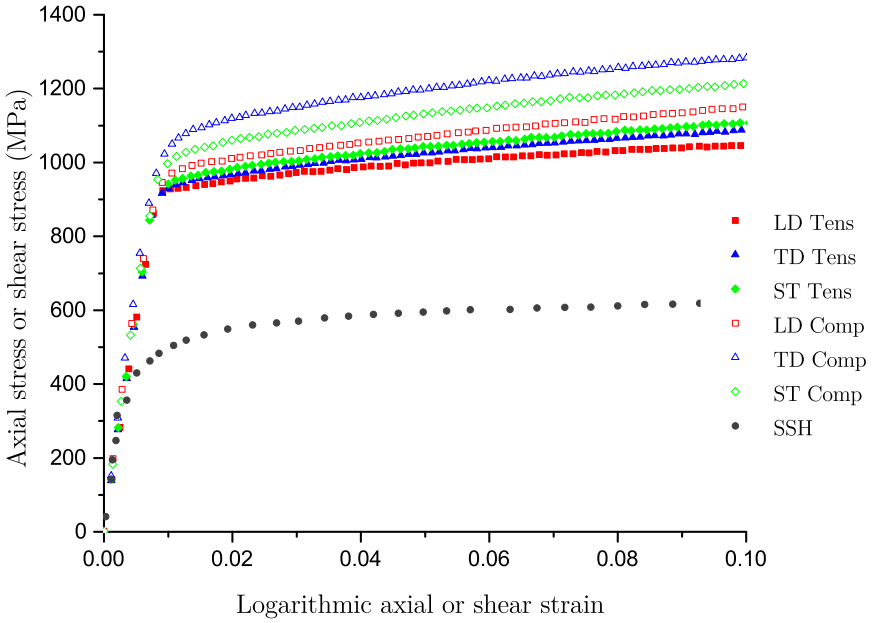

Figure 3.10: True stress strain curves for monotonic tensile and compression in three orthogonal material directions (LD,TD,ST) and simple shear (SSH in LD-ST plane) [34].

From the experimental results obtained by Tuninetti et al. it is possible to notice not only the significant strength asymmetry between the tension and compression for the Ti6Al4V alloy but also the presence of anisotropic hardening. It is possible to observe the stronger anisotropy in compression compared to tension as well as the variation with the loading direction.

3.6 Constitutive modelling

To predict the specific mechanical behaviour of particular materials, constitutive models that describe the stress-strain behaviour are necessary. These models can be classified as physically based models and phenomenological models. The first ones use physically based material constants and are used for both microscopic phenomena, like microstructure evolution, and the macroscopic behaviour through the measurement of deformation related quantities. On the other hand, the phenomenological models are based on the results of mechanical testing of a material and the respective material constants are "fitted" to the uniaxial stress-strain curves. Usually these constants don't have any physical meaning.

Crystal plasticity models offer a good framework for the description of the mechanical response and microstructure evolution of hcp metals. Models such as Taylor type [41] and the self consistent type [42] have been widely used and the incorporation of crystal plasticity models into finite element codes has received substantial attention [43]. A detailed overview can be found on [44]. However, the direct implementation of polycrystalline models into finite element codes, where each finite element integration point is associated with a polycrystalline aggregate, is computationally extremely expensive, thus limiting the applicability of these approaches to problems that do not require a fine spatial resolution. In view of more complex finite element simulations at a macroscopic level, more time efficient and robust models are necessary. The phenomenological plasticity approach offers the predictive capabilities and at the same time the convenience of a more easy implementation in finite element codes.

Overall, the general stress-strain relation for the plastic deformation of a material requires a yield criteria, that establishes the onset of plastic deformation, a flow rule and a hardening law describing the evolution of the initial yield stress. A review of the principal yield criteria and hardening law adequate for the description of plastic behaviour of titanium and other hcp materials will be given next.

3.6.1 Yield criteria

While the formulation, numerical implementation and validation of anisotropic formulations for materials with cubic structure is considerably developed (for a review of anisotropic plasticity models see [45]), macroscopic modelling of yielding and strain hardening of hcp materials is still progressing. Currently, classical anisotropic formulations for cubic metals are still being used in finite element simulations of hcp metals, however studies conducted by Kuwabara et al. [46] reported that the classic plasticity models (J2-flow theory or Hill criterion) are not able to capture the specifics of their plastic response.

Recently, three-dimensional yield criteria capable of describing both the tension compression asymmetry and the anisotropic behaviour of hcp metals have been developed. Cazacu and Barlat have proposed an isotropic criterion capable of describing the yielding asymmetry due to twinning for pressure insensitive metals [47]. This criterion is expressed in terms of all invariants of the stress deviator,

$$f \equiv (J_2)^{\frac{3}{2}} - cJ_3 = \tau_y^3, \tag{3.1}$$

where $J_2 = tr\mathbf{S}^2/2$ and $J_3 = tr\mathbf{S}^3/3$ are the second and third invariants of the stress deviator $\mathbf{S}$, τ_y is the yield stress in pure shear and c is a material parameter expressed solely in terms of the uniaxial yield stresses in tension and compression,

$$c = \frac{3\sqrt{3}(\sigma_T^3 - \sigma_C^3)}{2(\sigma_T^3 + \sigma_C^3)}. \tag{3.2}$$

If the yield stress in tension is equal to the yield stress in compression then $c = 0$ and the proposed criterion reduces to the von Mises yield criterion. For the yield function to be convex, c is limited to: $c \in [-3\frac{\sqrt{3}}{2}, 3\frac{\sqrt{3}}{4}]$. The proposed criterion was able to predict with great accuracy the crystal plasticity simulation results of Hosford and Allen [48].

The isotropic criterion expressed by equation (3.1) was then extended to include anisotropy using representation theorems to construct generalizations to anisotropic conditions of the classic invariants J_2 and J_3. This method was first proposed by Cazacu and Barlat in [49] and [50]. The generalization of J_2 to orthotropy is represented by J_2^0 and is expressed in the reference frame associated to the material symmetry as,

$$J_2^0 = \frac{a_1}{6}(\sigma_{xx} - \sigma_{yy})^2 + \frac{a_2}{6}(\sigma_{xx} - \sigma_{yy})^2 + \frac{a_3}{6}(\sigma_{xx} - \sigma_{yy})^2 + a_4\tau_{xy}^2 + a_5\tau_{xz}^2 + a_6\tau_{yz}^2, \tag{3.3}$$

where $\mathbf{x}$, $\mathbf{y}$ and $\mathbf{z}$ represent the rolling direction, the long transverse direction and the small transverse direction respectively. Note that if all the coefficients a_k $(k = 1, ..., 6)$ are set to unity then J_2^0 reduces to J_2. The generalization to orthotropy of J_3, is expressed as,

$$\begin{aligned} J_3^0 = {} & \frac{1}{27}(b_1 + b_2)\sigma_{xx}^3 + \frac{1}{27}(b_3 + b_4)\sigma_{yy}^3 + \frac{1}{27}[2(b_1 + b_4) - b_2 - b_3]\sigma_{zz}^3 + 2b_{11}\tau_{xy}\tau_{xz}\tau_{yz} \\ & + \frac{2}{9}(b_1 + b_2)\sigma_{xx}\sigma_{yy}\sigma_{zz} - \frac{1}{9}(b_1\sigma_{yy} + b_2\sigma_{zz})\sigma_{xx}^2 - \frac{1}{9}(b_3\sigma_{zz} + b_2\sigma_{xx})\sigma_{yy}^2 \\ & - \frac{1}{9}[(b_1 - b_2 + b_4)\sigma_{xx} + (b_1 + b_3 + b_4)\sigma_{yy}]\sigma_{zz}^2 - \frac{\tau_{yz}^2}{3}[(b_6 + b_7)\sigma_{xx} - b_6\sigma_{yy} - b_7\sigma_{zz}] \\ & - \frac{\tau_{xz}^2}{3}[2b_9\sigma_{yy} - b_8\sigma_{zz} - (2b_9 - b_8)\sigma_{xx}] - \frac{\tau_{xy}^2}{3}[2b_{10}\sigma_{zz} - b_5\sigma_{yy} - (2b_{10} - b_5)\sigma_{xx}], \end{aligned} \tag{3.4}$$

where all the coefficients b_k $(k = 1, ..., 11)$ reduce to the unity for isotropic conditions. Comparison between the theoretical yield loci given by this orthotropic criterion and experimental data on Mg, Mg-Th and Mg-Li alloys showed that this anisotropic model accurately captured both the anisotropy and tension/compression asymmetry [47].

More recently, Nixon et al. [32] proposed a full three-dimensional orthotropic yield criterion based on the isotropic yield function proposed by Cazacu and Barlat (equation (3.1)). Nixon extended this yield criterion to orthotropy using a linear transformation approach (see [51] for details) that consisted in replacing the Cauchy stress, σ, in equation (3.1), by $\mathbf{\Sigma} = \mathbf{L}\sigma$,

where $\mathbf{L}$ is a fourth order tensor. The proposed anisotropic criterion is of the form,

$$f(J_2^0, J_3^0) = (J_2^0)^{\frac{3}{2}} - cJ_3^0, \tag{3.5}$$

where $J_2^0 = \frac{1}{2}tr(\Sigma^2)$ and $J_3^0 = \frac{1}{3}tr(\Sigma^3)$.

The equivalent stress, $\bar{\sigma}$, associated to this orthotropic criterion is,

$$\bar{\sigma} = A_1[(J_2^0)^{\frac{3}{2}} - cJ_3^0]^{\frac{1}{3}}, \tag{3.6}$$

where A_1 is a constant defined such as $\bar{\sigma}$ reduces to the tensile yield stress in the rolling direction,

$$A_1 = 3[(a_2^2 + a_3^2 + a_2a_3)^{\frac{3}{2}} - c(a_2 + a_3)a_2a_3]. \tag{3.7}$$

Considering (x, y, z) the reference frame associated with the material symmetries with x corresponding to the rolling direction, y corresponding to the transverse direction, and z to the small transverse direction, the tensor $\mathbf{L}$ is represented by,

$$L = \begin{bmatrix} \frac{(a_2+a_3)}{3} & -\frac{a_3}{3} & -\frac{a_2}{3} & 0 & 0 & 0 \\ -\frac{a_3}{3} & \frac{(a_1+a_3)}{3} & -\frac{a_1}{3} & 0 & 0 & 0 \\ -\frac{a_2}{3} & -\frac{a_1}{3} & \frac{(a_1+a_2)}{3} & 0 & 0 & 0 \\ 0 & 0 & 0 & a_4 & 0 & 0 \\ 0 & 0 & 0 & 0 & a_5 & 0 \\ 0 & 0 & 0 & 0 & 0 & a_6. \end{bmatrix} \tag{3.8}$$

If the anisotropy of the material is fixed, i.e., the anisotropy of the material does not evolve with accumulated plastic strain, the coefficients a_i $(i = 1, ..., 6)$ are constants. In terms of the Cauchy stress, σ, the generalized invariants, J_2^0 and J_3^0, are given by,

$$\begin{aligned} J_2^0 = \frac{1}{9}[&(a_2^2 + a_3^2 + a_2a_3)\sigma_{xx}^2 + (a_1^2 + a_3^2 + a_1a_3)\sigma_{yy}^2 + (a_1^2 + a_2^2 + a_1a_2)\sigma_{zz}^2 \\ &+ (-2a_3^2 + a_1a_2 - a_1a_3 - a_2a_3)\sigma_{xx}\sigma_{yy} + (-2a_2^2 - a_1a_2 + a_1a_3 - a_2a_3)\sigma_{xx}\sigma_{zz} \\ &+ (-2a_1^2 - a_1a_2 - a_1a_3 + a_2a_3)\sigma_{yy}\sigma_{zz} + a_4^2\tau_{xy}^2 + a_5^2\tau_{xz}^2 + a_6^2\tau_{yz}^2], \end{aligned} \tag{3.9}$$

$$
\begin{aligned}
J_3^0 = \frac{1}{27}[&(a_2^2a_3 + a_2a_3^2)\sigma_{xx}^3 + (a_1^2a_3 + a_3^2a_1)\sigma_{yy}^3 + (a_1^2a_2 + a_1a_2^2)\sigma_{zz}^3 \\
&+ (-a_1a_2^2 + a_1a_3^2 - a_2^2a_3 - 2a_2a_3^2)\sigma_{xx}^2\sigma_{yy} + (a_1a_2^2 - a_1a_3^2 - a_2^2a_3 - 2a_2a^2a_3)\sigma_{xx}^2\sigma_{zz} \\
&+ (-a_1^2a_2 - a_1^2a_3 + a_2a_3^2 - 2a_1a_3^2)\sigma_{yy}^2\sigma_{xx} + (a_1^2a_2 - 2a_1^2a_3 - a_1a_3^2 - a_2a_3^2)\sigma_{yy}^2\sigma_{zz} \\
&+ (-a_1^2a_2 - a_1^2a_3 - 2a_1a_2^2 + a_2^2a_3)\sigma_{zz}^2\sigma_{xx} + (-2a_1^2a_2 + a_1^2a_3 - a_1a_2^2 - a_2^2a_3^2)\sigma_{zz}^2\sigma_{yy} \\
&+ 2(a_1^2a_2 + a_1^2a_3 + a_2^2a_1 + a_2^2a_3 + a_3^2a_1 + a_3^2a_2)\sigma_{xx}\sigma_{yy}\sigma_{zz}] \\
&+ \frac{1}{3}\{[a_2a_4^2\sigma_{xx} + a_1a_4^2\sigma_{yy} - (a_1a_4^2 + a_2a_4^2)\sigma_{zz}]\tau_{xy}^2 \\
&+ [a_3a_5^2\sigma_{xx} - (a_1a_5^2 + a_3a_5^2)\sigma_{yy} + a_1a_5^2\sigma_{zz}]\tau_{xz}^2 \\
&+ [(-a_2a_6^2 - a_3a_6^2)\sigma_{xx} - a_3a_6^2\sigma_{yy} + a_2a_6^2\sigma_{zz}]\tau_{yz}^2\} \\
&+ 2a_4a_5a_6\tau_{xy}\tau_{xz}\tau_{yz}.
\end{aligned}
\tag{3.10}
$$

If $\mathbf{L}$ is taken as the identity tensor, then $\mathbf{\Sigma} = \sigma$ and the generalized invariants reduce to the isotropic invariants J_2 and J_3.

Another isotropic pressure-insensitive yield criterion that accounts for yielding asymmetry between tension and compression, associated with deformation twinning, was proposed by Cazacu et al. [52]. This isotropic criterion involves all principal values of the stress deviator and is defined as,

$$
F = (|S_1| - kS_1)^a + (|S_2| - kS_2)^a + (|S_3| - kS_3)^a, \tag{3.11}
$$

where S_i $(i = 1, ..., 3)$ are the principal values of the stress deviator, k is the strength differential parameter and a is the degree of homogeneity. The strength differential parameter may be determined through uniaxial tests. The ratio of tensile to compressive uniaxial yield stress is, in accordance to the proposed criterion (3.11), given by,

$$
\frac{\sigma_T}{\sigma_C} = \left\{ \frac{(\frac{2}{3}(1+k))^a + 2(\frac{1}{3}(1-k))^a}{(\frac{2}{3}(1-k))^a + 2(\frac{1}{3}(1+k))^a} \right\}^{\frac{1}{a}}, \tag{3.12}
$$

or

$$
k = \frac{1 - h\left(\frac{\sigma_T}{\sigma_C}\right)}{1 + h\left(\frac{\sigma_T}{\sigma_C}\right)}, \tag{3.13}
$$

with,

$$
h\left(\frac{\sigma_T}{\sigma_C}\right) = \left[\frac{2^a - 2\left(\frac{\sigma_T}{\sigma_C}\right)^a}{\left(2\frac{\sigma_T}{\sigma_C}\right)^a - 2} \right]^{\frac{1}{a}}. \tag{3.14}
$$

Thus, for a fixed value of a, the parameter k can be expressed solely in terms of the ratio $\frac{\sigma_T}{\sigma_C}$. Note that for any value of $a \geq 1$, with a integer, if $k = 0$, there is no difference between the tension and compression yield stresses. Particularly, for $a = 2$ and $k = 0$, the proposed criterion reduces to the von Mises yield criterion.

To capture both the asymmetry between tension and compression and the anisotropy, Cazacu et al. extended the isotropic yield function to orthotropy by applying a fourth-order linear operator $\mathbf{C}$ on the stress deviator $\mathbf{S}$. On the expression of the isotropic criterion given by equation (3.11), the principal values of the Cauchy stress deviator are substituted by the principal values of the transformed tensor Σ. The transformed stress tensor is defined as,

$$\mathbf{\Sigma} = \mathbf{C}[\mathbf{S}]. \tag{3.15}$$

Thus, the proposed orthotropic criterion, commonly denominated as CPB06, is of the form,

$$F = (|\Sigma_1| - k\Sigma_1)^a + (|\Sigma_2| - k\Sigma_2)^a + (|\Sigma_3| - k\Sigma_3)^a, \tag{3.16}$$

where Σ_1, Σ_2, and Σ_3 are the principal values of Σ. Considering (x, y, z) the reference frame associated with orthotropy where x is the rolling directing, y is the transverse direction and z the small transverse direction, the tensor $\mathbf{C}$ is represented by,

$$\mathbf{C} = \begin{bmatrix} C_{11} & C_{12} & C_{13} & 0 & 0 & 0 \\ C_{12} & C_{22} & C_{23} & 0 & 0 & 0 \\ C_{13} & C_{23} & C_{33} & 0 & 0 & 0 \\ 0 & 0 & 0 & C_{44} & 0 & 0 \\ 0 & 0 & 0 & 0 & C_{55} & 0 \\ 0 & 0 & 0 & 0 & 0 & C_{66}. \end{bmatrix} \tag{3.17}$$

For 3-D stress states, 9 anisotropy coefficients are involved in the CPB06 criterion. For the reference frame and in the absence of any shear stresses, the values of Σ_{11}, Σ_{22} and Σ_{33} are the principal values of Σ. Otherwise the principal values of Σ are the roots of the third order algebraic equation,

$$X^3 + I_1 X^2 + I_2 X - I_3, \tag{3.18}$$

with the invariants I_1, I_2 and I_3 given by,

$$I_1 = \Sigma_{11} + \Sigma_{22} + \Sigma_{33}, \tag{3.19}$$

$$I_2 = \Sigma_{22}\Sigma_{33} + \Sigma_{33}\Sigma_{11} + \Sigma_{11}\Sigma_{22} - (\Sigma_{12}^2 + \Sigma_{13}^2 + \Sigma_{23}^2), \tag{3.20}$$

$$I_3 = 2\Sigma_{12}\Sigma_{23}\Sigma_{13} + \Sigma_{11}\Sigma_{22}\Sigma_{33} - \Sigma_{11}\Sigma_{23}^2 - \Sigma_{22}\Sigma_{13}^2 - \Sigma_{33}\Sigma_{12}^2. \tag{3.21}$$

To obtain the roots of the cubic equation (3.18) the intermediate quantities Q and R are first calculated,

$$Q = \frac{3I_2 - I_1^2}{9}, \tag{3.22}$$

$$R = \frac{2I_1^3 - 9I_1I_2 + 27I_3}{54}. \tag{3.23}$$

Then, the angle, θ, is determined

$$\theta = \cos^{-1}\left(\frac{R}{\sqrt{-Q^3}}\right). \tag{3.24}$$

Finally the principal values of Σ are obtained,

$$\Sigma_1 = 2\sqrt{-Q}\cos\left(\frac{\theta}{3} + \frac{I_1}{3}\right), \tag{3.25}$$

$$\Sigma_2 = 2\sqrt{-Q}\cos\left(\frac{\theta + 4\pi}{3} + \frac{I_1}{3}\right), \tag{3.26}$$

$$\Sigma_3 = 2\sqrt{-Q}\cos\left(\frac{\theta + 2\pi}{3} + \frac{I_1}{3}\right). \tag{3.27}$$

The predictive capabilities of the CPB06 orthotropic yield criteria were demonstrated for magnesium [52] and titanium alloys [30, 52].

For the improvement of the representation of the anisotropy, additional linear transformations can be incorporated into the isotropic criterion (3.16) [53].

In the following chapter the coefficients of both the CPB06 and the more recent Nixon yield criteria are presented for the Ti6Al4V and the theoretical yield loci are compared with the experimental data from Tuninetti [34].

3.6.2 Plastic flow rules

The onset of plastic deformation is established by means of a yield criterion, i. e., the material starts to deform plastically once the criterion is met. Upon further loading, the deformation produces plastic flow. The plastic flow rule defines the direction of the plastic strain rate and can be expressed as,

$$\dot{\varepsilon}_p = \dot{\gamma}\frac{\partial g}{\partial \sigma} \tag{3.28}$$

where the scalar function $\dot{\gamma}$ denotes the plastic multiplier (or consistency parameter) and g is the plastic potential function. The plastic flow rule is called associative if the plastic potential function, g, in equation (3.28) corresponds to the yield function. Otherwise the flow rule is considered non-associative. In the case of an associative flow rule, the direction of the strain rate is the outward normal of the yield surface, on the other hand, for a non-associative flow rule it is the gradient of the plastic potential surface.

3.6.3 Hardening

Modelling the plastic response of a metal requires not only a yield function and a flow rule but also a hardening law. The two most common hardening laws are isotropic hardening and kinematic hardening. Isotropic hardening laws describe a proportional expansion of the surface without any change in shape or position while kinematic hardening implies a pure translation of the initial yield surface.

For cubic metals, the evolution of the yield surface is reasonably well described by isotropic and/or kinematic hardening laws. But for hexagonal closed packed metals, as a result of twinning activity accompanied by grain reorientation and highly directional grain interactions, the yield surface not only changes its size but also distorts significantly, i.e., hardens anisotropically even for simple monotonic loading paths.

To correctly model the plastic behaviour of hcp metals, a hardening rule that accounts for the evolving texture with accumulated plastic deformation is necessary once classical isotropic and kinematic hardening laws do not consider the distortion of the yield surface. An alternative methodology was proposed by Plunkett et al. [54] that uses a reference hardening path and a set of yield surfaces for given levels of accumulated plastic strains.

The macroscopic anisotropic model proposed by Plunnkett et al. accounts for the evolution of the texture on the plastic response of hcp metals by allowing the variation of the anisotropic coefficients with the accumulated plastic strain. Based on experimental measurements and/or polycrystalline calculations, the anisotropic coefficients are determined for a finite set of equivalent plastic strains. Then an interpolation technique is used to construct the evolution of the yield surface.

An alternative method for the description of anisotropic hardening was proposed by Ertürk were the variation of the anisotropic coefficients and strength differential parameters with the accumulated plastic deformation was determined explicitly. This method was used in conjunction with the orthotropic criterion of Cazacu and Barlat [47] for the description of anisotropic hardening of magnesium. However, obtaining the analytical laws for the evolution of the yield function coefficients is not only a very difficult task but also requires a large amount of data.

The methodology proposed by Plunkett et al. [53] was used in this work. Having set the equivalent plastic strain as the hardening variable, the current equivalent stress (according to the given yield criterion) is obtained by piece-wise linear interpolation based on the current level of the equivalent plastic strain. Considering the finite set of equivalent plastic strains

$\bar{\varepsilon}_p^1 < \bar{\varepsilon}_p^2 < ... < \bar{\varepsilon}_p^n$ a weighting parameter can be defined as,

$$\xi = \frac{\bar{\varepsilon}_p^{j+1} - \bar{\varepsilon}_p}{\bar{\varepsilon}_p^{j+1} - \bar{\varepsilon}_p^j}, \tag{3.29}$$

for $\bar{\varepsilon}_p^j \leq \bar{\varepsilon}_p \leq \bar{\varepsilon}_p^{j+1}$, $j = 1, ..., n-1$.

Using the weighting parameter, ξ, the equivalent stress is given by,

$$\bar{\sigma}(\sigma, \bar{\varepsilon}_p)_{current} = \xi \bar{\sigma}^j + (1 - \xi)\bar{\sigma}^{j+1}. \tag{3.30}$$

The current yield function is then taken as,

$$f(\sigma, \bar{\varepsilon}_p)_{current} = \bar{\sigma}(\sigma, \bar{\varepsilon}_p)_{current} - \sigma_y(\bar{\varepsilon}_p), \tag{3.31}$$

where $\sigma_y(\bar{\varepsilon}_p)$ is a reference hardening curve. In this work, the uniaxial tensile curve in the rolling direction was used. The latter was approximated by the following expression,

$$\sigma_y(\bar{\varepsilon}_p) = A_0 + B_0 exp(-C_0 \bar{\varepsilon}_p), \tag{3.32}$$

where A_0, B_0 and C_0 are material constants.

Chapter 4

Material Parameter Identification

4.1 Introduction

Numerical simulation techniques are currently well established and constitute a fundamental part of the product development process as they lead to important time and cost savings. Considerable efforts have been made to improve the numerical methods, however the accurate simulation of structures is still intrinsically connected with the reliability of the implemented material models.

For materials with hexagonal closed packed crystal structure, constitutive models like the ones proposed by Nixon [32], by Cazacu and Barlat [47] or Cazacu et al. [52], proved to be adequate in the prediction of their specific deformation behaviour. However, more sophisticated yield criteria are often characterized by a greater number of material parameters. For example, the yield criterion proposed by Nixon requires the identification of a total of 7 parameters while the Cazacu and Barlat model, for a general stress state, has a total of 18 material parameters. The Cazacu et al. model (CPB06) has a total of 11 parameters and if additional linear transformations are considered then the number increases proportionally. The large amount of parameters not only increases the amount and type of experimental tests necessary but also requires more elaborate and robust identification techniques. In this chapter the calibration of the Nixon and CPB06 yield criteria will be addressed.

4.2 Identification Procedure

4.2.1 Objective Function

The identification of the material parameters for a given constitutive model is basically an optimization problem where the objective function consists in minimizing the gap between the experimental and the theoretical or predicted values given by the respective criterion. Thus the objective function can be formulated as the sum of the squared errors and can be

written as,

$$Error = \sum_j w_j (\sigma_j^{th} - \sigma_j^{exp})^2, \tag{4.1}$$

or equivalently as,

$$Error = \sum_j w_j \left(\frac{\sigma_j^{th}}{\sigma_j^{exp}} - 1 \right)^2, \tag{4.2}$$

where j is the number of experimental yield stresses available, w_j represents the weight assigned to each experimental values and σ_j^{th} and σ_j^{exp} are the theoretical stress value and the correspondent experimental stress value respectively. The optimization variables are the material parameters of the criterion. A vector, $\mathbf{x}$, of the optimization variables can be defined. Thus for the Nixon criterion $\mathbf{x} = [a_1, a_2, a_3, a_4, a_5, a_6, c]$ and for the CPB06 criterion $\mathbf{x} = [C_{11}, C_{12}, C_{13}, C_{22}, C_{23}, C_{33}, C_{44}, C_{55}, C_{66}, k, a]$.

The experimental data in the objective function may consist of flow stresses and Lankford coefficients (r-values) in tension and compression along different orientations of the material and biaxial flow stresses and r-values in tension and compression. If experimental data are not available for a given strain path they can be substituted with numerical data obtained from polycrystalline calculations as demonstrated by Plunkett [22]. The experimental data of Ti6Al4V alloy available from [34] consists of uniaxial tensile and compression tests in the longitudinal (LD), transverse (TD) and small transverse (ST) directions and simple shear in the LD-ST plane. Thus the full expression for the objective function used in this study can be written as,

$$Error(\mathbf{x}) = \sum_i w_i \left(\frac{\sigma_i^{T,th}}{\sigma_i^{T,exp}} - 1 \right)^2 + \sum_j w_j \left(\frac{\sigma_j^{C,th}}{\sigma_j^{C,exp}} - 1 \right)^2 + \sum_k w_k \left(\frac{\sigma_k^{SSH,th}}{\sigma_k^{SSH,exp}} - 1 \right)^2, \tag{4.3}$$

where all of the weights, w_i, w_j and w_k were considered equal and with the value of 1. The computation of the theoretical or predicted stresses, $\sigma^{T,th}$, $\sigma^{C,th}$ and $\sigma^{SSH,th}$ for the Nixon and CPB06 yield criteria are given in the following sections.

4.2.2 Theoretical Stress

Nixon yield criterion

The yield criteria proposed by Nixon [32] is of the form,

$$f(J_2^0, J_3^0) = \left(J_2^0\right)^{\frac{3}{2}} - cJ_3^0, \tag{4.4}$$

where $J_2^0 = \frac{1}{2}tr(\Sigma^2)$ and $J_3^0 = \frac{1}{3}tr(\Sigma^3)$. The tensor $\mathbf{\Sigma} = \mathbf{L}\sigma$ where $\mathbf{L}$ is a fourth order tensor of the yield criterion parameters. The equivalent stress, $\bar{\sigma}$, is given by,

$$\bar{\sigma} = A_1 \left[\left(J_2^0\right)^{\frac{3}{2}} - cJ_3^0 \right]^{\frac{1}{3}}, \tag{4.5}$$

where A_1 is a constant defined such as $\bar{\sigma}$ reduces to the tensile yield stress in the longitudinal direction,

$$A_1 = 3 \left[\left(a_2^2 + a_3^2 + a_2a_3\right)^{\frac{3}{2}} - c\left(a_2 + a_3\right)a_2a_3 \right]^{-\frac{1}{3}}. \tag{4.6}$$

Considering (x, y, z) the reference frame associated with the material symmetries with x being the longitudinal direction, the y the transverse direction and z the small transverse direction, the predicted uniaxial flow stress data normalized by the tensile yield stress in the longitudinal direction is given by:

- Uniaxial tension in LD

  For uniaxial tension in LD the generalized invariants, J_2^0 and J_3^0 are given by,

$$J_2^0 = \left(\frac{\sigma_{xx}}{3}\right)^2 \left(a_2^2 + a_2a_3 + a_3^2\right), \tag{4.7}$$

$$J_3^0 = \left(\frac{\sigma_{xx}}{3}\right)^3 \left(a_2^2a_3 + a_2a_3^2\right). \tag{4.8}$$

  The expression for the predicted tensile yield stress along the longitudinal direction is obtained by solving the equivalent stress, $\bar{\sigma}$ from equation (4.5) for tension σ_{xx},

$$\sigma_{LD}^T = \frac{3}{A_1} \left[\left(a_2^2 + a_2a_3 + a_3^2\right)^{\frac{3}{2}} - c\left(a_2^2a_3 + a_2a_3^2\right) \right]^{-\frac{1}{3}}. \tag{4.9}$$

- Uniaxial compression in LD

  For uniaxial compression in LD the generalized invariants, J_2^0 and J_3^0 are given by,

$$J_2^0 = \left(\frac{\sigma_{xx}}{3}\right)^2 \left(a_2^2 + a_2a_3 + a_3^2\right), \tag{4.10}$$

$$J_3^0 = -\left(\frac{\sigma_{xx}}{3}\right)^3 \left(a_2^2a_3 + a_2a_3^2\right). \tag{4.11}$$

Solving the equivalent stress, $\bar{\sigma}$, for tension in LD, σ_{xx},

$$\sigma_{LD}^{C} = \frac{3}{A_1}\left[\left(a_2^2 + a_2a_3 + a_3^2\right)^{\frac{3}{2}} + c\left(a_2^2a_3 + a_2a_3^2\right)\right]^{-\frac{1}{3}}. \tag{4.12}$$

- Uniaxial tension in TD

  For uniaxial tension in TD the generalized invariants, J_2^0 and J_3^0 are given by,

$$J_2^0 = \left(\frac{\sigma_{yy}}{3}\right)^2\left(a_1^2 + a_1a_3 + a_3^2\right), \tag{4.13}$$

$$J_3^0 = \left(\frac{\sigma_{yy}}{3}\right)^3\left(a_1^2a_3 + a_1a_3^2\right). \tag{4.14}$$

  Solving the equivalent stress, $\bar{\sigma}$, for tension in TD, σ_{yy},

$$\sigma_{TD}^{T} = \frac{3}{A_1}\left[\left(a_1^2 + a_1a_3 + a_3^2\right)^{\frac{3}{2}} - c\left(a_1^2a_3 + a_1a_3^2\right)\right]^{-\frac{1}{3}}. \tag{4.15}$$

- Uniaxial compression in TD

  For uniaxial compression in TD the generalized invariants, J_2^0 and J_3^0 are given by,

$$J_2^0 = \left(\frac{\sigma_{yy}}{3}\right)^2\left(a_1^2 + a_1a_3 + a_3^2\right), \tag{4.16}$$

$$J_3^0 = -\left(\frac{\sigma_{yy}}{3}\right)^3\left(a_1^2a_3 + a_1a_3^2\right). \tag{4.17}$$

  Solving the equivalent stress, $\bar{\sigma}$, for tension in TD, σ_{yy},

$$\sigma_{TD}^{C} = \frac{3}{A_1}\left[\left(a_1^2 + a_1a_3 + a_3^2\right)^{\frac{3}{2}} + c\left(a_1^2a_3 + a_1a_3^2\right)\right]^{-\frac{1}{3}}. \tag{4.18}$$

- Uniaxial tension in ST

  For uniaxial tension in ST the generalized invariants, J_2^0 and J_3^0 are given by,

$$J_2^0 = \left(\frac{\sigma_{yy}}{3}\right)^2\left(a_1^2 + a_1a_2 + a_2^2\right), \tag{4.19}$$

$$J_3^0 = \left(\frac{\sigma_{yy}}{3}\right)^3\left(a_1^2a_2 + a_1a_2^2\right). \tag{4.20}$$

Solving the equivalent stress, $\bar{\sigma}$, for tension in TD, σ_{yy},

$$\sigma_{ST}^{T} = \frac{3}{A_1}\left[\left(a_1^2 + a_1a_2 + a_2^2\right)^{\frac{3}{2}} - c\left(a_1^2a_2 + a_1a_2^2\right)\right]^{-\frac{1}{3}}. \tag{4.21}$$

- Uniaxial compression in ST

  For uniaxial compression in ST the generalized invariants, J_2^0 and J_3^0 are given by,

$$J_2^0 = \left(\frac{\sigma_{yy}}{3}\right)^2\left(a_1^2 + a_1a_2 + a_2^2\right), \tag{4.22}$$

$$J_3^0 = -\left(\frac{\sigma_{yy}}{3}\right)^3\left[\left(a_1^2a_2 + a_1a_2^2\right)\right]. \tag{4.23}$$

  Solving the equivalent stress, $\bar{\sigma}$, for compression in ST, σ_{yy},

$$\sigma_{ST}^{C} = \frac{3}{A_1}\left[\left(a_1^2 + a_1a_2 + a_2^2\right)^{\frac{3}{2}} + c\left(a_1^2a_2 + a_1a_2^2\right)\right]^{-\frac{1}{3}}. \tag{4.24}$$

- Simple shear in LD-ST

  For simple shear in LD-ST the generalized invariants, J_2^0 and J_3^0 are given by,

$$J_2^0 = a_6^2\sigma_{xz}^2, \tag{4.25}$$

$$J_3^0 = 0. \tag{4.26}$$

  Solving the equivalent stress, $\bar{\sigma}$, for shear tension in LD-ST, σ_{xz},

$$\sigma_{SSH} = \frac{1}{A_1a_6}. \tag{4.27}$$

CPB06 yield criterion

The CPB06 yield criterion is defined by,

$$F = (|\Sigma_1| - k\Sigma_1)^a + (|\Sigma_2| - k\Sigma_2)^a + (|\Sigma_3| - k\Sigma_3)^a, \tag{4.28}$$

where Σ_1, Σ_2 and Σ_3 are the principal values of the tensor $\mathbf{\Sigma}$ given by $\mathbf{\Sigma} = \mathbf{CS}$. $\mathbf{C}$ is the fourth order orthotropic tensor of the yield criterion parameters. The equivalent stress is

given by,

$$\bar{\sigma} = B\left[(|\Sigma_1| - k\Sigma_1)^a + (|\Sigma_2| - k\Sigma_2)^a + (|\Sigma_3| - k\Sigma_3)^a\right]^{\frac{1}{a}}, \tag{4.29}$$

where B is a constant defined such as $\bar{\sigma}$ reduces to the tensile yield stress in the longitudinal direction,

$$B = \left[\frac{1}{(|\Phi_1| - k\Phi_1)^a + (|\Phi_2| - k\Phi_2)^a + (|\Phi_3| - k\Phi_3)^a}\right]^{\frac{1}{a}}, \tag{4.30}$$

and,

$$\begin{aligned}
\Phi_1 &= \frac{1}{3}\left(2C_{11} - C_{12} - C_{13}\right), \\
\Phi_2 &= \frac{1}{3}\left(2C_{12} - C_{22} - C_{23}\right), \\
\Phi_3 &= \frac{1}{3}\left(2C_{13} - C_{23} - C_{33}\right).
\end{aligned} \tag{4.31}$$

Letting (x, y, z) be the reference frame associated with the material symmetries with x along the longitudinal direction, y along the transverse direction and z along the small transverse direction, the predicted uniaxial flow stress data normalized by the tensile yield stress in the longitudinal direction is given by:

- Uniaxial tension in LD

  For uniaxial tensile loading in the longitudinal direction, x,

$$\mathbf{\Sigma} = \begin{bmatrix} \sigma_{xx}\Phi_1 \\ \sigma_{xx}\Phi_2 \\ \sigma_{xx}\Phi_3 \\ 0 \\ 0 \\ 0 \end{bmatrix}. \tag{4.32}$$

  Thus the principal values of Σ are $\Sigma_1 = \sigma_{xx}\Phi_1$, $\Sigma_2 = \sigma_{xx}\Phi_2$, $\Sigma_3 = \sigma_{xx}\Phi_3$. Upon substitution in equation (4.29) the predicted yield stress in the longitudinal direction can be obtained,

$$\sigma_{xx} = \left[\frac{(|\Phi_1| - k\Phi_1)^a + (|\Phi_2| - k\Phi_2)^a + (|\Phi_3| - k\Phi_3)^a}{(|\Phi_1| - k\Phi_1)^a + (|\Phi_2| - k\Phi_2)^a + (|\Phi_3| - k\Phi_3)^a}\right]^{\frac{1}{a}}, \tag{4.33}$$

- Uniaxial compression in LD

  For uniaxial compression in LD,

$$\mathbf{\Sigma} = \begin{bmatrix} -\sigma_{xx}\Phi_1 \\ -\sigma_{xx}\Phi_2 \\ -\sigma_{xx}\Phi_3 \\ 0 \\ 0 \\ 0 \end{bmatrix}. \tag{4.34}$$

  The principal values are $\Sigma_1 = -\sigma_{xx}\Phi_1$, $\Sigma_2 = -\sigma_{xx}\Phi_2$ and $\Sigma_3 = -\sigma_{xx}\Phi_3$ and the predicted yield stress is given by,

$$\sigma_{xx} = \left[\frac{(|\Phi_1| - k\Phi_1)^a + (|\Phi_2| - k\Phi_2)^a + (|\Phi_3| - k\Phi_3)^a}{(|\Phi_1| + k\Phi_1)^a + (|\Phi_2| + k\Phi_2)^a + (|\Phi_3| + k\Phi_3)^a}\right]^{\frac{1}{a}}. \tag{4.35}$$

- Uniaxial tension in TD

  For uniaxial tensile loading along transverse direction, y,

$$\mathbf{\Sigma} = \begin{bmatrix} \sigma_{yy}\varphi_1 \\ \sigma_{yy}\varphi_2 \\ \sigma_{yy}\varphi_3 \\ 0 \\ 0 \\ 0 \end{bmatrix}. \tag{4.36}$$

  Thus the principal values are $\Sigma_1 = \sigma_{yy}\varphi_1$, $\Sigma_2 = \sigma_{yy}\varphi_2$ and $\Sigma_3 = \sigma_{yy}\varphi_3$ with,

$$\begin{aligned} \varphi_1 &= \frac{1}{3}\left(2C_{12} - C_{11} - C_{13}\right), \\ \varphi_2 &= \frac{1}{3}\left(2C_{22} - C_{12} - C_{23}\right), \\ \varphi_3 &= \frac{1}{3}\left(2C_{23} - C_{13} - C_{33}\right). \end{aligned} \tag{4.37}$$

  The predicted yield stress for tension in the transverse direction is given by,

$$\sigma_{yy} = \left[\frac{(|\Phi_1| - k\Phi_1)^a + (|\Phi_2| - k\Phi_2)^a + (|\Phi_3| - k\Phi_3)^a}{(|\varphi_1| - k\varphi_1)^a + (|\varphi_2| - k\varphi_2)^a + (|\varphi_3| - k\varphi_3)^a}\right]^{\frac{1}{a}}. \tag{4.38}$$

- Uniaxial compression in TD

For uniaxial compression in the transverse direction,

$$\mathbf{\Sigma} = \begin{bmatrix} -\sigma_{yy}\varphi_1 \\ -\sigma_{yy}\varphi_2 \\ -\sigma_{yy}\varphi_3 \\ 0 \\ 0 \\ 0 \end{bmatrix}. \tag{4.39}$$

The principal values are $\Sigma_1 = -\sigma_{yy}\varphi_1$, $\Sigma_2 = -\sigma_{yy}\varphi_2$ and $\Sigma_3 = -\sigma_{yy}\varphi_3$ and the predicted yield stress is given by,

$$\sigma_{yy} = \left[\frac{(|\Phi_1| - k\Phi_1)^a + (|\Phi_2| - k\Phi_2)^a + (|\Phi_3| - k\Phi_3)^a}{(|\varphi_1| + k\varphi_1)^a + (|\varphi_2| + k\varphi_2)^a + (|\varphi_3| + k\varphi_3)^a} \right]^{\frac{1}{a}}. \tag{4.40}$$

- Uniaxial tension in ST

  For uniaxial tensile loading in the small transverse direction, z,

$$\mathbf{\Sigma} = \begin{bmatrix} \sigma_{zz}\psi_1 \\ \sigma_{zz}\psi_2 \\ \sigma_{zz}\psi_3 \\ 0 \\ 0 \\ 0 \end{bmatrix}. \tag{4.41}$$

  Thus the principal values are $\Sigma_1 = \sigma_{zz}\psi_1$, $\Sigma_2 = \sigma_{zz}\psi_2$ and $\Sigma_3 = \sigma_{zz}\psi_3$ with,

$$\begin{aligned} \psi_1 &= \frac{1}{3}\left(2C_{13} - C_{11} - C_{12}\right), \\ \psi_2 &= \frac{1}{3}\left(2C_{23} - C_{12} - C_{22}\right), \\ \psi_3 &= \frac{1}{3}\left(2C_{33} - C_{13} - C_{23}\right). \end{aligned} \tag{4.42}$$

  The predicted yield stress for tension along the small transverse direction is given by,

$$\sigma_{yy} = \left[\frac{(|\Phi_1| - k\Phi_1)^a + (|\Phi_2| - k\Phi_2)^a + (|\Phi_3| - k\Phi_3)^a}{(|\psi_1| - k\psi_1)^a + (|\psi_2| - k\psi_2)^a + (|\psi_3| - k\psi_3)^a} \right]^{\frac{1}{a}}. \tag{4.43}$$

- Uniaxial compression in ST

For uniaxial compression along the small transverse direction,

$$\mathbf{\Sigma} = \begin{bmatrix} -\sigma_{zz}\psi_1 \\ -\sigma_{zz}\psi_2 \\ -\sigma_{zz}\psi_3 \\ 0 \\ 0 \\ 0 \end{bmatrix}. \tag{4.44}$$

And the principal values are $\Sigma_1 = -\sigma_{zz}\psi_1$, $\Sigma_2 = -\sigma_{zz}\psi_2$ and $\Sigma_3 = -\sigma_{zz}\psi_3$. Thus the predicted yield stress for compression along the small transverse direction is given by,

$$\sigma_{yy} = \left[\frac{(|\Phi_1| - k\Phi_1)^a + (|\Phi_2| - k\Phi_2)^a + (|\Phi_3| - k\Phi_3)^a}{(|\psi_1| + k\psi_1)^a + (|\psi_2| + k\psi_2)^a + (|\psi_3| + k\psi_3)^a} \right]^{\frac{1}{a}}. \tag{4.45}$$

- Simple shear in LD-ST

  Under simple shear in the LD-ST plane,

$$\mathbf{\Sigma} = \begin{bmatrix} 0 \\ 0 \\ 0 \\ 0 \\ 0 \\ \sigma_{xz}C_{66} \end{bmatrix}. \tag{4.46}$$

  The principal values are $\Sigma_1 = \sigma_{xz}C_{66}$, $\Sigma_2 = 0$, $\Sigma_3 = -\sigma_{xz}C_{66}$ and the predicted yield stress is given by,

$$\sigma_{xz} = \left[\frac{(|\Phi_1| - k\Phi_1)^a + (|\Phi_2| - k\Phi_2)^a + (|\Phi_3| - k\Phi_3)^a}{(|C_{66}| - kC_{66})^a + (|C_{66}| + kC_{66})^a} \right]^{\frac{1}{a}}. \tag{4.47}$$

As mentioned earlier, the calibration of the previously addressed yield criteria requires finding the material parameters that minimize the objective function. There are many optimization strategies to solve this problem namely direct search algorithms (pattern search, Powell or simplex methods), evolutionary algorithms (genetic algorithms, particle swarm optimization, ant colony) or gradient based algorithms (Steepest Descent Method, Newton Method, Quasi-Newton Method). In this study, an optimization strategy based on the combination of two methods was used to solve the minimization problem: a genetic algorithm and a direct search method. On the following section these optimization techniques are discussed.

4.3 Optimization Algorithms

There are many methods available to solve optimization problems each with its own limitations and capabilities. In this study, two procedures for the minimization of the objective function are addressed: a direct search method and a genetic algorithm.

The direct search methods, also known as derivative-free algorithms, are based on simple strategies that do not require the computation of the objective function derivatives. These optimization techniques rely exclusively on the values of the objective function. The classical direct search methods, developed during 1960-1971, can be categorized as pattern search methods, simplex methods and methods with adaptive sets of search directions. A comprehensive description of the classical direct search methods can be found in [55] and [56]. The main advantage associated with direct search methods is their simplicity and ease of implementation, however, they tend to converge to local minimums. The direct search method chosen in this study was the Nelder-Mead simplex method mainly due to it's availability in the commercial software MATLAB. A detailed description of the Nelder-Mead simplex method and variations can be found on the book by Walters et al. [57].

Genetic Algorithms are a class of evolutionary algorithms which are population-based optimization strategies that mimic the natural biological evolution and/or social behaviour of species. Besides genetic algorithms, memetic algorithms, particle swarm, ant-colony or shuffled frog leaping are examples of evolutionary algorithms [58]. Genetic Algorithms were the first evolutionary-based technique introduced in the literature whose concept is based on the Darwinian principle of the 'survival of the fittest' and the natural process of evolution through reproduction. The popularity of genetic algorithms has grown mainly with the increase in computer calculation capability and their broad applicability in many science and engineering fields. Their ability to reach near global optimum solutions is their main advantage. Local minima are generally avoided and thus the final solution is usually in the vicinity of the global minimum.

In this study, an efficient calibration of the material parameters was accomplished by combining the advantages of the genetic algorithms and the direct search methods through a two step approach. A genetic algorithm was first used to perform a global optimization thus avoiding the convergence to local minima and a direct search method was then used to accurately locate the optimum point within the vicinity of the genetic algorithms's solution.

4.3.1 Nelder-Mead simplex

The Nelder-Mead algorithm was originally published in 1965 [59] and is one of the most popular derivative free optimization methods. The basic algorithm is quite simple and easy to use. It only uses the function values at some points and does not compute or approximates the gradient at any of these points.

The Nelder-Mead method is simplex based. In the minimization of a function of n variables, a simplex is a set of $n+1$ points $\mathbf{x}_0, \ldots, \mathbf{x}_n$ in $\mathbb{R}^n$. Therefore one has a triangle in $\mathbb{R}^2$, a tetrahedron in $\mathbb{R}^3$, etc. A simplex based direct search method begins with the set of $p_1, ..., p_0 \in \mathbb{R}^n$, that are considered the vertices of the simplex, and the corresponding set of

function values at the vertices $f_j = f(\mathbf{x}_j), j = 0, \ldots, n$. The initial simplex has to be nondegenerate, i.e., the points $\mathbf{x}_0, \ldots, \mathbf{x}_n$ must not lie in the same hyperplane. Then a sequence of transformations of the simplex are performed in order to decrease the function values at its vertices. Being a minimization, the vertex with the highest function value is replaced by a newly reflected better point, which would be approximately located in the negative gradient direction. This process is terminated when the current simplex becomes sufficiently small in some sense or when the function values are close enough.

The general algorithm of the Nelder-Mean method comprises three main steps. The first step consisting of the construction of the initial simplex. The second step is the transformation algorithm and the last step consists of the termination conditions.

Initial simplex

The initial simplex is usually constructed by generating $n+1$ vertices around a given input point $\mathbf{x}_{in}$. In practice $\mathbf{x}_{in} = \mathbf{x}_0$ to allow proper restarts of the algorithm. The remaining n vertices are generated according to the relation,

$$\mathbf{x}_j = \mathbf{x}_0 + \lambda e_j, \tag{4.48}$$

for $j = 1, \ldots, n$ and where λ is a stepsize in the direction of the unit vector e_j in $\mathbb{R}^n$.

Transformation algorithm

Each single generic iteration, k, of the Nedler-Mead algorithm consists in the following steps:

1. Ordering

   At this step the highest, h, second highest, s and lowest, l, function values for the $n+1$ vertices of the current simplex are determined,

$$\begin{aligned} f_h &= max_j f_j \\ f_s &= max_{j \neq h} f_j \\ f_l &= min_j f_j \end{aligned} \tag{4.49}$$

2. Centroid

   The centroid, $\bar{\mathbf{x}}$, of the best side (the side opposite to the worst vertex) is determined,

$$\bar{\mathbf{x}} = \frac{1}{n} \sum_{j \neq h} \mathbf{x}_j \tag{4.50}$$

3. Transformation

The new simplex is computed from the current one. The replacement of the worst vertex, $\mathbf{x}_h$, is attempted using reflection, expansion or contraction with respect to the best side. All test points lie on the line defined by $\mathbf{x}_h$ and $\bar{\mathbf{x}}$ and at most two of them are computed in one iteration. The outcome of each iteration is either a single new vertex, the accepted point, which replaces $\mathbf{x}_h$ in the set of vertices for the next iteration, or if this fails, the simplex shrinks towards the best vertex $\mathbf{x}_l$, and in this case a set of n new points, together with $\mathbf{x}_l$, form the simplex at the next iteration.

The simplex transformations (reflection, expansion, contraction and shrinkage) are controlled by four parameters: the coefficients of reflection, ρ, expansion, χ, contraction, γ, and shrinkage σ. According to the original Nelder-Mead paper, these parameters should satisfy the following constraints,

$$\rho > 0, \qquad \chi > 1, \qquad \chi > \rho, \qquad 0 < \gamma < 1, \qquad 0 < \sigma < 1. \tag{4.51}$$

The standard values used in most implementations are,

$$\rho = 1, \qquad \chi = 2, \qquad \gamma = \frac{1}{2}, \qquad \sigma = \frac{1}{2}. \tag{4.52}$$

The various geometric transformations can be described as follows,

- Reflect

  The reflected point is computed from,

  $$\mathbf{x}_r = \bar{\mathbf{x}} + \rho(\bar{\mathbf{x}} - \mathbf{x}_h), \tag{4.53}$$

  and $f_r = f(\mathbf{x}_r)$ is evaluated. If $f_l \leq f_r \leq f_s$ the reflected point is accepted and the iteration is terminated.

- Expand

  If $f_r < f_l$ the expansion point, x_e is calculated,

  $$\mathbf{x}_e = c + \gamma(\mathbf{x}_r - c), \tag{4.54}$$

  and $f_e = f(\mathbf{x}_e)$ is evaluated. If $f_e < f_r$ then $\mathbf{x}_e$ is accepted and the iteration is terminated. Otherwise (if $f_e \geq f_r$), $\mathbf{x}_r$ is accepted and the iteration is terminated. This is called a "greedy minimization" approach because it includes the better of the two points, $\mathbf{x}_r$ or $\mathbf{x}_e$, in the new simplex. The simplex is expanded only if $f_e < f_r < f_l$. On the original Nelder-Mead paper $\mathbf{x}_e$ is accepted if $f_e < f_l$ and $f_r < f_l$, regardless of the relationship between f_r and f_e. It may happen that $f_r < f_e$ and so $\mathbf{x}_r$ is a better new point than $\mathbf{x}_e$ but $\mathbf{x}_e$ is still accepted as the new point. This is called a "greedy

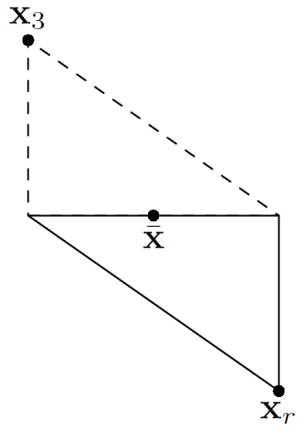

Figure 4.1: Melder-Mead simplex after a reflection (original simplex shown in a dashed line) [60].

expansion" and is intended to keep the simplex as large as possible to avoid premature termination of iterations.

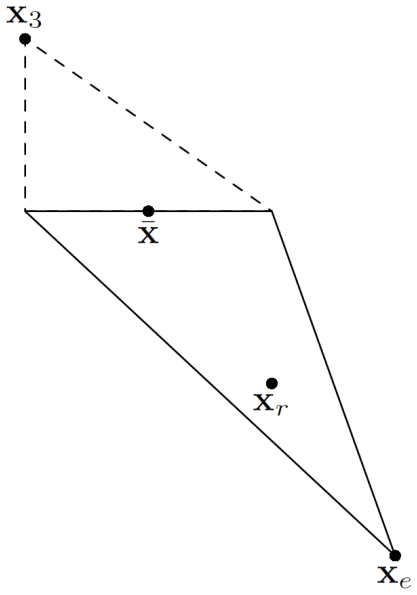

Figure 4.2: Melder-Mead simplex after an expansion (original simplex shown in a dashed line) [60].

- Contract

  If $f_r \geq f_s$ the contraction point $\mathbf{x}_c$ is computed using the better of the two points, $\mathbf{x}_h$ or $\mathbf{x}_r$.

  Outside: If $f_s \leq f_r < f_h$ then $\mathbf{x}_c = \bar{\mathbf{x}} + \gamma(\mathbf{x}_r - \bar{\mathbf{x}})$ and $f_c = f(\mathbf{x}_c)$ is evaluated. If $f_c \leq f_r$, $\mathbf{x}_c$ is accepted and the iteration is terminated. Otherwise a shrink transformation is performed.

Inside: If $f_r \geq f_h$ then $\mathbf{x}_c = \bar{\mathbf{x}} + \gamma(\mathbf{x}_h - \bar{\mathbf{x}})$ and $f_c = f(\mathbf{x}_c)$ is evaluated. If $f_c < f_h$, $\mathbf{x}_c$ is accepted and the iteration is terminated. Otherwise a shrink transformation is performed.

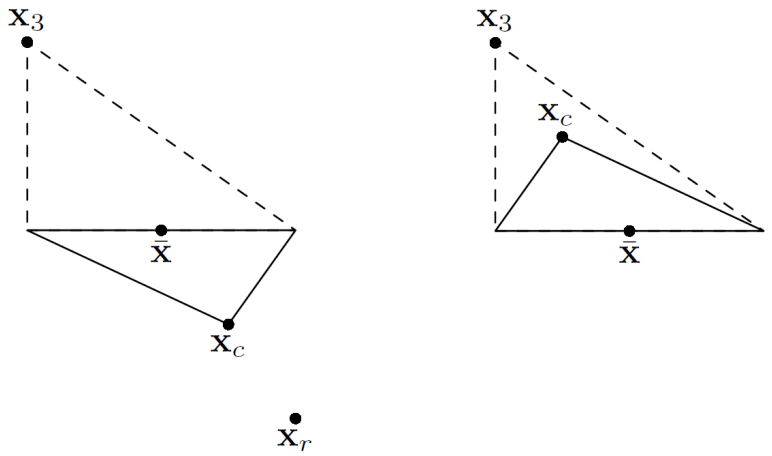

Figure 4.3: Melder-Mead simplex after an outside and inside contraction (original simplex shown in a dashed line) [60].

- Shrink

  A set of n new vertices is computed from,

$$\mathbf{x}_j = \mathbf{x}_l + \sigma(\mathbf{x}_j - \mathbf{x}_l), \tag{4.55}$$

  for $j = 0, ..., n$ with $j \neq l$

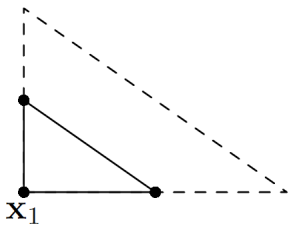

Figure 4.4: Melder-Mead simplex after a shrink (original simplex shown in a dashed line) [60].

Termination

A practical implementation of the Nelder-Mead algorithm must ensure the termination of the algorithm in a finite amount of time. Common termination tests often include 3 parts,

- Domain convergence: when the current simplex is sufficiently small, i.e., some or all vertices $\mathbf{x}_j$, are close enough.

- Function value convergence: when some or all function values, f_j, are small enough.
- No-convergence: when the number of iteration or function evaluations exceeds a prescribed maximum allowed value.

The termination of the algorithm is assured as soon as at least one of these conditions is verified.

4.3.2 Genetic Algorithm

The genetic algorithms were the first evolutionary-based technique introduced in the literature. They were formally presented in the mid 1970s by John Holland [61] and further described by Goldberg [62]. The attractiveness of genetic algorithms is mainly due to its flexibility, capability of performing global search without the need of an initial guess or condition and the fact that it can handle any kind of objective functions and any kind of constraints. They have been successfully applied to many complex optimization problems and have been particularly notable in systems with multiple optimum solutions.

Inspired by Darwin's theory of survival of the fittest, genetic algorithms, are based on principles of natural genetics and selection. The candidate solutions to the optimization problem are individuals in a population that evolves through the application of genetic operators and where the objective function value represents the fitness in natural genetics.

In genetic algorithms each individual is represented by a chromosome constituted by individual structures called genes. Chromosomes are usually coded as a binary string that represents a point in the search space, but other encoding schemes can also be used like permutation encoding, direct value encoding or tree encoding. During each iteration step, or generation, each individual is associated with a fitness function value that determines the robustness of the candidate solution, i.e., how well the individual solves the problem at hand.

A genetic algorithm usually begins its search from a randomly generated population of individuals, that will evolve over successive generations (iterations) based on the fitness of every individual in the population and through the application of the genetic operators.

Genetic Operators

The genetic operators used in genetic algorithms are used to create and maintain genetic diversity necessary for the evolution process ensuring at the same time the improvement of the fitness of the best candidate solution. There are three main types of operators: selection, crossover and mutation.

- Selection

  The selection operator is the first process applied to the population and consists in the selection of the best individuals to form a mating pool, i. e., strings are copied to the new population based on their fitness value for use in reproductive operations. There are three major types of selection strategies for choosing the best individuals: the fitness

proportionate selection also known as roulette-wheel selection, tournament selection and rank selection. The basic mechanism of each strategy will be described next. Other selection methods include stochastic universal sampling, local selection or truncation selection. More detailed information on selection methods can be found on [63–65].

- Fitness proportionate selection

  In fitness proportionate selection the fitness function is evaluated for each individual providing the fitness values. These are then normalized by dividing the fitness value by the sum of all fitness values so that the sum of all fitness values is 1. The population is then sorted by descending fitness values and the accumulated normalized fitness value of each individual is computed. A random number, r, between 0 and 1 is then chosen and the selected individual is the first one whose accumulated normalized value is grater than r.

- Tournament selection

  The tournament method performs the selection by choosing randomly n individuals from the population. These individuals will then compete against each other and the one with highest fitness wins. The number of individuals in a tournament is referred to as the tournament size and is usually 2 (called a binary tournament). Larger values of tournament size lead to higher expected loss of diversity.

- Rank selection

  On rank selection the probability of an individual of being selected is based on its fitness rank relative to the entire population. Rank based strategies first sort individuals in the population according to their fitness and then compute selection probabilities according to their ranks rather than fitness values. This selection method introduces a uniform scaling across the population to avoid the influence of individuals with very high fitness values and thus prevents premature convergence. However this method can lead to slower convergence since the best individuals won't differ much from the rest.

Retaining the best individuals in a generation unchanged in the next generation is called elitism. Elitism was introduced so that when a new population is created by crossover and mutation the best individuals would not be lost.

- Crossover

  Having selected the fittest individuals, the next step is to generate a new population by creating new chromosomes, called offsprings, from the exchange of parents information. Generally the crossover operator selects randomly two individuals from the previously selected group that will exchange portions of their strings. The simplest crossover operation is the single point in which a cut point is selected at random along the string length and the segments on the right side of the crossover point are swapped between the two individuals. More than one crossover point can be used and each second segment between subsequent crossover positions is exchanged. Another crossover strategy is the uniform crossover. In this method, instead of mixing segments of the parents strings the exchange is performed on a gene level, i. e., single bits. For each bit

the decision whether to exchange it or not is done by means of independent coin tosses. Additional crossover schemes include cut and splice crossover, three parent crossover, shuffle crossover, etc. [66].

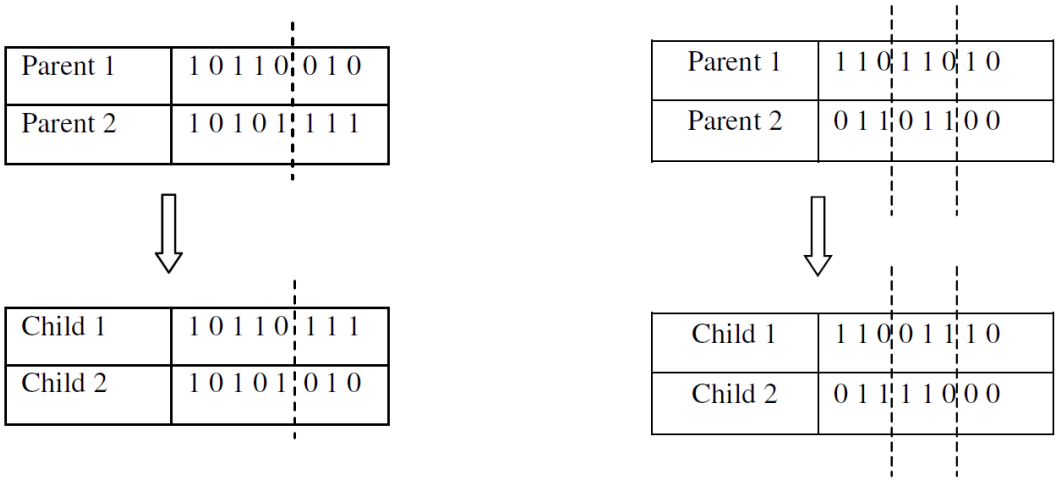

Figure 4.5: Single-point and two-point crossover [66].

Parent 1	1 0 1 1 0 0 1 1
Parent 2	0 0 0 1 1 0 1 0
Mask	1 1 0 1 0 1 1 0
Child 1	1 0 0 1 1 0 1 0
Child 2	0 0 1 1 0 0 1 1

Figure 4.6: Uniform crossover [66].

- Mutation

  The mutation operator is used to ensure genetic diversity from one generation to the next avoiding early convergence to a local minimum by helping the exploration of the whole search space. This operator works by generating random alteration of the chromosomes on the genes level. There are many different forms of mutation, the most simple consists in altering one or more gene values in an individual with a small probability. The probability is usually taken as 1/L where L is the length of the string. The mutation of a string can involve flipping of a bit changing it from 0 to 1 and vice-versa, interchanging two bits chosen from random positions or reversing the bits that are next to randomly picked positions.

A genetic algorithm is a stochastic based search method in which an iterative process modifies a giving population over several generations to attain a good or optimal solution. Consequently, a genetic algorithm will not terminate unless a stopping condition is provided. Common approaches are to set a upper limit on the number of fitness evaluations, the number

Parent	**1** 0 1 1 **0** 1 0 **1**
Mutation chromosome	**1** 0 0 0 **1** 0 0 **1**
Child	**0** 0 1 1 **1** 1 0 **0**

Parent	1 **0** 1 1 0 **1** 0 1
Child	1 **1** 1 1 0 **0** 0 1

Figure 4.7: Mutation by flipping and interchanging [66].

of generations or elapsed time. Also a stopping condition can be set for terminating the process when no change to the population's best fitness is verified over a specified number of generations or when there is no improvement in the objective function for a sequence of consecutive generations of a determined length called stall generations. A general version of a genetic algorithm is given in the flowchart of Figure 4.8.

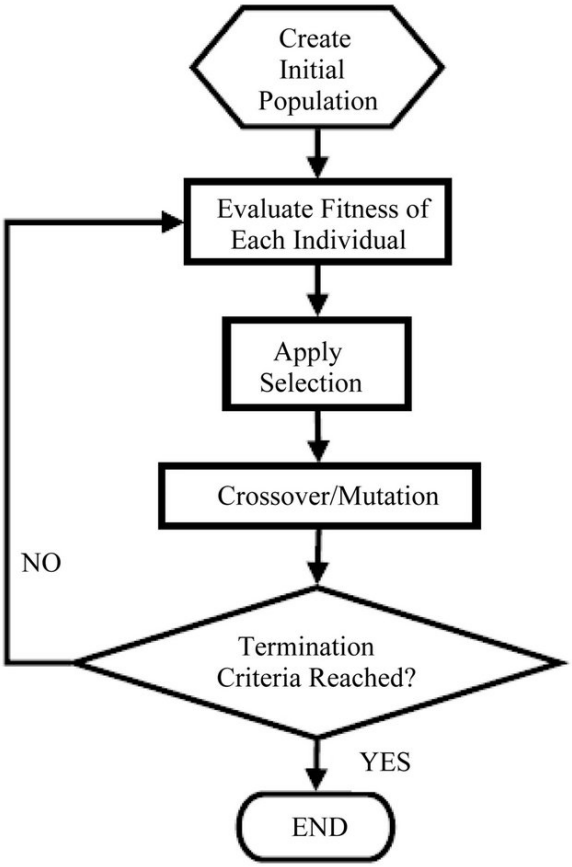

Figure 4.8: Flowchart of a generic GA.

4.3.3 Combined Nelder-Mead and Genetic Algorithm

The genetic algorithm can reach the region near an optimum point relatively quick but it can take many function evaluations to achieve convergence. On the other hand, search methods like the Nelder-Mead Simplex can be very effective on local search but are highly dependent on the initial guess. Hence, to take advantage of both optimization strategies, a hybrid technique

was used. This strategy consisted in locating a solution in the region of the global minimum using the genetic algorithm. Then, using the Nelder-Mead algorithm, a localized search could be performed to obtain the global minimum.

In this study, these optimization methods were applied to calibrate the material parameters of Ti6Al4V alloy for the CPB06 and Nixon yield criteria. The stress-strain data for this material was determined by Tuninetti et al. [34] and was presented in Chapter 3 Figure 3.10. The material parameters for 6 levels of equivalent plastic strain were determined and the yield loci obtained. The experimental input variables are given in Table 4.1.

Table 4.1: Material experimental input data for the calibration of the CPB06 and Nixon yield criteria.

$\bar{\varepsilon_p}$	σ_{LD}^T (MPa)	σ_{LD}^C(MPa)	σ_{TD}^T(MPa)	σ_{TD}^C(MPa)	σ_{ST}^T(MPa)	σ_{ST}^C(MPa)	σ_{SSH}(MPa)
0.0	927	970	931	1045	940	996	498
0.02	969	1032	992	1150	1004	1084	573
0.04	996	1069	1025	1198	1038	1127	596
0.06	1017	1100	1050	1237	1066	1163	611
0.08	1035	1129	1072	1268	1092	1194	620
0.09	1039	1146	1082	1283	1103	1206	628

For the CPB06 model, there are 9 anisotropy coefficients, C_{ij} with $i, j = 1, \ldots, 3$ and the strength differential parameter, k. The degree of homogeneity, a, was fixed and set to 2. Because the CPB06 yield function is a homogeneous function of degree one, the anisotropy coefficients can be scaled by C_{11}, i.e., we can take $C_{11} = 1$. To ensure convexity the parameter, k is limited to the range $[-1, 1]$. Due to the lack of data for the LD-TD and TD-ST planes the shear parameters C_{44} and C_{55} could not be determined and $C_{44} = C_{55} = C_{66}$ was assumed. Therefore the total number of parameters to calibrate is reduced to 7. The optimization variables vector is $\mathbf{x} = [C_{12}, C_{13}, C_{22}, C_{23}, C_{33}, C_{66}, k]$.

For the Nixon model, there are 6 anisotropic coefficients, $a_i, i = 1, \ldots, 6$ and the strength differential parameter, c. Also in this case a_1 was set to 1 and $a_4 = a_5 = a_6$ was assumed. Due to convexity the parameter c is limited to the range $\left[-3\sqrt{3}/2, 3\sqrt{3}/4\right]$. The optimization variables vector is $\mathbf{x} = [a_2, a_3, a_6, c]$.

The Nelder-Mead algorithm was first tested with the starting point set to the von Mises case. Both the CPB06 and the Nixon yield criteria can be reduced to the von Mises model, i.e., the von Mises yield criterion can be seen as a particular case of the former and thus the von Mises case can be used as the initial guess for Nelder-Mead optimization process. The equivalence between CPB06 and von Mises is obtained by taking $a = 2$, $k = 0$ and by reducing the fourth order orthotropy tensor, $\mathbf{C}$, to the isotropic case by setting $\mathbf{C} = \mathbf{I}$, where $\mathbf{I}$ is the identity tensor, so that the tensor $\mathbf{\Sigma} = \mathbf{S}$. For the Nixon model, the von Mises yield criterion is obtained by taking $c = 0$ and reducing the second and third invariants, J_2^0 and J_3^0 to the isotropic case, J_2 and J_3, by letting $a_i = 1, i = 1, \ldots, 6$. Therefore the vector of the starting points, $\mathbf{x_0}$, for CBPB06 and Nixon are given respectively by $\mathbf{x_0} = [0, 0, 1, 0, 1, 1, 0]$ and $\mathbf{x_0} = [1, 1, 1, 0]$. The calibrated material parameters are presented in Tables 4.2 and 4.3.

The intersections of the yield surfaces with the LD-TD, LD-ST and TD-ST planes, pre-

Table 4.2: Material parameters for the CPB06 yield criterion calibrated with Nelder-Mead Algorithm with initial guess set to the von Mises equivalent case.

$\bar{\varepsilon}_p$	C_{12}	C_{13}	C_{22}	C_{23}	C_{33}	C_{66}	k
0.0	-0.005	-0.0482	1.0425	-0.0031	0.9866	1.1546	-0.1152
0.02	0.1135	0.0423	1.0978	0.1515	0.9982	0.9708	-0.1468
0.04	0.1225	0.0459	1.0974	0.1630	0.9894	0.9541	-0.1527
0.06	0.0592	0.0388	1.055	0.1338	1.0351	0.9901	-0.1673
0.08	0.0733	0.0091	1.0653	0.1119	0.9707	0.994	-0.1772
0.09	0.0809	0.0188	1.0476	0.1128	0.9729	0.9729	-0.1847

Table 4.3: Material parameters for the Nixon yield criterion calibrated with Nelder-Mead Algorithm with initial guess set to the von Mises equivalent case.

$\bar{\varepsilon}_p$	a_2	a_3	a_6	c
0.0	1.0579	1.0207	1.1525	-0.2554
0.02	1.1114	1.0651	1.1068	-0.3384
0.04	1.1245	1.0764	1.1096	-0.3666
0.06	1.1333	1.0871	1.1183	-0.3938
0.08	1.1393	1.0978	1.1328	-0.4163
0.09	1.1483	1.1049	1.1338	-0.4403

dicted by the CPB06 and Nixon models with the parameters of Tables 4.2 and 4.3 were obtained for $\bar{\varepsilon}_p = 0$ and are shown in Figure 4.9 along with the yield loci given by the von Mises yield criteria and the experimental data.

In Figure 4.9 it is possible to note the agreement between the experimental values and the predicted yield locus of CPB06 and the Nixon yield criteria. The von Mises yield criterion, unlike CPB06 and Nixon, is not capable of capturing the behaviour of the titanium alloy studied. It was possible to note as well, that all the solutions obtained with the Nelder-Mead algorithm converged to points very close to the initial guess given, evidencing the efficiency of the search algorithm on one side but suggesting a convergence to a local minimum on the other. For higher values of the equivalent plastic strain the discrepancy between the experimental and the predicted data is higher, as can be seen in Figures 4.10 and 4.11, for equivalent plastic strains of 0.04 and 0.09 respectively.

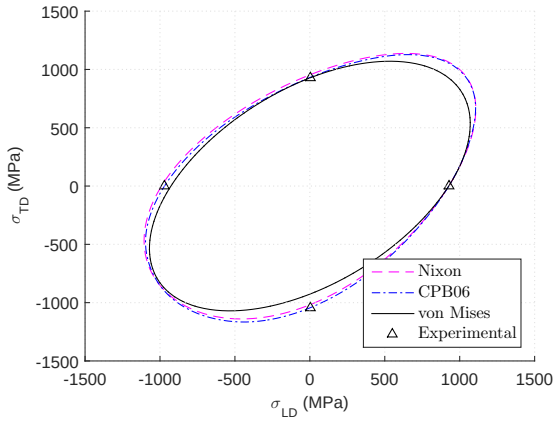

(a) LD-TD plane

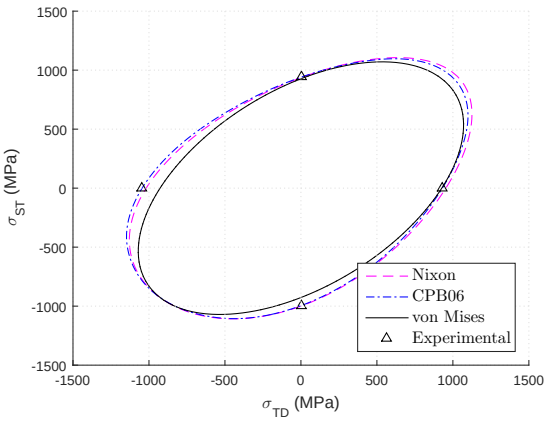

(b) TD-ST plane

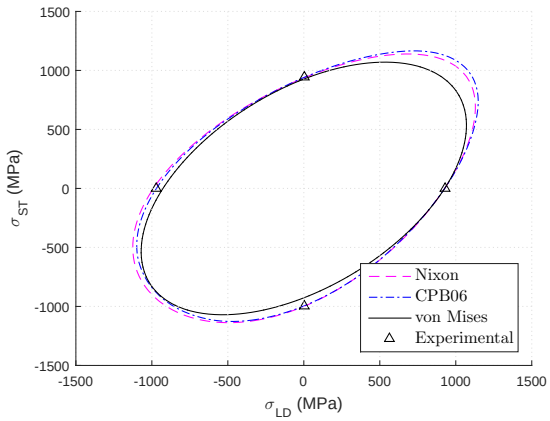

(c) LD-ST plane

Figure 4.9: Predicted yield locus of the CPB06, Nixon and von Mises yield criteria for $\bar{\varepsilon}_p = 0$ and parameters given by Tables 4.2 and 4.3.

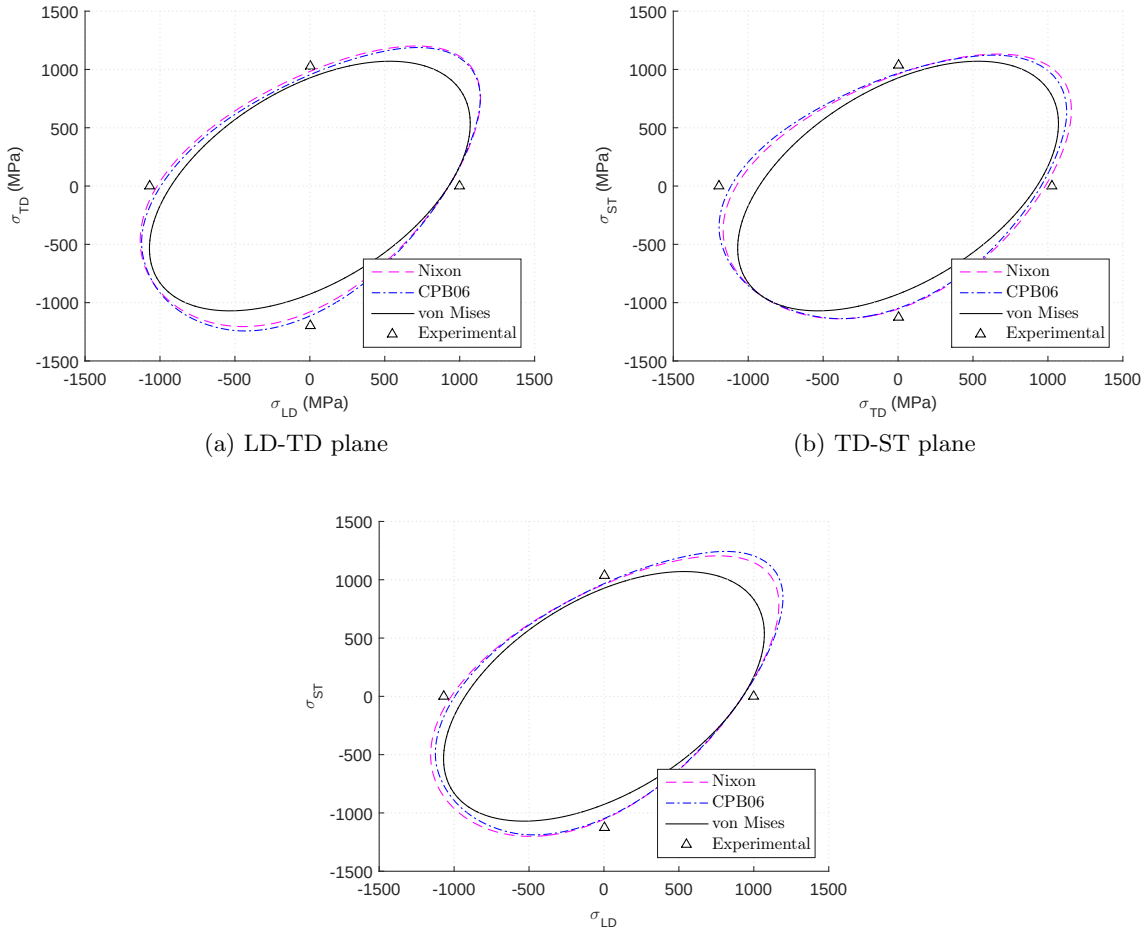

(a) LD-TD plane

(b) TD-ST plane

(c) LD-ST plane

Figure 4.10: Predicted yield locus of the CPB06, Nixon and von Mises yield criteria for $\bar{\varepsilon}_p = 0.04$ and parameters given by Tables 4.2 and 4.3.

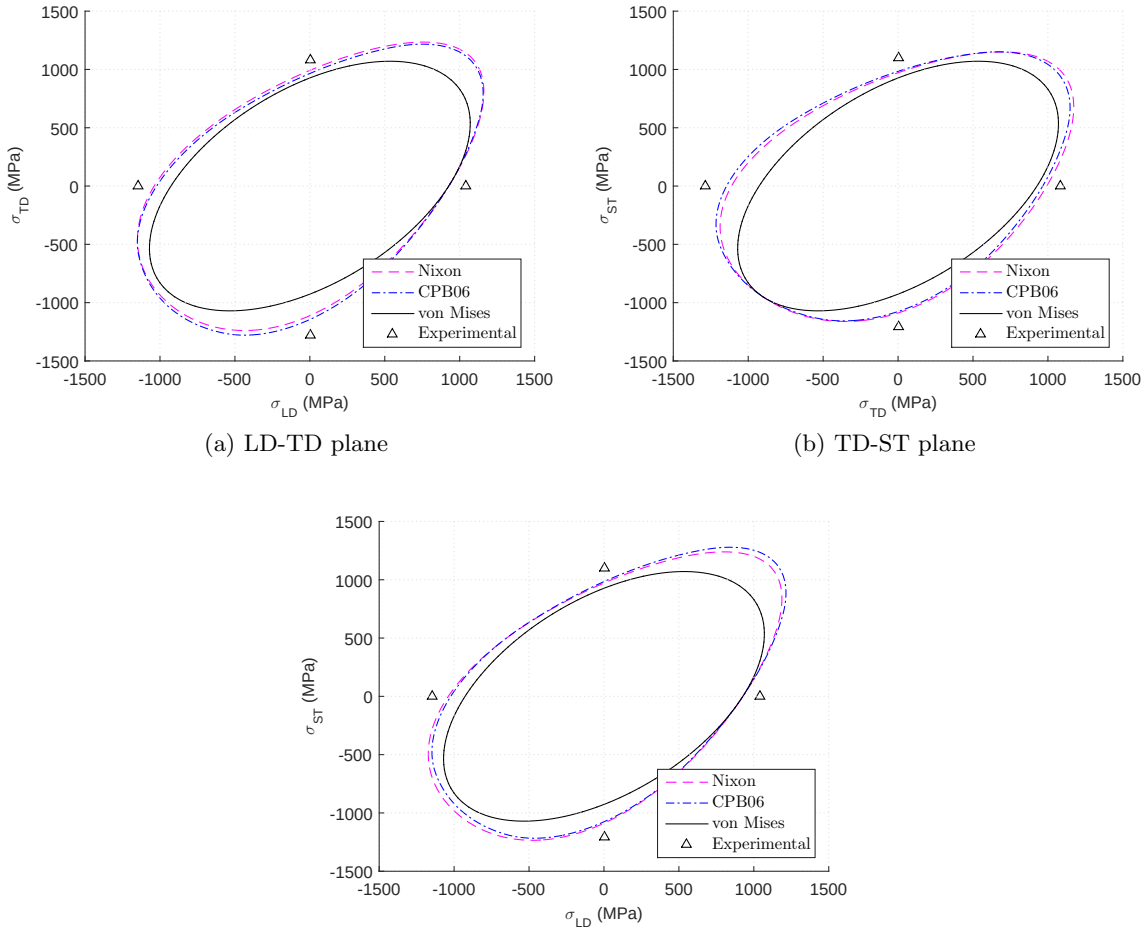

(a) LD-TD plane

(b) TD-ST plane

(c) LD-ST plane

Figure 4.11: Predicted yield locus of the CPB06, Nixon and von Mises yield criteria for $\bar{\varepsilon}_p = 0.09$ and parameters given by Tables 4.2 and 4.3.

To improve the previous solution, the calibration of the CPB06 and Nixon yield criteria was performed using the genetic algorithm. Note that the genetic algorithm does not require an initial guess and thus a solution near the global minimum is expected. The material parameters obtained are given in Tables 4.4 and 4.5 .

Table 4.4: Material parameters for the CPB06 yield criteria calibrated with Genetic Algorithm.

$\bar{\varepsilon}_p$	C_{12}	C_{13}	C_{22}	C_{23}	C_{33}	C_{66}	k
0.0	4.5481	4.8564	0.4714	4.4379	0.9250	-4.2856	0.1113
0.02	-2.1420	-2.3956	1.3570	-2.0005	1.0038	3.4458	-0.1466
0.04	-3.3652	-3.7007	1.4171	-3.1751	0.9519	-4.7126	-0.1580
0.06	-1.2111	-1.3745	1.1903	-1.1112	0.9622	-2.3773	-0.1699
0.08	-2.2329	-2.4562	1.2382	-2.0904	0.9083	3.4715	-0.1774
0.09	-2.8206	-3.0769	1.1952	-2.6898	0.8153	-4.0435	-0.1848

Table 4.5: Material parameters for the Nixon yield criteria calibrated with Genetic Algorithm.

$\bar{\varepsilon}_p$	a_2	a_3	a_6	c
0.0	0.0356	-1.0664	0.6698	-2.3991
0.02	-0.8916	-0.1562	0.5762	0.8834
0.04	-0.8147	-0.2387	0.5573	0.6171
0.06	-0.8367	-0.2211	0.5630	0.7257
0.08	-0.8450	-0.2162	0.5693	0.7944
0.09	-0.8627	-0.2021	0.5707	0.9082

The intersections of the predicted yield surfaces with the LD-TD, LD-ST and TD-ST planes for the CPB06 and Nixon, with the material parameters obtained using the GA, are shown in Figure 4.12 along with the von Mises yield loci for $\bar{\varepsilon}_p = 0$.

When using the parameters given by the genetic algorithm optimization, the yield locus of the CPB06 and Nixon yield criteria evidence again the better agreement of these models when compared to the von Mises. Furthermore it can be noted that relatively to the solution obtained with the NM algorithm, the CPB06 and Nixon yield curves are not as coincident. This may evidence the stochastic nature of the genetic algorithm and the convergence to a solution in the vicinity of a minimum. For higher values of the equivalent plastic strain, not only greater discrepancies were found between the experimental and predicted data but also between the CPB06 and Nixon yield locus, as can be seen in Figures 4.13 and 4.14.

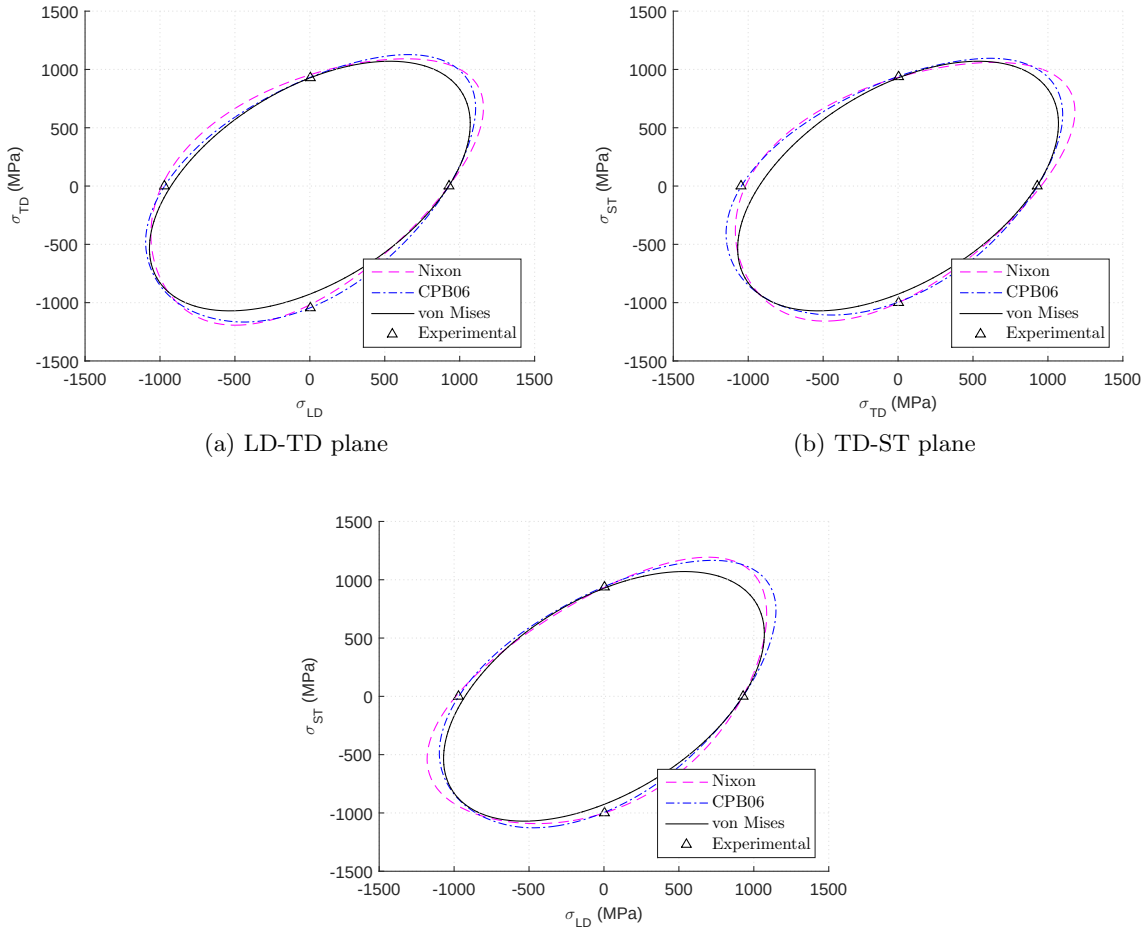

(a) LD-TD plane

(b) TD-ST plane

(c) LD-ST plane

Figure 4.12: Predicted yield locus of the CPB06, Nixon and von Mises yield criteria for $\bar{\varepsilon}_p = 0$ with parameters given by Tables 4.4 and 4.5.

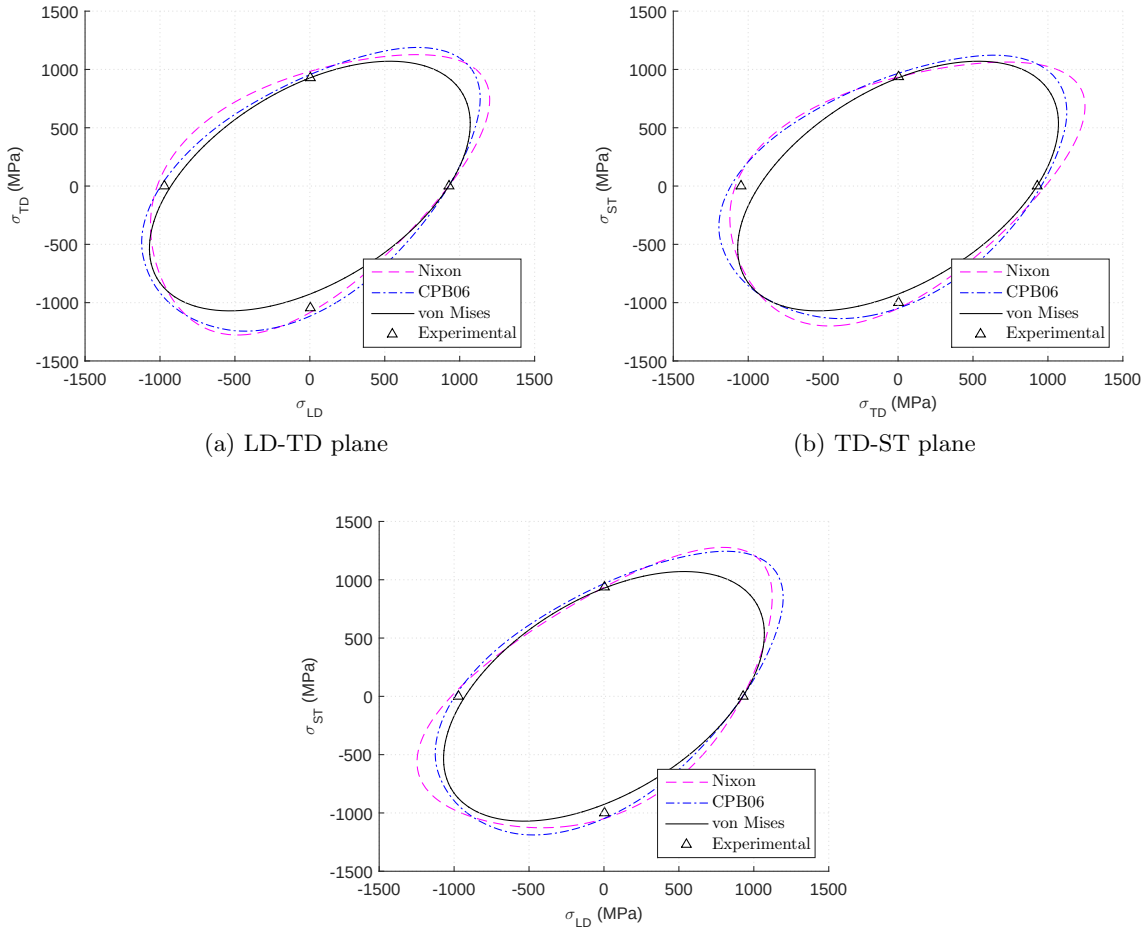

(a) LD-TD plane

(b) TD-ST plane

(c) LD-ST plane

Figure 4.13: Predicted yield locus of the CPB06, Nixon and von Mises yield criteria for $\bar{\varepsilon}_p = 0.04$ with parameters given by Tables 4.4 and 4.5.

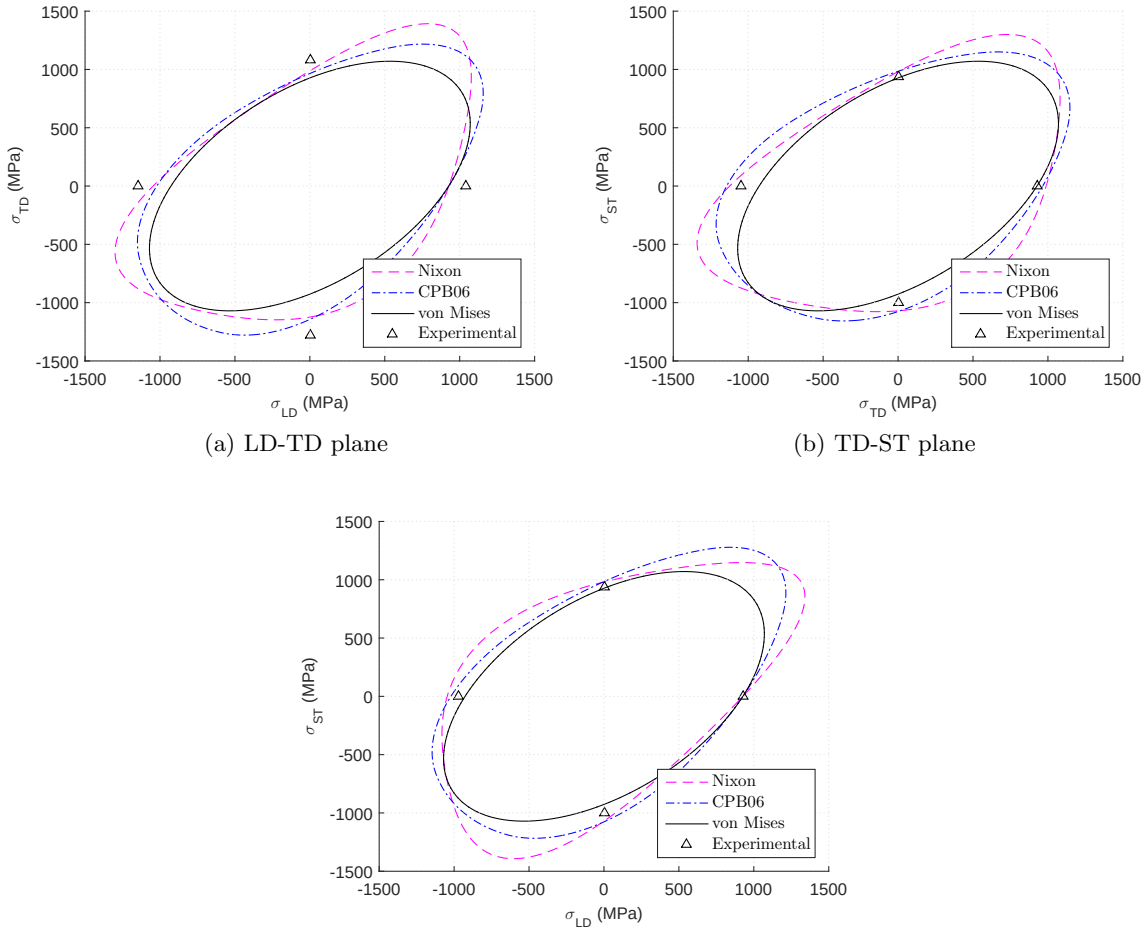

(a) LD-TD plane

(b) TD-ST plane

(c) LD-ST plane

Figure 4.14: Predicted yield locus of the CPB06, Nixon and von Mises yield criteria for $\bar{\varepsilon}_p = 0.09$ with parameters given by Tables 4.4 and 4.5.

Combining the two algorithms, by setting the initial point of the Nelder-Mead method with the solution provided by the genetic algorithm, ensures a more refined search in the region of the global minimum improving the accuracy of the solution of the optimization problem. The material parameters obtained using the combined method are given in Tables 4.6 and 4.7.

Table 4.6: Material parameters for the CPB06 yield criteria calibrated with the combined method.

$\bar{\varepsilon}_p$	C_{12}	C_{13}	C_{22}	C_{23}	C_{33}	C_{66}	k
0.0	4.5513	4.8573	0.4864	4.4482	0.9367	-4.2793	0.1112
0.02	-2.1377	-2.3897	1.3464	-2.0030	0.9938	3.4362	-0.1469
0.04	-3.3688	-3.7045	1.4186	-3.1776	0.9539	-4.7178	-0.1582
0.06	-1.2126	-1.3751	1.1867	-1.1151	0.9575	-2.3756	-0.1692
0.08	-2.2357	-2.4597	1.2280	-2.1008	0.8979	3.4706	-0.1772
0.09	-2.8219	-3.0801	1.1979	-2.6894	0.8160	-4.0459	-0.1847

Table 4.7: Material parameters for the Nixon yield criteria calibrated with combined method.

$\bar{\varepsilon}_p$	a_2	a_3	a_6	c
0.0	0.0331	-1.0632	0.6670	-2.5981
0.02	-0.8519	-0.1962	0.5674	0.6909
0.04	-0.8414	-0.2123	0.5627	0.6978
0.06	-0.8307	-0.2271	0.5618	0.7056
0.08	-0.8223	-0.2389	0.5647	0.7148
0.09	-0.8368	-0.2282	0.5655	0.7981

The predicted yield locus, represented in the LD-TD, LD-ST and TD-ST planes, for the CPB06 and Nixon with the material parameters obtained by the combined GA plus Nelder-Mead method are shown in Figure 4.15 for $\bar{\varepsilon}_p = 0$ along with the yield loci for the von Mises model and the experimental data.

The predicted yield locus for all levels of equivalent plastic strain, represented in the LD-TD plane, for the CPB06 and Nixon criteria are given in Figures 4.16 and 4.17 respectively along with the experimental data.

The intersection of the yield surfaces with the other two planes, LD-ST and TD-ST, were also obtained and are given in figures 4.18, 4.19 and 4.20, 4.21 for the CPB06 and Nixon yield criteria respectively.

The predicted yield curves in the LD-TD plane show a good agreement with the experimental data, with the CPB06 yield criteria showing slightly more accurate results particularly for higher values of the equivalent plastic strain. The predicted yield locus shows a slightly distorted shape, irrespective of the level of plastic strain, which is compatible with the deformation behaviour of the hexagonal closed packed materials. The distortion of the yield surface for Ti6Al4V is associated with the tension compression asymmetry and the anisotropic

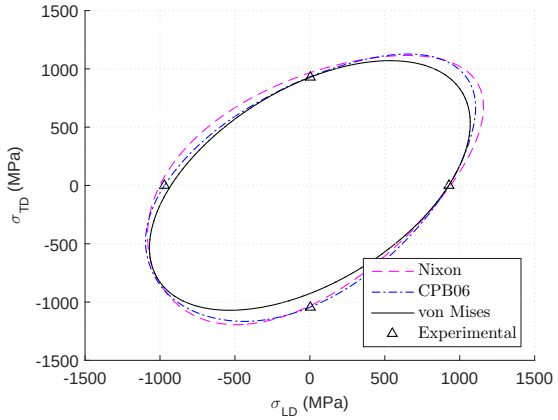

(a) LD-TD plane

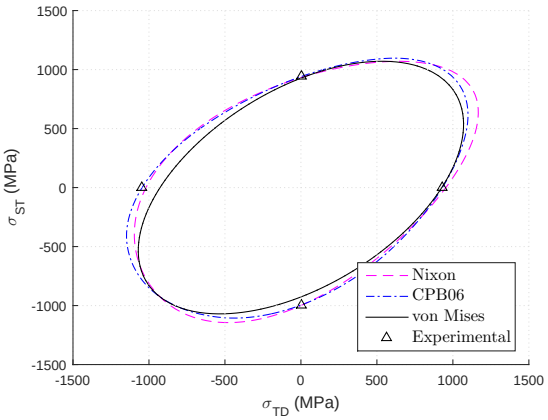

(b) TD-ST plane

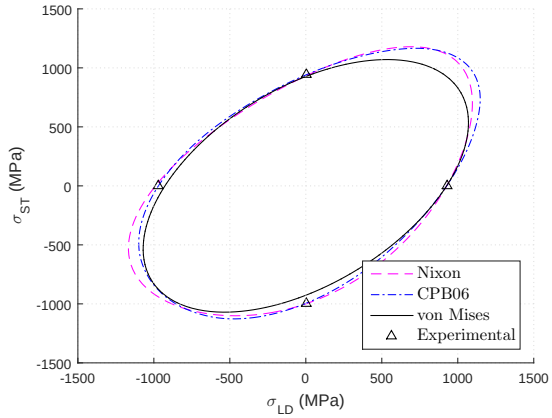

(c) LD-ST plane

Figure 4.15: Predicted yield locus of the CPB06, Nixon and von Mises yield criteria for $\bar{\varepsilon_p} = 0$.

hardening evidenced by the stress-strain data. It should be noted that for higher values of equivalent plastic strain, the Nixon yield criterion predicted a more triangular shaped yield loci and a more pronounced tension compression asymmetry. This change in shape was also shown by Nixon et al. [32] for a high purity α-titanium and occurred at the strain level associated with twin activation in the longitudinal direction. On the other hand, the yield loci of the CPB06 yield criteria presented a more elliptical shape with less distortion which is indicative of low levels of deformation twinning as was found for Ti6Al4V titanium alloy [67].

On the LD-ST and TD-ST planes, the predicted yield loci for both the Nixon and CPB06 models showed a satisfactory agreement with the experimental data. The higher discrepancies were registered for higher values of the equivalent plastic strain and for compressive stresses. Nevertheless, the distorted shape and the evolution of the yield loci shape with the equivalent plastic strain were captured by both the CPB06 and the Nixon yield criteria. The CPB06 model resulted, as was seen for the LD-TD plane, in a more elliptic like shape when compared to the Nixon model specifically for higher values of the equivalent plastic strain. The more triangular shape of the yield loci of the Nixon model has been reported for pure titanium and

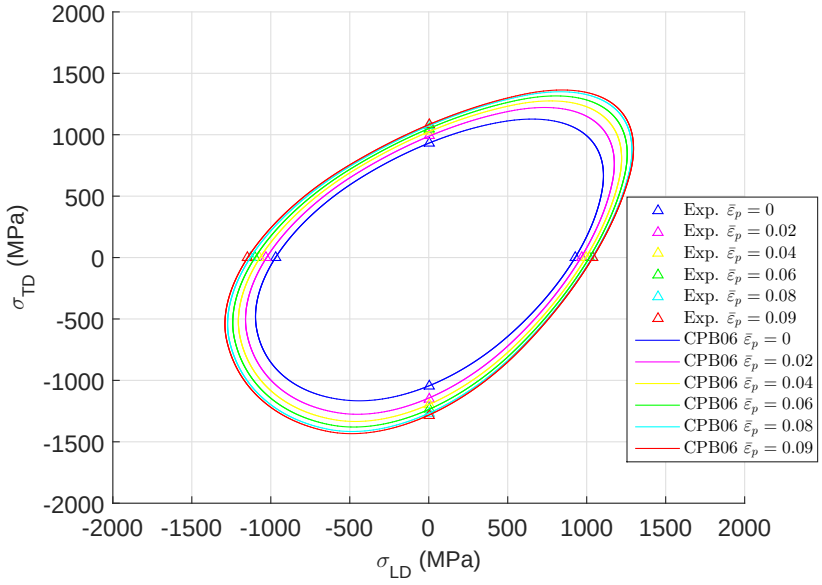

Figure 4.16: Predicted yield loci of the CPB06 yield criterion for all levels of $\bar{\varepsilon}_p$.

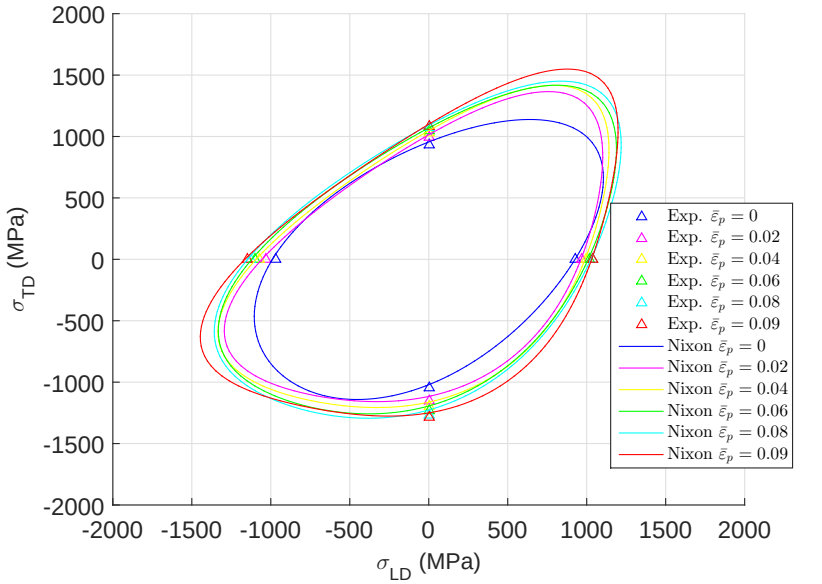

Figure 4.17: Predicted yield loci of the Nixon yield criterion for all levels of $\bar{\varepsilon}_p$.

is associated with twin activation. This triangular shape appears therefore more clearly in titanium alloys with a stronger α phase.

It should be noted that a limited number of experimental tests were available for the parameter identification procedure. The experimental tests should describe accurately the different material behaviours under different loading conditions and thus to fully capture the Ti6Al4V titanium alloy behaviour additional experimental shear data in other directions could

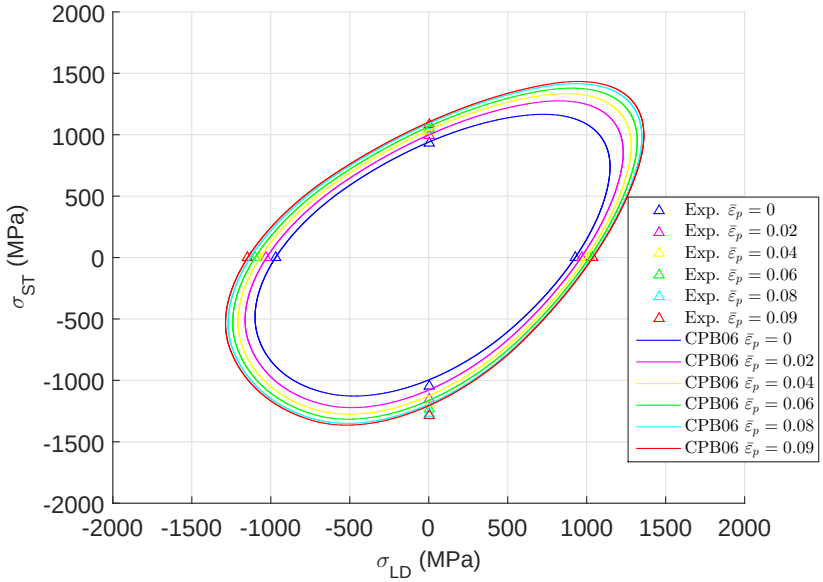

Figure 4.18: Predicted yield loci in the LD-ST plane of the CPB06 yield criterion for all levels of $\bar{\varepsilon}_p$.

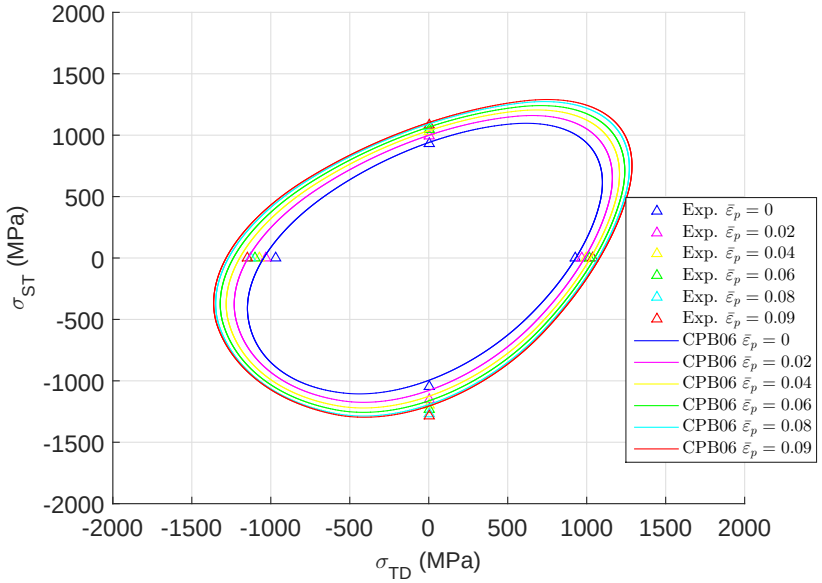

Figure 4.19: Predicted yield loci in the TD-ST plane of the CPB06 yield criterion for all levels of $\bar{\varepsilon}_p$.

be used as well as the Lankford coefficients that, as it is known, play an important role in the quantification of the degree of anisotropy. As shown by Tuninetti et al. [34] simulations using material models whose parameters are based on the largest number of tests and taking into account the evolution of the yield locus provided the best agreement with the experimental measurements. Nevertheless, assuming identical shear behaviour in the three orthogonal

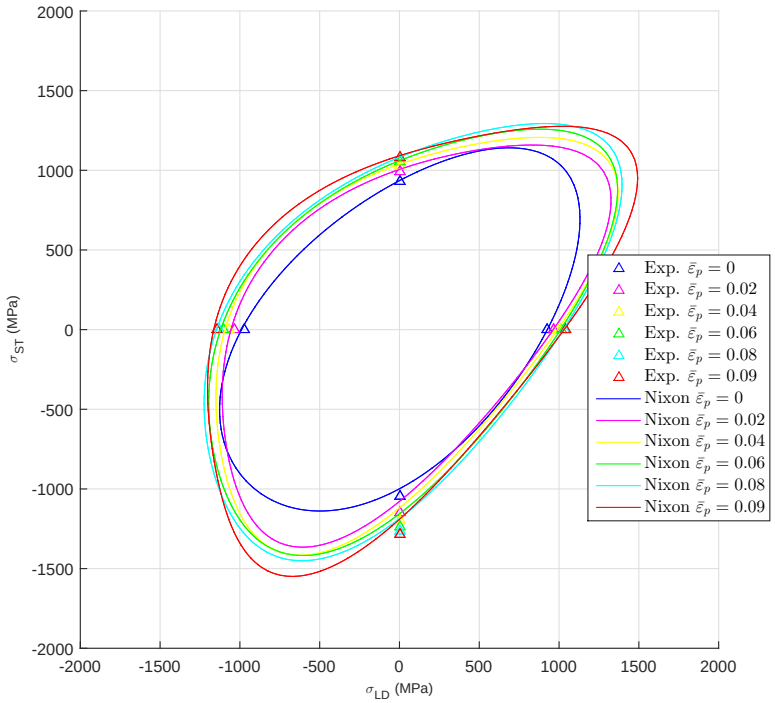

Figure 4.20: Predicted yield loci in the LD-ST plane of the Nixon yield criterion for all levels of $\bar{\varepsilon}_p$.

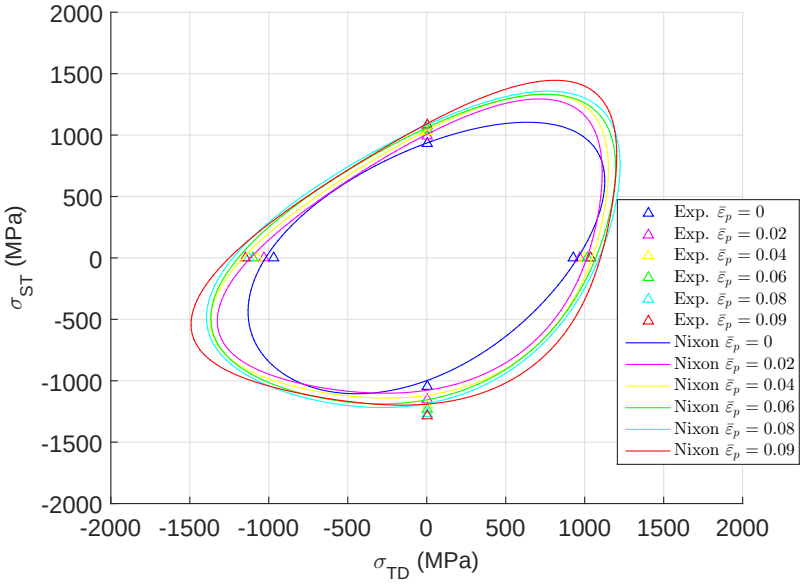

Figure 4.21: Predicted yield loci in the TD-ST plane of the Nixon yield criterion for all levels of $\bar{\varepsilon}_p$.

planes when only one experimental test is available still provided good predictions of load evolution. On the other hand, Gilles et al. [33], using the CPB06 yield criteria with three additional tensor transformations, that allow a better representation of the anisotropy, showed that given the little deformation twinning present in Ti6Al4V alloy, taking into account the evolution of the parameters had little impact on the predicted stress-strain behaviour both in tension and compression.

Chapter 5

Computational Implementation of Yield Criteria for Ti6Al4V

5.1 Introduction

The current specific yield criteria for hexagonal closed packed materials were presented in Chapter 3. The major advantage of these macroscopic formulations for the deformation behaviour is the easier implementation into finite element codes. In this Chapter, the numerical and computational procedures for the implementation of the constitutive models for the titanium alloy Ti6Al4V in the finite element framework are presented.

5.2 Plasticity Theory

Plasticity theory provides a general framework to understand and describe the deformation behaviour of materials where, beyond the elastic limit, permanent deformation occurs. Particularly, rate independent plasticity, is concerned with materials for which the permanent deformations do not depend on the rate of application of loads.

The scientific study of plasticity can be traced back to the middle of the nineteenth century with the publication of the experimental investigations on punching and extrusion by Tresca. Based on this preliminary work, Tresca proposed a yield criterion for metals that stated that a metal yielded plastically when the maximum shear stress attained a critical value. Previous yielding criteria for plastic solids, mainly soils, had been proposed by Coulomb (1773) and applied by Poncelet (1840) and Rankine (1853), however no earlier investigations for metals had been conducted [68]. Substantial developments on the theory of plasticity took place predominantly in the first half of the twentieth century mostly due to the investigation work of von Mises, Hencky, Prandtl and Reuss.

This section aims to provide a review of the mathematical theory of rate-independent plasticity that constitutes the basis for the numerical implementation of the constitutive models for elastoplastic solids, restricted to infinitesimal strains.

5.2.1 General elastoplastic constitutive model

Typical loading-unloading stress-strain relations for elastoplastic materials can be schematically represented for a one-dimensional case as shown in Figure 5.1. Although an uniaxial tension test may appear an oversimplified characterization, it introduces the key aspects of the plasticity theory. From the stress-strain curve given in Figure 5.1 a number of import-

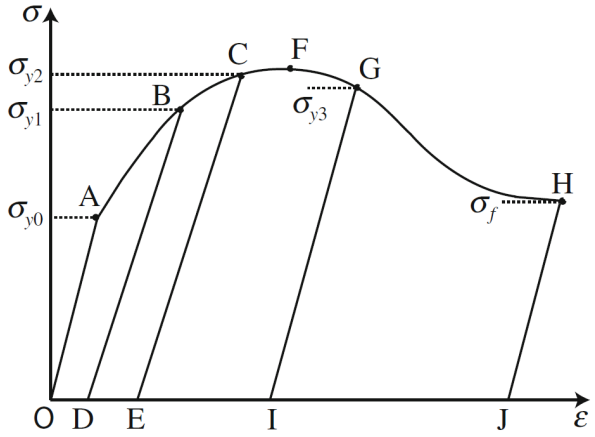

Figure 5.1: Typical loading-unloading uniaxial stress-strain relation for an elastoplastic material [69].

ant general phenomenological properties that characterize the elastoplastic behaviour can be identified:

- There exists an elastic domain, i.e., a range of stresses within which the behaviour of the material is purely elastic and no evolution of permanent strains takes place. Attending to Figure 5.1, during loading along the path OA and reloading along DB, EC, IG and JH the behaviour of the material is purely elastic. The stresses at points A, B, C, G and H are the yield stresses that delimit the elastic domain.
- When the material is loaded beyond the yield stress, plastic yielding (or plastic flow) occurs, i. e., there is an evolution of the plastic strain.
- Besides the evolution of the plastic strain there is an evolution of the yield stresses. From point O to F the yield stress increases ($\sigma_{y0} < \sigma_{y1} < \sigma_{y2}$) and beyond point F the yield stress decreases ($\sigma_{y3} <$ the yield stress at point F). When the yield stress increases the material is said to experience hardening (or strain hardening) and when it decreases it experienced softening (or strain softening). The hardening/softening behaviour is modeled by a hardening law.

For a generalised elastoplastic constitutive model the following set of fundamental points can be established:

1. An elastoplastic strain decomposition;
2. An elastic law;

3. A yield criterion, stated with the use of a yield function;

4. A plastic flow rule defining the evolution of the plastic strain;

5. A hardening law, characterising the evolution of the yield limit;

6. Loading/unloading conditions.

These concepts are developed in the following sections.

Additive decomposition of the strain tensor

One of the fundamental principles underlying small strain theory is the decomposition of the total strain tensor, $\boldsymbol{\varepsilon}$, into the sum of an elastic reversible component, $\boldsymbol{\varepsilon^e}$, and a plastic permanent component, $\boldsymbol{\varepsilon^p}$. That is,

$$\boldsymbol{\varepsilon = \varepsilon^e + \varepsilon^p.} \tag{5.1}$$

The decomposition of strain tensor can be written in rate form as,

$$\boldsymbol{\dot{\varepsilon} = \dot{\varepsilon}^e + \dot{\varepsilon}^p.} \tag{5.2}$$

Elastic law

In phenomenological constitutive models, where the internal variables are directly associated with the dissipative behaviour observed at a macroscopic level, we have the specific free energy, $\boldsymbol{\psi}$, represented by,

$$\boldsymbol{\psi(\varepsilon, \varepsilon^p, \alpha),} \tag{5.3}$$

which is a function of the total strain, $\boldsymbol{\varepsilon}$, the plastic strain, $\boldsymbol{\varepsilon^p}$ and a set of $\boldsymbol{\alpha}$ internal variables associated with hardening.

The free energy function can be decomposed into the sum of an elastic contribution, $\boldsymbol{\psi^e}$, and a contribution due to hardening, $\boldsymbol{\psi^p}$, i.e.,

$$\boldsymbol{\psi(\varepsilon, \varepsilon^p, \alpha) = \psi^e(\varepsilon - \varepsilon^p) + \psi^p(\alpha),} \tag{5.4}$$

where the strain decomposition, $\boldsymbol{\varepsilon^e = \varepsilon - \varepsilon^p}$, was taken into account.

The general constitutive elastic law for the stress is obtained from,

$$\boldsymbol{\sigma} = \bar{\boldsymbol{\rho}} \frac{\boldsymbol{\partial \psi^e}}{\boldsymbol{\partial \varepsilon^e}}. \tag{5.5}$$

For materials whose elastic behaviour is linear and isotropic, the elastic contribution to the free energy is given by,

$$\bar{\rho}\psi^e(\varepsilon^e) = \frac{\mathbf{1}}{\mathbf{2}}\varepsilon^e : \mathbf{D}^e : \varepsilon^e, \tag{5.6}$$

where $\mathbf{D}^e$ is the standard isotropic elasticity tensor. Thus, the general elastic law is given by,

$$\boldsymbol{\sigma} = \mathbf{D}^e : \varepsilon^e. \tag{5.7}$$

Yield criterion and the yield surface

For the uniaxial tensile stress-strain relation represented in Figure 5.1, it was shown that plastic flow occurs when the uniaxial stress attains a critical value, the yield stress. Above this critical stress the material can no longer be described by an elastic law. The generalisation of this concept to the three-dimensional case can be achieved by means of a scalar yield function, $\boldsymbol{\Phi}$. This function is negative when only elastic deformations are possible and reaches zero when plastic flow is initiated. During plastic flow, the stress state remains on the yield surface. Thus, plastic flow may occur only when,

$$\boldsymbol{\Phi}(\boldsymbol{\sigma}, \mathbf{A}) = \mathbf{0}, \tag{5.8}$$

where $\boldsymbol{\Phi}$ is the scalar yield function, $\boldsymbol{\sigma}$ the stress tensor and $\mathbf{A} \equiv \bar{\boldsymbol{\rho}}(\boldsymbol{\partial \psi^p / \partial \alpha})$ is the set of hardening thermodynamical forces.

The elastic domain can be defined as the set of stresses for which plastic yielding is not possible, i.e.,

$$\boldsymbol{\mathcal{E}} = \{\boldsymbol{\sigma} | \boldsymbol{\Phi}(\boldsymbol{\sigma}, \mathbf{A}) < \mathbf{0}\}. \tag{5.9}$$

The stress points lying in the elastic domain or on its boundary are said to be plastically admissible. Thus, the set of plastically admissible stresses is defined as,

$$\bar{\boldsymbol{\mathcal{E}}} = \{\boldsymbol{\sigma} | \boldsymbol{\Phi}(\boldsymbol{\sigma}, \mathbf{A}) \leq \mathbf{0}\}. \tag{5.10}$$

The set of stresses for which plastic yielding may occur is called the yield locus and is constituted by the points lying in the boundary of the plastically admissible domain, where $\boldsymbol{\Phi}(\boldsymbol{\sigma}, \mathbf{A}) = \mathbf{0}$. The representation of the yield locus on the space of stresses corresponds to a hypersurface called yield surface and is defined as,

$$\boldsymbol{\mathcal{Y}} = \{\boldsymbol{\sigma} | \boldsymbol{\Phi}(\boldsymbol{\sigma}, \mathbf{A}) = \mathbf{0}\}\,. \tag{5.11}$$

Plastic flow rule

Additional rules governing the evolution of plastic flow are required for the complete characterization of the general plasticity model. The yield condition is normally supplemented by an evolution law for the plastic strain tensor. Thus, the plastic flow rule is defined as,

$$\dot{\boldsymbol{\varepsilon}}^{\boldsymbol{p}} = \dot{\boldsymbol{\gamma}}\mathbf{N}, \tag{5.12}$$

where the tensor $\mathbf{N}$ is the flow vector and $\dot{\boldsymbol{\gamma}}$ is the plastic multiplier.

In multidimensional plasticity models the flow rule is commonly defined in terms of a flow (or plastic) potential. Letting $\boldsymbol{\Psi}$ represent a flow potential with general form

$$\boldsymbol{\Psi} = \boldsymbol{\Psi}(\boldsymbol{\sigma}, \mathbf{A}), \tag{5.13}$$

the flow vector can be obtained as,

$$\mathbf{N} = \frac{\boldsymbol{\partial \Psi}}{\boldsymbol{\partial \sigma}}. \tag{5.14}$$

For many plasticity models, particularly for ductile metals, the flow potential corresponds to the yield function, i.e.,

$$\boldsymbol{\Psi} = \boldsymbol{\Phi}. \tag{5.15}$$

These models are called associative plasticity models once the flow rule is associated with a particular yield function. The idea of a flow rule associated with the yield condition was first proposed by von Mises, who verified its validity for a simple model of plastic slip in crystals [70]. Associative flow rules preserve the validity of the principle of maximum plastic dissipation. The dissipation function is given by,

$$\boldsymbol{\Upsilon}\left(\boldsymbol{\sigma}, \mathbf{A}; \dot{\boldsymbol{\varepsilon}}^{\boldsymbol{p}}, \dot{\boldsymbol{\alpha}}\right) \equiv \boldsymbol{\sigma} : \dot{\boldsymbol{\varepsilon}}^{\boldsymbol{p}} - \mathbf{A} * \dot{\boldsymbol{\alpha}}, \tag{5.16}$$

where the symbol $*$ indicates the appropriate product between $\mathbf{A}$ and $\dot{\boldsymbol{\alpha}}$. The principle of maximum dissipation postulates that among all plastically admissible pairs, $(\boldsymbol{\sigma}^*, \mathbf{A}^*)$, the actual state $(\boldsymbol{\sigma}, \mathbf{A})$ maximizes the dissipation function (5.16) for a given plastic strain rate, $\dot{\boldsymbol{\varepsilon}}^p$, and rate $\dot{\boldsymbol{\alpha}}$ of hardening internal variables, i.e., it requires that,

$$\boldsymbol{\Upsilon}\left(\boldsymbol{\sigma}, \mathbf{A}; \dot{\boldsymbol{\varepsilon}}^p, \dot{\boldsymbol{\alpha}}\right) \geq \boldsymbol{\Upsilon}\left(\boldsymbol{\sigma}^*, \mathbf{A}^*; \dot{\boldsymbol{\varepsilon}}^p, \dot{\boldsymbol{\alpha}}\right), \forall\left(\boldsymbol{\sigma}^*, \mathbf{A}^*\right) \in \boldsymbol{\mathcal{A}}, \tag{5.17}$$

where $\boldsymbol{\mathcal{A}}$ is the set of all admissible stress states satisfying $\boldsymbol{\Phi}(\boldsymbol{\sigma}, \mathbf{A}) \leq \mathbf{0}$ [71]. Equation (5.17) may be interpreted as the condition that the projection of the admissible stress sates onto the direction of the plastic strain rate be maximized by the actual stress state. This condition holds if: (a) the elastic domain is convex, and (b) the direction of the plastic strain rate is normal to the yield surface. These two requirements are known as convexity and normality [70].

Since the yield surface is a graphical representation of $\boldsymbol{\Phi}$, the flow vector, $\mathbf{N}$, represents the gradient of $\boldsymbol{\Phi}$ and indicates the direction of the normal to the yield surface. Thus, the associative flow rule given by equation (5.12) can be interpreted as the increment in the plastic strain vector along the normal direction to the yield surface.

Hardening law

An evolution law for the set $\boldsymbol{\alpha}$ of hardening variables, i.e., a hardening law, is also required. As postulated for the plastic flow rule, the hardening law is defined by,

$$\dot{\boldsymbol{\alpha}} = \dot{\gamma}\mathbf{H}, \tag{5.18}$$

where $\mathbf{H} = \mathbf{H}(\boldsymbol{\sigma}, \mathbf{A})$ is the generalised hardening modulus that defines the evolution of the hardening variables.

Assuming that the hardening law is also derived from the plastic potential, $\boldsymbol{\Psi}$, we have,

$$\mathbf{H} \equiv -\frac{\boldsymbol{\partial}\boldsymbol{\Psi}}{\boldsymbol{\partial}\mathbf{A}}. \tag{5.19}$$

Loading/unloading conditions

Given the evolution laws, loading/unloading conditions need to be imposed to establish when the evolution of the plastic strains and internal variables may occur. These conditions may be expressed as,

$$\boldsymbol{\Phi} \leq \mathbf{0}, \qquad \dot{\gamma} \geq \mathbf{0}, \qquad \boldsymbol{\Phi}\dot{\gamma} = \mathbf{0}. \tag{5.20}$$

For the determination of the plastic multiplier, $\dot{\boldsymbol{\gamma}}$, the following additional condition needs to be established,

$$\dot{\boldsymbol{\Phi}}\dot{\boldsymbol{\gamma}} = \mathbf{0}, \tag{5.21}$$

which is known as the complementary condition.

As the plastic multiplier is a non-negative scalar and $\dot{\boldsymbol{\gamma}} \neq \mathbf{0}$ under plastic yielding ($\dot{\boldsymbol{\gamma}} = \mathbf{0}$ in the elastic regime where the plastic strain remain constant), equation (5.21) implies that,

$$\dot{\boldsymbol{\Phi}} = \mathbf{0}, \tag{5.22}$$

during plastic flow. Equation (5.22) is known as the consistency condition.

The differentiation of the yield function with respect to time is given by,

$$\dot{\boldsymbol{\Phi}} = \frac{\boldsymbol{\partial \Phi}}{\boldsymbol{\partial \sigma}} : \dot{\boldsymbol{\sigma}} + \frac{\boldsymbol{\partial \Phi}}{\boldsymbol{\partial A}} * \dot{\mathbf{A}}. \tag{5.23}$$

Taking into account the additive split of the strain tensor, the elastic law and the plastic flow rule, the rate form of the stress tensor, $\dot{\boldsymbol{\sigma}}$, is given by,

$$\dot{\boldsymbol{\sigma}} = \mathbf{D}^e : (\dot{\boldsymbol{\varepsilon}} - \dot{\boldsymbol{\varepsilon}}^p) = \mathbf{D}^e : (\dot{\boldsymbol{\varepsilon}} - \dot{\boldsymbol{\gamma}}\mathbf{N}). \tag{5.24}$$

Knowing that $\mathbf{A} \equiv \bar{\boldsymbol{\rho}}(\boldsymbol{\partial \Psi^p / \partial \alpha})$ and substituting equation (5.24) in (5.23),

$$\dot{\boldsymbol{\Phi}} = \frac{\boldsymbol{\partial \Phi}}{\boldsymbol{\partial \sigma}} : \mathbf{D}^e : (\dot{\boldsymbol{\varepsilon}} - \dot{\boldsymbol{\gamma}}\mathbf{N}) + \dot{\boldsymbol{\gamma}} \frac{\boldsymbol{\partial \Phi}}{\boldsymbol{\partial A}} \bar{\boldsymbol{\rho}} \frac{\boldsymbol{\partial^2 \psi^p}}{\boldsymbol{\partial \alpha^2}} \mathbf{H}. \tag{5.25}$$

The above expression can be solved to obtain the plastic multiplier,

$$\dot{\boldsymbol{\gamma}} = \frac{\boldsymbol{\partial \Phi / \partial \sigma} : \mathbf{D}^e : \dot{\boldsymbol{\varepsilon}}}{\boldsymbol{\partial \Phi / \partial \sigma} : \mathbf{D}^e : \mathbf{N} - \boldsymbol{\partial \Phi / \partial A}(\bar{\boldsymbol{\rho}} \boldsymbol{\partial^2 \psi^p / \partial \alpha^2})\mathbf{H}}. \tag{5.26}$$

The basic governing equations of the general rate independent plasticity model are resumed in Box 5.1.

Box 5.1: A general elastoplastic constitutive model.

1. Additive decomposition of the strain tensor

$$\boldsymbol{\varepsilon} = \boldsymbol{\varepsilon}^{\boldsymbol{e}} + \boldsymbol{\varepsilon}^{\boldsymbol{p}}$$

or

$$\dot{\boldsymbol{\varepsilon}} = \dot{\boldsymbol{\varepsilon}}^{\boldsymbol{e}} + \dot{\boldsymbol{\varepsilon}}^{\boldsymbol{p}}$$
$$\boldsymbol{\varepsilon}(\boldsymbol{t_0}) = \boldsymbol{\varepsilon}^{\boldsymbol{e}}(\boldsymbol{t_0}) + \boldsymbol{\varepsilon}^{\boldsymbol{p}}(\boldsymbol{t_0})$$

2. Elastic law

$$\boldsymbol{\sigma} = \mathbf{D^e} : \boldsymbol{\varepsilon}^{\boldsymbol{e}}$$

3. Yield function

$$\boldsymbol{\Phi} = \boldsymbol{\Phi}(\boldsymbol{\sigma}, \mathbf{A})$$

4. Plastic flow rule

$$\dot{\boldsymbol{\varepsilon}}^{\boldsymbol{p}} = \dot{\boldsymbol{\gamma}}\mathbf{N}(\boldsymbol{\sigma}, \mathbf{A})$$

5. Hardening law

$$\dot{\bar{\boldsymbol{\varepsilon}}}^{\boldsymbol{p}} = \dot{\boldsymbol{\gamma}}\mathbf{H}(\boldsymbol{\sigma}, \mathbf{A})$$

6. Loading/unloading criterion

$$\boldsymbol{\Phi} \leq \mathbf{0}, \quad \dot{\boldsymbol{\gamma}} \geq \mathbf{0}, \quad \dot{\boldsymbol{\gamma}}\boldsymbol{\Phi} = \mathbf{0}$$

5.3 Finite Elements for Plasticity Problems

Elastoplastic problems hardly ever can be solved analytically due to the complex nature of the underlying constitutive theories. The existing analytical solutions are normally restricted to perfectly plastic models with simple geometries. Thus, solutions of boundary value problems under more realistic conditions can only be obtained through adequate numerical techniques capable of producing approximate solutions within reasonably accuracy. The most commonly adopted numerical procedure for the solution of elastoplastic problems is the Finite Element Method. In this section, the computational procedures necessary to deal with small strain plasticity problems in the framework of the Finite Element Method will be described. The methodologies presented are derived taking the rate-independent plasticity model presented earlier as the underlying constitutive model. In this section, the approach will be kept as general as possible since the specifics of the equations for the models under analysis in this study will be presented later.

Elastoplastic constitutive models are history (or path) dependent. This particular feature of the plastic behaviour implies that there is no longer a one-to-one relationship between stresses and strains and thus, to know the state of stress corresponding to a given strain, it is necessary to know the history of loading. Therefore, numerical integration algorithms of the rate elastoplastic evolution equations are required. The problem consists in determining the stresses and internal variables at the end of a time increment $[\boldsymbol{t_n}, \boldsymbol{t_{n+1}}]$ given the internal variables at the beginning of the increment and the strains at the end of the increment. This is known as the state update procedure. The stress at time $\boldsymbol{n+1}$ provided by the integration algorithm is used to assemble the element internal force vector,

$$\mathbf{f}_{\boldsymbol{e}}^{\boldsymbol{int}} = \sum_{\boldsymbol{i=1}}^{\boldsymbol{n_{gausp}}} \boldsymbol{w_i j_i} \mathbf{B}_{\boldsymbol{i}}^{\boldsymbol{T}} \boldsymbol{\sigma_{n+1|i}}. \tag{5.27}$$

The numerical integration algorithm used in this study was based on the operator split method presented in [71]. In the following sections, this numerical procedure will be presented.

5.3.1 The constitutive initial value problem

Considering a point $\boldsymbol{p}$ of a body $\boldsymbol{\mathcal{B}}$ with an elastoplastic constitutive behaviour and that for a given time $\boldsymbol{t_0}$, the elastic strain, $\boldsymbol{\varepsilon^e}$, the plastic strain tensor, $\boldsymbol{\varepsilon^p}$ and the internal variables $\boldsymbol{\alpha}$ are known. Considering also that the motion of $\boldsymbol{\mathcal{B}}$ between $\boldsymbol{t_0}$ and a subsequent instant, $\boldsymbol{T}$, defines the history of the strain tensor, i.e., $\boldsymbol{\varepsilon(t)}$, $\boldsymbol{t \in [t_0, T]}$. Thus, the problem consists in finding the functions $\boldsymbol{\varepsilon^e(t)}$, $\boldsymbol{\alpha(t)}$ and $\boldsymbol{\dot{\gamma}(t)}$ for the elastic strain, hardening internal variable and plastic multiplier that satisfy the elastoplastic constitutive equations.

$$\begin{aligned} \dot{\boldsymbol{\varepsilon}}(\boldsymbol{t}) &= \dot{\boldsymbol{\varepsilon}}(\boldsymbol{t}) - \dot{\boldsymbol{\gamma}}(\boldsymbol{t})\mathbf{N}(\boldsymbol{\sigma}(\boldsymbol{t}), \mathbf{A}(\boldsymbol{t})), \\ \dot{\boldsymbol{\alpha}}(\boldsymbol{t}) &= \dot{\boldsymbol{\gamma}}(\boldsymbol{t})\mathbf{H}(\boldsymbol{\sigma}(\boldsymbol{t}), \mathbf{A}(\boldsymbol{t})), \end{aligned} \tag{5.28}$$

subjected to the constraints

$$\dot{\boldsymbol{\gamma}}(\boldsymbol{t}) \geq \mathbf{0}, \quad \boldsymbol{\Phi}(\boldsymbol{\sigma}(\boldsymbol{t}), \mathbf{A}(\boldsymbol{t})) \leq \mathbf{0}, \quad \dot{\boldsymbol{\gamma}}(\boldsymbol{t})\boldsymbol{\Phi}(\boldsymbol{\sigma}(\boldsymbol{t}), \mathbf{A}(\boldsymbol{t})) = \mathbf{0}, \tag{5.29}$$

for each instant $\boldsymbol{t} \in [\boldsymbol{t_0}, \boldsymbol{T}]$.

To eliminate the unknown $\dot{\boldsymbol{\varepsilon}}^{\boldsymbol{p}}(\boldsymbol{t})$ from the system of equations, the plastic flow rule $\dot{\boldsymbol{\varepsilon}}^{\boldsymbol{p}} = \dot{\boldsymbol{\gamma}}\mathbf{N}(\boldsymbol{\sigma}, \mathbf{A})$ was inserted into the additive strain rate decomposition, $\dot{\boldsymbol{\varepsilon}} = \dot{\boldsymbol{\varepsilon}}^{\boldsymbol{e}} + \dot{\boldsymbol{\varepsilon}}^{\boldsymbol{p}}$. Therefore, the only unknowns in the system of differential equations (5.28) are the elastic strain, the set of hardening internal variables and the plastic multiplier.

5.3.2 Solution of the constitutive initial value problem

A general framework for the numerical solution of the constitutive initial value problem of elastoplasticity described previously is required. The backward (or fully implicit) Euler scheme was adopted. Thus, for the integration within a generic time interval between $\boldsymbol{t_n}$ and $\boldsymbol{t_{n+1}}$, all rate quantities in equation (5.28) and (5.29) are replaced with corresponding incremental values and the functions $\mathbf{N}$, $\mathbf{H}$ and $\boldsymbol{\Phi}$ with their values at the end of the interval. Adopting the notation $\boldsymbol{\Delta}(\cdot) \equiv (\cdot)_{n+1} - (\cdot)_n$ the incremental elastoplastic constitutive problem is thus stated as,

$$\begin{aligned} \boldsymbol{\varepsilon}^{\boldsymbol{e}}_{\boldsymbol{n+1}} &= \boldsymbol{\varepsilon}^{\boldsymbol{e}}_{\boldsymbol{n}} + \boldsymbol{\Delta\varepsilon} - \boldsymbol{\Delta\gamma}\mathbf{N}(\boldsymbol{\sigma}_{\boldsymbol{n+1}}, \mathbf{A}_{\boldsymbol{n+1}}), \\ \boldsymbol{\alpha}_{\boldsymbol{n+1}} &= \boldsymbol{\alpha}_{\boldsymbol{n}} + \boldsymbol{\Delta\gamma}\mathbf{H}(\boldsymbol{\sigma}_{\boldsymbol{n+1}}, \mathbf{A}_{\boldsymbol{n+1}}), \end{aligned} \tag{5.30}$$

and subjected to the constrains

$$\boldsymbol{\Delta\gamma} \geq \mathbf{0}, \quad \boldsymbol{\Phi}(\boldsymbol{\sigma}_{\boldsymbol{n+1}}, \mathbf{A}_{\boldsymbol{n+1}}) \leq \mathbf{0}, \quad \boldsymbol{\Delta\gamma}\boldsymbol{\Phi}(\boldsymbol{\sigma}_{\boldsymbol{n+1}}, \mathbf{A}_{\boldsymbol{n+1}}) = \mathbf{0}. \tag{5.31}$$

Given a prescribed incremental strain, $\boldsymbol{\Delta\varepsilon}$, the system of algebraic equations must then be solved for the unknowns $\boldsymbol{\varepsilon}^{\boldsymbol{e}}_{\boldsymbol{n+1}}$, $\boldsymbol{\alpha}_{\boldsymbol{n+1}}$ and $\boldsymbol{\Delta\gamma}$.

To solve the incremental problem a solution scheme based on the complementary condition $\boldsymbol{\Delta\gamma}\boldsymbol{\Phi}(\boldsymbol{\sigma}_{\boldsymbol{n+1}}, \mathbf{A}_{\boldsymbol{n+1}}) = \mathbf{0}$ is used. Note that, because $\boldsymbol{\Delta\gamma} \geq \mathbf{0}$ two mutually exclusive possibilities arise: (1) $\boldsymbol{\Delta\gamma} = \mathbf{0}$ and (2) $\boldsymbol{\Delta\gamma} > \mathbf{0}$.

1. If $\boldsymbol{\Delta\gamma} = \mathbf{0}$, no plastic flow or evolution of internal variables is present within the considered time interval. This means that the step is purely elastic and that the constraint $\boldsymbol{\Delta\gamma}\boldsymbol{\Phi}(\boldsymbol{\sigma}_{\boldsymbol{n+1}}, \mathbf{A}_{\boldsymbol{n+1}}) = \mathbf{0}$ is automatically satisfied. Additionally, the constraint $\boldsymbol{\Phi}(\boldsymbol{\sigma}_{\boldsymbol{n+1}}, \mathbf{A}_{\boldsymbol{n+1}}) \leq \mathbf{0}$ must be satisfied.

$\boldsymbol{\varepsilon^e_{n+1}}$ and $\boldsymbol{\alpha_{n+1}}$ are given by,

$$\begin{aligned} \boldsymbol{\varepsilon^e_{n+1}} &= \boldsymbol{\varepsilon^e_n + \Delta\varepsilon}, \\ \boldsymbol{\alpha_{n+1}} &= \boldsymbol{\alpha_n}. \end{aligned} \tag{5.32}$$

2. If $\boldsymbol{\Delta\gamma > 0}$ the step is plastic and we have,

$$\begin{aligned} \boldsymbol{\varepsilon^e_{n+1}} &= \boldsymbol{\varepsilon^e_n + \Delta\varepsilon - \Delta\gamma \mathbf{N}(\sigma_{n+1}, \mathbf{A}_{n+1})}, \\ \boldsymbol{\alpha_{n+1}} &= \boldsymbol{\alpha_n + \Delta\gamma \mathbf{H}(\sigma_{n+1}, \mathbf{A}_{n+1})}, \end{aligned} \tag{5.33}$$

and the combination of constraint $(5.31)_2$ with $(5.31)_3$ results in the constraint,

$$\boldsymbol{\Phi(\sigma_{n+1}, \mathbf{A}_{n+1}) = 0}. \tag{5.34}$$

The solution of the elastoplastic problem is thus given either by (5.32) in which case the $(5.31)_2$ constraint must be satisfied or is the solution of the algebraic system (5.33) subjected to the constraint (5.34). Resuming, there are only two possibilities for the solution of the problem and so a two step procedure can be established in which the two possible sets of equations are employed sequentially and the final solution is selected as the only valid one. This procedure is called the elastic predictor/plastic corrector algorithm.

The elastic trial step

The first step of the procedure consists in assuming that the first of the aforementioned hypothesis occurs, i.e., the step is elastic ($\boldsymbol{\Delta\gamma = 0}$). The current solution is given by (5.32) and is called the elastic trial solution,

$$\begin{aligned} \boldsymbol{\varepsilon^{e,trial}_{n+1}} &= \boldsymbol{\varepsilon^e_n + \Delta\varepsilon}, \\ \boldsymbol{\alpha^{trial}_{n+1}} &= \boldsymbol{\alpha}. \end{aligned} \tag{5.35}$$

The corresponding stress can be obtained from,

$$\boldsymbol{\sigma^{trial}_{n+1} = \mathbf{D}^e \varepsilon^{e,trial}_{n+1}}. \tag{5.36}$$

As was stated, in this case the $(5.31)_2$ constraint must be satisfied. So the following check is made:

- If the elastic trial state lies within the elastic domain or on the yield surface, i.e.,

$$\boldsymbol{\Phi}^{\boldsymbol{trial}} \equiv \boldsymbol{\Phi}(\boldsymbol{\sigma}_{\boldsymbol{n+1}}^{\boldsymbol{trial}}, \mathbf{A}_{\boldsymbol{n+1}}^{\boldsymbol{trial}}) \leq \mathbf{0}, \tag{5.37}$$

  and is the solution to the problem, update

$$\begin{aligned} \boldsymbol{\varepsilon}_{\boldsymbol{n+1}}^{\boldsymbol{e}} &= \boldsymbol{\varepsilon}_{\boldsymbol{n+1}}^{\boldsymbol{e,trial}}, \\ \boldsymbol{\alpha}_{\boldsymbol{n+1}} &= \boldsymbol{\alpha}_{\boldsymbol{n+1}}^{\boldsymbol{trial}}. \end{aligned} \tag{5.38}$$

  and the algorithm is terminated.

- Otherwise, the elastic trial state is not plastically admissible and the solution must be obtained from a plastic corrector step.

The plastic corrector step (or return mapping)

Within the plastic corrector step the system of algebraic equations (5.33) subject to the constraint (5.34) is solved. Using the trial state definition, the algebraic system (5.33) can be rewritten,

$$\begin{aligned} \boldsymbol{\varepsilon}_{\boldsymbol{n+1}}^{\boldsymbol{e}} &= \boldsymbol{\varepsilon}_{\boldsymbol{n+1}}^{\boldsymbol{e,trial}} - \boldsymbol{\Delta\gamma}\mathbf{N}(\boldsymbol{\sigma}_{\boldsymbol{n+1}}, \mathbf{A}_{\boldsymbol{n+1}}), \\ \boldsymbol{\alpha}_{\boldsymbol{n+1}} &= \boldsymbol{\alpha}_{\boldsymbol{n+1}}^{\boldsymbol{trial}} + \boldsymbol{\Delta\gamma}\mathbf{H}(\boldsymbol{\sigma}_{\boldsymbol{n+1}}, \mathbf{A}_{\boldsymbol{n+1}}), \end{aligned} \tag{5.39}$$

with the constraint,

$$\boldsymbol{\Phi}(\boldsymbol{\sigma}_{\boldsymbol{n+1}}, \mathbf{A}_{\boldsymbol{n+1}}) = \mathbf{0}. \tag{5.40}$$

The plastic corrector stage of the algorithm consists in finding $\boldsymbol{\varepsilon}_{\boldsymbol{n+1}}^{\boldsymbol{e}}$, $\boldsymbol{\alpha}_{\boldsymbol{n+1}}$, and $\boldsymbol{\Delta\gamma}$ that satisfy $\boldsymbol{\Delta\gamma} > \mathbf{0}$.

The plastic corrector step can be schematically represented as illustrated in Figure 5.2. When the elastic trial stress lies outside of the plastically admissible domain the stress state is "returned" to the yield surface. The plastic consistency given by equation (5.40) is re-established upon solution of the algebraic system (5.39) so that the stress $\boldsymbol{\sigma}_{\boldsymbol{n+1}}$ at the end of the interval $[\boldsymbol{t_n}, \boldsymbol{t_{n+1}}]$ lies on the updated yield surface.

The elastic predictor/plastic corrector algorithm is summarized in box 5.2.

Solution of the return-mapping equations

The return mapping equation system (5.39) is generally nonlinear and in addition is subjected to the constraint (5.40). The procedure usually adopted for the solution of this algebraic

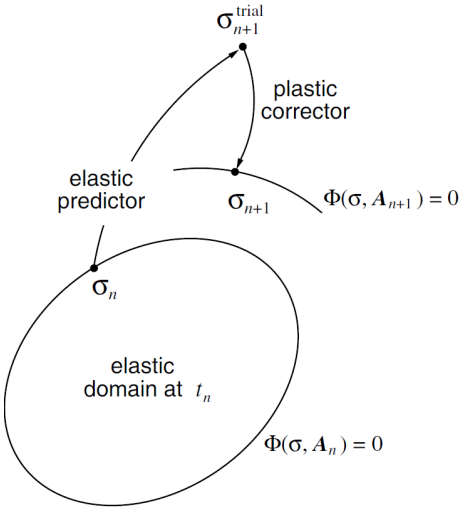

Figure 5.2: Geometric representation of the return mapping scheme with hardening plasticity [71].

system consists in first solving the system of equations on its own, i.e., without regarding the constraint equation, using an iterative procedure. If the solution satisfies the constraint then it is accepted as the solution. For the solution of the return-mapping equations the standard Newton-Raphson scheme can be used as a solution procedure. For simplicity a linear hardening law was assumed and the notation $\boldsymbol{\sigma_y} \equiv \boldsymbol{k}$ was adopted. The hardening law can be expressed as,

$$\boldsymbol{k} = \boldsymbol{k_0} + \boldsymbol{H}\boldsymbol{\alpha}, \tag{5.41}$$

where $\boldsymbol{H}$ is the hardening modulus. In the discrete setting the evolution of $\boldsymbol{k}$ is given by,

$$\boldsymbol{k_{n+1}} = \boldsymbol{k_n} + \boldsymbol{H}\boldsymbol{\Delta\gamma}. \tag{5.42}$$

With equation (5.42) and taking into account the linear elasticity law, the following vector function, for the Newton-Raphson algorithm, can be defined,

$$\mathbf{R} = \begin{cases} \mathbf{D}^{e-1}\left(\boldsymbol{\sigma_{n+1}} - \boldsymbol{\sigma_{trial}}\right) + \boldsymbol{\Delta\gamma}\mathbf{N_{n+1}} \\ \boldsymbol{H}^{-1}\left(\boldsymbol{k_{n+1}} - \boldsymbol{k_{trial}}\right) - \boldsymbol{\Delta\gamma} \\ \boldsymbol{\Phi}\left(\boldsymbol{\sigma_{n+1}}, \boldsymbol{k_{n+1}}\right) \end{cases} \tag{5.43}$$

this vector is called the residual vector and the problem can be stated as finding $\boldsymbol{\sigma_{n+1}}$, $\boldsymbol{k_{n+1}}$

Box 5.2: Elastic predictor/return-mapping algorithm.

1. Elastic predictor. Given $\boldsymbol{\Delta\varepsilon}$ and the state variables at $\boldsymbol{t_n}$, compute the elastic trial state

$$\begin{aligned} \boldsymbol{\varepsilon}^{\boldsymbol{e,trial}}_{\boldsymbol{n+1}} &= \boldsymbol{\varepsilon}^{\boldsymbol{e}}_{\boldsymbol{n}} + \boldsymbol{\Delta\varepsilon} \\ \boldsymbol{\alpha}_{\boldsymbol{n+1}} &= \boldsymbol{\alpha}_{\boldsymbol{n}} \\ \boldsymbol{\sigma}^{\boldsymbol{trial}}_{\boldsymbol{n+1}} &= \mathbf{D}^{\boldsymbol{e}}\boldsymbol{\varepsilon}^{\boldsymbol{e,trial}}_{\boldsymbol{n+1}} \end{aligned}$$

2. Check plastic admissibility

   IF $\boldsymbol{\Phi}^{\boldsymbol{trial}} \leq \mathbf{0}$
   THEN set $(\cdot)_{\boldsymbol{n+1}} = (\cdot)^{\boldsymbol{trial}}_{\boldsymbol{n+1}}$ and EXIT

3. Return Mapping. Solve the system

$$\begin{Bmatrix} \boldsymbol{\varepsilon}^{\boldsymbol{e}}_{\boldsymbol{n+1}} - \boldsymbol{\varepsilon}^{\boldsymbol{etrial}}_{\boldsymbol{n+1}} + \boldsymbol{\Delta\gamma}\mathbf{N}_{\boldsymbol{n+1}} \\ \boldsymbol{\alpha}_{\boldsymbol{n+1}} - \boldsymbol{\alpha}^{\boldsymbol{trial}}_{\boldsymbol{n+1}} - \boldsymbol{\Delta\gamma}\mathbf{H}_{\boldsymbol{n+1}} \\ \boldsymbol{\Phi}(\boldsymbol{\sigma}_{\boldsymbol{n+1}}, \mathbf{A}_{\boldsymbol{n+1}}) \end{Bmatrix} = \begin{Bmatrix} \mathbf{0} \\ \mathbf{0} \\ \mathbf{0} \end{Bmatrix}$$

   For $\boldsymbol{\varepsilon}^{\boldsymbol{e}}_{\boldsymbol{n+1}}$, $\boldsymbol{\alpha}_{\boldsymbol{n+1}}$ and $\boldsymbol{\Delta\gamma}$

4. EXIT

and $\boldsymbol{\Delta\gamma}$ that satisfies,

$$\mathbf{R} = \mathbf{0}. \tag{5.44}$$

The Newton-Raphson iterative procedure starts with a guess vector, $\mathbf{r}_{\boldsymbol{i}}$. The guess vector can be the correspondent to the trial state,

$$\mathbf{r}_{\boldsymbol{i}} = \begin{bmatrix} \boldsymbol{\sigma}_{\boldsymbol{i}} \\ \boldsymbol{k}_{\boldsymbol{i}} \\ \boldsymbol{\Delta\gamma}_{\boldsymbol{i}} \end{bmatrix} = \begin{bmatrix} \boldsymbol{\sigma}_{\boldsymbol{trial}} \\ \boldsymbol{k}_{\boldsymbol{trial}} \\ \mathbf{0} \end{bmatrix}. \tag{5.45}$$

By performing a Taylor series expansion of the original vector about the guess vector, $\mathbf{r}_{\boldsymbol{i}}$, and truncating the non-linear terms, an approximation of the original function is obtained,

i.e.,

$$\mathbf{R} \approx \mathbf{R}(\mathbf{r}_i) + \mathbf{A}(\mathbf{r} - \mathbf{r}_i), \tag{5.46}$$

where $\mathbf{A}$ is the derivative matrix of $\mathbf{R}$,

$$\mathbf{A} = \begin{bmatrix} \mathbf{D}^{e-1} + \boldsymbol{\Delta\gamma}\frac{\partial \mathbf{N}}{\partial \boldsymbol{\sigma}} & \mathbf{0} & \mathbf{N} \\ \mathbf{0} & \boldsymbol{H}^{-1} & \mathbf{-1} \\ \mathbf{N} & \mathbf{-1} & \mathbf{0} \end{bmatrix}. \tag{5.47}$$

The new guess, $\mathbf{r_{i+1}}$, is now simply obtained as the root of the linear approximation function 5.46,

$$\mathbf{r}_{i+1} = \mathbf{r}_i - \boldsymbol{\delta}\mathbf{r}, \tag{5.48}$$

where $\boldsymbol{\delta}\mathbf{r}$ is the solution of the linear system os equations,

$$\mathbf{A}\boldsymbol{\delta}\mathbf{r} = \mathbf{R}. \tag{5.49}$$

Having solved equation (5.49) for $\boldsymbol{\delta}\mathbf{r}$, the new guess can now be computed from (5.48).

Finally, a convergence check is performed. For a given tolerance, $\boldsymbol{\epsilon}$, if $\|\mathbf{R}\| \leq \boldsymbol{\epsilon}$ then $\mathbf{r_{i+1}}$ is the approximate solution of the return mapping equation, where

$$\|\mathbf{R}\| = \sqrt{\boldsymbol{R_1^2} + \boldsymbol{R_2^2} + \boldsymbol{R_3^2} + \boldsymbol{R_4^2} + \boldsymbol{R_5^2} + \boldsymbol{R_6^2}}. \tag{5.50}$$

Otherwise, if the convergence is not met, then the iterative procedure continues with a new guess. The Newton-Raphson algorithm is summarized in box 5.3.

Box 5.3: Newton-Raphson algorithm for the solution of the return mapping equations.

1. Set initial guess for $\boldsymbol{\sigma_{n+1}}$, $\boldsymbol{k_{n+1}}$, $\boldsymbol{\Delta\gamma}$

$$\begin{aligned}\boldsymbol{\sigma_{n+1}} &= \boldsymbol{\sigma_{n+1}^{trial}}\\ \boldsymbol{k_{n+1}} &= \boldsymbol{k^0}\\ \boldsymbol{\Delta\gamma} &= \mathbf{0}\end{aligned}$$

2. Compute correspondent yield function value

$$\boldsymbol{\Phi_{n+1}^i}(\boldsymbol{\sigma_{n+1}^i}, \boldsymbol{k_{n+1}^i})$$

Compute flow vector

$$\mathbf{N_{n+1}^i} = \frac{\boldsymbol{\partial\Phi}}{\boldsymbol{\partial\sigma}}$$

Compute Residual

$$\boldsymbol{R_{n+1}^i} = \begin{Bmatrix} [\mathbf{D^e}]^{-1}\left(\boldsymbol{\sigma_{n+1}^i} - \boldsymbol{\sigma^{trial}}\right) + \boldsymbol{\Delta\gamma}\mathbf{N}_{n+1} \\ \mathbf{H^{-1}}\left(\boldsymbol{k_{n+1}^i} - \boldsymbol{k^0}\right) - \boldsymbol{\Delta\gamma} \end{Bmatrix}$$

3. Check convergence

IF $\boldsymbol{\Phi_{n+1}^i} \leq \boldsymbol{tol}$ and $\|\mathbf{R}\| \leq \boldsymbol{tol}$
THEN set $(\cdot)_{n+1} = (\cdot)_{n+1}^i$ and EXIT
ELSE compute

$$\boldsymbol{A} = \begin{bmatrix} \left\{[\mathbf{D}^e]^{-1} + \boldsymbol{\Delta\gamma}\frac{\boldsymbol{\partial}\mathbf{N}}{\boldsymbol{\partial\sigma}}\right\}^{-1} & \mathbf{0} \\ \mathbf{0} & \mathbf{H} \end{bmatrix}$$

Compute increments

$$\boldsymbol{\delta\Delta\gamma^i} = \frac{\boldsymbol{\Phi^i} - \begin{bmatrix}\mathbf{N}^i & -\mathbf{1}\end{bmatrix}\boldsymbol{A^i R^i}}{\begin{bmatrix}\mathbf{N}^i & -\mathbf{1}\end{bmatrix}\boldsymbol{A^i}\begin{Bmatrix}\mathbf{N}^i \\ -\mathbf{1}\end{Bmatrix}}$$

$$\begin{Bmatrix}\boldsymbol{\delta\sigma^i} \\ \boldsymbol{\delta k^i}\end{Bmatrix} = -\boldsymbol{A^i}\left[\boldsymbol{R^i} + \boldsymbol{\delta\Delta\gamma}\begin{bmatrix}\boldsymbol{N^i} \\ -\mathbf{1}\end{bmatrix}\right]$$

Compute new quess

$$\begin{cases} \boldsymbol{\sigma_{n+1}^{i+1}} = \boldsymbol{\sigma_{n+1}^i} + \boldsymbol{\delta\sigma^i} \\ \boldsymbol{k_{n+1}^{i+1}} = \boldsymbol{k_{n+1}^i} + \boldsymbol{\delta k^i} \\ \boldsymbol{\Delta\gamma_{n+1}^{i+1}} = \boldsymbol{\Delta\gamma_{n+1}^i} + \boldsymbol{\delta\Delta\gamma^i} \end{cases}$$

GOTO (2)

5.4 Computational Implementation of Nixon and CPB06 Yield Criteria

As was previously mentioned, implementing adequate yield criteria capable of describing accurately the plastic behaviour of titanium and its alloys is crucial for the achievement of realistic finite element models and thus reliable simulations. In this section, the methodologies followed for the computational implementation of the CPB06 and Nixon yield criteria are presented. Both models were implemented in an Abaqus subroutine VUMAT following the elastic predictor/return mapping algorithm previously presented.

The yield function for the CPB06 or Nixon model can be described by,

$$\boldsymbol{\Phi(\sigma, \bar{\varepsilon}_p) = \bar{\sigma}(\sigma) - \sigma_y(\bar{\varepsilon}_p)}, \tag{5.51}$$

where $\boldsymbol{\bar{\sigma}}$ is the scalar effective stress, $\boldsymbol{\sigma_y}$ represents the material's reference hardening that is a function of the effective plastic strain, $\boldsymbol{\bar{\varepsilon}_p}$. In this study, the tensile stress-strain curve along the longitudinal direction was adopted as the reference. The effective or equivalent stress must be an homogeneous function of degree one and be able to reduce to the hardening relationship (i.e., uniaxial tension for a given direction) under that state of stress.

The effective stress for the CPB06 yield criterion, assuming that the hardening relationship, $\boldsymbol{\sigma_y(\bar{\varepsilon}_p)}$, is based upon uniaxial tension about the longitudinal direction, is given by,

$$\boldsymbol{\bar{\sigma} = B\left[(|\Sigma_1| - k\Sigma_1)^a + (|\Sigma_2| - k\Sigma_2)^a + (|\Sigma_3| - k\Sigma_3)^a\right]^{\frac{1}{a}}}, \tag{5.52}$$

where

$$\boldsymbol{B = \left[\frac{1}{(|\psi_1| - k\psi_1)^a + (|\psi_2| - k\psi_2)^a + (|\psi_3| - k\psi_3)^a}\right]^{\frac{1}{a}}}, \tag{5.53}$$

and

$$\boldsymbol{\psi_1 = \frac{1}{3}\left(2C_{11} - C_{12} - C_{13}\right)}, \tag{5.54}$$

$$\boldsymbol{\psi_2 = \frac{1}{3}\left(2C_{12} - C_{22} - C_{23}\right)}, \tag{5.55}$$

$$\boldsymbol{\psi_3 = \frac{1}{3}\left(2C_{13} - C_{23} - C_{33}\right)}. \tag{5.56}$$

$\boldsymbol{\Sigma_1}$, $\boldsymbol{\Sigma_2}$ and $\boldsymbol{\Sigma_3}$ are the principle values of the tensor $\boldsymbol{\Sigma}$ defined as,

$$\boldsymbol{\Sigma = C : S}. \tag{5.57}$$

where **C** is the fourth order tensor of the anisotropy coefficients and **S** is the deviatoric stress.

For the Nixon yield criterion the equivalent stress is given by,

$$\bar{\boldsymbol{\sigma}} = \boldsymbol{A_1}\left[(\boldsymbol{J_2^o})^{\boldsymbol{3/2}} - \boldsymbol{cJ_3^o}\right]^{\boldsymbol{1/3}}, \tag{5.58}$$

where $\boldsymbol{A_1}$ is defined so that $\bar{\boldsymbol{\sigma}}$ reduces to the tensile yield stress in the longitudinal direction,

$$\boldsymbol{A_1} = \boldsymbol{3}\left[(\boldsymbol{a_2^2} + \boldsymbol{a_3^2} + \boldsymbol{a_2a_3})^{\boldsymbol{3/2}} - \boldsymbol{c}(\boldsymbol{a_2} + \boldsymbol{a_3})\boldsymbol{a_2a_3}\right]^{\boldsymbol{-1/3}}. \tag{5.59}$$

$\boldsymbol{J_2^o}$ and $\boldsymbol{J_3^o}$ are the second and third invariants of tensor $\boldsymbol{\Sigma}$ defined by,

$$\boldsymbol{\Sigma} = \mathbf{L}\boldsymbol{\sigma}, \tag{5.60}$$

where **L** is a fourth order tensor of the anisotropic coefficients.

Concerning the reference hardening curve, the following exponential form of hardening was chosen,

$$\boldsymbol{\sigma_y}(\bar{\boldsymbol{\varepsilon}}_{\boldsymbol{p}}) = \boldsymbol{A_0} + \boldsymbol{B_0}\boldsymbol{exp}(-\boldsymbol{C_0}\bar{\boldsymbol{\varepsilon}}_{\boldsymbol{p}}) \tag{5.61}$$

where $\boldsymbol{A_0}$, $\boldsymbol{B_0}$ and $\boldsymbol{C_0}$ are material constants. The hardening relationship (5.61) was proposed by Voce [72] and assumes that the hardening eventually reaches a specified saturation (or maximum) stress. The parameters of the Voce type hardening law for the reference hardening curve are given in Table 5.1.

Table 5.1: Parameters of the Voce type hardening law for the reference LD curve.

$\boldsymbol{A_0}$	$\boldsymbol{B_0}$	$\boldsymbol{C_0}$
1070	150	20.0

The evolution of the internal variable $\bar{\boldsymbol{\varepsilon}}_{\boldsymbol{p}}$ is given by

$$\dot{\bar{\boldsymbol{\varepsilon}}}_{\boldsymbol{p}} = \dot{\boldsymbol{\gamma}}. \tag{5.62}$$

Furthermore, the additive decomposition of the total strain rate, into an elastic and plastic part was considered, as well as an elastic stress-strain relationship given by the Hooke's law and an associative flow rule.

To capture the change in shape of the yield loci of the Ti6Al4V alloy and other hcp materials, the evolution of the yield function coefficients was taken into consideration in this

study. Analytical expressions for all the yield function coefficients of the CPB06 and Nixon models in terms of the hardening variables are difficult to obtain. A way to include the evolution of the yield function coefficients with the equivalent plastic strain was proposed by Plunkett based on an interpolation technique [54]. In the previous chapter, with the available experimental data, the yield function coefficients and SD parameters were determined for the CPB06 and Nixon criteria, for fixed levels of effective plastic strain, say $\bar{\varepsilon}_p^1 < \bar{\varepsilon}_p^2 < \ldots < \bar{\varepsilon}_p^m$. Therefore the effective stress for each individual strain level, $\bar{\varepsilon}_p^j, j = 1, \ldots, m$, can then be obtained: $\bar{\sigma}^j = \bar{\sigma}\left\{\sigma, \mathbf{C}(\bar{\varepsilon}_p^j), k(\bar{\varepsilon}_p^j)\right\}$ for CPB06 yield criteria using equation (5.52) and $\bar{\sigma}^j = \bar{\sigma}\left\{\sigma, \mathbf{L}(\bar{\varepsilon}_p^j), c(\bar{\varepsilon}_p^j)\right\}$ for Nixon using equation (5.58). Thus, the determination of the yield surface corresponding to any level of accumulated plastic strain can be obtained using an interpolation method as follows,

$$\bar{\sigma} = \chi(\bar{\varepsilon}_p)\bar{\sigma}^j + (1 - \chi(\bar{\varepsilon}_p))\,\bar{\sigma}^{j+1}, \tag{5.63}$$

where

$$\chi(\bar{\varepsilon}_p) = \frac{\bar{\varepsilon}_p^{j+1} - \bar{\varepsilon}_p}{\bar{\varepsilon}_p^{j+1} - \bar{\varepsilon}_p^j}, \tag{5.64}$$

is a weighting parameter. Note that $\chi(\bar{\varepsilon}_p^j) = 1$ and $\chi(\bar{\varepsilon}_p^{j+1}) = 0$.

Given the effective plastic strain, the $\sigma_y^j = \sigma_y\left(\bar{\varepsilon}_p^j\right)$ can be computed from (5.61).

During a time step $\Delta t = t_{n+1} - t_n$, first the trial elastic stress is computed, assuming the step is purely elastic and using the elastic stress-strain relation,

$$\sigma_{n+1}^{trial} = \sigma_n + \mathbf{D}^e : \Delta\varepsilon_n. \tag{5.65}$$

The yield function value for the elastic trial state, $\Phi^{trial}(\sigma_{n+1}^{trial}, \bar{\varepsilon}_{p_n})$, is then obtained. If $\Phi^{trial}(\sigma_{n+1}^{trial}, \bar{\varepsilon}_{p_n}) \leq 0$ the trial stress is accepted as the current stress state and the total strain increment as an elastic strain increment,

$$\begin{aligned} \sigma_{n+1} &= \sigma_{n+1}^{trial}, \\ \bar{\varepsilon}_{p_{n+1}} &= \bar{\varepsilon}_{p_n}. \end{aligned} \tag{5.66}$$

If $\Phi(\sigma_{n+1}^{trial}, \bar{\varepsilon}_{p_n}) > 0$, there is plastic flow and the accumulated plastic strain increment for the $n+1$ step must be determined to bring the stress state back to the yield surface from the trial state through a local iterative process. The following nonlinear system of equations

can be established,

$$\begin{cases} \boldsymbol{\sigma}_{n+1} = \boldsymbol{\sigma}_{n+1}^{trial} - \boldsymbol{\Delta\gamma}_{n+1}\mathbf{D}^e : \mathbf{N}_{n+1} \\ \boldsymbol{\Phi}_{n+1} = \bar{\boldsymbol{\sigma}}(\boldsymbol{\sigma}_{n+1}, \bar{\varepsilon}_{p_{n+1}}) - \boldsymbol{\sigma}_y(\bar{\varepsilon}_{p_{n+1}}) \end{cases} \tag{5.67}$$

where $-\boldsymbol{\Delta\gamma}_{n+1}\mathbf{D}^e : \mathbf{N}_{n+1}$ is the stress correction due to the plastic strains. The iterative procedure starts at the elastic trial state which is denoted as iteration $\boldsymbol{i = 0}$ ($\boldsymbol{i}$ being the local iteration counter),

$$\begin{aligned} \boldsymbol{\sigma}_{n+1}^{\mathbf{0}} &= \boldsymbol{\sigma}_{n+1}^{trial}, \\ \boldsymbol{\Delta\gamma}_{n+1}^{\mathbf{0}} &= \mathbf{0}. \end{aligned} \tag{5.68}$$

The stress increment update for iteration $\boldsymbol{i > 0}$ takes the effects of the plastic strains and is expressed as,

$$\boldsymbol{\sigma}_{n+1}^{i+1} = \boldsymbol{\sigma}_{n+1}^{i} + \boldsymbol{\delta\sigma}_{n+1}^{i+1} = -\boldsymbol{\delta\gamma}_{n+1}^{i+1}\mathbf{D}^e : \mathbf{N}_{n+1}^{i+1}, \tag{5.69}$$

where $\boldsymbol{\delta}$ denotes the variation of the variable between iterations $\boldsymbol{i}$ and $\boldsymbol{i+1}$, i.e.,

$$\begin{aligned} \boldsymbol{\delta\sigma}_{n+1}^{i+1} &= \boldsymbol{\sigma}_{n+1}^{i+1} - \boldsymbol{\sigma}_{n+1}^{i}, \\ \boldsymbol{\delta\gamma}_{n+1}^{i+1} &= \boldsymbol{\Delta\gamma}_{n+1}^{i+1} - \boldsymbol{\Delta\gamma}_{n+1}^{i}. \end{aligned} \tag{5.70}$$

Considering that the stress state is returned to the yield surface along a vector normal to the current state the yield function gradient at the updated stress, $\mathbf{N}_{n+1}^{i+1}$ can be approximated by,

$$\mathbf{N}_{n+1}^{i+1} \approx \mathbf{N}_{n+1}^{i}, \tag{5.71}$$

so the stress correction is then given by,

$$\boldsymbol{\delta\sigma}_{n+1}^{i+1} = -\boldsymbol{\delta\gamma}_{n+1}^{i+1}\mathbf{D}^e : \mathbf{N}_{n+1}^{i}. \tag{5.72}$$

To obtain the incremental variation of the plastic multiplier, a Taylor expansion of the yield function about the current state is performed,

$$\boldsymbol{\Phi}(\boldsymbol{\sigma}_{n+1}^{i+1}, \bar{\varepsilon}_{p_{n+1}}^{i+1}) = \boldsymbol{\Phi}(\boldsymbol{\sigma}_{n+1}^{i}, \bar{\varepsilon}_{p_{n+1}}^{i}) + \mathbf{N}_{n+1}^{i}\boldsymbol{\delta\sigma}_{n+1}^{i+1} + \mathbf{Q}_{n+1}^{i}\boldsymbol{\delta\gamma}_{n+1}^{i+1}, \tag{5.73}$$

where $\mathbf{Q} = \frac{\partial \mathbf{\Phi}}{\partial \bar{\varepsilon}_p}$. Introducing the stress correction (5.69) in equation (5.73) and solving for $\mathbf{\Phi}(\boldsymbol{\sigma}_{n+1}^{i+1}, \bar{\varepsilon}_{p_{n+1}}^{i+1}) = \mathbf{0}$ leads to,

$$\mathbf{\Phi}(\boldsymbol{\sigma}_{n+1}^{i}, \bar{\varepsilon}_{p_{n+1}}^{i}) - \delta\gamma_{n+1}^{i+1}\mathbf{N}_{n+1}^{i} : \mathbf{D}^{e} : \mathbf{N}_{n+1}^{i} + \mathbf{Q}_{n+1}^{i}\delta\gamma_{n+1}^{i+1} = \mathbf{0}, \tag{5.74}$$

and rearranging gives,

$$\delta\gamma_{n+1}^{i+1} = \frac{\mathbf{\Phi}(\boldsymbol{\sigma}_{n+1}^{i}, \bar{\varepsilon}_{p_{n+1}}^{i})}{\mathbf{N}_{n+1}^{i} : \mathbf{D}^{e} : \mathbf{N}_{n+1}^{i} - \mathbf{Q}_{n+1}^{i}}. \tag{5.75}$$

The stresses and the plastic strains are then updated through $\boldsymbol{\delta\gamma}_{n+1}^{i+1}$.

The derivatives necessary for the plastic corrector step are evaluated as follows,

$$\mathbf{N} = \frac{\partial \mathbf{\Phi}}{\partial \boldsymbol{\sigma}} = \frac{\partial \bar{\sigma}}{\partial \boldsymbol{\sigma}} = \chi(\bar{\varepsilon}_p)\frac{\partial \bar{\sigma}^{j}}{\partial \boldsymbol{\sigma}} + (1 - \chi(\bar{\varepsilon}_p))\frac{\partial \bar{\sigma}^{j+1}}{\partial \boldsymbol{\sigma}}, \tag{5.76}$$

and

$$\mathbf{Q} = \frac{\partial \mathbf{\Phi}}{\partial \bar{\varepsilon}_p} = \frac{\partial \bar{\sigma}}{\partial \bar{\varepsilon}_p} - \frac{\partial \sigma_y}{\partial \bar{\varepsilon}_p}, \tag{5.77}$$

with

$$\frac{\partial \bar{\sigma}}{\partial \bar{\varepsilon}} = \frac{\partial \chi}{\partial \bar{\varepsilon}_p}\bar{\sigma}^{j} - \frac{\partial \chi}{\partial \bar{\varepsilon}_p}\bar{\sigma}^{j+1} = \frac{\bar{\sigma}^{j+1} - \bar{\sigma}^{j}}{\bar{\varepsilon}_p^{j+1} - \bar{\varepsilon}_p^{j}}, \tag{5.78}$$

$$\frac{\partial \sigma_y}{\partial \bar{\varepsilon}_p} = B_0 C_0 exp(-C_0 \bar{\varepsilon}_p). \tag{5.79}$$

The specific derivation procedure of the effective stress for the CPB06 and Nixon model are developed in the Apendix A and B respectively.

The flowchart in Figure 5.3 summarizes the implemented algorithm.

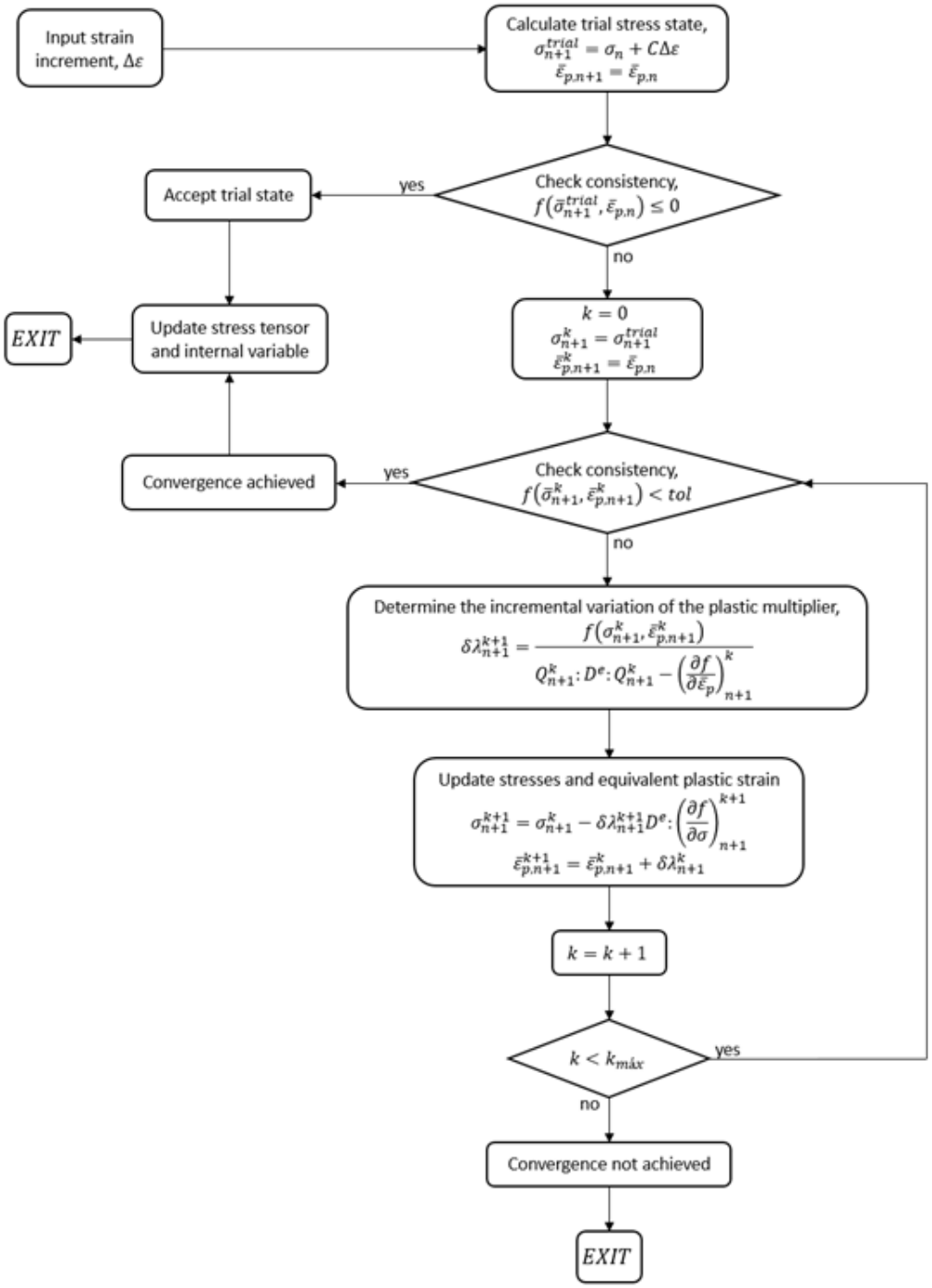

Figure 5.3: Flowchart of the implemented algorithm.

5.5 Validation

5.5.1 Single element tests

In order to verify the elastoplastic implementation of the Nixon and CPB06 models in the finite element code, single element simulations were carried out for specified loading conditions and directions. The single element tests constitute an important step in the validation process of a specific VUMAT implementation. The numerical results obtained for the uniaxial tensile and compressive tests in the three orthogonal material directions (LD-longitudinal direction, TD-transverse direction and TT-through thickness direction) as well as for the simple shear in the LD-TT direction, for both the Nixon and CPB06 model, were validated with data from the experimental tests previously presented in Chapter 3.

The model was created using a single eight-node brick element with one integration point. The initial dimension of the element was set to 1mm. For the simulation of the respective experimental tests, four nodes on one face of the element were restrained and the four nodes on the opposite face were given a constant velocity in either the tensile or compressive direction. The corresponding test cases performed are illustrated in Figure 5.4. The respective stress-strain curves obtained are presented in Figures 5.5 to 5.7 for the Nixon model and in Figures 5.8 to 5.10 for the CPB06 model. Additionally, to assess the stress-strain behaviour predicted by the models in directions different from those used in the calibration process biaxial tension (LD-TD), biaxial compression(LD-TD), plane strain (LD-TT) and simple shear (LD-TD) single element tests were performed. The predicted stress-strain curves are given in Figures 5.11 and 5.12 for the CPB06 and Nixon models respectively.

The analysis of the stress-strain curves obtained show that both the Nixon and the CPB06 models were capable of capturing the specifics of the deformation behaviour of the Ti6AL4V alloy for the loading conditions tested. The strength differential effect as well as the anisotropy were evidenced by the numerical results of the single element tests. It was thus demonstrated the necessity to use adequate models once classical models would clearly be insufficient to describe the mechanical behaviour of the Ti6Al4V alloy. Nevertheless, a slightly better agreement between the experimental and predicted data was obtained for the CPB06 model particularly for the tension tests in the transverse and through thickness directions as well as for the simple shear case. The larger number of anisotropy coefficients of the CPB06 yield criterion are more likely to be able to capture with more detail the anisotropy of the material. The simplicity of the Nixon model, although constitutes an important advantage, may compromise the accuracy of the results. Regardless of the results obtained in this study by using the Nixon model for the Ti6Al4V alloy, studies performed on high purity $\boldsymbol{\alpha}$-titanium have reported a good agreement between experimental and numerical data both in single element tests and in four point bending tests, thus demonstrating the suitability of the Nixon model for hcp metals, particularly in the case of pure titanium with a strong $\boldsymbol{\alpha}$-phase. The application of the Nixon model on high purity $\boldsymbol{\alpha}$-titanium can be found in [32] and [73].

Regarding the stress-strain results for the plane strain and simple shear in LD-TD direction and biaxial tension and compression, the typical concave down shape was obtained. The biaxial tension and compression simulation tests showed a pronounced strength differential effect in both the Nixon and the CPB06 yield criteria. The hardening rate was also found to

be different for tension and compression which is in accordance with the expected results for the Ti6Al4V alloy.

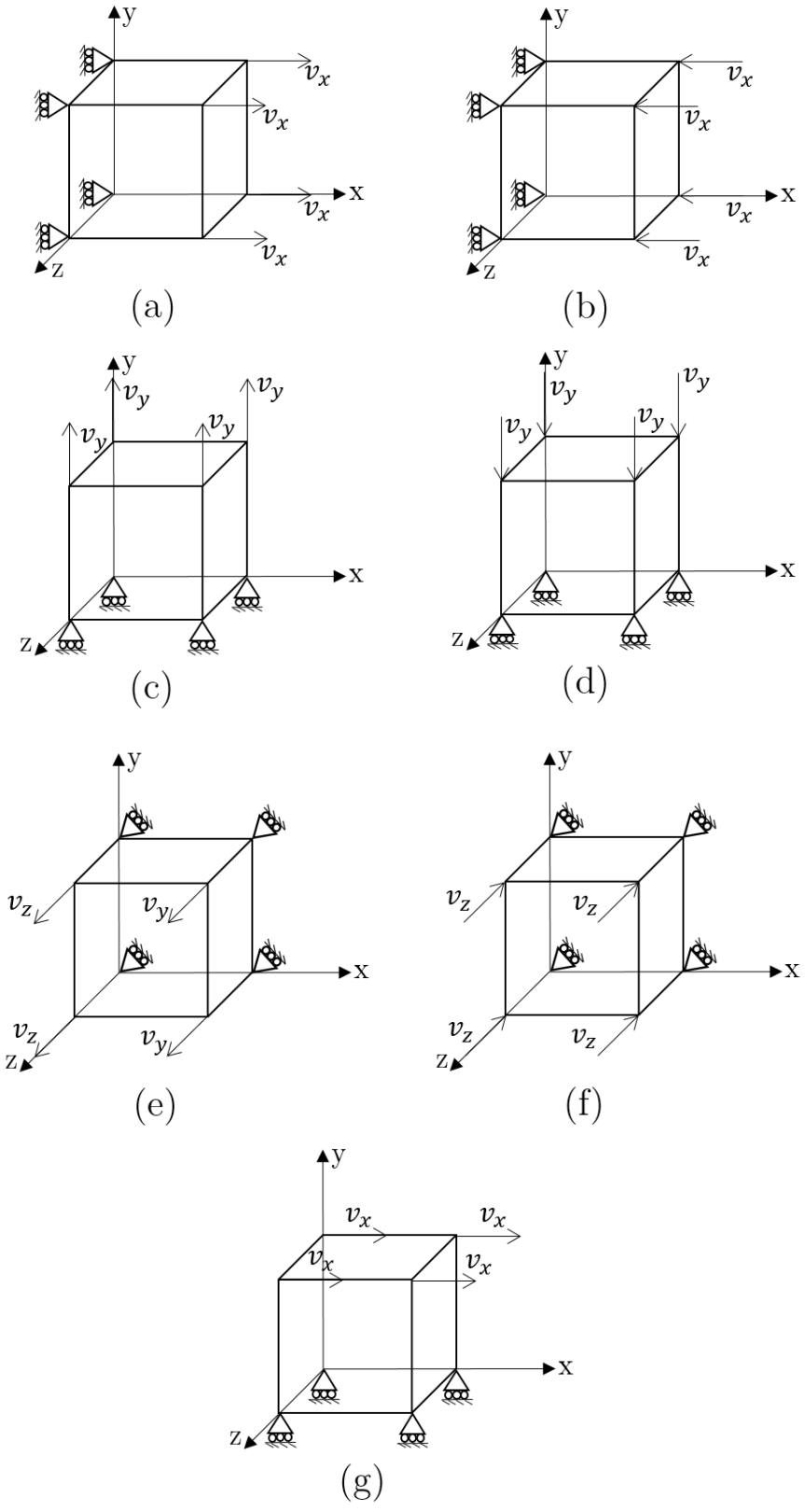

Figure 5.4: Single element tests.

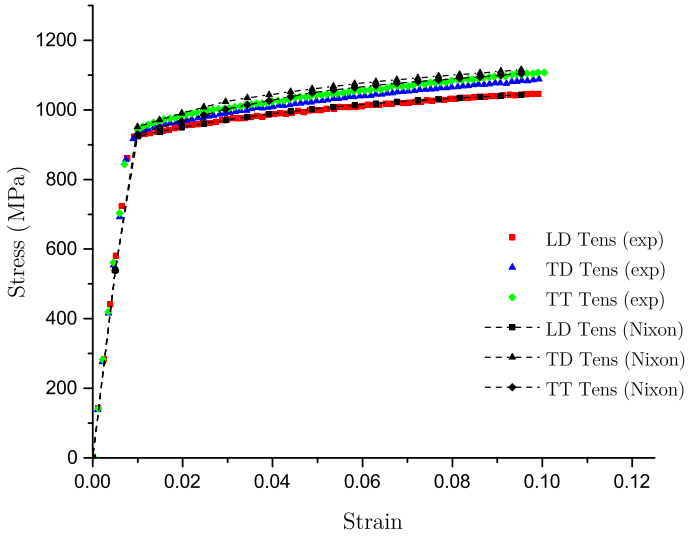

Figure 5.5: Experimental (exp) and predicted by the Nixon model stress-strain curves for tension tests in longitudinal (LD), transverse (TD) and through thickness (TT) directions.

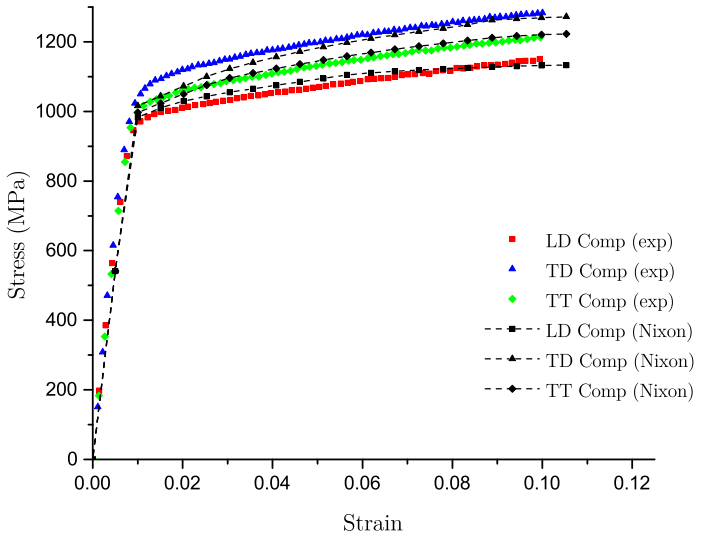

Figure 5.6: Experimental (exp) and predicted by the Nixon model stress-strain curves for compression tests in longitudinal (LD), transverse (TD) and through thickness (TT) directions.

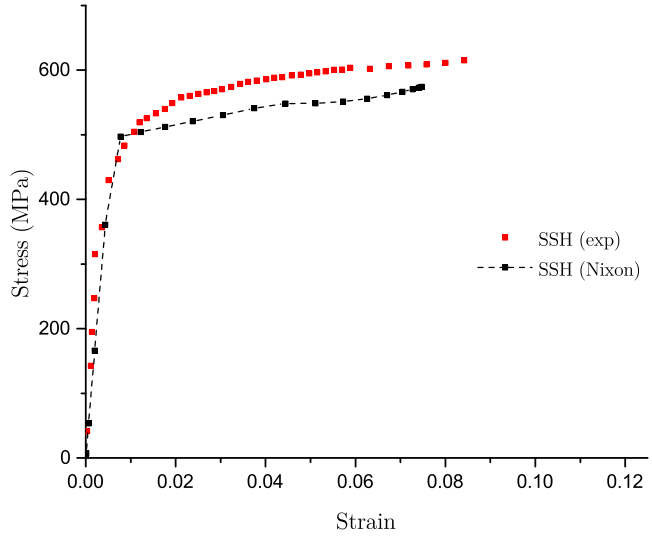

Figure 5.7: Experimental (exp) and predicted by the Nixon model stress-strain curves for simple shear (SSH) in LD-TT.

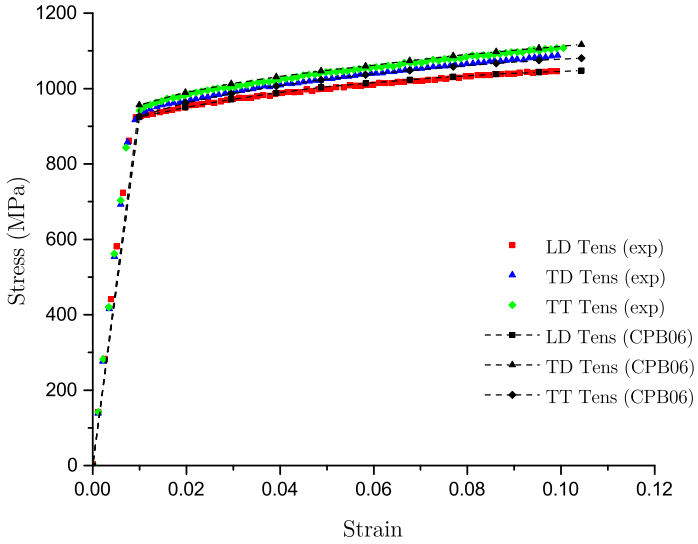

Figure 5.8: Experimental (exp) and predicted by the CPB06 model stress-strain curves for tension tests in longitudinal (LD), transverse (TD) and through thickness (TT) directions.

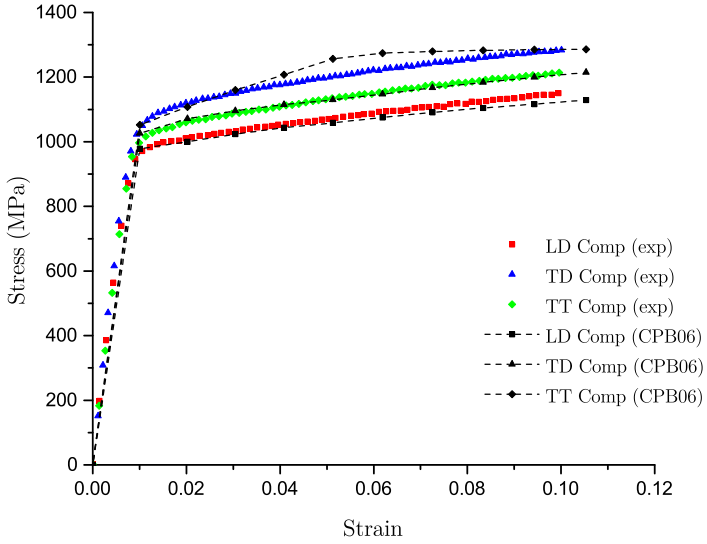

Figure 5.9: Experimental (exp) and predicted by the CPB06 model stress-strain curves for compression tests in longitudinal (LD), transverse (TD) and through thickness (TT) directions.

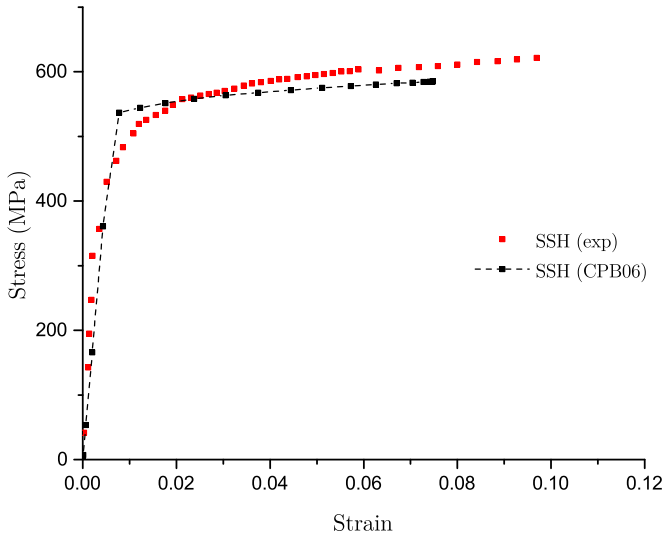

Figure 5.10: Experimental (exp) and predicted by the CPB06 model stress-strain curves for simple shear (SSH) in LD-TT.

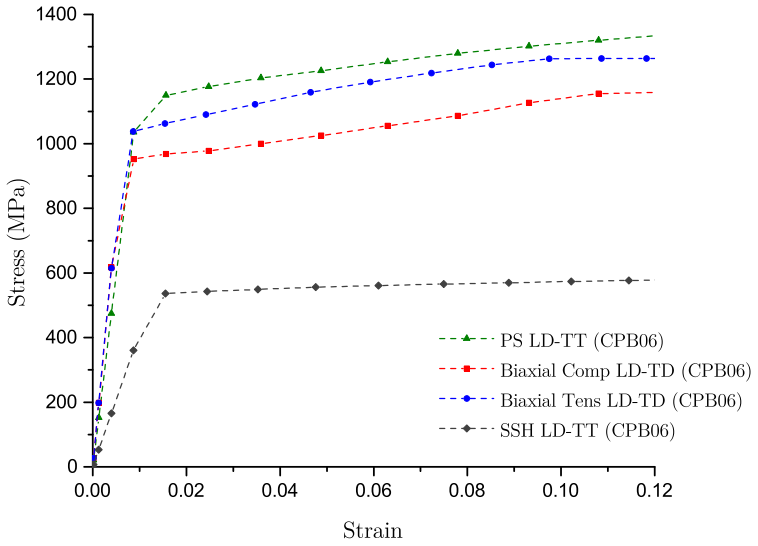

Figure 5.11: Experimental (exp) and predicted by the CPB06 model stress-strain curves for biaxial tension and compression in LD-TD, plane strain (PS) in LD-TT and simple shear (SSH) in LD-TD.

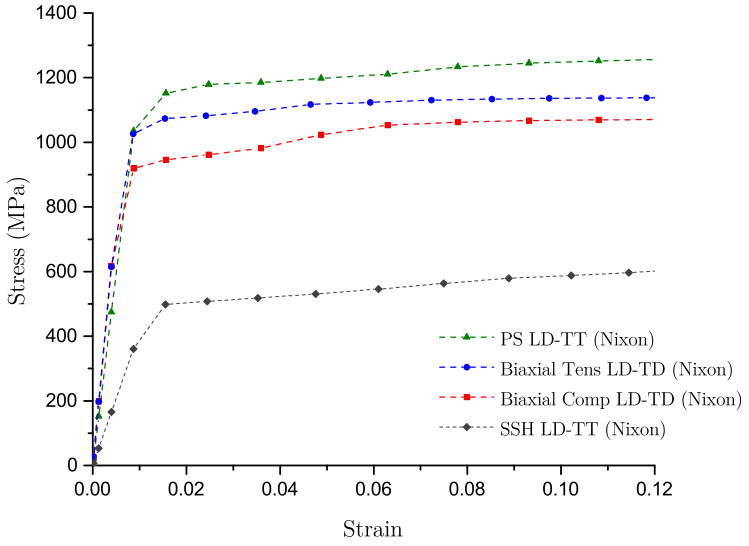

Figure 5.12: Experimental (exp) and predicted by the Nixon model stress-strain curves for biaxial tension and compression in LD-TD, plane strain (PS) in LD-TT and simple shear (SSH) in LD-TD.

5.5.2 Convergency assessment

The efficiency of the numerical implementation of the stress update algorithm was also assessed for different stress states. In view of the strength differential effect and the anisotropic properties found in hcp materials, that as was seen, translate into evolving distorted elliptical yield loci, a number of representative stress states were selected for which the convergency rate and number of iterations was determined: uniaxial tension and compression in the longitudinal direction (TLD and CLD), uniaxial tension and compression in the transverse direction (TTD and CTD), biaxial tension and compression (BiT and BiC), pure shear (SH and SH'), plane strain tension in transverse direction (PS Tens. in TD) and plane strain tension in longitudinal direction (PS Tens. in LD). Additionally, the yield surface corresponding to two effective plastic strain levels was considered: $\bar{\varepsilon}_p = \mathbf{0.0}$ and $\bar{\varepsilon}_p = \mathbf{0.09}$. The stress states and yield loci chosen are depicted in Figure 5.13.

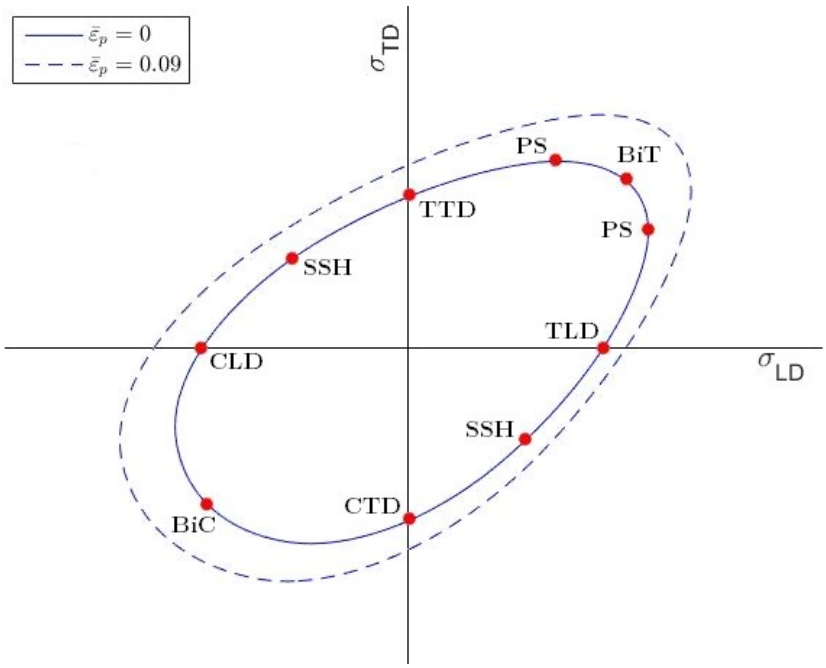

Figure 5.13: Yield loci for $\bar{\varepsilon}_p = \mathbf{0}$ and $\bar{\varepsilon}_p = \mathbf{0.09}$ and representative stress states.

The convergency rates as well as the total number of iterations at each stress state was evaluated for two increasing levels of strain increments: $\boldsymbol{\Delta\varepsilon} = \mathbf{0.005}$ and $\boldsymbol{\Delta\varepsilon} = \mathbf{0.01}$. Table 5.2 summarizes the typical convergence rates and number of iterations obtained for each of the representative stress states for $\bar{\varepsilon}_p = \mathbf{0}$ and increments of $\boldsymbol{\Delta\varepsilon} = \mathbf{0.005}$.

For higher strain increments at the stress states on the yield locus corresponding to $\bar{\varepsilon}_p = \mathbf{0}$, the same convergence rates and number of iterations were obtained. The convergence rates and number of iterations for the stress states on the yield locus corresponding to $\bar{\varepsilon}_p = \mathbf{0.09}$ are given in Table 5.3. Again, for higher strain increments the same convergence rates and total number of iterations were obtained.

According to the results depicted in Tables 5.2 and 5.3, the local stress update algorithm

Table 5.2: Convergency rates and total number of iterations for $\bar{\varepsilon}_p = \mathbf{0}$ and $\boldsymbol{\Delta\varepsilon} = \mathbf{0.005}$.

TLD		TTD		CLD		CTD		BiT	
Iter.	Residual	Iter.	Residual	Iter.	Residual	Iter.	Residual	Iter.	Residual
1	5.19E-01	1	5.33E-01	1	5.01E-01	1	4.71E-01	1	3.0E-01
2	1.02E-03	2	1.83E-03	2	1.94E-03	2	7.04E-03	2	1.17E-03
3	4.54E-09	3	1.80E-08	3	2.83E-08	3	1.39E-06	3	1.75E-08
						4	5.35E-14		
BiC		SH		SH'		PS Tens. in TD		PS Tens. in LD	
Iter.	Residual	Iter.	Residual	Iter.	Residual	Iter.	Residual	Iter.	Residual
1	3.20E-01	1	5.27E-01	1	5.45E-01	1	4.10E-01	1	4.01E-01
2	9.54E-04	2	5.84E-03	2	6.27E-04	2	5.62E-03	2	8.88E-04
3	8.67E-09	3	1.10E-06	3	1.56E-09	3	1.38E-06	3	3.60E-09
		4	3.97E-14			4	8.42E-14		

Table 5.3: Convergency rates and total number of iterations for $\bar{\varepsilon}_p = \mathbf{0.09}$ and $\boldsymbol{\Delta\varepsilon} = \mathbf{0.005}$.

TLD		TTD		CLD		CTD		BiT	
Iter.	Residual	Iter.	Residual	Iter.	Residual	Iter.	Residual	Iter.	Residual
1	4.12E-01	1	3.93E-01	1	3.57E-01	1	3.63E-01	1	1.98E-01
2	1.93E-04	2	2.96E-03	2	5.34E-03	2	1.91E-03	2	2.27E-03
3	1.95E-11	3	1.12E-09	3	6.77E-08	3	7.24E-08	3	3.84E-08
BiC		SH		SH'		PS Tens. in TD		PS Tens. in LD	
Iter.	Residual	Iter.	Residual	Iter.	Residual	Iter.	Residual	Iter.	Residual
1	2.21E-01	1	4.14E-01	1	4.01E-01	1	2.87E-01	1	2.94E-01
2	1.49E-03	2	3.57E-03	2	5.11E-03	2	4.07E-03	2	4.72E-03
3	1.40E-09	3	3.76E-07	3	2.81E-07	3	5.30E-07	3	8.99E-07

exhibits quadratic rates of convergence, typical of the Newton-Raphson method, for all stress states tested, demonstrating the efficiency of the return-mapping scheme. Concerning the yield loci for $\bar{\varepsilon}_p = \mathbf{0}$ and $\bar{\varepsilon}_p = \mathbf{0.09}$, no significant differences regarding convergency were identified for any of the stress states tested at these surfaces. Both the yield surfaces present a very elliptical-like shape and a very small change in shape with increasing equivalent plastic strain is present. Due to the lack of significant curvatures and the absence of a strong change in shape of the yield loci, no convergency issues resulted from the load of the strain increments. Major yield loci shape changes, as is the case for pure $\boldsymbol{\alpha}$-Ti, are more likely to affect convergence due to the alteration in curvature from elliptic to triangular shape. This causes a significant departure of the initial estimation in the plastic correction step to the final solution, particularly for higher strain increments. In shorten, for the Ti6Al4V alloy, with a yield surface displaying a smooth elliptic-like shape with no significant curvatures and no abrupt changes in the shape present during its evolution with increasing equivalent plastic strain, no convergency issues were obtained and high convergency rates were achieved.

5.5.3 Tension test on Notched specimens

To further validate the results obtained on single element tests, tensile tests on notched specimens were simulated. The objective is to verify the implemented models for stress states different than the ones used in the parameters identification procedure. The predicted results from the Nixon and CPB06 models were compared with the experimental results obtained by Tuninetti et al. [34]. Two geometries of the notched specimen were tested: R=1.5mm and R=5mm and a gauge length of 40mm was considered for both specimens. The specimen geometries and dimensions are shown in Figure 5.14.

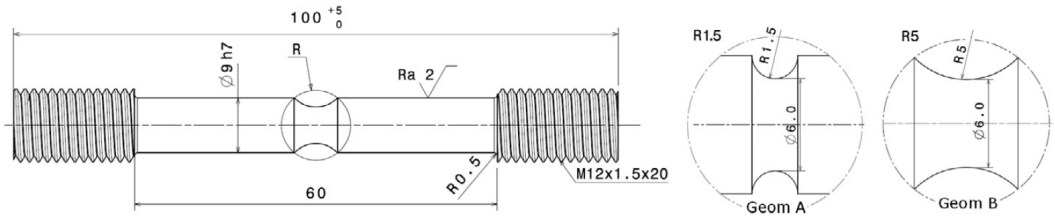

Figure 5.14: Specimen geometries and dimensions for the notched tensile test in the LD direction (dimensions in mm) [34].

The numerical simulation was performed considering only one eighth of each of the specimens and appropriate boundary conditions were given to the corresponding faces. The top face of the specimens was constrained to a reference point and a displacement was imposed by applying the load condition on the reference point. The specimen was modelled with continuum eight node elements with one integration point (C3D8R). The finite element model is represented in Figure 5.15. The longitudinal direction of the material was oriented along the axial direction of the specimen. In order to correctly capture the necking pattern a relatively fine mesh was used with elements with an average size of 0.2mm.

The variation of the load as a function of displacement predicted by the implemented Nixon and CPB06 models was determined and compared with the experimental results from [34].

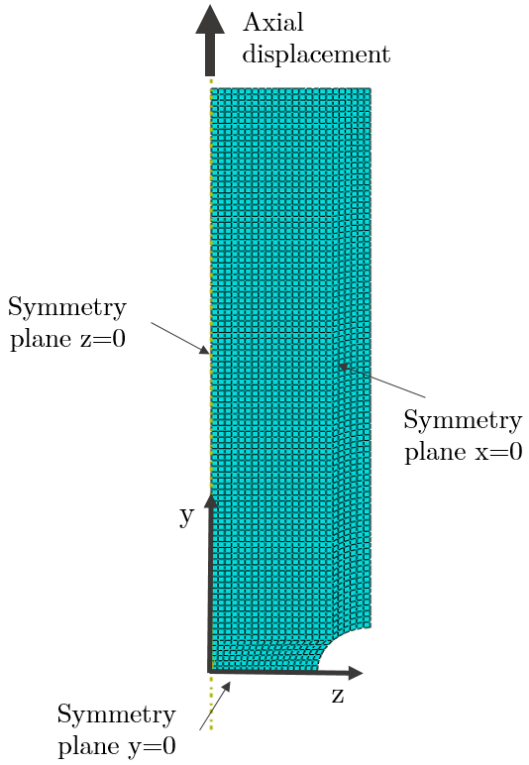

Figure 5.15: Finite element model of the notched specimen.

The results are shown in Figures 5.16 and 5.17 for the R=1.5mm and R=5mm geometries respectively.

The dimensions of the cross section at 0.8mm of axial displacement, just before fracture, were measured experimentally by 3D-DIC by Tuninetti et al. [34]. This data was compared with the predicted results obtained from the Nixon and CPB06 model and represented as radius as function of $\boldsymbol{\theta}$ (see Figure 5.18). The results are shown in Figures 5.19 and 5.20 for the R=1.5mm and R=5mm geometries respectively.

The deformed cross sections, at 0.8mm displacement, predicted by both the Nixon and CPB06 models are consistent with each other, having in both cases diverged relatively to the experimentally measured profile. The greater discrepancies were verified for a 0º angle which corresponds to the TT material direction. A maximum variation of the measured radius of 9% and 6% was verified for the 1.5mm and 5mm notched specimens respectively. It should be noted that the smaller discrepancies were verified for the specimen with the smoother notch radius (5mm) and were larger plastic deformation is allowed before fracture.

The longitudinal profile of the notch of the smoother specimen was also experimentally determined by Tuninetti et al. [34]. The experimental results were compared with the predicted profile of the notch obtained by the Nixon and CPB06 models. The results for both the TD and TT directions are shown in Figures 5.21 and 5.22.

The results obtained by the Nixon and CPB06 models showed a reasonably good agreement with the experimental measurements. Overall, both the Nixon and CPB06 models

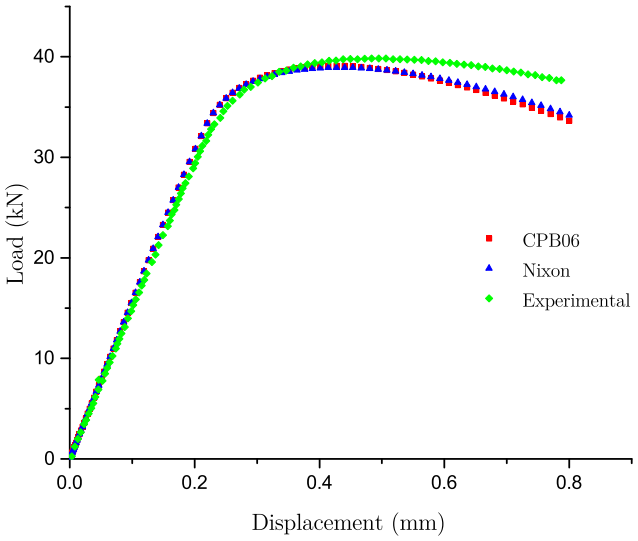

Figure 5.16: Experimental and predicted load vs. displacement for the specimen geometry with 1.5mm notched radius.

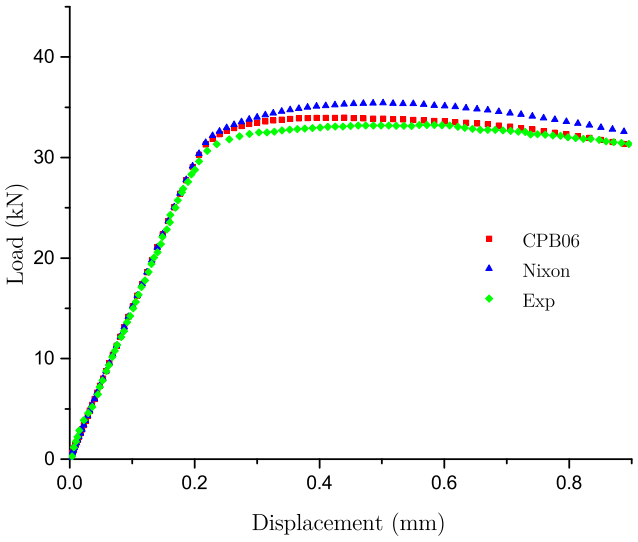

Figure 5.17: Experimental and predicted load vs. displacement for the specimen geometry with 5mm notched radius.

showed good results in the prediction of the deformation behaviour of the TI6AL4V titanium alloy. An improvement of the results could be obtained with the use of a greater number of experimental data for the calibration of the models parameters.

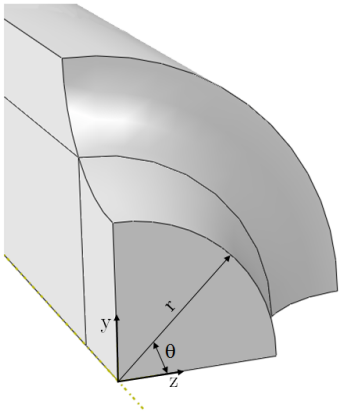

Figure 5.18: Cross-section profile.

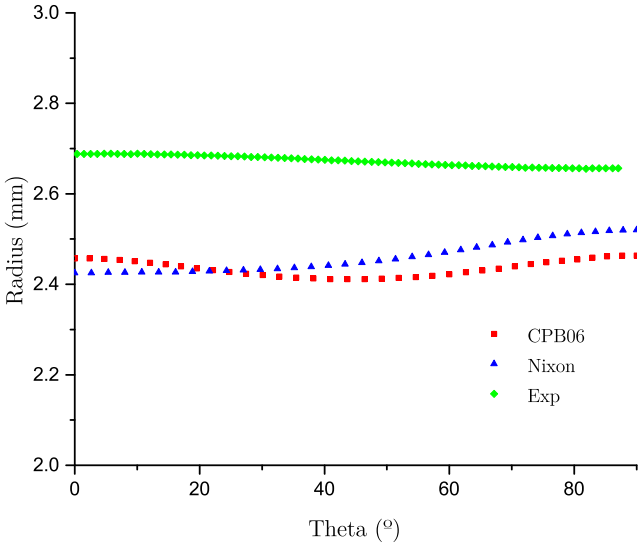

Figure 5.19: Experimental and predicted cross-section for the specimen geometry with 1.5mm notched radius at 0.8mm displacement.

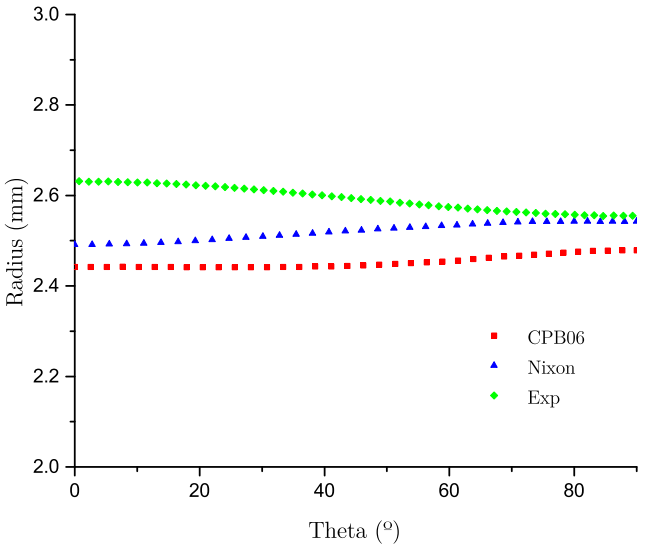

Figure 5.20: Experimental and predicted cross-section for the specimen geometry with 5mm notched radius at 0.8mm displacement.

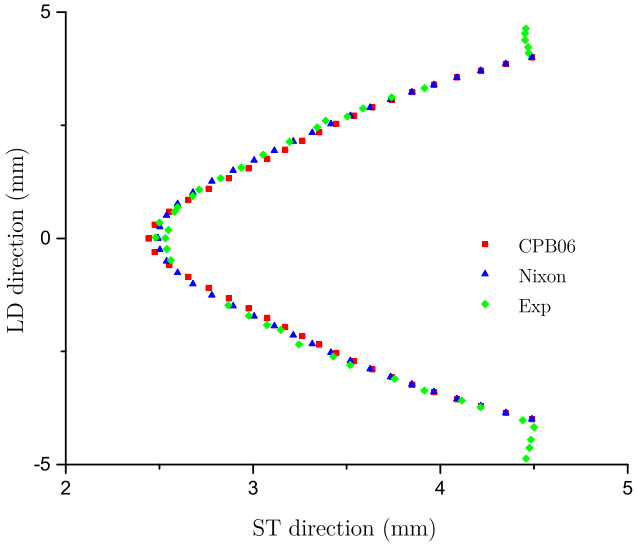

Figure 5.21: Experimental and predicted notch profile for the specimen geometry with 5mm notched radius at 1mm displacement in the ST direction.

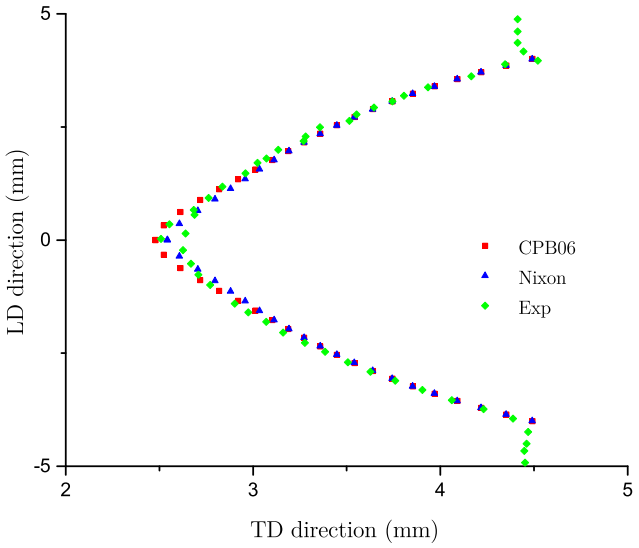

Figure 5.22: Experimental and predicted notch profile for the specimen geometry with 5mm notched radius at 1mm displacement in the TD direction.

5.5.4 Compression test on elliptical specimen

To validate the Nixon and CPB06 models under compression states a simulation of a compression test of an elliptical cross-section specimen was performed and the results were compared with the experimental data from [74]. The elliptical nature of the specimen is due to the fact that axial strain distribution is very sensitive to the material anisotropy in elliptical cross-section specimens. The variation of the axial strain field on the middle surface of an elliptic cylinder specimen was evaluated by Tuninetti et al. [75]. It was shown that in the presence of friction a non-negligible inhomogeneous strain field is found on the surface of the specimen for plastic anisotropic materials.

The geometry and dimensions of the specimen are shown in Figure 5.23.

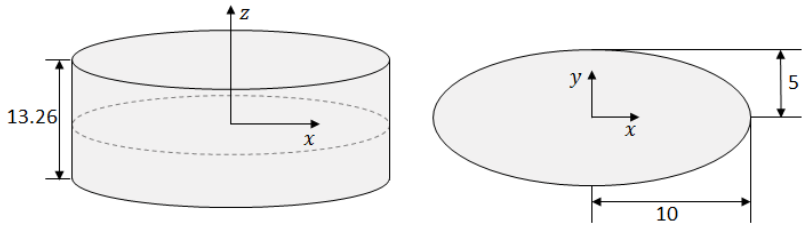

Figure 5.23: Geometry and dimensions in mm of the elliptical cross section specimen.

The numerical simulation was performed considering one eighth of the specimen with adequate boundary conditions imposed to the respective surfaces. Continuum eight node elements with one integration point were used. The finite element model is represented in Figure 5.24. The friction between the compression dies and the surface of the specimen was simulated by establishing a contact interaction based on a Coulomb friction law. The Coulomb friction coefficient was considered constant and equal to **0.08**. This value was determined by fitting the measured and predicted barrelling by Tuninetti et al. in [74].

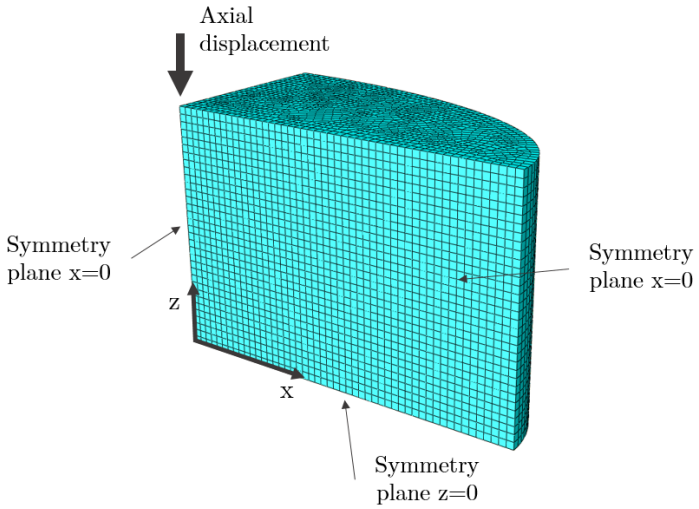

Figure 5.24: Finite element model of the elliptical cross section specimen.

The finite element results for the compression tests in the TT material direction using the Nixon and CPB06 models were compared with the experimental results from [34]. In Figure 5.25, the load predictions for the CPB06 and Nixon models are shown. A reasonable correlation between the predicted and experimental data was obtained.

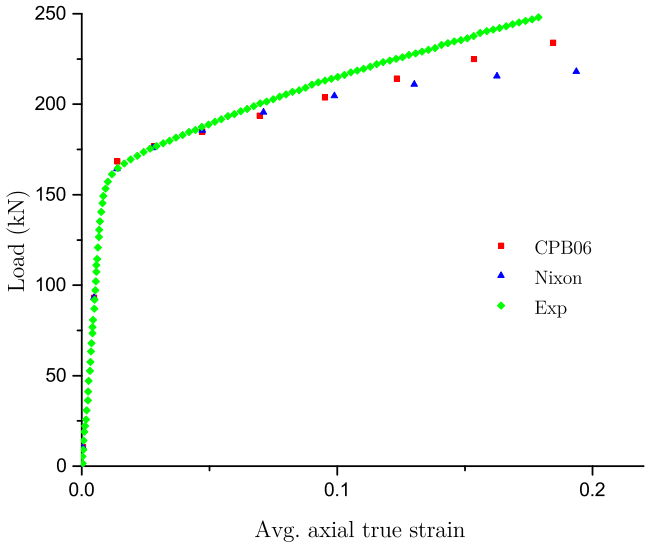

Figure 5.25: Load vs average axial strain predicted by CPB06 and Nixon models and experimentally measured for the compression test on elliptical specimens.

In the presence of friction, compression specimens deform into a barrel shape and the plastic deformation is not homogeneous. Additionally, the plastic anisotropy of the Ti6Al4V alloy leads to a non-negligible inhomogeneous strain field on the surface of the middle cross section of the elliptical specimen [34]. The numerical and experimental axial strain distributions along the surface of the middle cross-section of the specimen are shown in Figure 5.26. It can be seen that both the CPB06 as well as the Nixon model are capable of capturing the non homogeneous strain field and that reasonable agreement with the experimental results is obtained particularly for the Nixon model.

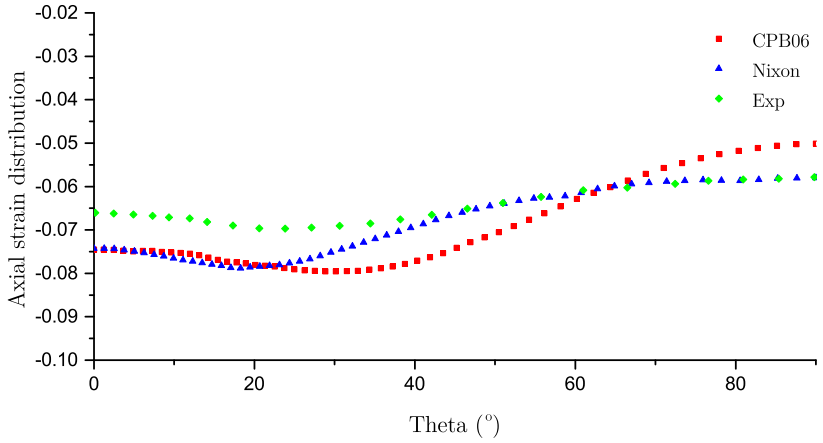

Figure 5.26: CPB06 and Nixon model predictions of the axial strain distribution along the surface of the middle cross-section of elliptical specimens compressed along TT compared with experimental data.

The barrel profiles predicted by the CBP06 and Nixon models were compared with the experimental result and are given in Figure 5.27.

Overall, the Nixon and CPB06 models demonstrated good capacity for correctly predicting the barrel shape, however, the CPB06 showed a better correlation with the experimental data for both longitudinal and transverse material direction.

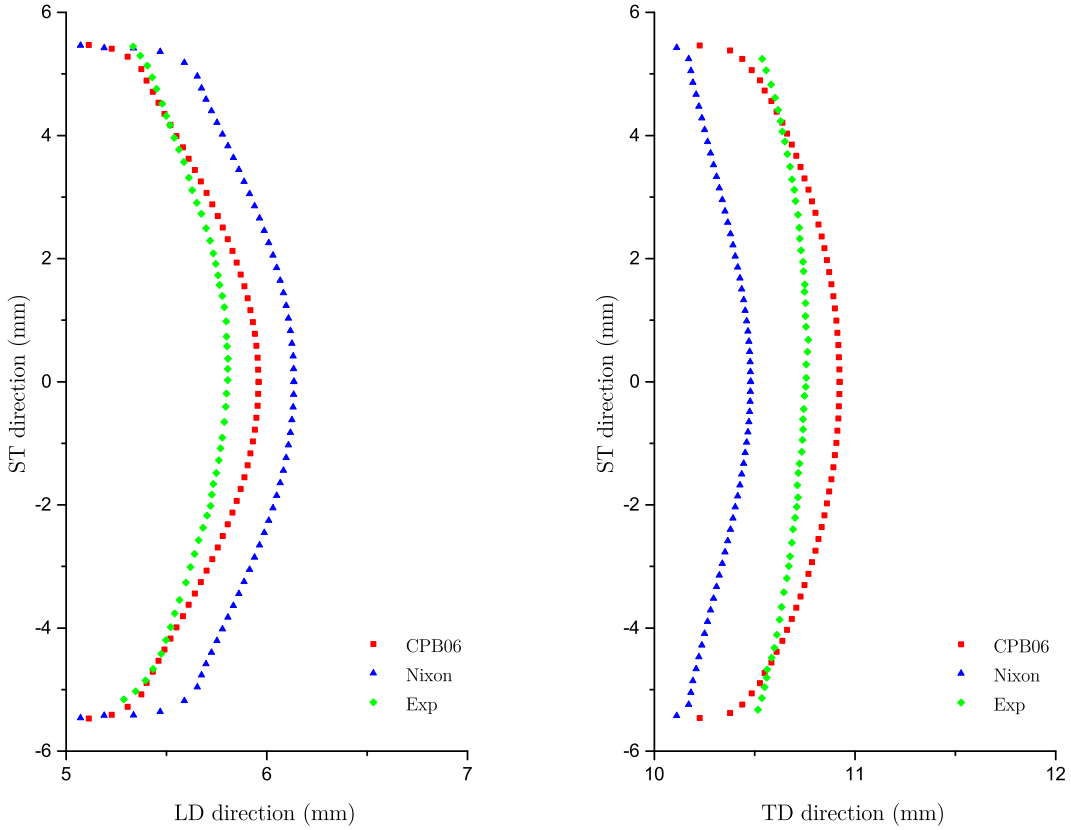

(a) (b)

Figure 5.27: Predicted barreling by the CPB06 and Nixon models compared with the experimentally obtained for the (a) LD direction (b) TD direction.

Chapter 6

Ductile Damage

6.1 Introduction

In the last decade, interest in the ductile failure research field has grown, driven not only by the growing knowledge of the mechanisms involved in the progressive deterioration of materials, but also by the fast development of computational mechanics techniques that allowed the use of computational tools capable of performing realistic life/failure predictions. In the structural integrity framework, the assessment of ductile fracture constitutes a critical aspect in the optimization design process of real components. Particularly, in the aerospace design, the prediction of damage progression is imperative in order to improve both performance and safety while stretching the design to the limit. Thus, the simulation of ductile fracture is becoming a strategic issue in numerical simulations, not only in the simulation of forming processes but also in the simulation of impact damage and evaluation of residual integrity in the analysis of crashworthiness of aerospace structures.

The internal damage in ductile materials is normally associated with the presence of large plastic deformations in the neighbourhood of crystalline defects. Common engineering metal materials contain impurities such as sulphur, brittle inclusions and precipitates. Under specific loading conditions the metal matrix separates from the inclusions, precipitates and particles of alloy elements, leading to the formation of micro voids. Under further evolution of the local plastic deformation these micro voids can grow and coalesce leading to the formation of macro cracks resulting in fracture. This ductile damage mechanism is schematically illustrated in Figure 6.1.

Based on the ductile damage mechanism concepts, numerous models have been proposed for the description of the failure behaviour of ductile materials. In view of the interactions between theoretical models and material responses, two main categories of models can be identified: ductile fracture models or uncoupled models and the coupled models that include the continuum damage mechanics models and the porous solid mechanics models. Overall, uncoupled models neglect the effects of damage on the yield surface of the materials. The damage parameter is computed empirically or semi-empirically in terms of the deformation state variables. Due to their simplicity these models are still widely used in the industry mainly due to the ease of implementation in numerical softwares. Coupled models, on the

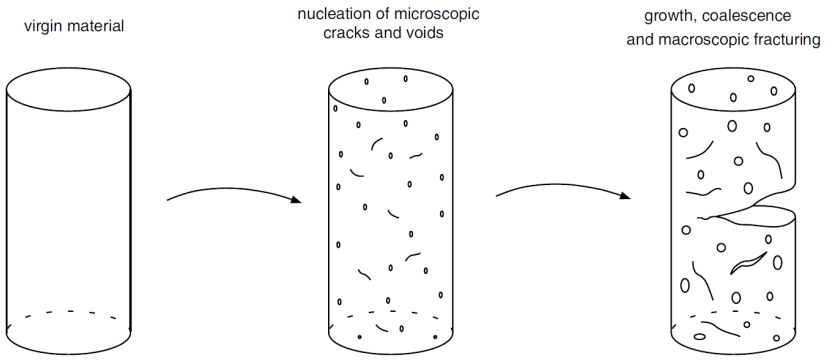

Figure 6.1: Schematic illustration of ductile damage in metals [71].

other hand, incorporate damage accumulation in the constitutive equations and allow the yield surface to be modified by the damage. Although these models are closer to the physical damage phenomenon and give a better representation of the progressive damage evolution within the material, their numerical implementation is more complex.

As we have seen so far, titanium and its alloys, as well as other hcp materials, present deformation and failure properties that differ significantly from that of typical materials with cubic crystalline structures. It was also seen that significant progress has been made on modelling the room temperature plastic deformation of hcp metals within the framework of elastoplasticity. A number of macroscopic elastic/plastic constitutive models (Cazacu and Barlat [47], Cazacu et al. [52], Nixon et al. [32]) capable of capturing both the anisotropy and the tension-compression asymmetry have been developed and validated. However, the understanding of the damage processes in titanium and other hcp metals is still limited.

Within the framework of coupled damage models for porous ductile materials, Cazacu and Stewart [76] developed a plastic potential for porous solids by extending Gurson's [77] analysis of the hollow sphere to the case where the matrix plastic behaviour is governed by the isotropic Cazacu et al. (CPB06) criterion that accounts for the tension-compression asymmetry of hcp metals. Using the Cazacu and Stewart [76] plastic potential, Baudard et al. [78] and Baudard and Cazacu [79] analysed the porosity evolution and the location of the zone corresponding to maximum porosity in notched specimens loaded in uniaxial tension. The finite element simulations of the notched specimens showed that for materials for which the matrix uniaxial tensile strength is larger than its uniaxial compressive strength, void growth and porosity distribution are similar to that in porous materials with von Mises matrix. On the other hand, for porous materials for which the matrix tensile strength is lower than its compressive strength, the void growth rate is much slower, and if the strength differential is pronounced the location of the maximum damage zone shifts from the center to the surface of the specimen.

Also recently Guzmán et al. [80] investigated the damage modelling of the Ti6Al4V alloy. Guzmán extended the Gurson-Tvergaard-Needleman (GTN) damage model based on the Hill'48 [81] yield criteria and assessed the prediction capability of this model on notched axisymmetric bars and notched specimens as well as the Hill'48 and CPB06 criteria up until fracture.

In the context of continuum damage mechanics models, Allahverdizadeh et al. [82] have recently performed a series of experimental tests concerning the determination of the Lemaitre's model [83] parameters using the method of the elastic modulus degradation for the Ti6Al4V alloy. In the application of Lemaitre damage model in numerical simulations no considerations were done concerning the specificities of the material deformation behaviour like the strength differential effect. The Lemaitre damage model is implemented considering the von Mises model that, as it is known, is insufficient for the correct description of the deformation behaviour of hcp metals.

Following a phenomenological approach, Giglio et al. [84] as well as Allahverdizadeh et al. [85] performed the fracture calibration of Ti6Al4V using respectively the Bao-Wierzbicki [86] and the Modified Mohr-Coulomb (MMC) [87] ductile failure criteria. The prediction of the failure behaviour of specimens of different geometries was evaluated.

This chapter deals with the application of damage models to hcp materials, namely the Ti6Al4V alloy, in the framework of coupled and uncoupled models. In spite of the current importance of Ti6Al4V alloy particularly in the aerospace industry, studies regarding its damage and fracture are still quite limited [84,85,88,89]. In this study some of the most representative uncoupled fracture criteria were considered and implemented in a VUMAT subroutine and the fracture initiation site was evaluated for two representative axisymmetric specimens for the Ti6Al4V alloy. The distribution of damage and fracture prediction of the uncoupled models is assessed in a post-processing step, hence constituting an *a posteriori* damage criteria. Using a coupled approach to account for the effects of damage on the yield surface of the material, the continuum damage model proposed by Lemaitre was implemented in a VUMAT subroutine using the Cazacu et al. [52] (CPB06) yield criterion. The predicted damage initiation and evolution was assessed for a smooth and a notched axisymmetric specimen and the impact of the tension compression asymmetry on the damage evolution was evaluated.

6.2 Uncoupled ductile fracture criteria

Uncoupled ductile damage criteria are empirical or semi-empirical models that describe, at the macro or meso scale, the effect of phenomena occurring at the microscopic level either through experimental data or through physical/mathematical models. The damage accumulation is defined in terms of deformation state variables such as equivalent plastic strain, tensile stress and hydrostatic stress which are most relevant to fracture initiation and propagation. Overall these criteria should take into account the deformation path once the current stress/strain state is not sufficient for the characterization of the damage state [90]. Another key aspect is the influence of the stress field during void nucleation and growth. The hydrostatic stress, $\boldsymbol{\sigma_H}$, drives the nucleation and growth of the voids thus the void dimensions increase with the increasing value of the hydrostatic stress, in other words, ductility grows with the decrease of $\boldsymbol{\sigma_H}$ [84]. The deviatoric stress also has an influence on the fracture mechanics as it changes the void geometry and consequently the associated energy. The deviatoric stress is responsible for the change of the void geometry from a sphere-like void into an ellipsoid like void [84]. The ratio between stresses namely the hydrostatic stress, $\boldsymbol{\sigma_H}$, and the equivalent stress, $\bar{\boldsymbol{\sigma}}$, is commonly denominated as stress triaxiality and is often used to better describe the general state of plasticity and fracture. Recently the lode angle also has been taken into account as

major influential factor of ductile fracture mechanisms. The hydrostatic stress, $\boldsymbol{\sigma_H}$, stress triaxiality, $\boldsymbol{\eta}$ and lode angle,$\boldsymbol{\zeta}$ are given by,

$$\boldsymbol{\sigma_H = -\sigma_m = -\frac{tr(\sigma)}{3}}, \tag{6.1}$$

$$\boldsymbol{\eta = \frac{\sigma_m}{\bar{\sigma}}}, \tag{6.2}$$

$$\boldsymbol{\zeta = \frac{27}{2}\frac{J_3}{\sigma_m^3}}. \tag{6.3}$$

The effects of the hydrostatic stress and stress triaxiality on the fracture mechanisms was discussed by Bao and Wierzbicki [86] while Bai and Wierzbicki [91] and Gao et. al [92] studied the noteworthy effects of the lode angle on plastic deformation and ductility.

In a general form, a ductile fracture criterion could be represented as,

$$\boldsymbol{I = \int_0^{\bar{\varepsilon}^p} f(\sigma_H, \bar{\sigma}, ...) d\bar{\varepsilon}_p}, \tag{6.4}$$

where $\boldsymbol{I}$ is the fracture indicator, $\boldsymbol{f(\sigma_H, \bar{\sigma}, ...)}$ represents the fracture criteria and $\boldsymbol{\bar{\varepsilon}_p}$ is the equivalent plastic strain.

There are many fracture criteria available, however this study will not cover them all, focusing instead on the most representative ones. The ductile fracture criteria covered in this study may be divided in two groups: the micromechanical based and those based on the growth of defects. In the following sections these fracture criteria are described in more detail.

6.2.1 Criteria based on micromechanics

The criteria based on micromechanics includes the criterion of total plastic work, also known as Freudenthal's fracture criterion [93] and the criterion of equivalent plastic strain proposed by Datsko [94].

The criterion of total plastic work postulates that the initiation and propagation of a crack is dominated by a critical value of the absorbed plastic energy, thus following the definition given by equation (6.4), the integration over the equivalent stress provides the physical meaning of the energy required to initiate a crack tip per unit area. The Freudenthal

criterion is formulated as follows,

$$I_{Wp} = W_p = \int_0^{\bar{\varepsilon}_p^f} \bar{\sigma} d\bar{\varepsilon}_p, \tag{6.5}$$

where W_p is the specific total plastic work, $\bar{\varepsilon}_p$ is the equivalent plastic strain and $\bar{\varepsilon}_p^f$ is the equivalent plastic strain at fracture.

The criterion of equivalent plastic strain was suggested by Datsko [94]. This investigator stated that the ductile fracture in forming processes depends on the plastic deformation limit for a given material and technological process and that this limit could be represented as the equivalent plastic strain. The criterion of equivalent plastic strain assumes that fracture is initiated when the equivalent plastic strain reaches a critical value and is represented by,

$$I_{\bar{\varepsilon}^p} = \int_0^{\bar{\varepsilon}_p^f} d\bar{\varepsilon}_p^f, \tag{6.6}$$

where $\bar{\varepsilon}_p^f$ is the equivalent plastic strain at fracture.

6.2.2 Criteria based on models based on the growth of defects

As previously stated, ductile fracture is commonly described through the mechanisms of nucleation, growth and coalescence. These mechanisms constitute the base of some fracture criteria. According to different physical aspects the criteria covered in this study can be based on the geometry of the voids, the void growth mechanism or on constitutive material models.

Geometry of defects

One of the first models to be proposed for the ductile fracture was developed by McClintock [95]. The McClintock model assumes that the material is divided in quadrilateral elements containing elliptical cylindrical voids and fracture occurs when the boundary of the void reaches the boundary of the element. In his work, McClintock showed the dependence of the ductile fracture on the deformation path and underlined the inverse dependence of the deformation with hydrostatic stress. These results were important as they established a new approach on the ductile fracture driving the development of new models.

Another model was proposed by Rice and Tracey [96] based on the analysis of the growth of micro voids with sphere shape in a general remote stress field. The criterion was established through the Rayleigh-Ritz variational principle as a function of the void radius average deformation rate and the imposed remote average deformation rate. The criterion may be

expressed by,

$$I_R = \int_0^{\bar{\varepsilon}_p^f} 0.283 exp\left(\frac{\sqrt{3}}{2}\frac{\sigma_H}{\bar{\sigma}}\right) d\bar{\varepsilon}_p. \tag{6.7}$$

This criterion shows the close dependence of failure with the stress triaxiality.

Growth mechanism

Assuming that the principal stress is the most relevant in the initiation of fracture, Cockcroft and Latham [97] proposed a criterion defined in terms of traction plastic work associated to the principal stress along the path of the equivalent plastic strain. The Cockcroft criterion was developed for bulk forming and is applicable to the deformation with low stress triaxiality. This criterion can be expressed as,

$$I_{\sigma_1} = \int_0^{\bar{\varepsilon}_p^f} \sigma_1 d\bar{\varepsilon}_p, \tag{6.8}$$

where σ_1 is the maximum principal stress.

Later, based on the evidence that ductility diminishes with the hydrostatic stress, Brozzo, De Luca and Rendina [98] proposed a modification of the Cockcroft and Latham model. This new model included an explicit dependence of the fracture indicator on the hydrostatic stress, σ_H. The Brozzo, De Luca and Rendina criterion is expressed as,

$$I_{\sigma_1,\sigma_H} = \int_0^{\bar{\varepsilon}_p^f} \frac{2\sigma_1}{3(\sigma_1 - \sigma_H)} d\bar{\varepsilon}_p. \tag{6.9}$$

This criterion confirmed the importance of the hydrostatic stress in ductile fracture which was then further reinforced by Norris et. al [99] and Atkins [100] that proposed new models based only on the hydrostatic stress.

Continuous Damage Mechanics

The models based on the theory of Continuous Damage Mechanics not only give a good description of the materials behaviour but also provide an approach to the fracture analysis from the initiation of the fracture, its evolution and final failure [101, 102]. The damage variable has been used as a failure indicator in many situations (see for example [101–103]) and has even been identified by Cescotto and Zhu [104] as the only criterion capable of predicting the location of the fracture initiation.

Lemaitre [105] proposed a criterion considering that an energetic approach using the elastic

energy release rate is the most adequate for the characterization of the fracture initiation. Lemaitre's fracture criterion can be expressed by,

$$-\boldsymbol{Y_c} = \frac{\bar{\boldsymbol{\sigma}}^{\boldsymbol{2}}}{\boldsymbol{2E(1-D)^2}}\left[\frac{\boldsymbol{2}}{\boldsymbol{3}}\boldsymbol{(1+\nu)} + \boldsymbol{3(1-2\nu)}(\frac{\boldsymbol{\sigma_H}}{\bar{\boldsymbol{\sigma}}})^{\boldsymbol{2}}\right], \tag{6.10}$$

where $\boldsymbol{D}$ is a damage variable and $\boldsymbol{Y_c}$ represents the elastic energy release rate with damage at the fracture initiation.

Following the same premise as Lemaitre, Tai and Yang assumed that the property that controls the initiation and evolution of a crack may be treated as a constitutive property of the material and thus proposed a new model. The Tai and Yang fracture criterion is based on the nucleation, growth and coalescence of voids and is given by,

$$\boldsymbol{V_D} = \int_{\bar{\varepsilon}_p^o}^{\bar{\varepsilon}_p}\left[\frac{\boldsymbol{2}}{\boldsymbol{3}}\boldsymbol{(1+\nu)} + \boldsymbol{3(1-2\nu)}\left(\frac{\boldsymbol{\sigma_H}}{\bar{\boldsymbol{\sigma}}}\right)^{\boldsymbol{2}}\right]\boldsymbol{d\bar{\varepsilon}_p}, \tag{6.11}$$

where $\boldsymbol{V_D}$ is the critical damage parameter. A simplified version of equation (6.11) is used to predict fracture initiation in notched tensile specimens and is given by,

$$\boldsymbol{V_D} = \left[\frac{\boldsymbol{2}}{\boldsymbol{3}}\boldsymbol{(1+\nu)} + \boldsymbol{3(1-2\nu)}\left(\frac{\boldsymbol{\sigma_H}}{\bar{\boldsymbol{\sigma}}}\right)^{\boldsymbol{2}}\right]\boldsymbol{\bar{\varepsilon}_p}. \tag{6.12}$$

Based on experimental observations, Tai and Yang estimated the critical value of $\boldsymbol{V_D}$ to vary between 0.75 and 1.15 for low carbon steels.

Motivated by the suitability of the energy measure as a ductile fracture criterion as proposed by Lemaitre, Vaz Jr. [106] and Vaz Jr. et al. [107] proposed a fracture indicator based on the total damage work expressed as,

$$\boldsymbol{I_{WD}} = \int_{\boldsymbol{0}}^{\boldsymbol{t}}\boldsymbol{(-Y)\dot{D}dt}, \tag{6.13}$$

or

$$\boldsymbol{I_{WD}} = \int_{\boldsymbol{0}}^{\boldsymbol{D_c}}\boldsymbol{(-Y)dD} = \int_{\boldsymbol{0}}^{\boldsymbol{D_c}}\frac{\bar{\boldsymbol{\sigma}}^{\boldsymbol{2}}}{\boldsymbol{2E(1-D)^2}}\left[\frac{\boldsymbol{2}}{\boldsymbol{3}}\boldsymbol{(1+\nu)} + \boldsymbol{3(1-2\nu)}\left(\frac{\boldsymbol{\sigma_H}}{\bar{\boldsymbol{\sigma}}}\right)^{\boldsymbol{2}}\right]\boldsymbol{dD}, \tag{6.14}$$

where $\boldsymbol{I_{WD}}$ represents the critical damage parameter. This definition is consistent with the thermodynamics of irreversible processes and the parameter of the energy release rate, $\boldsymbol{-Y}$, contains the representation of the damage state through the variable $\boldsymbol{D}$ and also takes into consideration the hydrostatic stress through the triaxiality factor, $\boldsymbol{\sigma_H/\bar{\sigma}}$.

The same author proposed a simplified version of the fracture criterion given by (6.14) that is obtained by integrating the uncoupled damage model.

$$\boldsymbol{I_D} = \int_0^{\bar{\varepsilon}_p} \left\{ \frac{\bar{\sigma}^2}{2ES_0} \left[\frac{2}{3}(1+\nu) + 3(1-2\nu) \left(\frac{\sigma_H}{\bar{\sigma}} \right)^2 \right] \right\}^{s_0} \bar{\varepsilon}_p, \tag{6.15}$$

where $\boldsymbol{I_D}$ is the fracture indicator. Although this simplified criterion preserves the dependency on the triaxiality plastic flow, the mutual interaction between the material degradation and the plastic deformation are lost which may affect the prediction of the fracture location [106].

Table 6.1 resumes the uncoupled fracture criteria covered in this study.

Table 6.1: Summary of selected fracture criteria.

Criterion	Formula
Total Plastic Work	$\int_0^{\bar{\varepsilon}_p^f} \bar{\sigma} d\bar{\varepsilon}_p$
Equivalent Plastic Deformation	$\int_0^{\bar{\varepsilon}_p^f} d\bar{\varepsilon}_p^f$
Rice and Tracey	$\int_0^{\bar{\varepsilon}_p^f} 0.283 exp\left(\frac{\sqrt{3}}{2}\frac{\sigma_H}{\bar{\sigma}}\right) d\bar{\varepsilon}_p$
Cockcroft and Latham	$\int_0^{\bar{\varepsilon}_p^f} \sigma_1 d\bar{\varepsilon}_p$
Brozzo et al.	$\int_0^{\bar{\varepsilon}_p^f} \frac{2\sigma_1}{3(\sigma_1-\sigma_H)} d\bar{\varepsilon}_p$
Lemaitre, Tai and Yang	$\int_{\bar{\varepsilon}_p^o}^{\bar{\varepsilon}_p} \left[\frac{2}{3}(1+\nu) + 3(1-2\nu)\left(\frac{\sigma_H}{\bar{\sigma}}\right)^2\right] d\bar{\varepsilon_p}$
Vaz Jr.	$\int_0^{\bar{\varepsilon}_p} \left\{\frac{\bar{\sigma}^2}{2ES_0}\left[\frac{2}{3}(1+\nu) + 3(1-2\nu)\left(\frac{\sigma_H}{\bar{\sigma}}\right)^2\right]\right\}^{s_0} d\bar{\varepsilon_p}$

6.2.3 Computational implementation and assessment of the selected criteria

The simplicity of the computational implementation of the fracture criteria is one of the main advantages contributing to its widespread use. Because the damage accumulation is not incorporated in the constitutive equations, the computation of the fracture indicators is subsequently added to the integration algorithm. To ensure that no convergence or stability issues can occur, the time step should be sufficiently small which in explicit simulations is usually assured.

The discretization of the general fracture criteria represented by equation (6.4) can be expressed as,

$$\boldsymbol{I^{n+1}} = \boldsymbol{I^n} + \boldsymbol{f}\left(\boldsymbol{\sigma_h^{n+1}}, \bar{\boldsymbol{\sigma}}^{\boldsymbol{n+1}}, \dots\right) \boldsymbol{\Delta}\bar{\boldsymbol{\varepsilon}}_{\boldsymbol{p}}^{\boldsymbol{n+1}}, \tag{6.16}$$

where $\boldsymbol{I^{n+1}}$ and $\boldsymbol{I^n}$ are the fracture indicators in the step time $\boldsymbol{n+1}$ and $\boldsymbol{n}$ respectively and $\boldsymbol{\Delta}\bar{\boldsymbol{\varepsilon}}_{\boldsymbol{p}}$ is the equivalent plastic strain increment. In the fracture indicators based on damage

models the damage increment, $\boldsymbol{\Delta D^{n+1}}$, between step time $\boldsymbol{n}$ and $\boldsymbol{n+1}$ should be used instead.

The fracture criteria given in table 6.1 were implemented in the VUMAT previously developed and the assessment and comparison of the different criteria was then performed. The numerical examples were based on the experimental work of Giglio et al. [84] in which several specimens with different geometries made of Ti6Al4V alloy were tested. Two representative geometries were selected and used in this study: a smooth axisymmetric tensile specimen and a notched axisymmetric specimen that were subjected to monotonic tensile loading. During the simulation, the value of the various fracture indicators are calculated in each integration point and the point at which the maximum value is found represents the predicted fracture initiation site which should be consistent with the experimental evidence.

The geometries of the specimens are given in Figure 6.2. The specimen A represented in Figure 6.2(a) corresponds to a classical smooth tensile test designed according to ISO 6892 standard and evaluates pure tensile conditions. The specimen B represented in Figure 6.2(b) has a notched axisymmetric geometry.

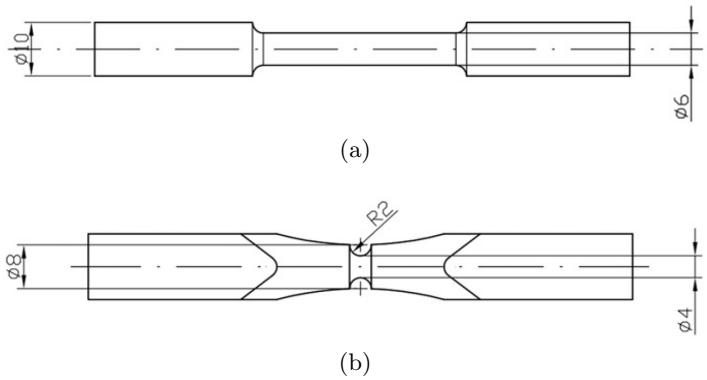

Figure 6.2: Specimen geometries: (a) smooth axisymmetric and (b) notched axisymmetric.

The specimen B with the semi-circular notch allows reaching a high stress triaxiality ratio in the centre of the specimen and a high plastic deformation near the notch where the maximum value of the equivalent plastic strain occurs. In the smooth specimen the maximum equivalent plastic strain is at the centre of the specimen as well as the maximum stress triaxiality. The levels of equivalent plastic strain and stress triaxiality at fracture for specimen A and B are shown in Figure 6.3.

The material of the specimens is the titanium alloy Ti6Al4V with the properties previously defined (Chapter 3) with the undamaged material response given by the CPB06 and a Voce type hardening law for the reference hardening curve. A new set of parameters for the Voce hardening law was used. The previous parameters were obtained based on the stress-strain data until 0.1 axial strain which leads to axial stress values that are not in accordance with the experimental data for higher values of the axial strain. Following the experimental tensile data performed in the LD direction until fracture obtained by Guzmán et al. [80] using a 3D optical strain measuring system, the new set of parameters were determined and are given in Table 6.2.

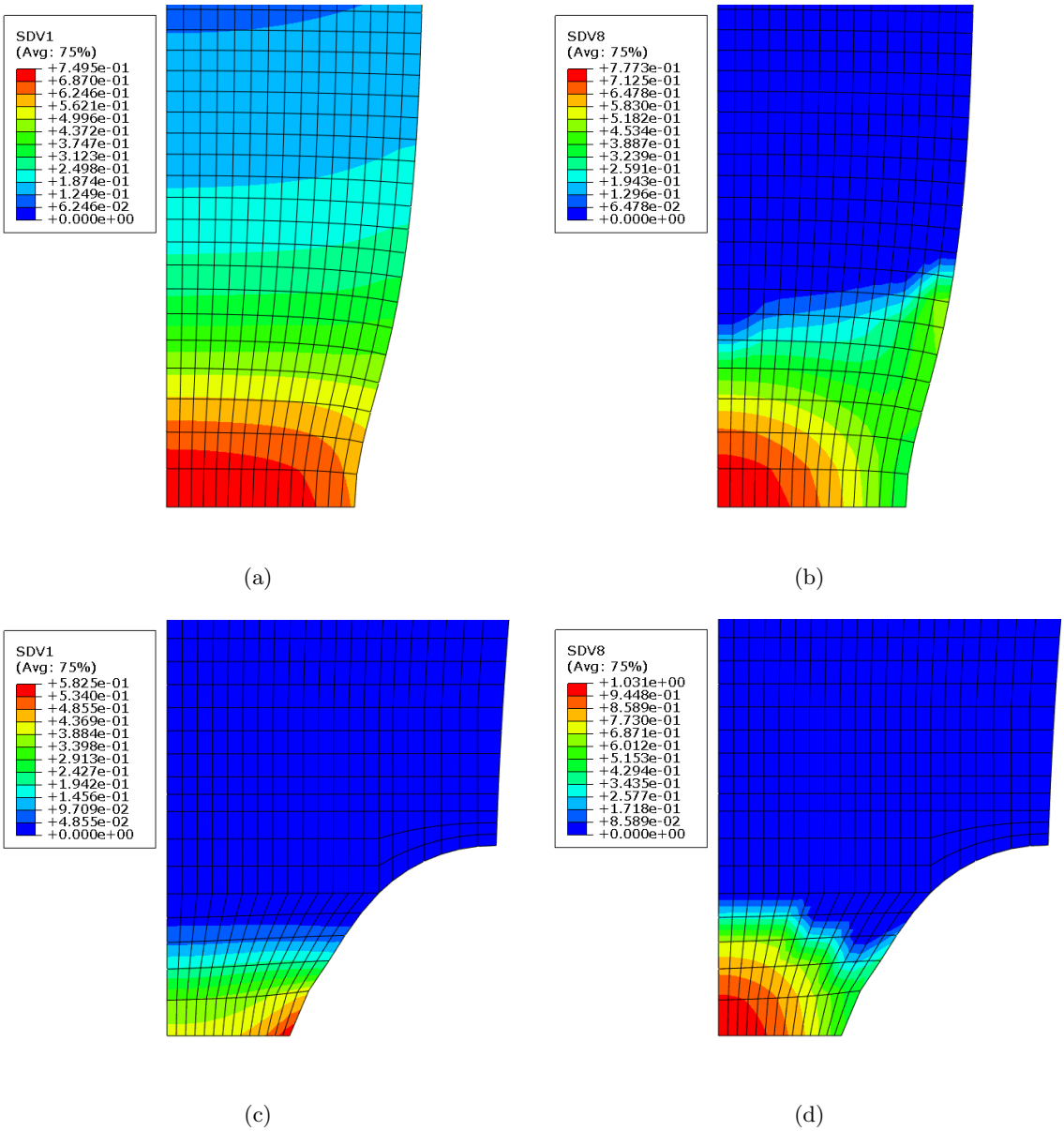

Figure 6.3: Specimen A: (a) Equivalent plastic strain and (b) Stress triaxiality. Specimen B: (c) Equivalent plastic strain and (d) Stress triaxiality.

Table 6.2: New Voce-type hardening law parameters for Ti6Al4V.

A_0	B_0	C_0
1197	277	7.5

In the finite element model an eighth of the specimen is considered and adequate symmetry boundary conditions are imposed on the corresponding faces (Figure 6.4). The applied loading consists of a constant displacement along the longitudinal direction of the specimen,

imposed on a reference point that controls the top nodes behaviour. The longitudinal direction associated with the material was set coincident with the longitudinal direction of the specimen. Three dimensional linear brick elements with eight nodes and reduced integration were used. A relatively fine mesh was used with elements with an average length of 0.2mm.

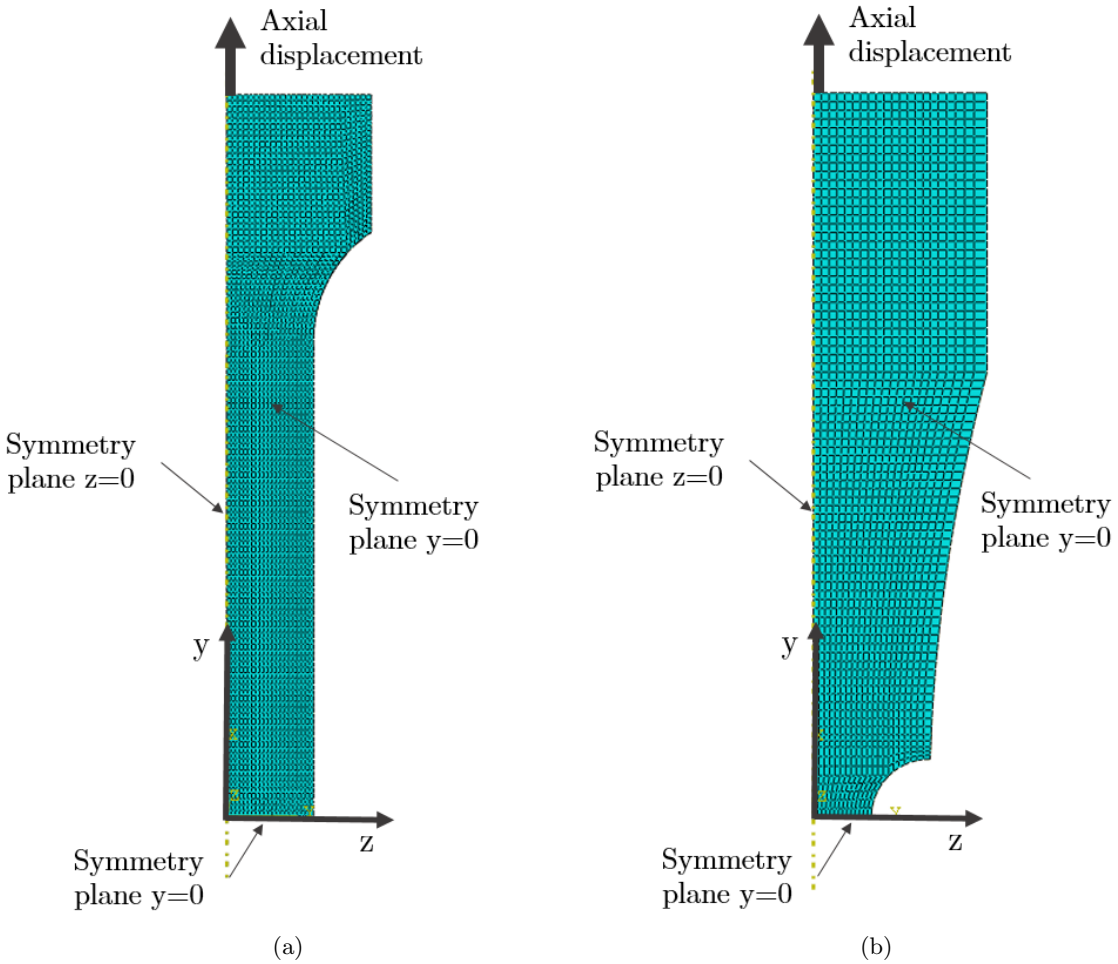

Figure 6.4: Finite element models: (a) the classical specimen and (b) the notched specimen.

The results given by the fracture criteria studied for each specimen are given in the following sections. All the results were compared for the onset of necking that occurs according to the experimental data provided by [84] for a displacement of 3.5mm for specimen A and 0.25mm for specimen B.

Criteria based on micromechanics

The results obtained for the two geometries studied regarding the equivalent plastic strain and the Freudenthal criteria are shown in Figures 6.5 and 6.6 respectively.

The equivalent plastic strain as well as the total plastic work criteria indicate fracture in

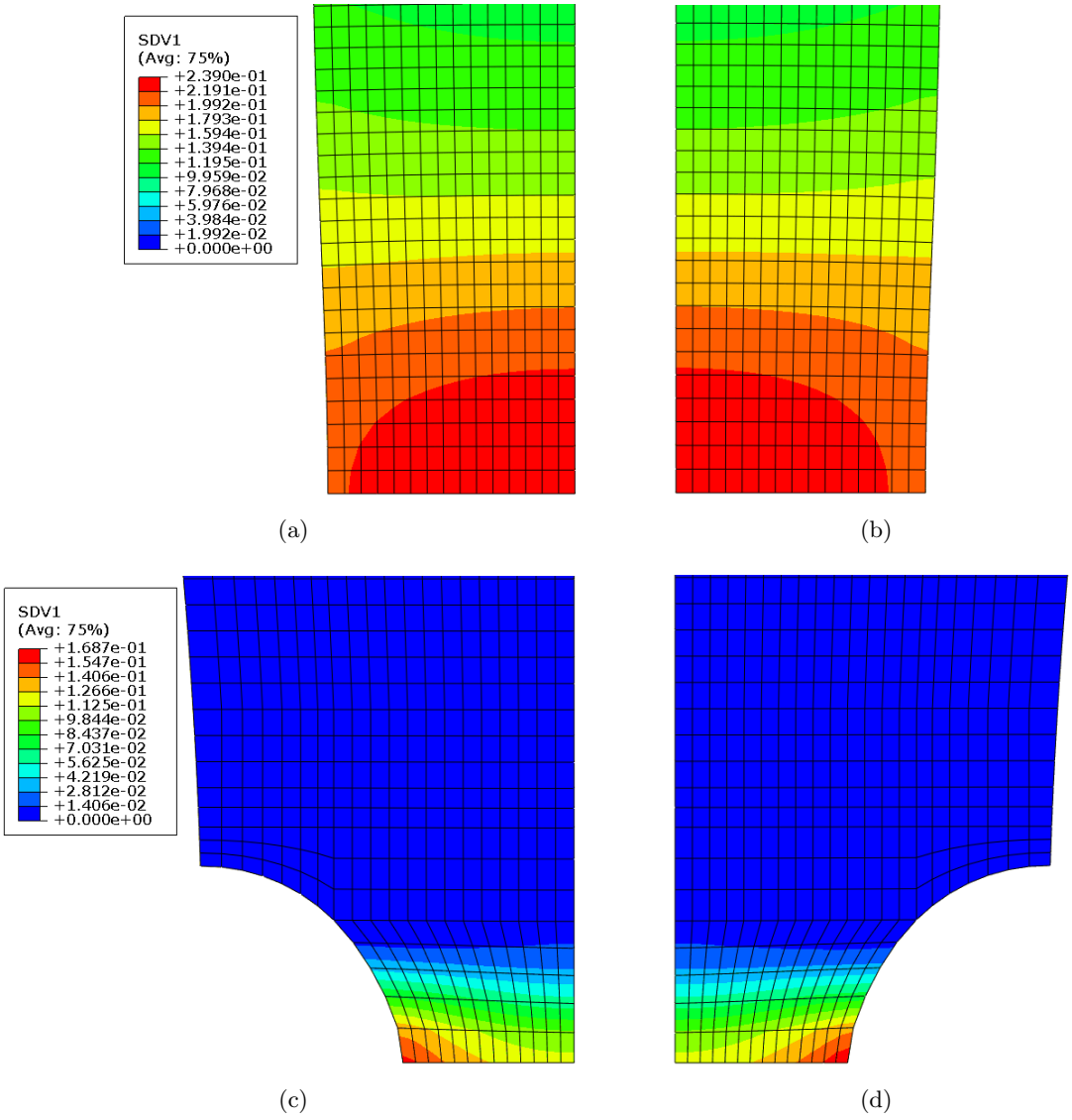

Figure 6.5: Criterion of equivalent plastic strain for the smooth axisymmetric specimen on (a) LD-ST plane and (b) LD-TD plane and for the notched specimen on (c) the LD-ST plane and (d) LD-TD plane.

regions where plastic deformation concentrates, which may not correspond to experimental observations. In fact, in this study, the results show that these models although predict correctly the fracture initiation for the smooth axisymmetric specimen, they wrongly predict fracture initiation near the notch for the notched specimen, which does not comply with experimental evidence.

The total plastic work criteria proposed by Freudenthal has been invalidated by some investigators that did not found an accurate fracture initiation prediction for different specimen geometries and loading conditions (see for example Gouveia et al. [108] or F.M.A. Pires [109]). Nevertheless Cliff et al. [110] has previously assured the fracture prediction capability of this

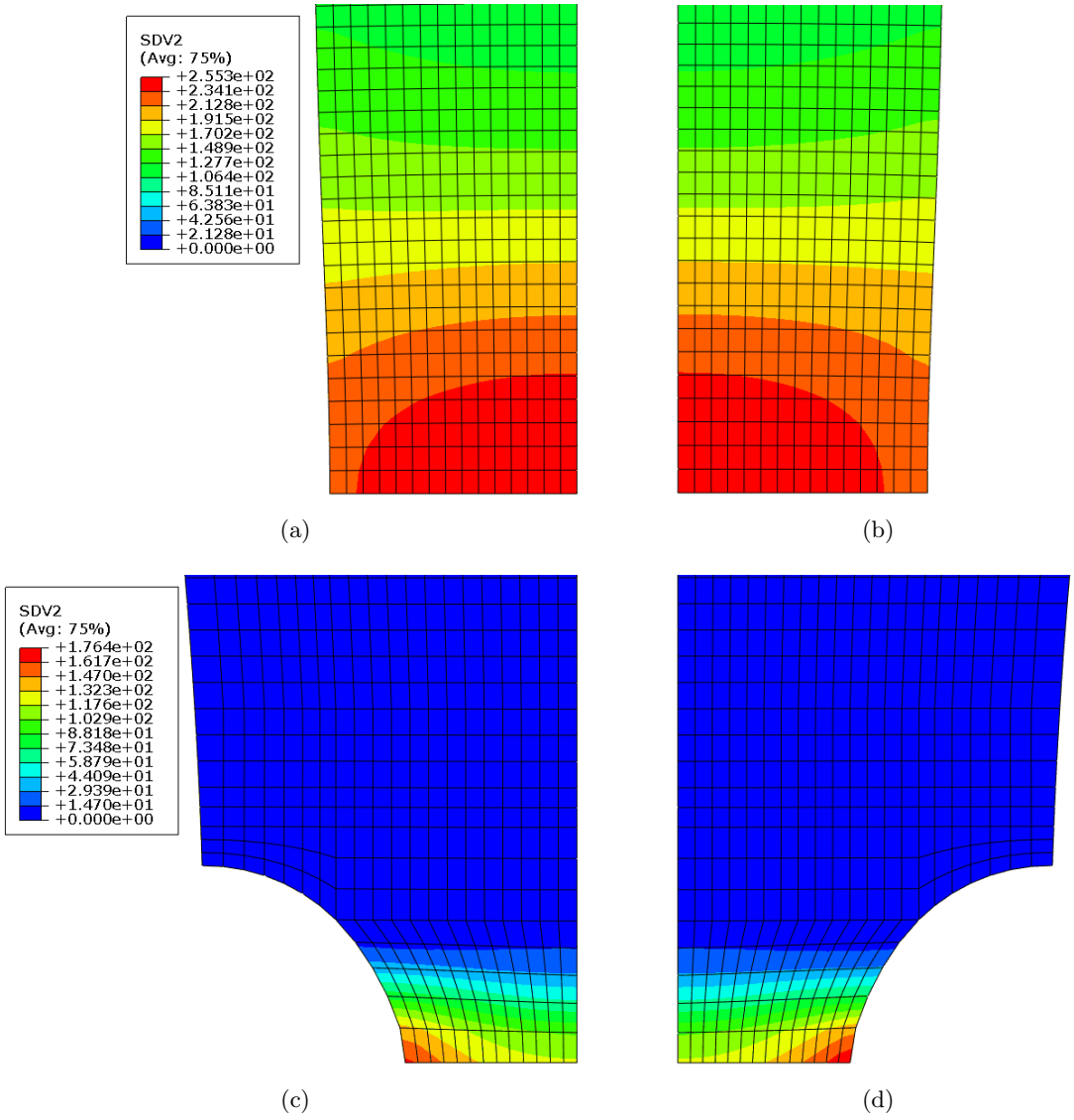

Figure 6.6: Criterion of the total plastic work (Freudenthal) for the smooth axisymmetric specimen on (a) LD-ST plane and (b) LD-TD plane and for the notched specimen on (c) the LD-ST plane and (d) LD-TD plane.

criterion based on the results obtained for axisymmetric extrusion and compression tests. The equivalent plastic strain proposed by Datsko [94] in its turn, has been refuted as a fracture indicator due to the fact that the value of the equivalent plastic strain is highly dependent on the forming process and cannot be considered a material property [111].

Overall the criteria based on micromechanics fail in predicting the fracture initiation site as they tend to indicate the points of maximum plastic deformation, which may not correspond to the correct site fracture initiation point as is the case of the notched specimen.

Criteria based on models based on the geometry of defects

The results obtained for the two geometries regarding the Rice and Tracey fracture criterion are shown in Figure 6.7.

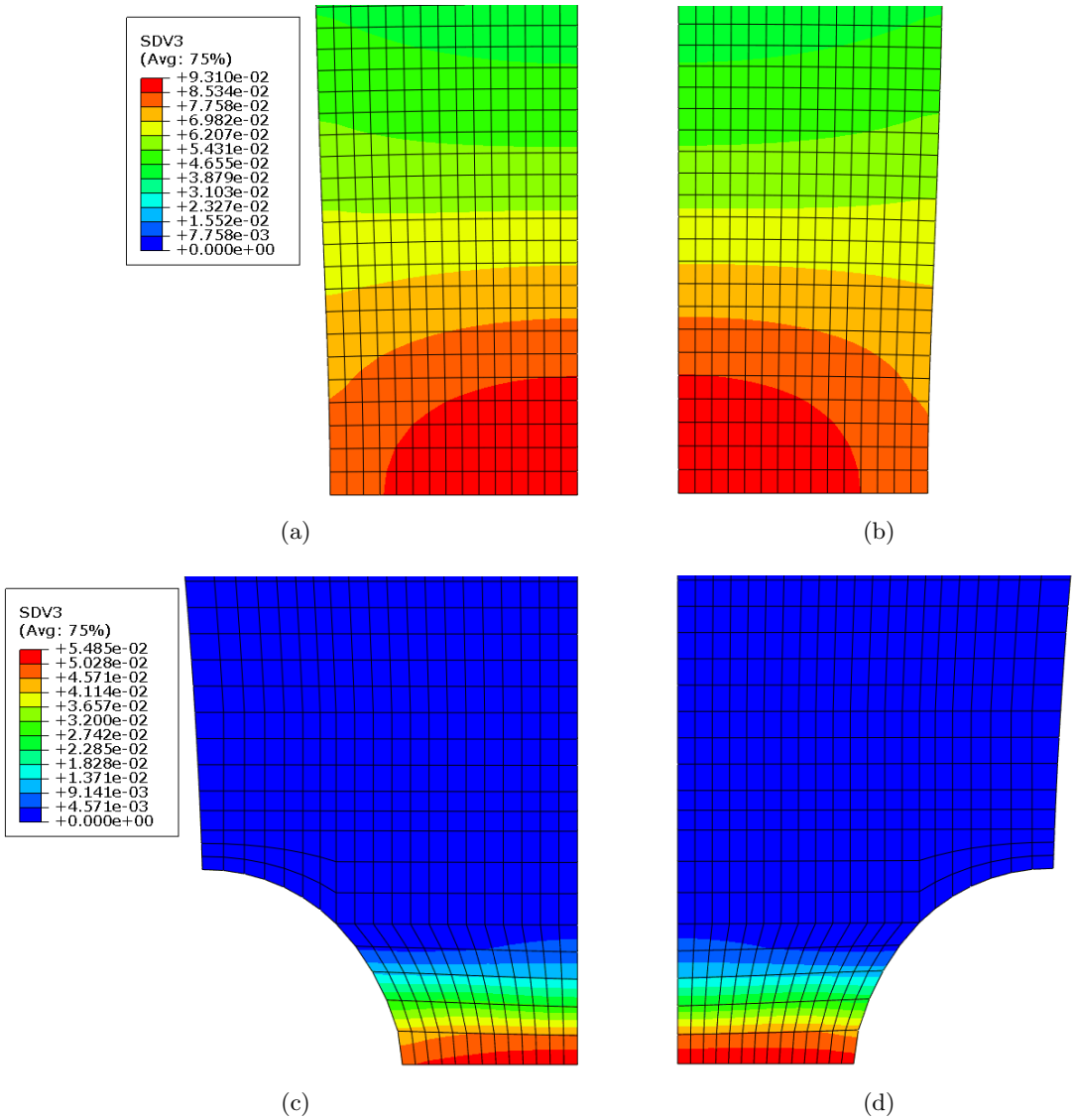

Figure 6.7: Criterion based on the geometry of defects (Rice and Tracey) for the smooth axisymmetric specimen on (a) LD-ST plane and (b) LD-TD plane and for the notched specimen on (c) the LD-ST plane and (d) LD-TD plane.

This criterion correctly predicts the fracture initiation site located in the centre for the smooth axisymmetric specimen. However, for the notched specimen, the predicted fracture initiation site extends throughout the middle section. The prediction given by the Rice and Tracey criterion for the notched specimen is very diffuse as its extends along a larger region in both the LD-ST and the LD-TD planes. Overall, this criterion is also considered to fail in

the fracture initiation site prediction.

Criteria based on the growth mechanism of defects

The fracture initiation predictions regarding the Cockcroft and Latham and the Brozzo et al. criteria are given in Figures 6.8 and 6.9 respectively.

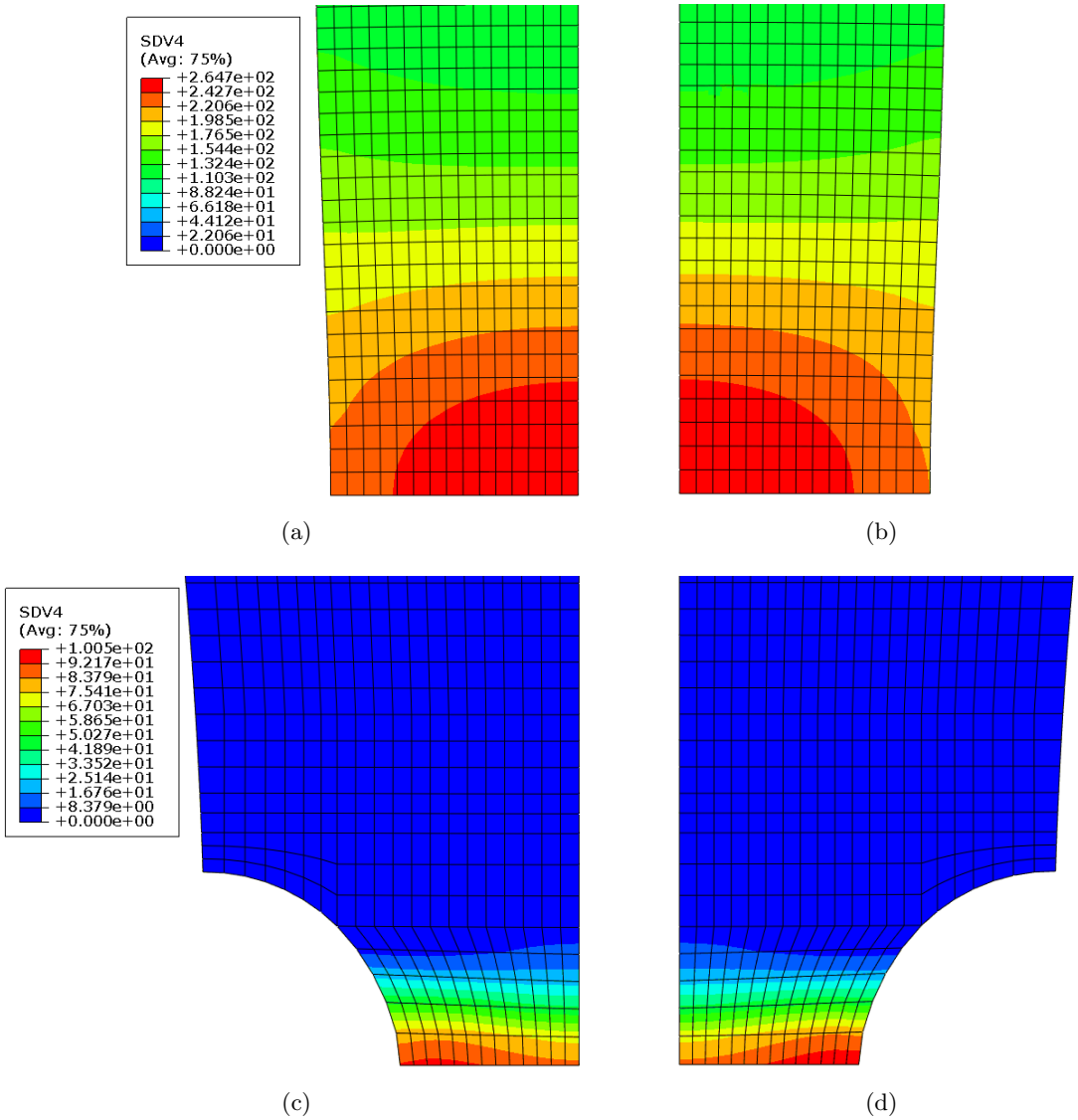

Figure 6.8: Criterion based on the growth of defects due to the maximum principal stress (Cockcroft and Latham) for the smooth axisymmetric specimen on (a) LD-ST plane and (b) LD-TD plane and for the notched specimen on (c) the LD-ST plane and (d) LD-TD plane.

As its shown by the results, the criterion based on the growth of defects by Cockcroft and Latham also fails in the prediction of the fracture initiation in the case of the notched

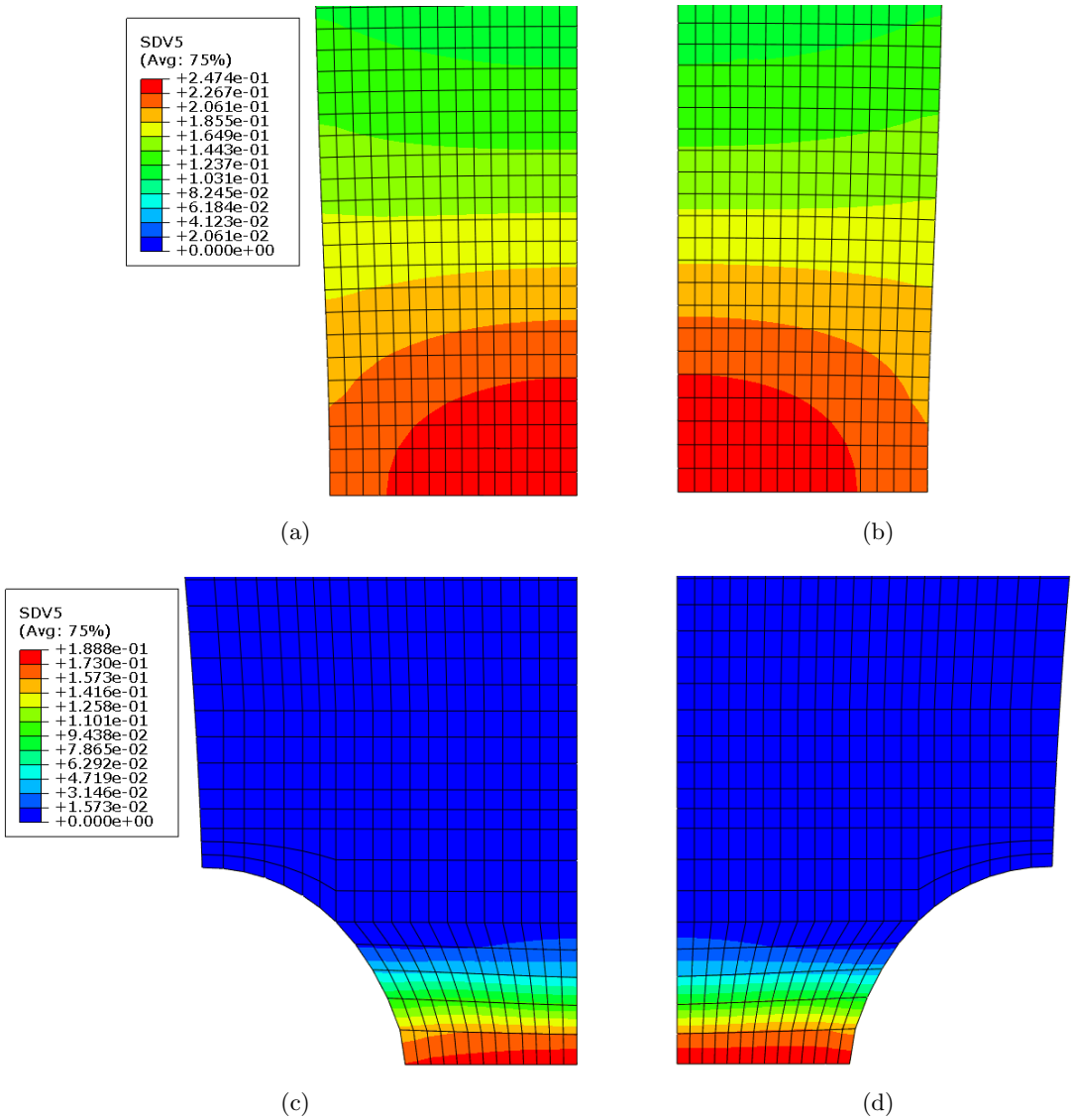

Figure 6.9: Criterion based on the growth of defects due to the maximum principal stress (Brozzo et al.) for the smooth axisymmetric specimen on (a) LD-ST plane and (b) LD-TD plane and for the notched specimen on (c) the LD-ST plane and (d) LD-TD plane.

specimen. The maximum value of the fracture indicator is located near the notch which is inconsistent with experimental evidence. Nevertheless the results obtained for the smooth specimen are accurate and in agreement with the experimental evidence.

Regarding this criterion, Gouveia et al. [108] draws attention to the fact that a negative accumulation of damage is possible if the largest principal stress is temporarily negative and thus it predicts accumulation of negative damage. Moreover, this criterion is not sensitive to changes between the largest and second largest principal stresses that may occur during deformation once the critical value of the damage at failure is a scalar quantity. Nevertheless, good results have been reported for the Cockcroft and Latham criterion particularly under

compression tests (see [108] and [109]), where the principal stress plays and important role [90].

Similar results were obtained using the criterion by Brozzo et al. The incorporation of the hydrostatic stress does not change the prediction of fracture initiation relatively to the Cockcroft and Latham model. It is however noteworthy the asymmetry between the ST and TD directions. While along the ST direction the predicted initiation site does not include the notch surface, in the TD direction the predicted initiation site is more diffuse along the middle section and includes both the centre as well as the notch surface.

Criteria based on Continuous Damage Mechanics

Regarding the criteria based on Continuous Damage Mechanics the results for the Lemaitre, Tay and Yang and Vaz Jr. criteria are shown in Figures 6.10 and 6.11 respectively.

The criterion proposed by Lemaitre, Tay and Yang which is based on the theory of Continuous Damage Mechanics gave better results especially concerning the notched specimen for which no other criteria was able to correctly predict the fracture initiation site. This criteria indicates a fracture initiation point near the centre which is in agreement with the experimental observations. However, under compression, this criteria has shown poor results as was reported in the work of F.M.Pires [109].

Regarding the criterion proposed by Vaz Jr. which is also based on the theory of Continuous Damage Mechanics, the results are quite similar to the results obtained by the Lemaitre, Tay and Yang criterion. Note that the uncoupled version of the model was implemented in this study with the integration being done in the equivalent plastic strain trajectory rather than in the damage evolution trajectory. This criterion has also shown poor results under compression (see [109]).

From the results, obtained for the several criteria analysed, we could assess the influence of the various factors influencing the fracture indicators like the hydrostatic stress, equivalent stress or the maximum principal stress. The fracture indicators are essentially *a-poteriori* criteria, which are computed independently and where the degradation of the material has no influence on the elastoplastic behaviour of the material. The comparison of the numerical results obtained for each of the criterion has shown that almost all fail in the prediction of the fracture initiation site for the notched specimen. The point with higher plastic deformation, near the notch, was identified by the majority of the criteria as the fracture initiation point. However, experimental evidence has shown that the fracture initiation point is in fact in the centre of the specimen. The presence of the semi circular notch allows reaching a high stress triaxiality condition in the centre at the notched specimen. The importance of the stress triaxiality in the prediction of ductile fracture was affirmed by the better suitability of the models proposed by Lemaitre and Vaz Jr. which incorporate this factor in their formulation. On the other hand, the smooth axisymmetric specimen under monotonic tensile load, poses no challenge in the prediction of fracture initiation. All fracture indicators have correctly predicted the centre of the specimen as the fracture initiation site.

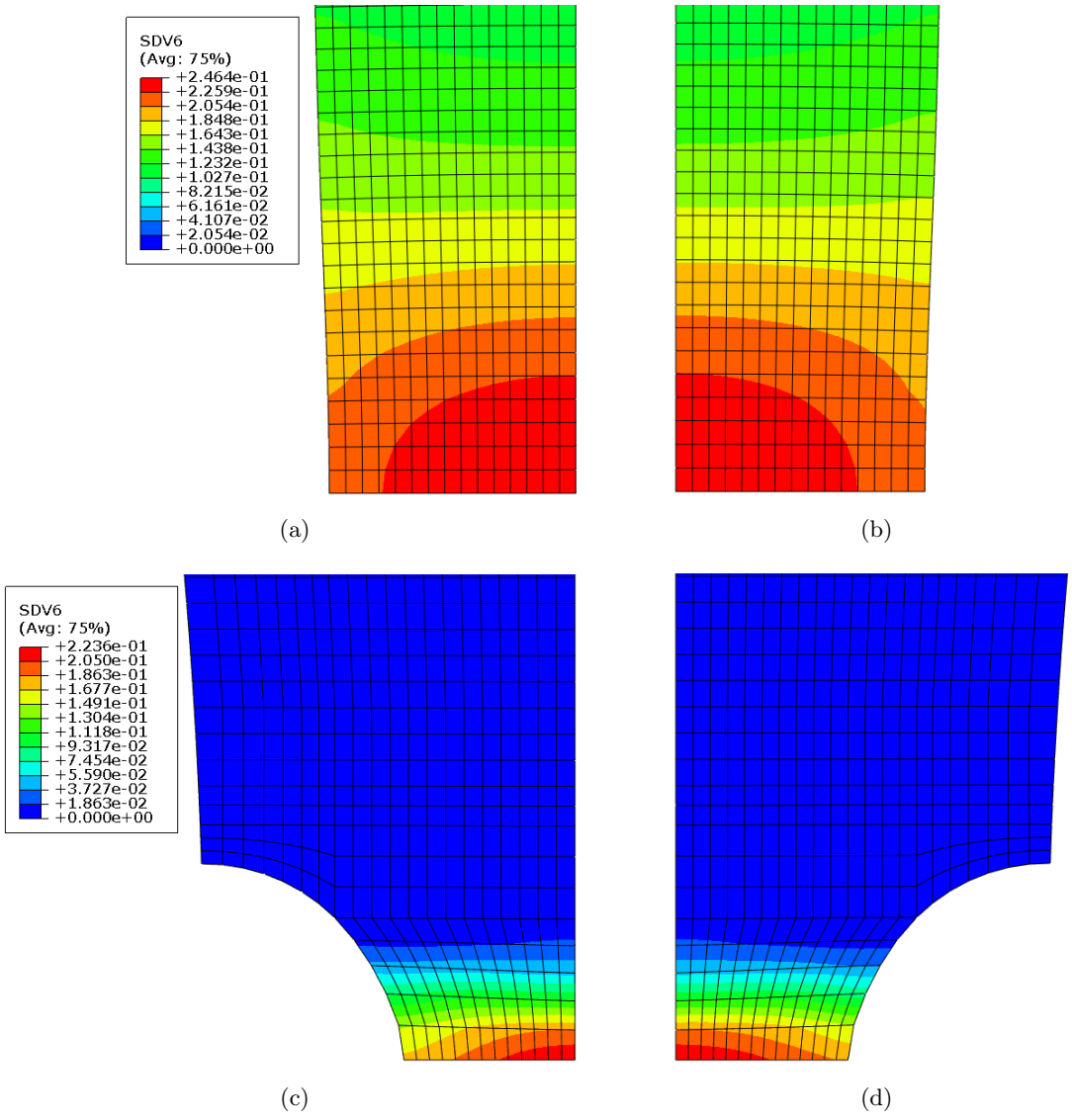

Figure 6.10: Criterion based on Continuous Damage Mechanics (Lemaître, Tay and Yang) for the smooth axisymmetric specimen on (a) LD-ST plane and (b) LD-TD plane and for the notched specimen on (c) the LD-ST plane and (d) LD-TD plane.

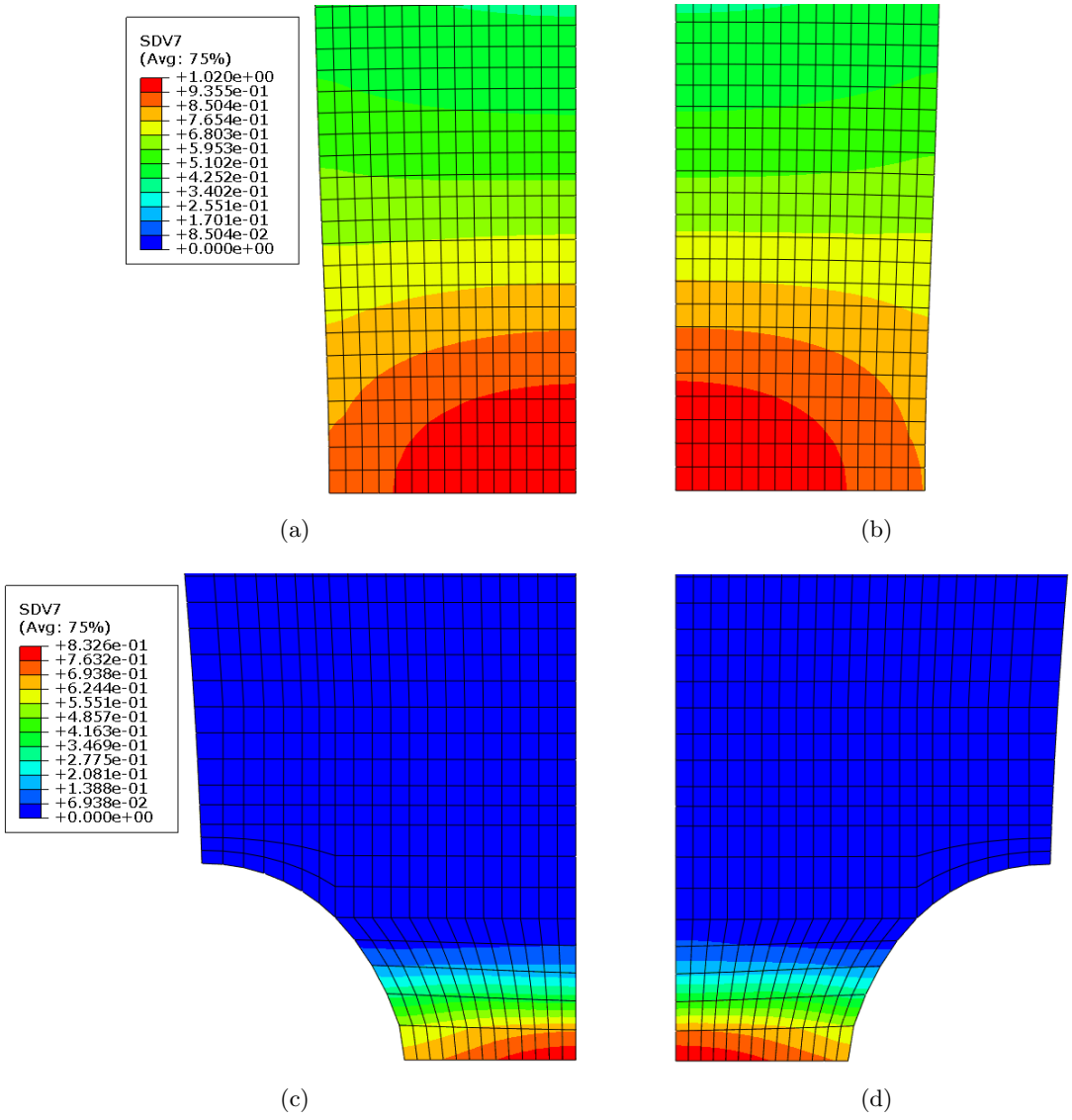

Figure 6.11: Criterion based on Continuous Damage Mechanics (Vaz Jr.) for the smooth axisymmetric specimen on (a) LD-ST plane and (b) LD-TD plane and for the notched specimen on (c) the LD-ST plane and (d) LD-TD plane.

6.3 Coupled ductile damage models

The uncoupled models introduced previously are able to describe the critical conditions under which ductile fracture initiates and benefit extensively from their ease implementation and computational simplicity. However, these models estimate failure without considering the relevant physical background, neglecting the effect of damage on the elastoplastic behaviour. This approach inevitably disregards stress and strain redistributions caused by damage growth and the consequent softening behaviour. More accurate engineering applications require the coupling between elastoplastic constitutive equations and damage. The so-called fully coupled approach is required.

In the framework of the coupled ductile damage models two main general approaches have been extensively considered: the micromechanical based (or physical) constitutive theories based on porous materials models and the phenomenological theories motivated by the Continuum Damage Mechanics as Lemaitre-based models. The micromechanical approach is related with the original work performed by Gurson [77]. In his model, Gurson proposed the use of an internal variable representing the volume fraction of spherical voids, $\boldsymbol{f}$, defined as the ratio between the accumulated volume of individual voids and the total volume. The coupling between plasticity and damage was established using a macroscopic yield function for an ideally plastic matrix containing a certain volume of fraction voids and considering the effects of hydrostatic stress. The original model proposed by Gurson was later developed by Tvergaard [112] and Tvergaard and Needleman [113] that modified Gurson's yield function in order to account for rate sensitivity and necking instabilities in plastically deforming solids and to provide better representation of final void coalescence.

In this section the Continuum Damage Mechanics theory proposed by Lemaitre [83], [114] will be described in more detail as it is later used coupled with the Cazacu et al. (CPB06) [52] yield criterion for modelling the ductile damage of the Ti6Al4V titanium alloy.

6.3.1 Continuum Damage Mechanics

Continuum Damage Mechanics (CDM) constitutes a practical tool to describe the various damaging microprocesses in materials and structures at a macroscopic level. CDM models rely upon the works of Kachanov [115] and Rabotnov [116] whose concepts constitute the first modern damage formulations. Kachanov was the first to introduced a scalar internal variable to model the creep failure of metals and only later Rabotonov introduced a damage variable with a physical significance. Since the pioneering works of these investigators the concept of damage variables has considerably developed leading to the formulation of constitutive models capable of describing the internal degradation of solids and thus initiating the development of what is currently known as Continuum Damage Mechanics [117, 118].

Original developments and basic concepts

On the base of the continuum damage models is the definition of the damage variable. At a microscopic scale, damage is related to the decohesion of interatomic bonds or the plastic magnifications of microvoids. A damage variable needs to quantify these microscopic processes

in terms of a measurable macroscopic variable that can be used in structural computations.

Kachanov [115] was the first author to define a continuous internal variable to measure the density of the microscopic irreversible defects and characterize the observable material degradation. Later, Rabotonov [116] provided a physical significance for the damage variable by proposing the reduction of the cross sectional area due to the presence of cracks and cavities as a measure of the state of internal damage.

According to the original developments and considering a Representative Volume Element (RVE) of a damaged body, if $\boldsymbol{S}$ is the overall area of the element and $\tilde{\boldsymbol{S}}$ represents the effective resisting area which carries the internal force on the surface element and is given by $\tilde{\boldsymbol{S}} = \boldsymbol{S} - \boldsymbol{S_D}$ (see Figure 6.12), the damage variable, $\boldsymbol{D}$, may be expressed as,

$$\boldsymbol{D} = \frac{\boldsymbol{S} - \tilde{\boldsymbol{S}}}{\boldsymbol{S}}, \tag{6.17}$$

where $\boldsymbol{D} = \boldsymbol{0}$ corresponds to the initial undamaged state and $\boldsymbol{D} = \boldsymbol{1}$ represents the final fractured state with total loss of load carrying capacity.

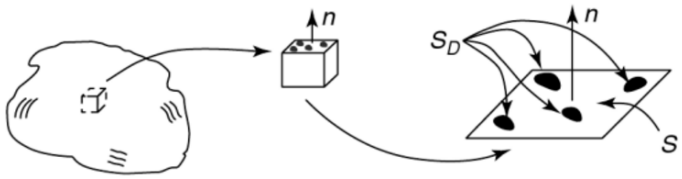

Figure 6.12: Damaged representative volume element [119].

Physically, the damage variable, $\boldsymbol{D}$, can be interpreted as the fraction of decrease in the effective area due to damage development.

The definition of damage, together with the effective resisting area, allowed Kachanov to define the concept of effective stress, $\tilde{\boldsymbol{\sigma}}$ [115, 116]. Considering that the area $\boldsymbol{S}$ is subjected to a tensile load, $\boldsymbol{F}$, in the damage state, the actual load carrying area is the effective area, $\tilde{\boldsymbol{S}}$. Thus, using equation (6.17), the effective area can be written as $\tilde{\boldsymbol{S}} = \boldsymbol{(1 - D)S}$ and the expression for the effective stress is obtained,

$$\tilde{\boldsymbol{\sigma}} = \frac{\boldsymbol{F}}{\boldsymbol{d\tilde{S}}} = \frac{\boldsymbol{\sigma}}{\boldsymbol{1 - D}}. \tag{6.18}$$

The effective stress defined by equation (6.18) can be understood as the magnifying effect of the stress induced by the external force due to the smaller load carrying area.

Following the Kachanov and Rabotnov pioneering work, essentially applied to the description of creep failure in metallic materials, further developments have emerged not only for creep rupture but also for describing the internal degradation of the materials in other areas of solid mechanics including other types of damage: elastic-brittle [120, 121], brittle [122, 123]

and fatigue [124–126].

Ductile Damage

In the framework of the phenomenological approach, based on the classical CDM theory, Lemaitre [127] proposed a purely phenomenological model for ductile isotropic damage. Lemaitres original development was based on the definition of an intrinsic damage variable represented by a scalar $\boldsymbol{D}$. By considering the strain equivalence hypotheses which states that *the deformation behaviour of the damaged material is represented by the constitutive laws of the virgin material with the true stress replaced by the effective stress*, Lemaitre postulated the following elastic constitutive law for a damaged material,

$$\tilde{\boldsymbol{\sigma}} = \boldsymbol{E}\boldsymbol{\varepsilon}, \tag{6.19}$$

or equivalently,

$$\boldsymbol{\sigma} = \tilde{\boldsymbol{E}}\boldsymbol{\varepsilon}, \tag{6.20}$$

where $\boldsymbol{E}$ and $\tilde{\boldsymbol{E}} = (\boldsymbol{1}-\boldsymbol{D})\boldsymbol{E}$ are the Young's moduli of the undamaged and damaged material respectively. Hence, the variation of the Young's modulus with the progression of damage can be used as a measure of the damage. The damage variable can thus be redefined as,

$$\boldsymbol{D} = \frac{\boldsymbol{E} - \tilde{\boldsymbol{E}}}{\boldsymbol{E}}. \tag{6.21}$$

The original theory proposed by Lemaitre was further developed [83, 114] and ageing effects were included later by Marquis and Lemaitre [128]. Lemaitre et al. [129] extended the original developments in order to account for the anisotropy of damage and the partial closure of microcracks under compressive stresses. As opposed to the strain equivalence principle, Cordebois and Sideroff [130], proposed another model for elastoplastic damage based on the energy equivalence principle. Lemaitre's strain equivalence hypothesis together with the stress equivalence hypothesis were used by Simo and Ju [131, 132] in the formulation of strain and stress-based damage models that were applied in the description of the brittle damage in concrete.

The thermodynamically consistent model proposed by Lemaitre [83, 114] has been developed over the last decades by several authors and alternative formulations have been suggested derived not only from the different equivalence hypothesis considered but also from the different forms of state coupling (inclusion of damage in the Helmoltz free energy) and from the different coupling of dissipations (coupling between damage and plasticity mechanisms).

6.3.2 Lemaitre's Ductile Damage Model

The original constitutive model proposed by Lemaitre for the description and modelling of the ductile damage phenomenon is presented in the following sections. The ductile damage model proposed by Lemaitre is based on CDM concepts and in the framework of thermodynamics of irreversible processes.

State Potential and State Relations

The starting point of the theory is the assumption of a state or thermodynamic potential, $\boldsymbol{\psi}$, from which the state laws are derived. The Helmoltz free energy is taken as the thermodynamic potential and can be defined as a function of the set $\{\boldsymbol{\varepsilon^e}, \boldsymbol{R}, \mathbf{X}, \boldsymbol{D}\}$ of state variables,

$$\boldsymbol{\psi} = \boldsymbol{\psi}(\boldsymbol{\varepsilon^e}, \boldsymbol{R}, \mathbf{X}, \boldsymbol{D}), \tag{6.22}$$

where $\boldsymbol{\varepsilon^e}$ is the elastic strain tensor and $\boldsymbol{R}$ and $\boldsymbol{D}$ are the scalar internal variables associated, respectively, with isotropic hardening and isotropic damage. The second order tensor $\boldsymbol{X}$ is the internal variable related to kinematic hardening. Assuming that damage only affects elasticity, the Helmoltz free energy can be expressed by an additive decomposition of two state potentials related to the elastic-damage and hardening contributions to the free energy. Thus, the specific free energy is given by the sum,

$$\boldsymbol{\psi} = \boldsymbol{\psi^{ed}}(\boldsymbol{\varepsilon^e}, \boldsymbol{D}) + \boldsymbol{\psi^P}(\boldsymbol{R}, \mathbf{X}), \tag{6.23}$$

where $\boldsymbol{\psi^{ed}}$ and $\boldsymbol{\psi^p}$ are, respectively the elastic-damage and plastic terms of the free energy.

In the present theory, the elastic-damage potential is defined as,

$$\bar{\boldsymbol{\rho}}\boldsymbol{\psi^{ed}}(\boldsymbol{\varepsilon^e}, \boldsymbol{D}) = \frac{\mathbf{1}}{\mathbf{2}}\boldsymbol{\varepsilon^e} : \tilde{\mathbf{D}}^{\boldsymbol{e}} : \boldsymbol{\varepsilon^e} = \frac{\mathbf{1}}{\mathbf{2}}\boldsymbol{\varepsilon^e} : (\mathbf{1} - \boldsymbol{D})\mathbf{D}^{\boldsymbol{e}} : \boldsymbol{\varepsilon^e}, \tag{6.24}$$

where $\mathbf{D}^{\boldsymbol{e}}$ is the standard isotropic elasticity tensor. For this particular potential the elasticity state law is given by,

$$\boldsymbol{\sigma} = \bar{\boldsymbol{\rho}}\frac{\boldsymbol{\partial\psi}}{\boldsymbol{\partial\varepsilon^e}} = (\mathbf{1} - \boldsymbol{D})\mathbf{D}^{\boldsymbol{e}} : \boldsymbol{\varepsilon^e}. \tag{6.25}$$

Equivalently, the above damaged elastic law can be written as,

$$\tilde{\boldsymbol{\sigma}} = \mathbf{D}^{\boldsymbol{e}} : \boldsymbol{\varepsilon^e}, \tag{6.26}$$

where $\tilde{\boldsymbol{\sigma}}$ is the effective stress tensor. The effective stress tensor is related to the Cauchy stress tensor by the expression,

$$\tilde{\boldsymbol{\sigma}} = \frac{\mathbf{1}}{(\mathbf{1}-\boldsymbol{D})}\boldsymbol{\sigma}. \tag{6.27}$$

The thermodynamical force associated with the damage internal variable, $\boldsymbol{Y}$, also derives from the elastic-damage state potential and can be expressed as,

$$\boldsymbol{Y} \equiv \bar{\rho}\frac{\partial \psi^{ed}}{\partial \boldsymbol{D}} = -\frac{\mathbf{1}}{\mathbf{2}}\varepsilon^{e} : \mathbf{D}^{e} : \varepsilon^{e}, \tag{6.28}$$

or, using the inverse of the elastic stress-strain law as,

$$\begin{aligned} \boldsymbol{Y} &= \frac{-\mathbf{1}}{\mathbf{2}(\mathbf{1}-\boldsymbol{D})^{\mathbf{2}}}\boldsymbol{\sigma} : [\mathbf{D}^{e}]^{-\mathbf{1}} : \boldsymbol{\sigma} \\ &= \frac{-\mathbf{1}}{\mathbf{2}\boldsymbol{E}(\mathbf{1}-\boldsymbol{D})^{\mathbf{2}}}\left[(\mathbf{1}+\boldsymbol{\upsilon})\boldsymbol{\sigma} : \boldsymbol{\sigma} - \boldsymbol{\upsilon}(\boldsymbol{tr}\boldsymbol{\sigma})^{\mathbf{2}}\right] \\ &= \frac{-\boldsymbol{q}^{\mathbf{2}}}{\mathbf{2}\boldsymbol{E}(\mathbf{1}-\boldsymbol{D})^{\mathbf{2}}}\left[\frac{\mathbf{2}}{\mathbf{3}}(\mathbf{1}+\boldsymbol{\upsilon}) + \mathbf{3}(\mathbf{1}-\mathbf{2}\boldsymbol{\upsilon})\left(\frac{\boldsymbol{p}}{\boldsymbol{q}}\right)^{\mathbf{2}}\right], \end{aligned} \tag{6.29}$$

where E and $\boldsymbol{\upsilon}$ are respectively, the Young's modulus and Poisson ratio, $\boldsymbol{p}$ is the hydrostatic stress and $\boldsymbol{q}$ is the von Mises effective stress. $-\boldsymbol{Y}$ is commonly known as the damage energy release rate and represents the variation of internal energy density due to damage growth at constant stress [133]. The product $-\boldsymbol{Y}\dot{\boldsymbol{D}}$ represents the power dissipated by the process of internal deterioration.

The plastic contribution $\boldsymbol{\psi^{p}(R, \mathbf{X})}$ to the free energy is considered as the sum of independent contributions of isotropic and kinematic hardenings. The plastic state potential is thus given by,

$$\bar{\rho}\psi^{p}(\boldsymbol{R}, \mathbf{X}) = \bar{\rho}\psi^{\boldsymbol{I}}(\boldsymbol{R}) + \frac{\boldsymbol{a}}{\mathbf{2}}\mathbf{X} : \mathbf{X}, \tag{6.30}$$

where $\boldsymbol{a}$ is a material constant associated with kinematic hardening, and the isotropic hardening contribution, $\boldsymbol{\Psi^{I}(R)}$, is an arbitrary scalar function of the internal isotropic variable $\boldsymbol{R}$. The thermodynamical forces associated with isotropic and kinematic hardening (the back

stress tensor), $\boldsymbol{\kappa}$ and $\boldsymbol{\beta}$ respectively, are thus defined as,

$$\boldsymbol{\kappa} \equiv \bar{\boldsymbol{\rho}} \frac{\partial \boldsymbol{\psi}^{\boldsymbol{p}}(\boldsymbol{R}, \mathbf{X})}{\partial \boldsymbol{R}} = \bar{\boldsymbol{\rho}} \frac{\partial \boldsymbol{\psi}^{\boldsymbol{I}}(\boldsymbol{R})}{\partial \boldsymbol{R}} = \boldsymbol{\kappa}(\boldsymbol{R}), \tag{6.31}$$

$$\boldsymbol{\beta} \equiv \bar{\boldsymbol{\rho}} \frac{\partial \boldsymbol{\psi}}{\partial \mathbf{X}} = \boldsymbol{a}\mathbf{X}. \tag{6.32}$$

Flow potential and evolution of internal variables

To establish the evolution laws for the dissipative state variables, a second potential, complementary to the state potential, written in terms of the thermodynamic forces is used. This dissipation potential is given by an additive decomposition of hardening, $\boldsymbol{\Psi}^{\boldsymbol{p}}$, and damage, $\boldsymbol{\Psi}^{\boldsymbol{d}}$, potentials as,

$$\boldsymbol{\Psi} = \boldsymbol{\Psi}^{\boldsymbol{p}}(\boldsymbol{\kappa}, \boldsymbol{\beta}) + \boldsymbol{\Psi}^{\boldsymbol{d}}(-\boldsymbol{Y}) = \boldsymbol{\Phi} + \frac{\boldsymbol{b}}{\boldsymbol{2a}} \boldsymbol{\beta} : \boldsymbol{\beta} + \frac{\boldsymbol{r}}{(\mathbf{1} - \boldsymbol{D})(\boldsymbol{s} + \mathbf{1})} \left(\frac{-\boldsymbol{Y}}{\boldsymbol{r}} \right)^{\boldsymbol{s}+\mathbf{1}}, \tag{6.33}$$

where $\boldsymbol{a}$, $\boldsymbol{b}$, $\boldsymbol{r}$ and $\boldsymbol{s}$ are material constants and $\boldsymbol{\Phi}$ is the yield function. In the case of the von Mises yield function, $\boldsymbol{\Phi}$ is given by the following expression,

$$\boldsymbol{\Phi}(\boldsymbol{\sigma}, \boldsymbol{\kappa}, \boldsymbol{\beta}, \boldsymbol{D}) = \frac{\sqrt{\mathbf{3} \boldsymbol{J}_{\mathbf{2}}(\mathbf{S} - \boldsymbol{\beta})}}{\mathbf{1} - \boldsymbol{D}} - \boldsymbol{\sigma}_{\boldsymbol{y}_{\mathbf{0}}} - \boldsymbol{\kappa}, \tag{6.34}$$

where $\boldsymbol{\sigma}_{\boldsymbol{y}_{\mathbf{0}}}$ is the uniaxial yield stress of the undamaged material. According to the hypothesis of generalised normalty, the plastic flow is given by,

$$\dot{\boldsymbol{\varepsilon}}^{\boldsymbol{p}} = \dot{\boldsymbol{\gamma}} \frac{\partial \boldsymbol{\Psi}}{\partial \boldsymbol{\sigma}} = \dot{\boldsymbol{\gamma}} \mathbf{N}, \tag{6.35}$$

where $\mathbf{N}$ is the flow vector that can be expressed, for the von Mises case, as,

$$\mathbf{N} = \sqrt{\frac{\mathbf{3}}{\mathbf{2}}} \frac{(\mathbf{S} - \boldsymbol{\beta})}{(\mathbf{1} - \boldsymbol{D}) \parallel \mathbf{S} - \boldsymbol{\beta} \parallel}, \tag{6.36}$$

where $\mathbf{S}$ represents the deviatoric stress tensor. The evolution equations for $\boldsymbol{R}$ and $\boldsymbol{\beta}$ are given by,

$$\dot{\boldsymbol{R}} = \dot{\boldsymbol{\gamma}}, \tag{6.37}$$

$$\dot{\boldsymbol{\beta}} = \dot{\boldsymbol{\gamma}} \left(\boldsymbol{a}\mathbf{N} - \boldsymbol{b}\boldsymbol{\beta} \right), \tag{6.38}$$

and the damage evolution law is given by

$$\dot{\boldsymbol{D}} = \dot{\gamma}\frac{\mathbf{1}}{\mathbf{1}-\boldsymbol{D}}\left(\frac{-\boldsymbol{Y}}{\boldsymbol{r}}\right)^{\boldsymbol{s}}, \tag{6.39}$$

where $\dot{\boldsymbol{\gamma}}$ is the plastic parameter that must satisfy the standard complementary law of rate independent plasticity,

$$\dot{\gamma} \geq \mathbf{0}; \quad \boldsymbol{\Phi} \leq \mathbf{0}; \quad \dot{\gamma}\boldsymbol{\Phi} = \mathbf{0}, \tag{6.40}$$

The equivalent plastic strain rate, $\dot{\bar{\boldsymbol{\varepsilon}}}^{\boldsymbol{p}}$, for the von Mises criterion can be obtained, assuming the equivalence of plastic work rate,

$$\dot{\boldsymbol{W}}^{\boldsymbol{p}} = \boldsymbol{\sigma} : \dot{\boldsymbol{\varepsilon}}^{\boldsymbol{p}} = \bar{\boldsymbol{\sigma}}\dot{\bar{\boldsymbol{\varepsilon}}}^{\boldsymbol{p}}, \tag{6.41}$$

using equation (6.35) and the definition of the equivalent stress for the von Mises criterion,

$$\bar{\boldsymbol{\sigma}} = \sqrt{\frac{\mathbf{3}}{\mathbf{2}}}\left(\mathbf{s} : \mathbf{s}\right)^{\frac{\mathbf{1}}{\mathbf{2}}}. \tag{6.42}$$

The equivalent plastic strain rate is calculated from the equivalence in Equation (6.41) as,

$$\dot{\bar{\boldsymbol{\varepsilon}}}^{\boldsymbol{p}} = \frac{\dot{\boldsymbol{\gamma}}}{\mathbf{1}-\boldsymbol{D}}. \tag{6.43}$$

Using Equation (7.44) and (6.43), the expression for the damage evolution can be rewritten as,

$$\dot{\boldsymbol{D}} = \dot{\bar{\boldsymbol{\varepsilon}}}^{\boldsymbol{p}}\left(\frac{-\boldsymbol{Y}}{\boldsymbol{r}}\right)^{\boldsymbol{s}}. \tag{6.44}$$

The constitutive equations of Lemaitre's ductile damage model are summarized in Box 6.1.

Box 6.1: Lemaitre's ductile damage model.

1. Elastoplastic split of the strain tensor

$$\boldsymbol{\varepsilon} = \boldsymbol{\varepsilon}^{\boldsymbol{e}} + \boldsymbol{\varepsilon}^{\boldsymbol{p}}$$

2. Coupled elastic-damage law

$$\boldsymbol{\sigma} = (\mathbf{1} - \boldsymbol{D})\mathbf{D}^{\mathbf{e}} : \boldsymbol{\varepsilon}^{\boldsymbol{e}}$$

3. Yield function (von Mises)

$$\boldsymbol{\Phi} = \frac{\sqrt{\mathbf{3}\boldsymbol{J}_{\mathbf{2}}(\mathbf{S} - \boldsymbol{\beta})}}{\mathbf{1} - \boldsymbol{D}} - \boldsymbol{\sigma}_{\boldsymbol{y}}(\boldsymbol{R})$$

4. Plastic flow and evolution equations for R, $\boldsymbol{\beta}$ and D

$$\begin{aligned}
\dot{\boldsymbol{\varepsilon}}^{\boldsymbol{p}} &= \dot{\boldsymbol{\gamma}}\mathbf{N} \\
\dot{\boldsymbol{R}} &= \dot{\boldsymbol{\gamma}} \\
\dot{\boldsymbol{\beta}} &= \dot{\boldsymbol{\gamma}}\,(\boldsymbol{a}\mathbf{N} - \boldsymbol{b}\boldsymbol{\beta}) \\
\dot{\boldsymbol{D}} &= \dot{\boldsymbol{\gamma}}\frac{\mathbf{1}}{\mathbf{1} - \boldsymbol{D}}\left(\frac{-\boldsymbol{Y}}{\boldsymbol{r}}\right)^{\boldsymbol{s}}
\end{aligned}$$

5. Loading/unloading criterion

$$\boldsymbol{\Phi} \leq \mathbf{0}, \quad \dot{\boldsymbol{\gamma}} \geq \mathbf{0}, \quad \dot{\boldsymbol{\gamma}}\boldsymbol{\Phi} = \mathbf{0}$$

Damage Threshold

At low values of accumulated plastic strain, a limited apparent deterioration is observed and its effects on the physical properties can be neglected. Hence, it can be assumed that damage growth starts only at a critical value of the accumulated plastic strain denoted by $\bar{\varepsilon}^{p}_{D}$. This damage threshold corresponds to the value below which no damage occurs and it is generally considered a material parameter. The damage threshold can be included in the model using the Heaviside step function, $\hat{H}$, and the damage evolution law is redefined as,

$$\dot{D} = \dot{\gamma} \frac{\hat{H}\left(\bar{\varepsilon}^{p} - \bar{\varepsilon}^{p}_{D}\right)}{1 - D} \left(\frac{-Y}{r}\right)^{s}, \tag{6.45}$$

where the Heaviside step function is defined as,

$$\hat{H}(a) = \begin{cases} a & \text{if } a \geq 0 \\ 0 & \text{if } a < 0 \end{cases} \tag{6.46}$$

6.3.3 Lemaitre's Simplified Damage Model

A simplified version of the Lemaitre's original damage model can be achieved by disregarding the effects of kinematic hardening. This simplified version benefits from a simple and efficient numerical implementation and can be used whenever the effects of kinematic hardening are not relevant, i.e., in any processes where reverse plastic loading does not occur or has little influence on the overall evolution of damage and plastic flow.

The constitutive equations of the simplified Lemaitre damage model are obtained from those of the original model by rewriting the equations without the terms related to kinematic hardening, i.e., by setting $\beta = 0$ and $a = b = 0$. The constitutive equations for the simplified Lemaitre model, considering the von Mises yield criterion and isotropic hardening only, are given in Box 6.2.

Box 6.2: Simplified Lemaitre ductile damage model with isotropic hardening.

1. Elastoplastic split of the strain tensor

$$\varepsilon = \varepsilon^e + \varepsilon^p$$

2. Coupled elastic-damage law

$$\boldsymbol{\sigma} = (\mathbf{1} - \boldsymbol{D})\mathbf{D^e} : \varepsilon^e$$

3. Yield function (von Mises)

$$\boldsymbol{\Phi} = \frac{\sqrt{\mathbf{3}\boldsymbol{J_2}(\mathbf{s})}}{\mathbf{1} - \boldsymbol{D}} - \boldsymbol{\sigma_y}$$

4. Plastic flow and evolution equations for R and D

$$\begin{aligned} \dot{\varepsilon}^{\boldsymbol{p}} &= \dot{\boldsymbol{\gamma}}\mathbf{N} \\ \dot{\boldsymbol{R}} &= \dot{\boldsymbol{\gamma}} \\ \dot{\boldsymbol{D}} &= \dot{\boldsymbol{\gamma}}\frac{\mathbf{1}}{\mathbf{1} - \boldsymbol{D}}\left(\frac{-\boldsymbol{Y}}{\boldsymbol{r}}\right)^{\boldsymbol{s}} \end{aligned}$$

5. Loading/unloading criterion

$$\boldsymbol{\Phi} \leq \mathbf{0}, \quad \dot{\boldsymbol{\gamma}} \geq \mathbf{0}, \quad \dot{\boldsymbol{\gamma}}\boldsymbol{\Phi} = \mathbf{0}$$

6.3.4 Coupling with CPB06 yield criterion and numerical implementation

Titanium, its alloys and other hcp materials are known to display, at room temperature, plastic anisotropy and a strong tension-compression asymmetry. Consequently, the modelling of their mechanical behaviour requires adequate constitutive models able to capture the main features of the plastic deformation of these materials. It is generally agreed that classical plasticity models such as von Mises or Hill cannot capture the specificities of the plastic deformation of titanium and its alloys. Moreover, the modelling of the room-temperature damage and failure of titanium materials is currently done using damage models whose core hypotheses is that the plastic behaviour is governed by the von Mises criterion which is a criterion critically inadequate for hcp materials.

In this work, a fully coupled continuum damage model using the more adequate CPB06 criterion developed by Cazacu et al. [52] is proposed. The CPB06 yield criterion has shown to be adequate in capturing not only the plastic anisotropy but also the strength differential effect. Thus, the CPB06 yield criterion is used in replacement of the von Mises yield function in the simplified Lemaitre's damage formulation. The expression of the yield function in this approach is given by,

$$\boldsymbol{\Phi(\sigma, \bar{\varepsilon}^p, D) = \frac{\bar{\sigma}}{1 - D} - \sigma_y(\bar{\varepsilon}^p)}, \tag{6.47}$$

where $\bar{\boldsymbol{\sigma}}$ is the equivalent yield stress of the Cazacu's model as presented previously in Chapter 3.

The Lemaitre's continuum damage formulation coupled with the Cazacu's yield criterion was implemented numerically by means of a fully implicit elastic predictor/return mapping scheme as is presented in the subsequent section.

Numerical Implementation

The algorithm for the numerical integration of the simplified Lemaitre constitutive model starts with the definition of the elastic trial state. Within a pseudo-time interval $[\boldsymbol{t_n}, \boldsymbol{t_{n+1}}]$, the constitutive variables $\boldsymbol{\varepsilon^p_n}$, $\boldsymbol{\sigma_n}$, $\boldsymbol{\bar{\varepsilon}^p_n}$ and $\boldsymbol{D_n}$ at time $\boldsymbol{t_n}$ are known and the for the given incremental strain, $\boldsymbol{\Delta\varepsilon}$, the updated values $\boldsymbol{\varepsilon^p_{n+1}}$, $\boldsymbol{\sigma_{n+1}}$, $\boldsymbol{\bar{\varepsilon}^p_{n+1}}$ and $\boldsymbol{D_{n+1}}$ at $\boldsymbol{t_{n+1}}$ need to be found. In the typical finite element framework the material points correspond to the Gauss integration points.

The first step consists in the determination of the elastic trial state. In the elastic trial state, the solution of the material problem is assumed to be purely elastic, hence neither damage nor hardening takes place. Given the total strain increment, $\boldsymbol{\Delta\varepsilon}$, the elastic trial strain is given by,

$$\boldsymbol{\varepsilon^e_{n+1}{}^{trial} = \varepsilon^e_n + \Delta\varepsilon}, \tag{6.48}$$

the elastic trial stress is given by,

$$\boldsymbol{\sigma}_{n+1}^{trial} = (\mathbf{1} - \boldsymbol{D}_n)\mathbf{D}^e : \varepsilon_{n+1}^{e\ trial}, \tag{6.49}$$

and $\boldsymbol{D_{n+1}} = \boldsymbol{D_n}$ and $\bar{\varepsilon}_{p_{n+1}} = \bar{\varepsilon}_{p_n}$. Given the trial stress state, the equivalent stress for the CPB06 yield criterion can be computed and the plastic admissibility check is then performed. In this step the yield function value is evaluated to check whether the pseudoincrement is elastic or plastic. If the yield function,

$$\boldsymbol{\Phi}^{trial} = \frac{\bar{\boldsymbol{\sigma}}^{trial}}{\mathbf{1} - \boldsymbol{D}_n} - \boldsymbol{\sigma}_y(\bar{\varepsilon}_n) \leq \mathbf{0}, \tag{6.50}$$

the trial stress is accepted as the current state, $(\cdot)_{n+1} = (\cdot)_{n+1}$. Otherwise the return mapping algorithm is used. Following the standard procedures of elastic predictor/return mapping schemes, Lemaitre's constitutive model can be written in its (pseudo) time-discretized version by the following system of equations,

$$\left\{ \begin{array}{c} \boldsymbol{\sigma}_{n+1} - (\mathbf{1} - \boldsymbol{D}_{n+1})\mathbf{D}^e : (\varepsilon_{n+1}^{e\ trial} - \boldsymbol{\Delta\gamma}\mathbf{N}_{n+1}) \\ \boldsymbol{D}_{n+1} - \boldsymbol{D}_n - \frac{1}{1-\boldsymbol{D}_{n+1}} \left(\frac{-\boldsymbol{Y}_{n+1}}{r}\right)^{\boldsymbol{s}} \boldsymbol{\Delta\gamma} \\ \frac{\bar{\boldsymbol{\sigma}}}{1-\boldsymbol{D}_{n+1}} - \boldsymbol{\sigma}_y(\boldsymbol{R}_n + \boldsymbol{\Delta\gamma}) \end{array} \right\} = \left\{ \begin{array}{c} \mathbf{0} \\ \mathbf{0} \\ \mathbf{0} \end{array} \right\} \tag{6.51}$$

where $\boldsymbol{\sigma_{n+1}}$, $\boldsymbol{R_{n+1}}$, $\boldsymbol{\Delta\gamma}$ and $\boldsymbol{D_{n+1}}$ are the unknowns of the incremental initial boundary value constitutive problem. The last equation of the system is the consistency condition.

This highly non linear system of equations can be linearized and solved using the Newton-Raphson method. Two methods can be used to obtain the solution of the problem by considering either a strong coupling in which all the equations are solved simultaneously to obtain the unknowns or alternatively a weak coupling can be used. A weak coupling consists in solving the problem disregarding the damage evolution equation and considering that $\boldsymbol{D_{n+1}} = \boldsymbol{D_n}$ in order to obtain $\boldsymbol{\sigma_{n+1}}$, $\bar{\varepsilon}_{p_{n+1}}$ and $\boldsymbol{\Delta\gamma}$. Thus, by performing a Taylor expansion of the yield function about the current state the incremental plastic multiplier can be obtained,

$$\boldsymbol{\delta\Delta\gamma}_{n+1}^{k+1} = \frac{\boldsymbol{f}(\boldsymbol{\sigma}_{n+1}^{k}, \bar{\boldsymbol{\varepsilon}}_{n+1}^{k})}{\mathbf{N}_{n+1}^{k} : \mathbf{D}^e : \mathbf{N}_{n+1}^{k}(\mathbf{1} - \boldsymbol{D}_{n+1}^{k}) - \left(\frac{\partial \boldsymbol{f}}{\partial \bar{\varepsilon}}\right)_{\boldsymbol{n+1)}}^{\boldsymbol{k}}}, \tag{6.52}$$

where $\boldsymbol{k}$ and $\boldsymbol{k+1}$ represent two consecutive iterations and $\mathbf{N}$ is defined as,

$$\boldsymbol{N} = \frac{\partial \boldsymbol{\Phi}}{\partial \boldsymbol{\sigma}} = \frac{\mathbf{1}}{\mathbf{1} - \boldsymbol{D}} \left(\frac{\partial \bar{\boldsymbol{\sigma}}}{\partial \boldsymbol{\sigma}}\right). \tag{6.53}$$

Then the damage evolution equation is solved to compute updated damage value, $\boldsymbol{D_{n+1}}$.

Although more accurate results are expected by using a strong coupling, the weak coupling is in this case easier to implement and computationally more advantageous. The algorithm for the implemented stress update procedure using Lemaitre's simplified model is given in Box 6.3.

Box 6.3: Stress update algorithm for coupled simplified Lemaitre ductile model.

1. Elastic predictor. Given $\boldsymbol{\Delta\varepsilon}$ evaluate the elastic trial state at $\boldsymbol{t_n}$

$$\boldsymbol{\sigma}_{n+1}^{trial} = (1 - \boldsymbol{D}_n)\mathbf{D}^e : \boldsymbol{\varepsilon}_{n+1}^{e\,trial}$$
$$\bar{\boldsymbol{\varepsilon}}_{p,n+1} = \bar{\boldsymbol{\varepsilon}}_{p,n}$$

2. Check plastic consistency

IF $\quad \boldsymbol{\Phi}^{trial} = \dfrac{\bar{\boldsymbol{\sigma}}}{1 - \boldsymbol{D}_n} - \boldsymbol{\sigma}_y(\bar{\boldsymbol{\varepsilon}}_{p,n}) \leq \mathbf{0}$ THEN

Set $\quad (\cdot)_{n+1} = (\cdot)_{n+1}^{trial}$ and EXIT

ELSE goto **(3)**

3. Assume $\boldsymbol{D}_{n+1} \approx \boldsymbol{D}_n$ and solve the system

$$\left\{ \begin{array}{c} \boldsymbol{\sigma}_{n+1} - (1 - \boldsymbol{D}_n)\mathbf{D}^e : (\boldsymbol{\varepsilon}_{n+1}^{etrial} - \boldsymbol{\Delta\gamma}\mathbf{N}_{n+1}) \\ \frac{\bar{\sigma}}{(1-D_n)} - \boldsymbol{\sigma}_y(\bar{\boldsymbol{\varepsilon}}_{p,n+1}) \end{array} \right\} = \left\{ \begin{array}{c} \mathbf{0} \\ \mathbf{0} \end{array} \right\}$$

for $\boldsymbol{\Delta\gamma}$ and $\boldsymbol{\sigma}_{n+1}$ using the Newton-Raphson method.

4. Compute new damage. Solve the equation

$$\boldsymbol{D}_{n+1} = \boldsymbol{D}_n + \frac{\boldsymbol{\Delta\gamma}}{1 - \boldsymbol{D}_{n+1}} \left(\frac{-\boldsymbol{Y}}{\boldsymbol{r}} \right)^{\boldsymbol{s}}$$

for $\boldsymbol{D}_{n+1}$ using the Newton-Raphson method.

5. EXIT

6.3.5 Validation and Numerical Results

In order to validate the proposed coupled ductile damage model, finite element simulations were conducted. A single element test was performed as well as two numerical examples of a smooth and a notched axisymmetric specimen subjected to monotonic tensile loading. The geometries of the specimens are based on the experimental work performed by Giglio et al. [84] and were given in Figure 6.2. The respective boundary conditions and meshes were previously illustrated in Figure 6.4.

Single Element Test

The single element test was performed using an eight node element with one integration point (C3D8R) with dimensions 1mm×1mm×1mm. The nodes on one face of the element were restrained while the nodes on the opposite face were given a constant velocity in the tensile direction. By performing a simple single element test an analysis of the implemented coupled ductile damage model can be performed taking into account the variation of the damage parameters to assess its influence on the materials mechanical behaviour. The damage evolution law, given by Equation (6.39), is directly influenced by two damage material parameters, the denominator $\boldsymbol{r}$ and the exponent $\boldsymbol{s}$. The influence of each of these damage parameters on the stress strain curves was assessed by varying each one independently. The stress-strain curves obtained for different values of the parameter $\boldsymbol{r}$ and $\boldsymbol{s}$ are shown in Figure 6.13.

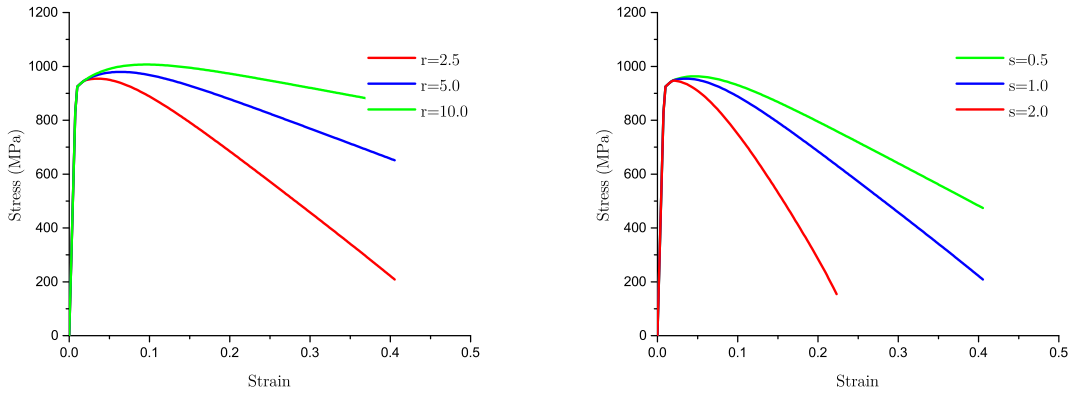

(a) (b)

Figure 6.13: Influence of damage parameters: (a) Denominator parameter $\boldsymbol{r}$. (b) Exponent parameter, $\boldsymbol{s}$.

Regarding the influence of the damage parameter, $\boldsymbol{r}$, it is possible to observe from the stress-strain curves from Figure 6.13a that with increasing values of $\boldsymbol{r}$, the damage rate decreases which translates into a lower degradation of the mechanical properties of the material. In the case of the exponent damage parameter, $\boldsymbol{s}$, it is important to note that if the ratio $\boldsymbol{Y/r}$ (see damage evolution equation (7.44)) is lower than the unity, the damage evolution decreases with increasing value of $\boldsymbol{s}$. On the other hand when the ratio $\boldsymbol{Y/r}$ takes values

greater than unity, damage grows exponentially with increasing values of s (for values of s greater than 1).

The stress-strain curve obtained from the single element test was also compared with the experimental uniaxial loading-unloading test results obtained by Allaverdizadeh et al. [82] used for the determination of the variation of the Young modulus. Loading-unloading tests are commonly used to determine the reduction of the modulus of elasticity during uniaxial test which allows the determination of the damage variable. The experimental uniaxial tensile stress-strain curve obtained from loading-unloading cycles at low strain rate, together with the predicted stress-strain curves obtained from the implemented fully coupled ductile damage model, are shown in Figure 6.14. The hypothesis of absence of damage for validation purposes was also considered. To obtain the stress-strain curves without damage evolution a very high value for the damage threshold was used. From Figure 6.14 it can be seen the capability of

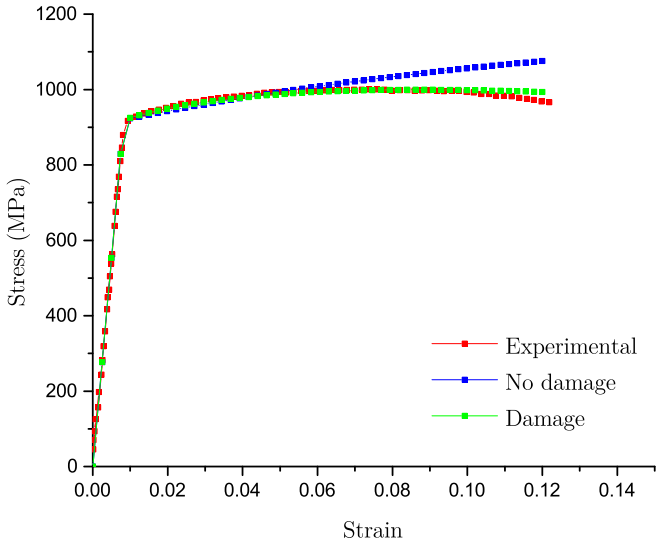

Figure 6.14: Experimental and predicted stress-strain curves.

the implemented model to capture the effect of damage evolution in the degradation of the mechanical properties.

The convergency of the implemented algorithm was also assessed. In Table 6.3, the typical convergence rate obtained is depicted for the stress and damage update. As can be seen, quadratic convergence rates are present in both iterative schemes. Thus, considering a weak coupling between stress and damage update algorithms provides an efficient numerical approach for complex constitutive models as is the case for the hcp material.

Table 6.3: Typical convergence of the Newton-Raphson algorithm on the stress and damage update procedures.

Iteration	Residual	
	Stress update	Damage update
1	0.1027E+01	0.1001E+01
2	0.9990E-02	0.6516E-03
3	0.6809E-06	0.3061E-09

Smooth and Notched tensile test

The fully coupled continuum damage model implemented was used to simulate damage onset and evolution on two axisymmetric specimens (a smooth and a notched) subjected to monotonic axial tensile loading. With these examples the predictive capabilities of the proposed model were assessed. The geometries of the specimens, boundary conditions and meshes coincide with the ones used for the uncoupled analysis and were previously illustrated in Figures 6.2 and 6.4. The loading consists of a vertical displacement applied on the top nodes of the mesh. The longitudinal direction of the material was oriented along the loading direction. The adopted damage parameters for the Ti6Al4V alloy were experimentally identified and reported by Allahverdizadeh et al. [82] and are given in Table 6.4.

The evolution of the damage variable field for the smooth and notched specimens is illustrated in the contour plots shown in Figure 6.15 and Figure 6.16 respectively. Regarding the notched specimen it can be seen that damage initiates at the root of the notch and as the specimen continues to be stretched, the maximum damage area moves towards the centre where it reaches its critical value. It indicates that fracture initiation is expected to start at this point. In the smooth specimen, as the specimen is stretched, the maximum damage localizes at the centre until it reaches its critical value. The predicted results for both the notched and the smooth specimen are in accordance with the experimental evidence.

It is important to note the differences observed between the stress distributions obtained with the uncoupled and coupled analysis. The stress distributions obtained from the uncoupled approach are unaffected by damage with the maximum stresses occurring at the centre region of the notch as can be seen on Figure 6.17. On the other hand, for the implemented coupled model, the redistribution of stresses due to damage is captured and lower stresses are obtained at the centre of the notch area. The use of coupled formulations is therefore of crucial importance in failure simulations.

Table 6.4: Material damage parameters.

r	s	$\boldsymbol{D_{cr}}$
2.52 MPa	1.0	0.35

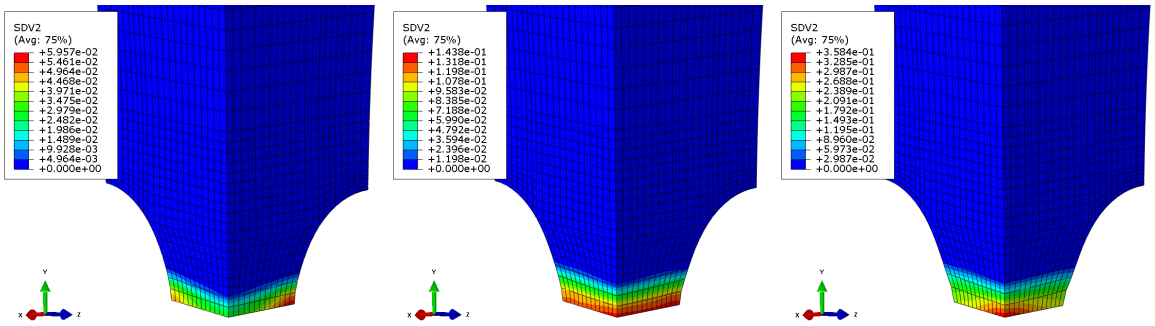

(a) u=0.15mm (b) u=0.2mm (c) u=0.24mm

Figure 6.15: Damage contour plots for the axisymmetric notched specimen.

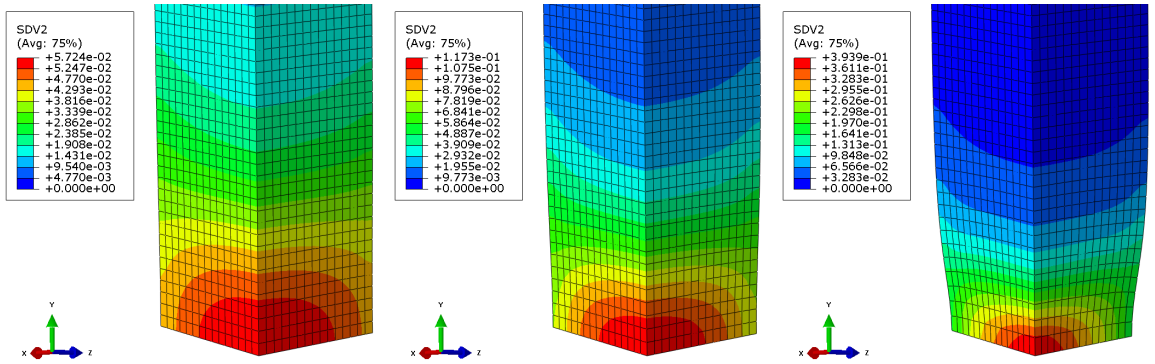

(a) u=1.5mm (b) u=1.9mm (c) u=2.4mm

Figure 6.16: Damage contour plots for the axisymmetric smooth specimen.

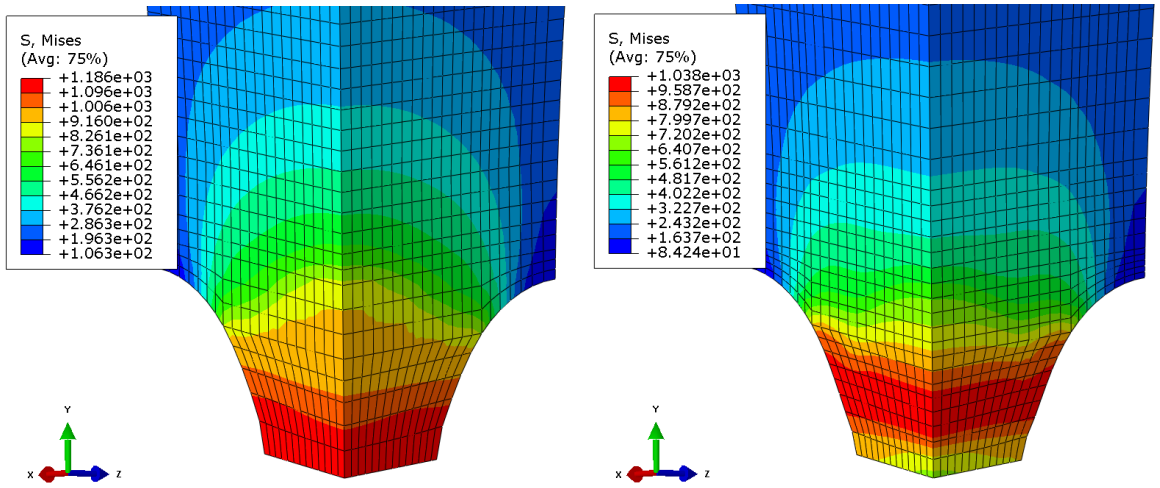

(a) Uncoupled analysis. (b) Coupled analysis.

Figure 6.17: Equivalent stress distributions for the notched axisymmetric tensile specimen.

Mesh dependency

A large number of ductile damage continuum models, like Lemaitre's model, rely on the assumption that the material behaviour is independent of the influence of the surrounding material, i.e., they are local continuum theories. Moreover, it is assumed that the material is continuous at any scale and thus neglects the influence of the microstructure on the global behaviour. By this, the introduction of damage in large deformation problems experiencing softening results in a pathological effect of discretization dependency. It causes plastic strain and other dissipative variables, like damage, to concentrate into a single element or a layer of elements as the mesh refinement increases.

In order to demonstrate this mesh dependency, the mesh of the smooth specimen was further refined and the damage contour at the critical region was obtained. Upon refinement, the elements on the more refined mesh had approximately half the size of the elements on the previous mesh. The damage contours, at 2.4mm displacement, for the two levels of mesh refinement are depicted in Figure 6.18.

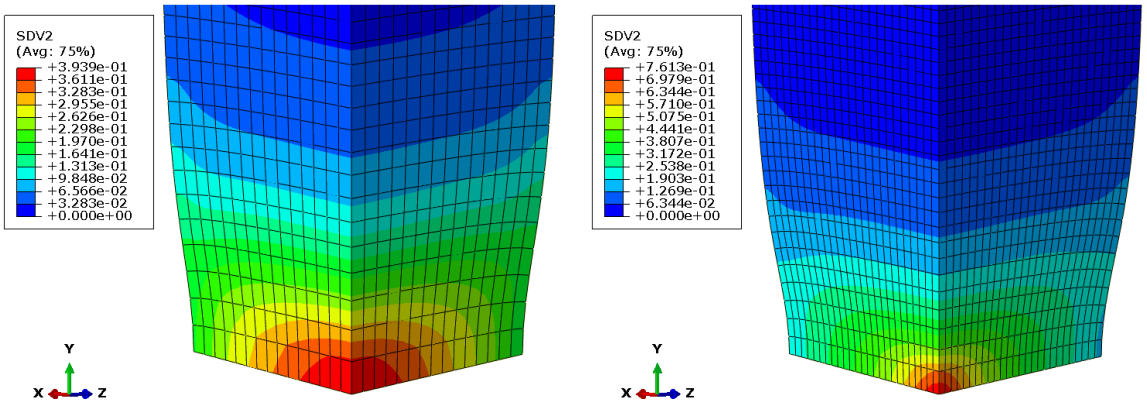

(a) (b)

Figure 6.18: Damage contour plot for two levels of mesh refinement: (a) Mesh 1 and (b) Mesh 2

As can be seen from Figure 6.18, damage distribution tends to concentrate into the central area in a single element upon mesh refinement. Moreover, for the same displacement, on the more refined mesh, damage attained a much higher value. In other words, critical damage is attained at lower displacements.

In order to attenuate the pathological mesh dependency, non-local theories have emerged has an alternative framework that incorporates intrinsic material length parameters in the material constitutive model using spatially weighted averages in the evolution equations of the respective internal state variables describing plastic and damage growth [119]. Two main approaches can be considered: integral and gradient formulations. In integral-type formulations, the non-local damage variable, $\bar{\boldsymbol{D}}$, is defined by means of the spatially weighted averaging

integral as,

$$\boldsymbol{D}(\bar{\boldsymbol{x}}) = \int_{\boldsymbol{V}} \boldsymbol{\beta}(\boldsymbol{x}, \boldsymbol{\xi}) \boldsymbol{D}(\boldsymbol{\xi}) d\boldsymbol{V}(\boldsymbol{\xi}), \tag{6.54}$$

where $\boldsymbol{D}$ is the local damage variable and $\boldsymbol{\beta}(\boldsymbol{x}, \boldsymbol{\xi})$ is a weighted averaging operator.

The gradient-enhanced models have been developed as an alternative to the classical non-local theory and incorporate the gradients of the variables into originally local models. Further details on these models can be found for example in [134–136]. Although non-local approaches were not considered in the context of this study, they are mentioned here as a suggestion for future work.

The tension-compression asymmetry on damage evolution

The strength differential (SD) effect is characterized by a variation in the yield stresses in tension versus compression. Particularly, in hcp materials a strong and evolving tension-compression asymmetry is found, the strength in uniaxial compression is higher than the strength in uniaxial tension (see [33, 34, 73]). This tension-compression asymmetry at a macroscopic level is a consequence of deformation mechanisms like twinning and slip at the single crystal level. In this section, the numerical assessment of the tension-compression asymmetry of the plastic flow on the prediction of the location of the zone corresponding to maximum damage is performed. Simulations considering different tensile-compressive strength ratios were performed on axisymmetric notched specimens.

The strength differential material parameter, for the CPB06 model (see Chapter 3 equation (3.16)), is given by $\boldsymbol{k}$. According to this criterion, the SD parameter is given by,

$$\boldsymbol{k} = \frac{\mathbf{1} - \left(\frac{\boldsymbol{\sigma_T}}{\boldsymbol{\sigma_C}}\right)}{\mathbf{1} + \boldsymbol{h}\left(\frac{\boldsymbol{\sigma_T}}{\boldsymbol{\sigma_C}}\right)}, \tag{6.55}$$

where $\boldsymbol{\sigma_T} \backslash \boldsymbol{\sigma_C}$ is the ratio of tensile to compressive uniaxial yield stress and,

$$\boldsymbol{h}\left(\frac{\boldsymbol{\sigma_T}}{\boldsymbol{\sigma_C}}\right) = \left[\frac{\mathbf{2}^{\boldsymbol{a}} - \mathbf{2}\left(\frac{\boldsymbol{\sigma_T}}{\boldsymbol{\sigma_C}}\right)^{\boldsymbol{a}}}{\left(\mathbf{2}\frac{\boldsymbol{\sigma_T}}{\boldsymbol{\sigma_C}}\right)^{\boldsymbol{a}} - \mathbf{2}}\right]^{\frac{\mathbf{1}}{\boldsymbol{a}}}, \tag{6.56}$$

with $\boldsymbol{a} = \mathbf{2}$.

From Equation (6.55) it follows that for the material parameter $\boldsymbol{k}$ to be real, $\mathbf{1} \backslash \sqrt{\mathbf{2}} \leq \boldsymbol{\sigma_T} \backslash \boldsymbol{\sigma_C} \leq \sqrt{\mathbf{2}}$. Thus, three different tension-compression ratios were evaluated: for tensile yield strength larger than compressive yield strength, $\boldsymbol{\sigma_T} \backslash \boldsymbol{\sigma_C} = \mathbf{1.41}$ and $\boldsymbol{k} = \mathbf{0.9}$, for tensile yield strength lower than compressive yield strength, $\boldsymbol{\sigma_T} \backslash \boldsymbol{\sigma_C} = \mathbf{0.71}$ and $\boldsymbol{k} = \mathbf{-0.9}$

and without tension-compression asymmetry, $\boldsymbol{\sigma_T} \backslash \boldsymbol{\sigma_C} = \mathbf{1}$ and $\boldsymbol{k} = \mathbf{0}$. The damage initiation and evolution were evaluated and are depicted in Figure 6.19.

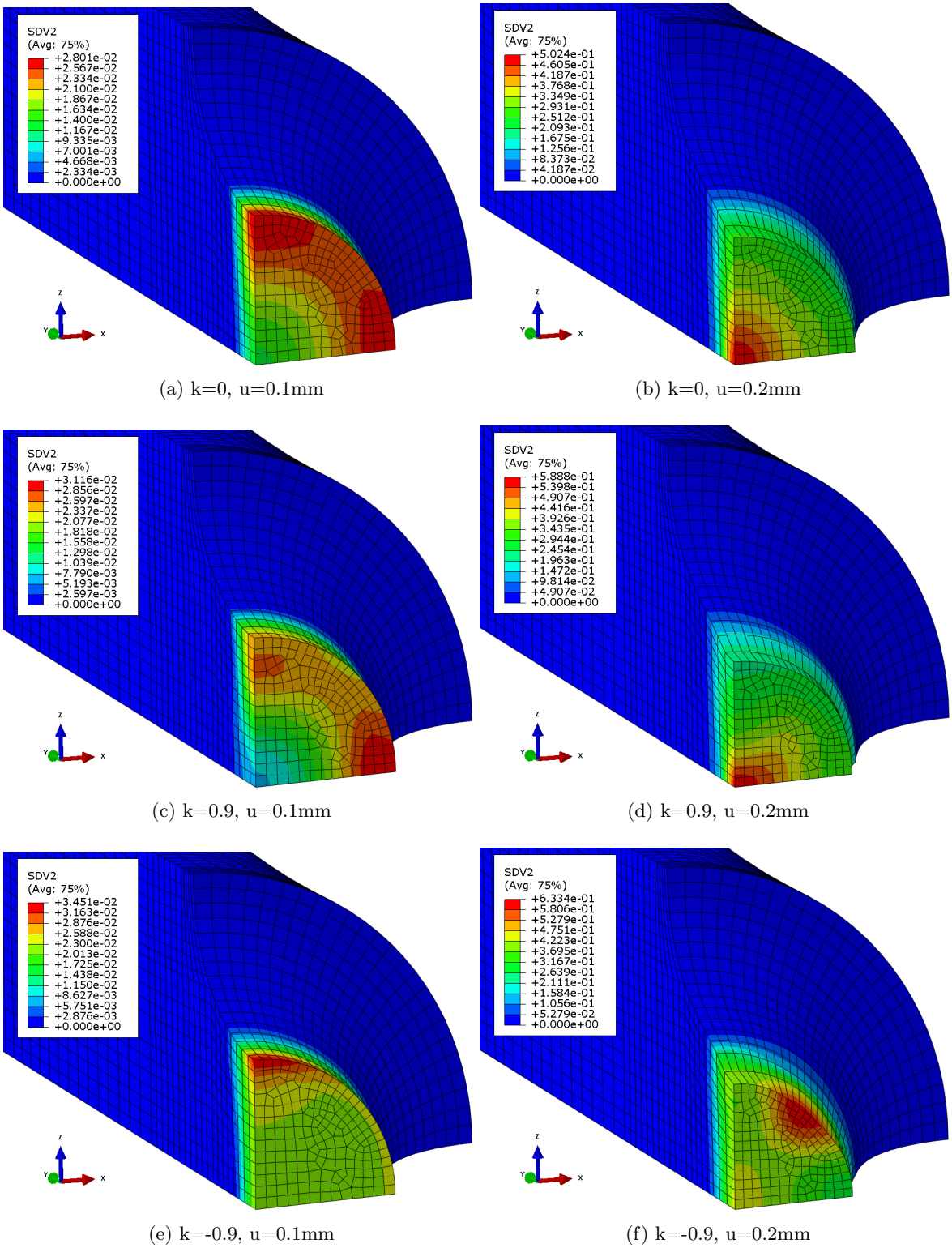

(a) k=0, u=0.1mm

(b) k=0, u=0.2mm

(c) k=0.9, u=0.1mm

(d) k=0.9, u=0.2mm

(e) k=-0.9, u=0.1mm

(f) k=-0.9, u=0.2mm

Figure 6.19: Finite element predictions for the initiation and evolution of damage for different SD material parameters.

The finite element predictions of the damage distribution for different values of the strength differential parameter exhibit significant differences both in damage initiation as well as on damage evolution. For $\boldsymbol{k = 0}$, i.e., if the material has no tension-compression asymmetry in its plastic response, the model predicts the initiation of damage at the outer surface of the notch and further grow towards the centre of the specimen. However, if strong tension-compression asymmetry is present, the initiation of damage is predicted at the surface of the notch along the transverse or small transverse direction only. There is a higher localization of damage in only one of the orthogonal directions of the material and the asymmetry in the distribution of damage in the middle cross section of the specimen is evident when compared with the solution of the material with no SD effect. Additionally, for $\boldsymbol{k = -0.9}$, which corresponds to the case of higher uniaxial compressive strength relative to tensile strength, the predicted evolution of damage was not towards the centre of the specimen but instead moved along the notch root. Thus, for materials with a very strong SD effect where $\boldsymbol{\sigma_C > \sigma_T}$, the model was able to predict the damage initiation but not its further growth towards the centre of the specimen. The consideration of strong SD effects influences not only the damage initiation site but also damage evolution. It is therefore of crucial importance the consideration of the SD effects on the numerical evaluation of damage when using fully coupled damage constitutive models.

Chapter 7

Material Models for Composites

7.1 Introduction

The expansion of the use of fibre reinforced polymer composites, particularly in the aerospace industry and also more recently in the automotive industry, emphasized the need to obtain reliable numerical tools capable of accurately predicting the mechanical response of composite laminates. The complex nature of composite materials has motivated extensive research in the last decades specifically regarding the effects of damage and failure mechanisms. The development and use of advanced numerical models for the prediction of the mechanical behaviour of composites is a key factor, not only for the assessment of the structural integrity of composite structures, but also in the reduction of product development costs and in the efficient design and manufacture of more competitive products.

As a result of their complex structure and manufacturing processes, composites display a wide variety of failure mechanisms, namely fibre failure, matrix cracking, delamination and buckling [137]. Fibre failure occurs when the loads applied to a composite structure cause the fracture of the fibres. Matrix cracking involves voids and cracks between the fibres within a composite layer or lamina and delaminations are separations between internal layers of a composite laminate. Buckling is a structural phenomenon and does not necessarily cause failure, however the large deformations, bending and loss of structural capacity involved, typically promotes other types of damage and leads to structural collapse.

In this chapter, an overview of the numerical modelling of damage onset and evolution of fibre reinforced composites is given. The damage mechanisms are reviewed and the continuum damage model subsequently used in the hybrid joint simulations, proposed by Maimí et al. [7, 138] is presented.

7.2 Damage mechanisms and idealization scale

At a macroscopic level, failure mechanisms can be viewed as a result of discrete damage events that lead to the fracture of composite structures, namely fibre/matrix debonding and subsequent pull-out, matrix cracking and yielding, delamination between plies, fibre break-

age or fibre kinking/buckling and fibre splitting. The damage mechanisms can be divided into intralaminar and interlaminar damage. Intralaminar damage corresponds to fibre fracture/buckling, matrix cracking and fibre/matrix debonding whereas interlaminar damage mechanisms correspond to the interfacial separation of the plies (delamination). Intralaminar and interlaminar damage mechanisms are shown in Figure 7.1.

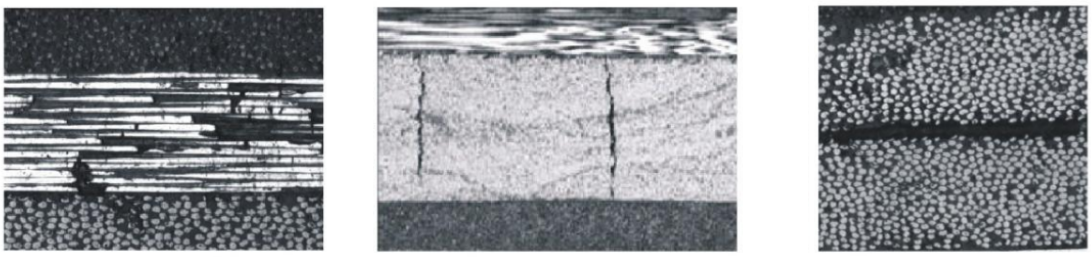

(a) (b) (c)

Figure 7.1: Damage mechanisms in laminated composites: (a)fibre fracture, (b) matrix transverse crack and (c) delamination [139].

Due to the presence of two constituents, the fibre and the matrix, and the high anisotropy in both strength and stiffness, the details of the mechanisms that lead to failure occur at different levels. The governing physical principles of damage can be described at different length scales ranging from micro-mechanical scale models, with a discrete representation of the constituents and their interfaces, to structural mechanics.

Micro-mechanical models represent the smallest scale of composite damage idealization. At this scale, the constituents are seen as individual homogeneous materials and the experimental data on the properties of the fibres and matrix materials are used to predict the properties of the individual layer and finally the structure. Detailed matrix damage mechanisms, such as matrix plasticity and damage, and fibre/matrix interface cracking can be easily represented. The major developments regarding the investigation of micro-mechanical models was performed by Totry et al. [140], González and Llorca [141] and Melro et al. [142]. At the structural level the material is assumed homogeneous and the effects of the constituents are represented only by averaged apparent properties of the composite material. By assuming the composite as an homogeneous material, preliminary design and optimization becomes easier and more rapidly available. The structural level models include the works of Camanho and Lambert [143] Camanho et al. [144] and Whitney and Nuismer [145]. An intermediate length scale corresponds to that of the individual ply. At this level, the layers are considered an homogenized material with orthotropic material properties related to the directions of the fibres. Both the failure mechanisms of the plies and the interfaces between the plies are considered. Important models regarding the length scale of the ply were proposed by Tay et al. [146], Abisset et al. [147], Iarve et al. [148], van der Meer et al. [149], Ling et al. [150], Maimí et al. [7, 138], Wisnom [151], Schuecker and Pettermann [152], Turon et al. [153], Qiu et al. [154] and Schipperen and de Borst [155].

One of the most common idealizations for composite damage are continuum damage mechanics (CDM) models at the ply length scale. The continuum damage approach is defined in

the framework of the thermodynamics of irreversible processes and regards damage initiation and propagation as the ultimate consequence of a gradual loss of material integrity. The damage modes include fibre fracture, fibre kinking, matrix cracking and delamination that are represented through a reduction in corresponding stiffnesses using continuous damage variables and interacting activation functions that describe the loss of material integrity.

7.3 Strength based failure criteria

Strength based failure criteria are commonly used to predict failure in composite materials particularly in the definition of damage initiation. Numerous continuum-based criteria have been developed in the past decades to relate internal stresses and experimental measures of the material strength to the onset of failure.

One of the most important contributions to the development of failure criteria in composites is attributed to Hashin [156, 157]. In his work, Hashin established the need for failure criteria based on failure mechanisms. Based on experimental observations of failure of tensile specimens he proposed two different failure criteria, one related to the fibre failure and the other related to matrix failure. The criteria assumes a quadratic interaction between the tractions acting on the plane of failure. Later, Hashin introduced fibre and matrix failure that distinguished between tension and compression failure. To overcome the difficulty in obtaining the plane of failure in the 3D case, Hashin proposed another criteria using a quadratic interaction between stress invariants [158]. The 2D version of the failure criteria proposed by Hashin are given in Table 7.1.

Table 7.1: Hashin Criteria for plane stress.

Matrix Failure	
Matrix Tension, $\boldsymbol{\sigma_{22} \geq 0}$	Matrix Compression, $\boldsymbol{\sigma_{22} < 0}$
	$\boldsymbol{FI_M = \left(\frac{\sigma_{22}}{Y^C}\right)^2 + \left(\frac{\tau_{12}}{S^L}\right)^2, 1973}$
$\boldsymbol{FI_M = \left(\frac{\sigma_{22}}{Y^T}\right)^2 + \left(\frac{\tau_{12}}{S^L}\right)^2}$	$\boldsymbol{FI_M = \left(\frac{\sigma_{22}}{2S^T}\right)^2 + \left[\left(\frac{Y^C}{2S^T}\right)^2 - 1\right]\frac{\sigma_{22}}{Y^C} + \left(\frac{\tau_{12}}{S^L}\right)^2, 1980}$
Fibre Failure	
Fibre Tension, $\boldsymbol{\sigma_{11} \geq 0}$	Fibre Compression, $\boldsymbol{\sigma_{11} < 0}$
$\boldsymbol{FI_F = \left(\frac{\sigma_{11}}{X^T}\right)^2 + \left(\frac{\tau_{12}}{S^L}\right)^2}$	$\boldsymbol{FI_F = \frac{\sigma_{11}}{X^C}}$

Numerous studies have demonstrated that the stress interactions proposed by Hashin do not always fit the experimental results particularly for fibre and matrix compression. Moderate transverse compression ($\boldsymbol{\sigma_{22} < 0}$) increases the apparent shear strength of a ply which is not well predicted by the Hashin criterion. Furthermore, Hashin's fibre compression

criterion does not account for the effects of in-plane shear, which reduce significantly the effective compressive strength of a ply. To improve Hashin's criteria predictive capabilities several researchers have proposed a number of modifications.

One empirical modification to Hashin's criterion for matrix compression failure was proposed by Sun et al. [159]. The proposed modification accounted for the beneficial role that compressive $\boldsymbol{\sigma_{22}}$ has on shear strength. The criterion proposed by Sun is,

$$\left(\frac{\boldsymbol{\sigma_{22}}}{\boldsymbol{Y^C}}\right)^{\mathbf{2}} + \left(\frac{\boldsymbol{\tau_{12}}}{\boldsymbol{S^L - \eta\sigma_{22}}}\right)^{\mathbf{2}} = \mathbf{1}, \tag{7.1}$$

where $\boldsymbol{\eta}$ is an experimentally determined constant and may be regarded as an internal material friction parameter. The denominator $\boldsymbol{S^L - \eta\sigma_{22}}$ can be considered an effective in-plane shear strength that increases with transverse compression $\boldsymbol{\sigma_{22}}$. However, as in Hashin's theories, the angle of the fracture plane is not determined.

Another modification was proposed by Puck [160] to account for the influence of transverse compression on matrix shear strength. He suggested an increase of the shear strength by a term proportional to the normal stress, $\boldsymbol{\sigma_n}$, acting at the fracture plane (see Figure 7.2). The matrix failure criteria under transverse compression proposed by Puck is,

$$\left(\frac{\boldsymbol{\tau^T}}{\boldsymbol{S^T - \eta^T\sigma_n}}\right)^{\mathbf{2}} + \left(\frac{\boldsymbol{\tau^L}}{\boldsymbol{S^L - \eta^L\sigma_n}}\right)^{\mathbf{2}} = \mathbf{1}, \tag{7.2}$$

where $\boldsymbol{\tau^T}$ and $\boldsymbol{\tau^L}$ are the shear stresses acting on the fracture plane defined in Figure 7.2. The coeficients $\boldsymbol{\eta^L}$ and $\boldsymbol{\eta^T}$ represent the internal material friction.

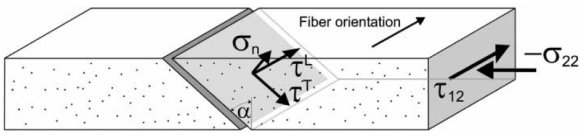

Figure 7.2: Fracture of a unidirectional lamina subjected to transverse compression and in-plane shear [161].

By assuming that fracture initiation is independent of the transverse compressive strength, the direct contribution of $\boldsymbol{\sigma_{22}}$ was eliminated. The key aspect of Puck's proposal is the determination of the angle of the fracture plane, $\boldsymbol{\alpha}$. Puck determined that matrix failures dominated by in-plane shear occur in a plane that is normal to the ply and parallel to the fibres ($\boldsymbol{\alpha = 0}$). For increasing values of transverse compression, the angle of the fracture plane, $\boldsymbol{\alpha}$ changes to about 40^o and increases to $53^o \pm 2^o$ for pure transverse compression. Although Puck's predicted failure envelopes correlated reasonably well with test results, this approach uses several material parameters that are not physical and may be difficult to obtain.

7.3.1 LaRC03 failure criterion

Following the work of Hashin and Puck, Dávila et al. [161] proposed a new set of criteria for matrix fracture based on the Mohr-Coulomb (M-C) effective stresses known as LaRC03.

Matrix failure under transverse compression

The Mohr-Coulomb criterion is known for its use in applications where fracture under tension is different from fracture under compression loading. The M-C model can be represented geometrically by a state of uniaxial compression in the Mohr's circle (see Figure 7.3). The angle of the plane of fracture is $\boldsymbol{\alpha_0}$ is 53°, which is a typical fracture angle for laminated composites under transverse compression loading. The line $\boldsymbol{AB}$ is the Coulomb fracture line.

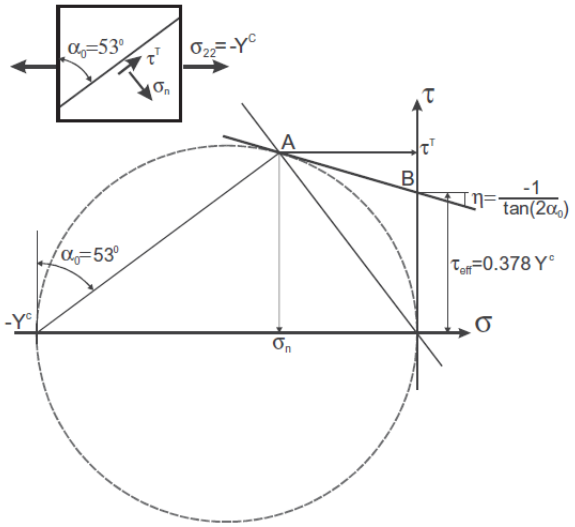

Figure 7.3: Mohr's circle for uniaxial compression and the effective transverse shear [161].

According to the M-C criterion, in a state of biaxial normal stress, fracture occurs for any Mohr's circle tangent to the Coulomb fracture line. The effective stress, $\boldsymbol{\tau_{eff}}$ is related to the stresses $\boldsymbol{\tau^T}$ and $\boldsymbol{\sigma_n}$ acting on the fracture plane by the expression $\boldsymbol{\tau_{eff} = \tau^T + \eta\sigma_n}$ and $\boldsymbol{\tan^{-1}(\eta)}$ is the angle of internal friction that is assumed to be a material constant. According to the criterion proposed, and taking into account that a fracture plane can be subjected to stresses in both orthogonal directions, matrix failure under compression loading is assumed to result from a quadratic interaction between the effective stresses acting on the fracture plane. The LaRC03 criteria for matrix failure under transverse compression ($\boldsymbol{\sigma_{22} < 0}$) is,

$$\boldsymbol{FI_M = \left(\frac{\tau^T_{eff}}{S^T}\right)^2 + \left(\frac{\tau^L_{eff}}{S^L_{is}}\right) \leq 1,} \tag{7.3}$$

where S^T and S^L_{is} are the transverse and longitudinal shear strengths respectively. The subscript *is* refers to the *in situ* longitudinal shear strength. The *in situ* effect regards to the constraining effect that a ply has due to adjacent plies which increase its effective strength. It is assumed that the transverse shear strength is independent of *in situ* effects.

The stress components can be expressed as a function of the fracture angle and the in plane stresses as,

$$\begin{aligned} \sigma_n &= \sigma_{22} \cos^2 \alpha, \\ \tau^T &= -\sigma_{22} \sin \alpha \cos \alpha, \\ \tau^L &= \tau_{12} \cos \alpha. \end{aligned} \tag{7.4}$$

The effective stresses in the orthogonal directions are given by,

$$\begin{aligned} \tau^T_{eff} &= \langle |\tau^T| + \eta^T \sigma_n \rangle, \\ \tau^L_{eff} &= \langle |\tau^L| + \eta^L \sigma_n \rangle, \end{aligned} \tag{7.5}$$

which with Equations (7.4) can be expressed as,

$$\begin{aligned} \tau^T_{eff} &= \langle -\sigma_{22} \cos \alpha \left(\sin \alpha - \eta^T \cos \alpha \right) \rangle, \\ \tau^L_{eff} &= \langle \cos \alpha \left(|\tau_{12}| + \eta^L \sigma_{22} \cos \alpha \right) \rangle. \end{aligned} \tag{7.6}$$

Matrix failure under transverse tension

Transverse matrix cracking normally causes a very small reduction in the overall stiffness of a structure, however, it can affect the development of damage and also provide the primary leakage path for gases in pressurized vessels. The prediction of matrix cracking in a laminate subject to in plane shear and transverse tensile stresses requires the determination of the *in situ* strengths. Accurate *in situ* strengths are necessary for any stress-based failure criterion for matrix cracking in constrained plies due to the higher transverse tensile and shear strengths of the these plies constrained by plies of different fibre orientations when compared to the same ply in a unidirectional laminate. The *in situ* strengths are determined based on fracture mechanics solutions for the propagation of cracks in a constrained ply.

The LaRC03 criterion proposed by Dávila et al. can be expressed in terms of the ply stresses and *in situ* strengths Y^T_{is} and S^L_{is} as,

$$FI_M = (1-g) \frac{\sigma_{22}}{Y^T_{is}} + g \left(\frac{\sigma_{22}}{Y^T_{is}} \right)^2 + \left(\frac{\tau_{12}}{S^L_{is}} \right) \leq 1, \tag{7.7}$$

where $\boldsymbol{g}$ is a material constant defined by

$$\boldsymbol{g = \frac{G_{Ic}}{G_{IIc}} = \frac{\Lambda^0_{22}}{\Lambda^0_{44}} \left(\frac{Y^T_{is}}{S^L_{is}} \right)^2}, \tag{7.8}$$

where $\boldsymbol{G_{Ic}}$ and $\boldsymbol{G_{IIc}}$ are the fracture toughnesses in Mode I and Mode II respectively and the parameters $\boldsymbol{\Lambda^0_{jj}}$ are given by [162] as,

$$\begin{aligned} \boldsymbol{\Lambda^0_{22}} &= \boldsymbol{2\left(\frac{1}{E_2} - \frac{\nu^2_{12}}{E_1} \right)}, \\ \boldsymbol{\Lambda^0_{44}} &= \boldsymbol{\frac{1}{G_{12}}}. \end{aligned} \tag{7.9}$$

It is noteworthy that the *in situ* strengths are dependent not only of the number of plies clustered together but also on the fibre orientation of the constraining plies and the thickness of the plies. Thinner plies exhibit higher transverse tensile strength. The prediction of the crack propagation in thin and thick plies was determined by Dávila et al. [161] for the proposed criterion given by (7.7), where the *in situ* strengths are calculated from the respective components of the fracture toughness in the transverse and longitudinal directions in Mode I and Mode II.

Fibre tension failure

For fibre tension failure, the LaRC03 criterion is a noninteracting maximum allowable strain criterion that is simple to measure and is independent of fibre volume fraction and Young's modulus. The LarC03 failure index for fibre tensile failure proposed by Dávila et al. is,

$$\boldsymbol{FI_F = \frac{\varepsilon_{11}}{\varepsilon^T_1} \leq 1.} \tag{7.10}$$

Fibre compression failure

Compressive failure of aligned fibre composites occurs from the collapse of the fibres as a result of shear kinking and damage of the supporting matrix. Fibre kinking occurs as shear deformation, leading to the formation of a kink band. The kinking phenomenon was first analysed by Argon [163] that assumed a local initial fibre misalignment. Fibre misalignment leads to shearing stresses between fibres that rotate, increasing the shearing stress and leading to instability. The approach proposed by Dávila et al. [161] assumes that the compressive strength, $\boldsymbol{X^C}$ is a known material property and can be used in the LaRC03 matrix damage criterion (7.3) to determine the fibre misalignment angle that would cause matrix failure under uniaxial compression.

The calculation of the fibre misalignment angle as proposed by Dávila et al. considers that an imperfection in fibre alignment exists and is idealized as a local wave as shown in Figure 7.4.

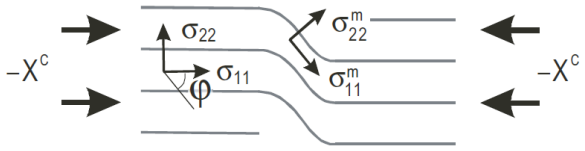

Figure 7.4: Imperfection in fibre alignment idealized as local waviness [161].

Accordingly, the ply stresses in the misalignment coordinate frame $\boldsymbol{m}$ are given by,

$$\begin{aligned}
\boldsymbol{\sigma_{11}^m} &= \mathbf{cos^2}\,\boldsymbol{\varphi\sigma_{11}} + \mathbf{sin^2}\,\boldsymbol{\varphi\sigma_{22}} + \mathbf{2\sin\varphi\cos\varphi|\tau_{12}|},\\
\boldsymbol{\sigma_{22}^m} &= \mathbf{sin^2}\,\boldsymbol{\varphi\sigma_{11}} + \mathbf{cos^2}\,\boldsymbol{\varphi\sigma_{22}} - \mathbf{2\sin\varphi\cos\varphi|tau_{12}|},\\
\boldsymbol{\tau_{12}^m} &= -\,\mathbf{\sin\varphi\cos\varphi\sigma_{11}} + \mathbf{\sin\varphi\cos\varphi\sigma_{22}} + \left(\mathbf{cos^2}\,\boldsymbol{\varphi} - \mathbf{sin^2}\,\boldsymbol{\varphi}\right)|\boldsymbol{\tau_{12}}|.
\end{aligned} \tag{7.11}$$

At failure under uniaxial compression $\boldsymbol{\sigma_{11}} = -\boldsymbol{X^C}$ and $\boldsymbol{\sigma_{22}} = \boldsymbol{\tau_{12}} = \mathbf{0}$. Thus the ply stresses from Equations (7.11) can be rewritten as

$$\begin{aligned}
\boldsymbol{\sigma_{22}^m} &= -\,\mathbf{sin^2}\,\boldsymbol{\varphi^C X^C},\\
\boldsymbol{\tau_{12}^m} &= \mathbf{\sin\psi^C\cos\varphi^C X^C},
\end{aligned} \tag{7.12}$$

where the angle $\boldsymbol{\varphi^C}$ is the total misalignment angle under pure axial compression loading.

Attending to the fact that the mode of failure in fibre kinking is dominated by shear stress, $\boldsymbol{\tau_{12}}$ rather than by $\boldsymbol{\sigma_{22}}$, the angle of the fracture plane is then equal to 0°, $\boldsymbol{\tau_{eff}^T} = \mathbf{0}$ and $\boldsymbol{\tau_{eff}^L}$ is given by,

$$\boldsymbol{\tau_{eff}^L} = \boldsymbol{X^C}\left(\mathbf{\sin\varphi^C\cos\varphi^C} - \boldsymbol{\eta^L}\,\mathbf{sin^2}\,\boldsymbol{\varphi^C}\right) = \boldsymbol{S_{is}^L}, \tag{7.13}$$

where $\boldsymbol{S_{is}^L}$ is the *in situ* longitudinal shear strength determined for thin or thick plies accordingly. Solving equation (7.13) for $\boldsymbol{\varphi^C}$ leads to a quadratic equation,

$$\mathbf{tan^2}\,\boldsymbol{\varphi^C}\left(\frac{\boldsymbol{S_{is}^L}}{\boldsymbol{X^C}} + \boldsymbol{\eta^L}\right) - \mathbf{\tan\varphi^C} + \left(\frac{\boldsymbol{S_{is}^L}}{\boldsymbol{X^C}}\right), \tag{7.14}$$

that can be solved for $\boldsymbol{\varphi^C}$.

By decomposing the misalignment angle into an initial angle representing a manufacturing imperfection and an additional rotational component that results from shear loading, $\boldsymbol{\varphi} =$

$\boldsymbol{\varphi^0 + \varphi^R}$, the misalignment angle can be obtained as a function of $\boldsymbol{\varphi^C}$ as,

$$\boldsymbol{\varphi = \frac{|\tau_{12}| + (G_{12} - X^C)\,\varphi^C}{G_{12} + \sigma_{11} - \sigma_{22}}}, \tag{7.15}$$

Using the stresses from Equation (7.11) and the failure criterion for matrix tension (7.3) with $\boldsymbol{\alpha = 0^o}$ and $\boldsymbol{\tau^T_{eff} = 0}$, the LarC03 criterion for fibre kinking is

$$\boldsymbol{FI_F = \langle \frac{|\tau^m_{12}| + \eta^L \sigma^m_{22}}{S^L_{is}} \rangle \leq 1.} \tag{7.16}$$

If instead, the failure criterion for matrix tension (7.7) is used, the LaRC03 for fibre compression with matrix tension criterion is

$$\boldsymbol{FI_F = (1-g)\left(\frac{\sigma^m_{22}}{Y^T_{is}}\right) + g\left(\frac{\sigma^m_{22}}{Y^T_{is}}\right)^2 + \left(\frac{\tau^m_{12}}{S^L_{is}}\right)^2 \leq 1,} \tag{7.17}$$

Matrix damage in biaxial compression

In the presence of high transverse compression combined with moderate fibre compression, matrix damage can occur without the formation os kink bands or damage to the fibres. Dávila et. al proposed the calculation of this matrix damage mode using the stresses on the misaligned frame in the failure criterion of Equation (7.3) resulting in,

$$\boldsymbol{FI_M = \left(\frac{\tau^{mT}_{eff}}{S^T}\right)^2 + \left(\frac{\tau^{mL}_{eff}}{S^L_{is}}\right)^2 \leq 1,} \tag{7.18}$$

where $\boldsymbol{\tau^{mT}_{eff}}$ and $\boldsymbol{\tau^{mL}_{eff}}$ are defined as in Equation (7.6) but in terms of the in-plane stresses in the misalignment frame given by Equations (7.11), resulting in

$$\begin{aligned} \boldsymbol{\tau^{mT}_{eff}} &= \boldsymbol{\langle -\sigma^m_{22}\cos\alpha\,(\sin\alpha - \eta^T\cos\alpha)\rangle,} \\ \boldsymbol{\tau^{mL}_{eff}} &= \boldsymbol{\langle \cos\alpha\,(|\tau^m_{12}| + \eta^L\sigma^m_{22}\cos\alpha)\rangle.} \end{aligned} \tag{7.19}$$

7.3.2 LaRC04 failure criterion

Following the concepts of the LaRC03 criterion, Pinho et al. [164] proposed new failure criteria by extending the LaRC03 plane stress criteria to account for general three-dimensional loading and in-plane shear non-linearity.

Matrix failure under tension

The failure criterion proposed by Pinho et al. [164] for the prediction of the matrix cracking in a ply subjected to in plane shear and transverse tension is based on the fracture mechanics analysis of a slit crack in a ply as proposed by Dvorak and Laws [162] and as suggested by Dávila et al. for LaRC03 [158].

Here, the transverse tensile stress, $\boldsymbol{\sigma_{22}}$, is associated with Mode I loading, whereas the in-plane and transverse shear stresses, $\boldsymbol{\tau_{12}}$ and $\boldsymbol{\tau_{23}}$ respectively, are associated with Mode II loading. The components of the energy release rates were presented by Pinho et al. as an extension of the analysis of Dvorak and Laws [162] for non-linear shear behaviour. The Mode II and Mode III components of the energy release rate are combined in a shear mode, $\boldsymbol{G_{SH} = G_{II} + G_{III}}$, so that the relative orientation of the crack front with respect of the in-plane displacements does not need to be determined. The energy release rates and corresponding components of the fracture toughness are obtained for the the transverse and longitudinal directions.

The failure index proposed by LaRC04 depends on the ply stresses and *in situ* strengths and is expressed as,

$$\boldsymbol{FI_M = (1-g)\,\frac{\sigma_{22}}{Y_{is}^T} + g\left(\frac{\sigma_{22}}{Y_{is}^T}\right)^2 + \frac{\Lambda_{23}^0 \tau_{23}^2 + \chi(\gamma_{12})}{\chi(\gamma_{12|is}^u)} = 1.} \tag{7.20}$$

The criterion proposed by Pinho et al. has a linear and a quadratic term in $\boldsymbol{\sigma_{22}}$, a quadratic term in $\boldsymbol{\tau_{23}}$ and a term on the in-plane shear internal energy, $\boldsymbol{\chi(\gamma_{12})}$.

Matrix failure under compression

For matrix failure under compression, Pinho et al. suggested the use of the failure criterion proposed by Puck and Schürmann [160,165] but with the use of the *in situ* longitudinal shear strength as was proposed in LaRC03 [161]. The LaRC04 failure criterion is

$$\boldsymbol{FI_M = \left(\frac{\tau^T}{S^T - \eta^T \sigma_n}\right)^2 + \left(\frac{\tau^L}{S_{is}^L - \eta^L \sigma_n}\right)^2 \leq 1.} \tag{7.21}$$

This failure criterion requires the determination of the tractions, that for a 3D formulation are obtained from the components of the stress tensor and the fracture plane angle,$\boldsymbol{\alpha}$, as

$$\begin{aligned}
\boldsymbol{\sigma_n} &= \boldsymbol{\frac{\sigma_{22}+\sigma_{33}}{2} + \frac{\sigma_{22}-\sigma_{33}}{2}\cos(2\alpha) + \tau_{23}\sin(2\alpha),} \\
\boldsymbol{\tau^T} &= \boldsymbol{-\frac{\sigma_{22}-\sigma_{33}}{2}\sin(2\alpha) + \tau_{23}\cos(2\alpha),} \\
\boldsymbol{\tau^L} &= \boldsymbol{\tau_{12}\cos(\alpha) + \tau_{31}\sin(\alpha).}
\end{aligned} \tag{7.22}$$

Although for 3D stress states, the fracture angle cannot be analytically determined, Pinho et al. showed that it is possible to obtain the failure envelope for this criterion using a very small number of trial angles.

Fibre failure under tension

The LaRC04 criterion for fibre tensile failure is a non-interacting maximum allowable stress criterion. The failure index for LaRC04 for fibre tensile failure is,

$$\boldsymbol{FI_F = \frac{\sigma_{11}}{X^T} \leq 1.} \tag{7.23}$$

Fibre failure under compression

For fibre compression failure different modes of failure can be identified. The most common failure mode observed is kinking. Kinking can be defined as the localized shear deformation of the matrix along a band in which the fibres have rotated by a large amount. For a material with non-linear shear behaviour, kinking can result either from matrix failure (through the verification of a matrix failure criterion) or instability due to the loss of (shear) stiffness for large shear strain values.

The 2D model for fibre kinking assumes that the initiation of kink band formation is triggered by matrix failure due to initial fibre misalignment and kinking happens in the plane of the lamina. The kink-band formation in 3D happens in a kink plane at an angle $\boldsymbol{\psi}$ as illustrated in Figure 7.5.

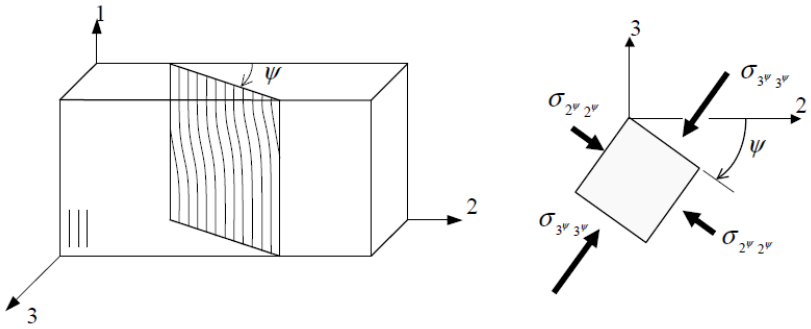

Figure 7.5: 3D kinking model [164].

The value of $\boldsymbol{\psi}$ depends on the particular stress state. The stresses in the kink plane are

defined as,

$$\begin{aligned}
\boldsymbol{\sigma_{2^\psi 2^\psi}} =& \frac{\boldsymbol{\sigma_{22}+\sigma_{33}}}{\mathbf{2}} + \frac{\boldsymbol{\sigma_{22}-\sigma_{33}}}{\mathbf{2}}\mathbf{cos(2\psi)} + \boldsymbol{\tau_{23}}\,\mathbf{sin(2\psi)},\\
\boldsymbol{\sigma_{3^\psi 3^\psi}} =& \boldsymbol{\sigma_{22}+\sigma_{33}-\sigma_{2^\psi 2^\psi}},\\
\boldsymbol{\tau_{12^\psi}} =& \boldsymbol{\tau_{12}}\,\mathbf{cos(\psi)} + \boldsymbol{\tau_{31}}\,\mathbf{sin(\psi)},\\
\boldsymbol{\tau_{2^\psi 3^\psi}} =& \mathbf{0},\\
\boldsymbol{\tau_{3^\psi 1}} =& \boldsymbol{\tau_{31}}\,\mathbf{cos(\psi)} - \boldsymbol{\tau_{12}}\,\mathbf{sin(\psi)},
\end{aligned} \tag{7.24}$$

and the angle $\boldsymbol{\psi}$ is given by,

$$\boldsymbol{\psi} = \frac{\boldsymbol{\tau_{12^\psi}}}{|\boldsymbol{\tau_{12^\psi}}|}\left(\boldsymbol{\psi^0} + \boldsymbol{\gamma_{1^m 2^m}}\right). \tag{7.25}$$

The misalignment frame is defined by determining $\boldsymbol{\gamma_{1^m 2^m}}$ by solving iteratively the following equation

$$\boldsymbol{f_{CL}(\gamma_{1^m 2^m})} = -\frac{\boldsymbol{\sigma_{11}-\sigma_{2^\psi 2^\psi}}}{\mathbf{2}}\,\mathbf{sin}\left(\mathbf{2}\left(\boldsymbol{\varphi^0}+\boldsymbol{\gamma_{1^m 2^m}}\right)\right) + |\boldsymbol{\tau_{12^\psi}}|\,\mathbf{cos}\left(\mathbf{2}\left(\boldsymbol{\varphi^0}+\boldsymbol{\gamma_{1^m 2^m}}\right)\right). \tag{7.26}$$

According to Pinho et al. failure occurs by instability if equation (7.26) has no solution. Otherwise the stresses in the misalignment frame are determined by,

$$\begin{aligned}
\boldsymbol{\sigma_{1^m 1^m}} =& \frac{\boldsymbol{\sigma_{11}+\sigma_{2^\psi 2^\psi}}}{\mathbf{2}} + \frac{\boldsymbol{\sigma_{11}-\sigma_{2^\psi 2^\psi}}}{\mathbf{2}}\mathbf{cos}\left(\mathbf{2\varphi}\right) + \boldsymbol{\tau_{12^\psi}}\,\mathbf{sin(2\varphi)},\\
\boldsymbol{\sigma_{2^m 2^m}} =& \boldsymbol{\sigma_{11}+\sigma_{2^\psi 2^\psi}-\sigma_{1^m 1^m}},\\
\boldsymbol{\tau_{1^m 2^m}} =& -\frac{\boldsymbol{\sigma_{11}-\sigma_{2^\psi 2^\psi}}}{\mathbf{2}}\,\mathbf{sin(2\varphi)} + \boldsymbol{\tau_{12^\psi}}\,\mathbf{cos(2\varphi)},\\
\boldsymbol{\tau_{2^m 3^\psi}} =& \boldsymbol{\tau_{2^\psi 3^\psi}}\boldsymbol{cos(\varphi)} - \boldsymbol{\tau_{3^\psi 1}}\,\mathbf{sin(\varphi)},\\
\boldsymbol{\tau_{3^\psi 1^m}} =& \boldsymbol{\tau_{3^\psi 1^\psi}}\,\mathbf{cos(\varphi)}.
\end{aligned} \tag{7.27}$$

The prediction of matrix failure by LaRC04 is obtained using the LaRC04 matrix tension failure (Equation (7.20)) and matrix compression failure (Equation (7.21)) in the misalignment frame. In matrix failure fibre kinking may or may not occur. Thus, for the criterion proposed by Pinho et al., with $\boldsymbol{\sigma_{2^m 2^m}}$ fibre kinking is predicted with,

$$\boldsymbol{FI_F} = \frac{|\boldsymbol{\tau_{1^m 2^m}}|}{\boldsymbol{S_{is}^L}} - \boldsymbol{\eta^L \sigma_{2^m 2^m}} \leq \mathbf{1}, \tag{7.28}$$

and matrix failure under biaxial compression is predicted by

$$\boldsymbol{FI_M = \left(\frac{\tau^{Tm}}{S^T - \eta^T \sigma_n^m}\right)^2 + \left(\frac{\tau^{Lm}}{S^L - \eta^L \sigma_n^m}\right)^2 \leq 1,} \tag{7.29}$$

with

$$\begin{aligned} \boldsymbol{\sigma_n^m} =& \boldsymbol{\frac{\sigma_{2^m 2^m} + \sigma_{3^\psi 3^\psi}}{2} + \frac{\sigma_{2^m 2^m} - \sigma_{3^\psi 3^\psi}}{2} \cos(2\alpha) + \tau_{2^m 3^\psi} \sin(2\alpha),} \\ \boldsymbol{\tau^{Tm}} =& \boldsymbol{-\frac{\sigma_{2^m 2^m} - \sigma_{3^\psi 3^\psi}}{2} \sin(2\alpha) + \tau_{2^m 3^\psi} \cos(2\alpha),} \\ \boldsymbol{\tau^{Lm}} =& \boldsymbol{\tau_{1^m 2^m} \cos(\alpha) + \tau_{3^\psi 1^m} \sin(\alpha),} \end{aligned} \tag{7.30}$$

where the angle $\boldsymbol{\alpha}$ is comprised in the interval $\boldsymbol{]0, \pi]}$ and is obtained by trying a small number of tentative angles.

For $\boldsymbol{\sigma_{2^m 2^m} \geq 0}$, the proposed LaRC04 predicts from Equation (7.20), matrix tensile failure under longitudinal compression (with eventual fibre-kinking) from,

$$\boldsymbol{FI_{M/F} = (1-g)\frac{\sigma_{2^m 2^m}}{Y_{is}^T} + g\left(\frac{\sigma_{2^m 2^m}}{Y_{is}^T}\right)^2 + \frac{\Lambda_{23}^0 \tau_{2^m 3^\psi}^2 + \chi(\gamma_{1^m 2^m})}{\chi(\gamma_{12|is}^u)} \leq 1.} \tag{7.31}$$

7.4 Continuum damage mechanics model

For composite structures that can accumulate damage, failure criteria are not sufficient to predict ultimate failure. To model the quasi-brittle failure of laminates resulting from the accumulation of several failure mechanisms, continuum damage mechanics models have been developed and implemented in recent years.

Continuum damage mechanics models for composite materials were pioneered by Ladevéze and LeDantec [166], Matzenmiller et al. [167], and others based on the work of Kachanov [168], Lemaitre et al. [129] and others. The thermodynamics of irreversible processes provides a rigorous framework from which the constitutive models can be developed.

The continuum damage model presented in the following sections was developed and implemented by Maimí et al. [7,138]. This model predicts the onset and evolution of intralaminar failure mechanisms (matrix cracking and fibre fracture) and collapse in fibre reinforced plastic laminates. The main characteristics of the intralaminar failure mechanisms establish the basis for the failure criteria and damage variables used. Under longitudinal tensile loading, failure occurs in both constituents and fracture occurs in a plane whose normal is parallel to the fibre direction. Under longitudinal compression, failure occurs from the collapse of the fibres due to shear kinking and damage of the matrix. Under transverse loading, failure includes both matrix cracking and fibre-matrix debonding. Tensile and in-plane shear stresses trigger transverse cracks that extend through the thickness of the ply. For compressive transverse

stress, matrix cracking occurs in a fracture plane at an angle of $53^o \pm 3^o$ with respect to the thickness direction. In Figure 7.6 the four fracture planes considered in the Maimí et al. model are schematically represented.

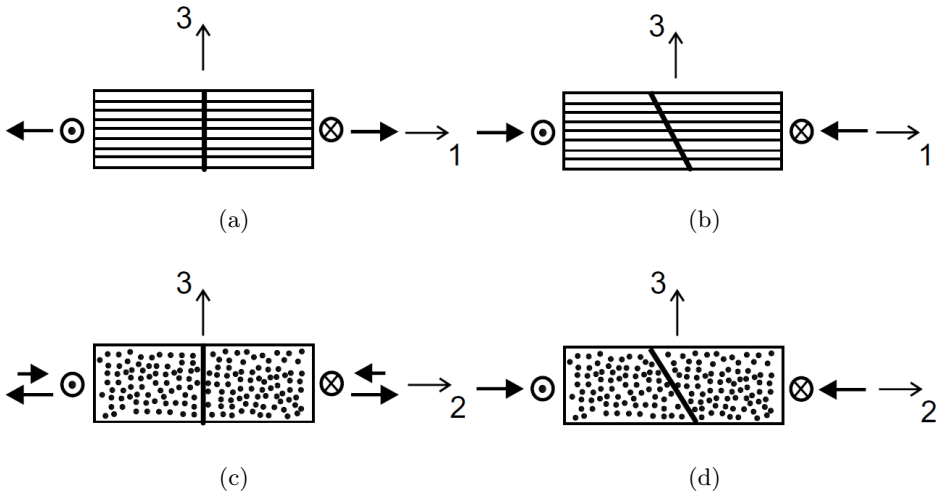

Figure 7.6: Ply fracture planes considered in Maimí et al. CDM model: (a)longitudinal tensile fracture, (b) longitudinal compressive fracture, (c) transverse fracture with $\boldsymbol{\alpha = 0^o}$ and (d)Transverse fracture with $\boldsymbol{\alpha = 53^o}$ [7].

Constitutive damage model

The complementary free energy density function proposed by Maimí et al. is given by,

$$\begin{aligned} G =& \frac{\boldsymbol{\sigma_{11}^2}}{\boldsymbol{2(1-d_1)E_1}} + \frac{\boldsymbol{\sigma_{22}^2}}{\boldsymbol{2(1-d_2)E_2}} - \frac{\boldsymbol{\nu_{12}}}{\boldsymbol{E_1}}\boldsymbol{\sigma_{11}\sigma_{22}} \\ &+ \frac{\boldsymbol{\sigma_{12}^2}}{\boldsymbol{2(1-d_6)G_{12}}} + \boldsymbol{(\alpha_{11}\sigma_{11} + \alpha_{22}\sigma_{22})\,\Delta T} \\ &+ \boldsymbol{(\beta_{11}\sigma_{11} + \beta_{22}\sigma_{22})\,\Delta M}, \end{aligned} \tag{7.32}$$

where $\boldsymbol{E_1}$, $\boldsymbol{E_2}$, $\boldsymbol{\nu_{12}}$, and $\boldsymbol{G_{12}}$ are the in-plane elastic orthotropic properties of a unidirectional lamina. $\boldsymbol{\alpha_{11}}$ and $\boldsymbol{\alpha_{22}}$ are the coefficients of thermal expansion in the longitudinal and transverse directions respectively. $\boldsymbol{\beta_{11}}$ and $\boldsymbol{\beta_{22}}$ are the coefficients of hygroscopic expansion in the longitudinal and transverse directions respectively. $\boldsymbol{\Delta T}$ and $\boldsymbol{\Delta M}$ are the differences of temperature and moisture content with respect to the corresponding reference values. $\boldsymbol{d_1}$, $\boldsymbol{d_2}$ and $\boldsymbol{d_6}$ are damage scalar variables associated respectively with longitudinal (fibre) failure, transverse matrix cracking and longitudinal and transverse cracking.

The damage process is a thermodynamical irreversible process, thus the dissipated energy

has to be positive which can be expressed by the following inequality,

$$\dot{\boldsymbol{G}} - \dot{\boldsymbol{\sigma}} : \boldsymbol{\varepsilon} \geq \mathbf{0}. \tag{7.33}$$

The derivative of the complementary free energy density with respect to the stress tensor gives the strain tensor,

$$\boldsymbol{\varepsilon} = \frac{\partial \boldsymbol{G}}{\partial \boldsymbol{\sigma}} = \mathbf{H} : \boldsymbol{\sigma} + \boldsymbol{\alpha}\boldsymbol{\Delta T} + \boldsymbol{\beta}\boldsymbol{\Delta M}, \tag{7.34}$$

where $\mathbf{H}$ is the compliance tensor that is given, in Voight notation, as

$$\mathbf{H} = \frac{\partial^2 \boldsymbol{G}}{\partial \boldsymbol{\sigma}^2} = \begin{Bmatrix} \frac{1}{(1-d_1)E_1} & -\frac{\varepsilon_{21}}{E_2} & \mathbf{0} \\ -\frac{\varepsilon_{12}}{E_1} & \frac{1}{(1-d_2)E_2} & \mathbf{0} \\ \mathbf{0} & \mathbf{0} & \frac{1}{(1-d_6)G_{12}} \end{Bmatrix}. \tag{7.35}$$

The crack-closure effect under tension-compression load reversal is taken into account by considering four damage variables defining longitudinal and transverse damage modes as

$$\begin{aligned} \boldsymbol{d_1} =& \boldsymbol{d_{1+}} \frac{\langle \boldsymbol{\sigma_{11}} \rangle}{|\boldsymbol{\sigma_{11}}|} + \boldsymbol{d_{1-}} \frac{\langle -\boldsymbol{\sigma_{11}} \rangle}{|\boldsymbol{\sigma_{11}}|}, \\ \boldsymbol{d_2} =& \boldsymbol{d_{2+}} \frac{\langle \boldsymbol{\sigma_{22}} \rangle}{|\boldsymbol{\sigma_{22}}|} + \boldsymbol{d_{2-}} \frac{\langle -\boldsymbol{\sigma_{22}} \rangle}{|\boldsymbol{\sigma_{22}}|}. \end{aligned} \tag{7.36}$$

The shear damage variable, $\boldsymbol{d_6}$ is not affected by the closure effect.

Damage activation functions

The model proposed by Maimí et al. considers four damage activation functions, $\boldsymbol{F_N}$, associated with the failure mechanisms in the longitudinal ($\boldsymbol{N} = \mathbf{1+}, \mathbf{1-}$) and transverse ($\boldsymbol{N} = \mathbf{2+}, \mathbf{2-}$) directions. These functions define four surfaces that delimit the elastic domain, each of them accounting for one failure mechanism, and are defined as

$$\begin{aligned} \boldsymbol{F_{1+}} =& \boldsymbol{\phi_{1+}} - \boldsymbol{r_{1+}} \leq \mathbf{0}, \qquad \boldsymbol{F_{1-}} = \boldsymbol{\phi_{1-}} - \boldsymbol{r_{1-}} \leq \mathbf{0}, \\ \boldsymbol{F_{2+}} =& \boldsymbol{\phi_{2+}} - \boldsymbol{r_{2+}} \leq \mathbf{0}, \qquad \boldsymbol{F_{2-}} = \boldsymbol{\phi_{2-}} - \boldsymbol{r_{2-}} \leq \mathbf{0}, \end{aligned} \tag{7.37}$$

where $\boldsymbol{r_N}, \boldsymbol{N} = \mathbf{1+}, \mathbf{1-}, \mathbf{2+}, \mathbf{2-}$ are the elastic domain thresholds that take an initial value of 1 for the undamaged materials and increase with damage. The elastic domain thresholds are related to the damage variables ($\boldsymbol{d_M}, \boldsymbol{M} = \mathbf{1+}, \mathbf{1-}, \mathbf{2+}, \mathbf{2-}, \mathbf{6}$) by the damage evolution

laws. $\phi_N, N = 1+, 1-, 2+, 2-$, are the loading functions that depend on the strain tensor and material constants corresponding to the failure criteria:

- Longitudinal tensile fracture: the non-interacting maximum allowable strain LaRC04 criterion for fibre tension is used

$$\phi_{1+} = \frac{E_1}{X_T}\varepsilon_{11} = \frac{\tilde{\sigma}_{11} - \nu_{12}\tilde{\sigma}_{22}}{X_T}, \tag{7.38}$$

  where $\tilde{\boldsymbol{\sigma}}$ is the undamaged effective stress tensor.

- Longitudinal compressive fracture: the damage activation function for longitudinal compression depends on the initial fibre misalignment and the rotation of the fibres and is a function of the components of the stress tensor in the coordinate system representing the fibre misalignment (m),

$$\phi_{1-} = \frac{\langle|\tilde{\sigma}^m_{12}| + \eta^L\tilde{\sigma}^m_{22}\rangle}{S_L}, \tag{7.39}$$

  where $\eta^L \approx -\frac{S_L\cos(2\alpha_0)}{Y_C\cos^2\alpha_0}$. The misalignment angle is determined using the following expression as proposed by Dávila et al. [161].

$$\Phi_C = arctan\left(\frac{1 - \sqrt{1 - 4\left(\frac{S_L}{X_C} + \eta^L\right)\frac{S_L}{X_C}}}{2\left(\frac{S_L}{X_C} + \eta^L\right)}\right). \tag{7.40}$$

- Transverse fracture perpendicular to the mid-plane ($\alpha_0 = 0$): Transverse matrix cracks perpendicular to the mid-plane of the ply are predicted by the following LaRC04 failure criterion,

$$\phi_{2+} = \begin{cases} \sqrt{(1-g)\frac{\tilde{\sigma}_{22}}{Y_T} + g\left(\frac{\tilde{\sigma}_{22}}{Y_T}\right)^2 + \left(\frac{\tilde{\sigma}_{12}}{S_L}\right)^2} & \text{if } \tilde{\sigma}_{22} \geq 0 \\ \frac{1}{S_L}\langle|\tilde{\sigma}_{12}| + \eta^L\tilde{\sigma}_{22}\rangle & \text{if } \tilde{\sigma}_{22} < 0 \end{cases} \tag{7.41}$$

- Transverse fracture with $\alpha_0 = 53^o$: the damage activation function under high transverse compressive stresses is given by the LaRC04 matrix failure criterion as,

$$\phi_{2-} = \sqrt{\left(\frac{\tilde{\tau}^T_{eff}}{S_T}\right)^2 + \left(\frac{\tilde{\tau}^L_{eff}}{S_L}\right)^2}, \tag{7.42}$$

where $\tilde{\tau}^{T}_{eff}$ and $\tilde{\tau}^{L}_{eff}$ are the effective stresses calculated as proposed by Pinho et al. [164].

The current elastic domain thresholds, r_N, are obtained using the loading functions according to the following equations,

$$\begin{aligned} r_{1+} &= \max\left\{1, \max_{s=0,t}\{\phi^{s}_{1+}\}, \max_{s=0,t}\{\phi^{s}_{1-}\}\right\}, \\ r_{1-} &= \max\left\{1, \max_{s=0,t}\{\phi^{s}_{1-}\}\right\}, \\ r_{2+} &= \max\left\{1, \max_{s=0,t}\{\phi^{s}_{2-}\}, \max_{s=0,t}\{\phi^{2}_{2+}\}\right\}, \\ r_{2-} &= \max\left\{1, \max_{s=0,t}\{\phi^{s}_{2-}\}\right\}. \end{aligned} \tag{7.43}$$

Damage evolution

In addition to the damage activation functions it is necessary to define the evolution laws for the damage variables. The damage evolution laws need to ensure that the computed energy dissipated is independent of the refinement of the mesh. For strain-softening constitutive models, the material response produces results that are mesh-dependent, i.e., the solution is non-objective with respect to the mesh refinement and the computed dissipated energy decreases with a reduction of the element size. To ensure a correct computation of the energy dissipated, independent of the refinement of the mesh, a characteristic length of the finite elements (l^*), based on a procedure proposed by Bažant and Oh [169], is used in the definition of the constitutive model. The definition of the damage evolution laws proposed by Maimí et al. is therefore related to the computational model.

Exponential damage evolution laws were proposed for all failure modes, except for the longitudinal tension damage related to the damage variable d_{1+}. These are expressed in the following general form,

$$d_M = 1 - \frac{1}{f_N(r_N)} \exp\left\{A_M \left[1 - f_N(r_N)\right]\right\} f(r_K), \tag{7.44}$$

where the function $f_N(r_N)$ is selected to force the softening of the constitutive relation and it is taken as being independent of the material. The specific damage evolution laws for each

damage variable are:

$$\begin{aligned} \boldsymbol{d_{1+}} &= \mathbf{1} - \left(\mathbf{1} - \boldsymbol{d_{1+}^{L}}\right)\left(\mathbf{1} - \boldsymbol{d_{1+}^{E}}\right), \\ \boldsymbol{d_{1-}^{*}} &= \mathbf{1} - \frac{\mathbf{1}}{\boldsymbol{r_{1-}}}\boldsymbol{exp}\left[\boldsymbol{A_1}\left(\mathbf{1} - \boldsymbol{r_{1-}}\right)\right], \\ \boldsymbol{d_{2+}} &= \mathbf{1} - \frac{\mathbf{1}}{\boldsymbol{f_{2+}(r_{2+})}}\boldsymbol{exp}\left[\boldsymbol{A_{2+}}\left(\mathbf{1} - \boldsymbol{f_{2+}}\left(\boldsymbol{r_{2+}}\right)\right)\right], \\ \boldsymbol{d_{2-}} &= \mathbf{1} - \frac{\mathbf{1}}{\boldsymbol{r2-}}\boldsymbol{exp}\left[\boldsymbol{A_{2-}}\left(\mathbf{1} - \boldsymbol{r_{2-}}\right)\right], \\ \boldsymbol{d_6^{*}}\left(\boldsymbol{r_{2+}}\right) &= \mathbf{1} - \frac{\mathbf{1}}{\boldsymbol{r_{2+}}}\boldsymbol{exp}[\boldsymbol{A_6}\left(\mathbf{1} - \boldsymbol{r_{2+}}\right)]. \end{aligned} \tag{7.45}$$

The term $(\boldsymbol{f(r_K)})$ represents the coupling factor between damage laws and elastic threshold domains. The evolution law related to the damage variable $\boldsymbol{d_{1+}}$ consists of a linear softening response until the stress reaches the pull-out stress , $\boldsymbol{X_{PO}}$, with the energy dissipation per unit area given by $\boldsymbol{G_{1+}^{L}}$, followed by an exponential law with the energy dissipated per unit area is $\boldsymbol{G_{1+}^{E}}$. Thus the damage variables $\boldsymbol{d_{1+}^{L}}$ and $\boldsymbol{d_{1+}^{E}}$ are given by,

$$\begin{aligned} \boldsymbol{d_{1+}^{L}} &= \mathbf{1} + \frac{\boldsymbol{K_1}}{\boldsymbol{E_1}} - \left(\frac{\boldsymbol{K_1}}{\boldsymbol{E_1}} + \mathbf{1}\right)\frac{\mathbf{1}}{\boldsymbol{r_{1+}^{L}}}, \\ \boldsymbol{d_{1+}^{E}} &= \mathbf{1} - \frac{\mathbf{1}}{\boldsymbol{r_{1+}^{E}}}\boldsymbol{exp}\left[\boldsymbol{A_{1+}}\left(\mathbf{1} - \boldsymbol{r_{1+}^{E}}\right)\right], \end{aligned} \tag{7.46}$$

where $\boldsymbol{K_1}$ is the slope of the linear softening law. The damage thresholds, $\boldsymbol{r_{1+}^{L}}$ and $\boldsymbol{r_{1+}^{E}}$ are given by,

$$\begin{aligned} \boldsymbol{r_{1+}^{L}} &= \boldsymbol{max}[\mathbf{1}, \boldsymbol{min}\left(\boldsymbol{r_{1+}}, \boldsymbol{r_{1+}^{F}}\right)], \\ \boldsymbol{r_{1+}^{E}} &= \boldsymbol{max}\left[\mathbf{1}, \left(\mathbf{1} - \boldsymbol{d_{1+}^{F}}\right)\frac{\boldsymbol{X_T}}{\boldsymbol{X_{PO}}}\boldsymbol{r_{1+}}\right] \end{aligned} \tag{7.47}$$

where $\boldsymbol{r_{1+}^{F}}$ is the damage threshold function at the transition between the linear and exponential damage evolution laws.

The regularization of the energy dissipated per unit volume is performed by integrating the rate of energy dissipation for each failure mode. The energy dissipated in each failure mode must be independent of the element size and must be equal to the fracture energies measured experimentally,

$$\boldsymbol{g_M} = \int_{\mathbf{1}}^{\infty} \frac{\boldsymbol{\partial G}}{\boldsymbol{\partial d_M}}\frac{\boldsymbol{\partial d_M}}{\boldsymbol{\partial r_M}}\boldsymbol{dr_M} = \frac{\boldsymbol{G_M}}{\boldsymbol{l^{*}}}, \qquad \boldsymbol{M} = \mathbf{1+}, \mathbf{1-}, \mathbf{2+}, \mathbf{2-}, \mathbf{6}. \tag{7.48}$$

Using the damage evolution (7.44) and integrating the resulting equation it is possible to calculate the damage law parameters $\boldsymbol{A_M}$ that ensure a mesh-independent solution [170].

To guarantee the correct energy dissipation without a snap-back in the constitutive response, for each damage law $\boldsymbol{M}$, there is a maximum size for the finite element so that the elastic energy of the element at the onset of localization is lower or equal than the fracture energy. The maximum size for the finite element is,

$$\boldsymbol{l^* = \frac{2E_M G_M}{X_M^2}, \qquad M = 1+, 1-, 2+, 2-, 6} \tag{7.49}$$

where $\boldsymbol{E_M}$, $\boldsymbol{G_M}$ and $\boldsymbol{X_M}$ are the Young modulus, fracture energies and strengths respectively.

The computational implementation and validation of the model are described in detail in [138].

The CDM model as proposed by Maimí et al. was used to predict strength and size effects in notched carbon-epoxy laminates by Camanho et al. [171]. The CDM model predicted with good accuracy hole size effects in notched tensile specimens. Furthermore, the model provided not only the final failure load, but also information concerning the integrity of the material during the load history. Bessa [172] also used the CDM model proposed by Maimí et al. to predict the strength and failure model of open-hole carbon epoxy specimens subjected to tensile and compressive loading, and carbon-epoxy specimens subjected to off-axis loading. To take into account the physical progressive failure behaviour of fibres, matrix and interfaces between plies, Lopes et al. [173] extended the plane stress formulations proposed by Maimí et al. for in-plane behaviour and used the cohesive elements as proposed by Turon et al. [153] for the simulation of the interfaces between plies. González [174] also used a combination of the CDM model proposed by Maimí et al. and the cohesive elements proposed by Turon et al. [153] for the analysis of the low velocity impact event and subsequent compression after impact testing.

Chapter 8

Numerical Analysis of Hybrid Joints

8.1 Introduction

The reinforcement of composite joints by means of metal hybridization techniques, as previously presented in Chapter 2, has shown important potential design improvements in terms of joint simplification and weight efficiency. Extensive experimental research has been performed demonstrating the improved coupling efficiency by substituting CFRP plies for high-strength metal foils in the joining area [4–6, 15]. An increase in the bearing strength, in the coupling stiffness and a reduction of the sensitivity of the mechanical properties to the laminate configuration as well as environmental effects have been reported. The use of embedded metal plies has also the major advantage of eliminating any laminate thickening keeping the membrane loads undeflected and thus eliminating secondary stresses.

In this chapter, a numerical investigation of the mechanical response of bolted joints using hybrid composite laminates, based on the substitution of CFRP plies with Titanium plies is presented. Among the different failure modes of composite bolted joints, the non-catastrophic bearing failure mode is considered in this study. The objective is to advance the sate-of-the-art on the analysis methods of hybrid CFRP/Titanium joints by developing and validating advanced material models that enable accurate analysis of the composite and titanium components and also their interactions. Currently, the state-of-the-art analysis methods for the bearing response of CFRP-metal bolted joints are based on continuum damage models for the CFRP plies and on plasticity models for the metal sheets established with plane stress formulations [15]. These formulations are readily available in commercial finite element codes, however plane stress formulation cannot account for the pressure-dependent material response of the constituents used in the joints and the corresponding effect of the clamping pressure. Moreover, regarding the titanium plies, adequate constitutive models that account for the strength differential effect as well as the anisotropy have to be taken into account. Therefore, a fully three dimensional model for the bearing region was developed in Abaqus finite element code and suitable material models were included by means of adequate user defined materials subroutines (VUMAT). The VUMAT used for the titanium plies was detailed and

presented previously in Chapter 5 for the CPB06 constitutive model while the VUMAT for the mechanical constitutive behaviour of the CFRP plies was developed and implemented by Maimí et al. [7, 138, 170] and presented in Chapter 7. Maimí applies a combination of the LaRC03 and LaRC04 criteria for damage initiation [161, 164].

8.1.1 Transition region

A hybrid joint can be divided into three main sections: the bearing region, the transition region and the full composite region. In Figure 8.1 a schematic representation of the different regions considered in hybrid joints is shown.

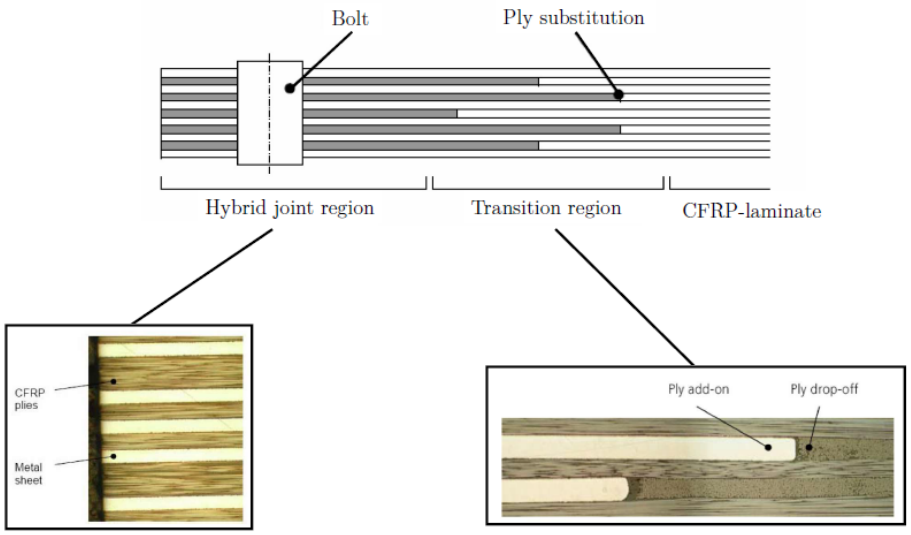

Figure 8.1: Hybrid composite regions.

In order to attain the full reinforcement capabilities of the hybridization, the transition region has to reach equal or better joint efficiencies in comparison to the bolt bearing region. Thus, the present study is mainly focused on the analysis of the bearing region as it governs the failure of the joint.

Experimental investigations concerning the transition zone, based on ply substitution methods, were conducted by Kolesnikov et al. [4] and Camanho et al. [15]. The experimental results clearly demonstrated that the transition region does not represent the weak point of the reinforcement technique as the hybrid joint does not fail prematurely at this zone. Higher strengths for the transition region were reported for all the specimens tested displaying different titanium contents. In this section, an overview of the most relevant aspects regarding the transition region will be addressed as the numerical analysis will focus solely on the critical region of the hybrid joint that is the bolt bearing region.

There are two main mechanisms that influence the strength of the transition region: the delamination of the interrupted plies of composite and metal and the overstressing of the continuous plies adjacent to the substitution points [14]. The delamination resistance is affected, on one hand, by the interlaminar fracture toughness, that depends on the matrix

properties, the fibre-resin interaction and the adhesion strength between the metal and the resin. On the other hand, delamination is affected by the total effective stiffness (modulus times thickness) of the metal sheets. Metal sheets with larger modulus and CTE, like steel, are more likely to delaminate than titanium sheets. Furthermore, the consideration of the laminate thickness on the design of the transition region is essential. This and compliant metal foils as well as a staggered configuration of the substitution points enable a smooth longitudinal and flexural stiffness change [175].

The efficiency of different transition region configurations, defined as the ratio of the transition region ultimate strength to the composite laminate ultimate strength, is shown in Figure 8.2.

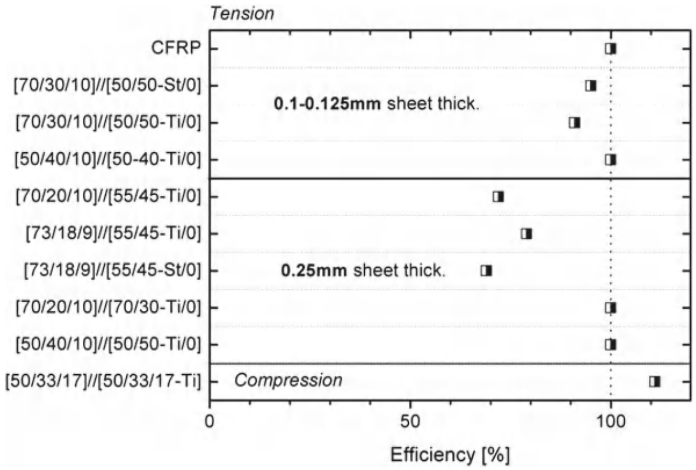

Figure 8.2: Strength efficiency of exemplary transition regions with different metal contents and sheet thicknesses under tension and compression loading [175].

The higher efficiencies are achieved under tension loading for transitions with no interruption of the 0^o layers irrespective of the foil thickness. The substitution of the load carrying 0^o plies leads to a reduction of the load capability, more pronounced for thicker metal sheets. Nevertheless, the efficiencies are still higher than the bolted joint's efficiency. In hybrid laminates with thinner foils, fibre failure due to overstressing is present while for steel laminates with thicker foils failure is triggered by delamination. For compression there is no strength loss in comparison to the reference composite laminate being the excess of efficiency associated to the peculiarities of compression testing [175].

8.2 Bolt bearing region

Taking into account that the strength of the transition region is higher than that of the bolt bearing region, the assessment of the hybrid bolted joint performance can be realized irrespective of the transition from the pure composite to the hybrid laminate. In this section a numerical investigation focused on the bolt bearing region is performed. The hybrid joint specimens representative of this region were defined from a reference conventional design where CFRP plies were substituted by Ti6Al4V titanium sheets. The geometry and dimensions of

the bearing laminates analysed are given in Figure 8.3 and Table 8.1 and ensure the promotion of a pure bearing failure.

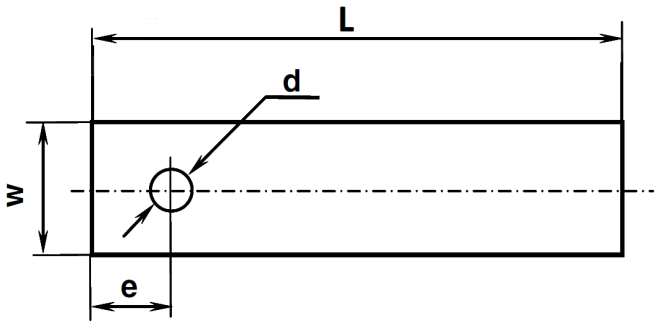

Figure 8.3: Geometry of the bearing test specimen.

Table 8.1: Dimensions of the bearing test specimen.

	Dimensions (mm)
Length, L	170
Width, w	45
Hole diameter, d	6.35
End distance, e	25
Thickness, th	3

Three hybrid laminates with different contents of titanium were simulated. The configuration and stacking sequence of the laminates together with the reference conventional design are given in Figure 8.4 and Table 8.2. A 6mm bolt was used and a washer with an outer-diameter of 12mm was considered on either side of the laminate.

Table 8.2: Stacking sequence of the bearing test specimen.

Specimen	Lay-up
Reference	$\mathbf{[0/+45/0/90/-45/0]_s}$
L6	$\mathbf{[0/+45/0/}\mathrm{Ti}\mathbf{/-45/0]_s}$
L7	$\mathbf{[0/}\mathrm{Ti}\mathbf{/0/90/}\mathrm{Ti}\mathbf{/0]_s}$
L8	$\mathbf{[0/}\mathrm{Ti}\mathbf{+45/0/}\mathrm{Ti}\mathbf{90/}\mathrm{Ti}\mathbf{-45/0]_s}$

On the L6 laminate the 90° ply is substituted by the titanium sheet due to their lowest load carrying capability whereas on the L7 specimen the $\mathbf{\pm 45^o}$ are substituted. The 0° plies which contribute most to the total load carrying are maintained uninterrupted and pass through the transition zone into the bearing region assuring also the adhesion between the inserted metal plies.

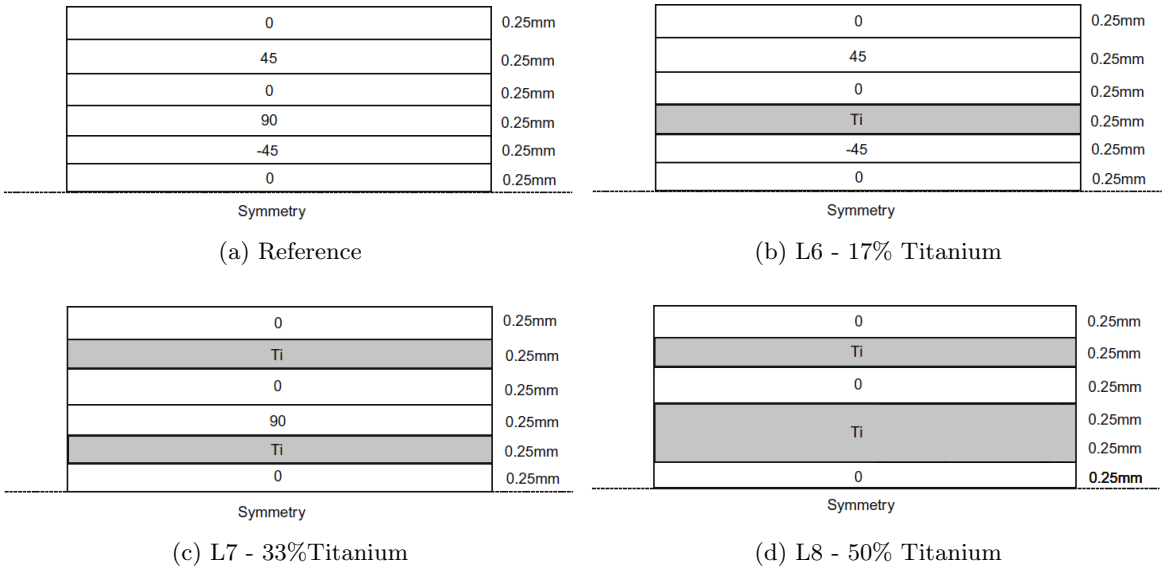

(a) Reference

(b) L6 - 17% Titanium

(c) L7 - 33%Titanium

(d) L8 - 50% Titanium

Figure 8.4: Configuration of the bearing test specimens.

8.2.1 Material characterization

The materials used in the hybrid joint are the Ti6Al4V titanium alloy and the IM7-8552 CFRP. The standard material properties of the IM7-8552 are given in Table 8.3. $\boldsymbol{X_T}$ and

Table 8.3: Ply elastic properties and strengths of IM7-8552 carbon epoxy.

$\boldsymbol{E_1}$ (MPa)	$\boldsymbol{E_2 = E_3}$(MPa)	$\boldsymbol{G_{12} = G_{13}}$(MPa)	$\boldsymbol{G_{23}}$(MPa)	$\boldsymbol{\upsilon_{12} = \upsilon_{13}}$(-)	$\boldsymbol{\upsilon_{23}}$(-)
171420	9080	5290	3980	0.30	0.5
$\boldsymbol{X_T}$(MPa)	$\boldsymbol{X_C}$(MPa)	$\boldsymbol{Y_T}$(MPa)	$\boldsymbol{Y_C}$(MPa)	$\boldsymbol{S_L}$(MPa)	
2226.2	1200.1	62.3	199.8	92.3	

$\boldsymbol{Y_T}$ are the longitudinal and transverse ply tensile strengths respectively, $\boldsymbol{X_C}$ and $\boldsymbol{Y_C}$ are the ply longitudinal and transverse compressive strengths respectively and $\boldsymbol{S_L}$ is the ply in-plane shear strength. The coefficients of thermal expansion are given in Table 8.4.

Table 8.4: Coefficient of thermal expansion of IM7-8552 carbon epoxy.

	Coeficient of thermal expansion ($/^o$)
$\boldsymbol{\alpha_{11}}$	$\boldsymbol{-5.5 \times 10^{-6}}$
$\boldsymbol{\alpha_{22}}$	$\boldsymbol{25.8 \times 10^{-6}}$

The in-situ ply strengths were also considered and are given in Table 8.5. The in-situ effect is characterised by higher transverse and shear strengths for a ply constrained by plies with different fibre orientations when compared to the strengths of the same ply in a unidirectional

laminate. The in-situ strengths can be calculated as proposed by Camanho et al. [176]. The other necessary material properties to the model are the fracture energies given in Table 8.6.

Table 8.5: In-situ strengths for IM7-8552 carbon epoxy.

Ply configuration	Y_{is}^{T}	S_{is}^{L}
thin outer	101.4	107.0
thin embedded	160.2	130.2
thin embedded (2t)	113.3	107.0

Table 8.6: Fracture energies (kJ/m^2).

	Fracture Energies (kJ/m^2)
Fibre tension, G_{1+}	81.5
Fibre compression, G_{1-}	106.5
Matrix tension, G_{2+}	0.28
Matrix compression, G_{2-}	5.62

The titanium alloy used in the metal plies was the two phase α-β Ti6Al4V where the α-phase represents 94% of the volume. The experimental characterization of Ti6Al4V titanium alloy in quasi-static conditions at room temperature was performed by Tuninetti et al. [34] for an initial ingot form and by Gilles et al. [33] in sheet form. Tension-compression asymmetry as well as anisotropic yielding and anisotropic strain-hardening were reported in both studies. The elastic properties of the Ti6Al4V used in this study are shown in Table 8.7. The yield strengths for the longitudinal (LD), transverse (TD) and small transverse (ST) direction for tension and compression are given in table 8.8.

Table 8.7: Elastic parameters of Ti6Al4V.

Young modulus, E (GPa)	Poisson ratio, υ
111	0.3

Table 8.8: Experimental yield stresses of Ti6Al4V.

Test	Direction	Yield strength, σ_0 (MPa)
Tension	LD	927
	TD	933
	ST	941
Compression	LD	968
	TD	1040
	ST	1002

The full characterization of the Ti6Al4V alloy requires also the definition of a hardening curve. In this study the isotropic hardening is defined by a representative hardening curve that is used as input for the VUMAT subroutine. The hardening curve in the longitudinal direction was used. A Voce type hardening law expressed as,

$$\boldsymbol{Y(\bar{\varepsilon}_p) = A_0 + B_0 exp(-C_0 \bar{\varepsilon}_p)}, \tag{8.1}$$

was adopted with the parameters given in table 8.9.

Table 8.9: Voce hardening law parameters.

A_0	B_0	C_0
1070	150	20.0

Because the rate of hardening for the Ti6Al4V depends on the loading direction, evolving anisotropic coefficients were considered. The determination of the anisotropic coefficients for several values of equivalent plastic strain was previously explained in Chapter 4. In table 8.10 the anisotropic coefficients used in this study for the characterization of the titanium alloy are given.

Table 8.10: Anisotropic coefficients for the yield function CPB06 for Ti6Al4V.

$\bar{\varepsilon}_p$	C_{11}	C_{12}	C_{13}	C_{22}	C_{23}	C_{33}	$C_{44} = C_{55} = C_{66}$	k
0.0	1.0	-2.373	-2.364	-1.838	1.196	-2.444	-3.607	-0.136
0.01	1.0	-2.495	-2.928	-2.283	1.284	-2.446	4.015	-0.136
0.05	1.0	-2.428	-2.920	1.652	-2.236	1.003	-3.996	-0.165
0.1	1.0	-2.573	-2.875	1.388	-2.385	0.882	-3.926	-0.164
0.2	1.0	-2.973	-2.927	0.534	-2.963	0.436	-3.883	-0.180

8.2.2 Finite element model

The finite element models developed for the simulation of the bolt bearing region were performed in Abaqus/Explicit using a three dimensional approach in which the material models were implemented in a VUMAT subroutine for both the CFRP and titanium plies. Additionally, a two dimensional approach using the built-in Abaqus material models which are based on the Hashin criteria [177] for CFRP progressive damage modelling and an elastic-plastic material model for the titanium plies based on the von Mises criterion and isotropic hardening was performed.

Depending on the approach, different finite element models need to be considered: the Abaqus built-in models for the CFRP progressive damage is limited to elements with plane-stress formulation, hence continuum shell elements (SC8R) were used for the composite plies while for the VUMAT models three-dimensional continuum elements with one integration

point (C3D8R) were used throughout. Two levels of mesh refinement were considered. A finer mesh was defined near the hole, where damage takes place, using elements with an average dimension of **0.25**mm×**0.25**mm×**0.25**mm. Away from the hole a coarser mesh approximately four times less refined was used. In the coarse mesh a linear-elastic response was adopted for both the composite and titanium plies. In the mesh transition region a TIE constraint connecting the two meshes was used to ensure a correct stress distribution. In the thickness direction each ply was discretized with one element per ply thickness. The bolt and the washer were modelled using three dimensional C3D8R elements. Both the bolt and the washer were given a linear elastic material model. Taking into account the symmetry conditions of the specimens analysed, one fourth of the L7 and L8 specimens and half of the reference and L6 specimens were considered. Adequate symmetry boundary conditions were applied to the laminates symmetry planes. The presence of the $\pm\mathbf{45^o}$ CFRP layers in the reference and L6 specimens prevent the application of symmetry conditions on the longitudinal direction on these specimens. The finite element model, including the symmetry boundary conditions and mesh, is shown in Figure 8.5.

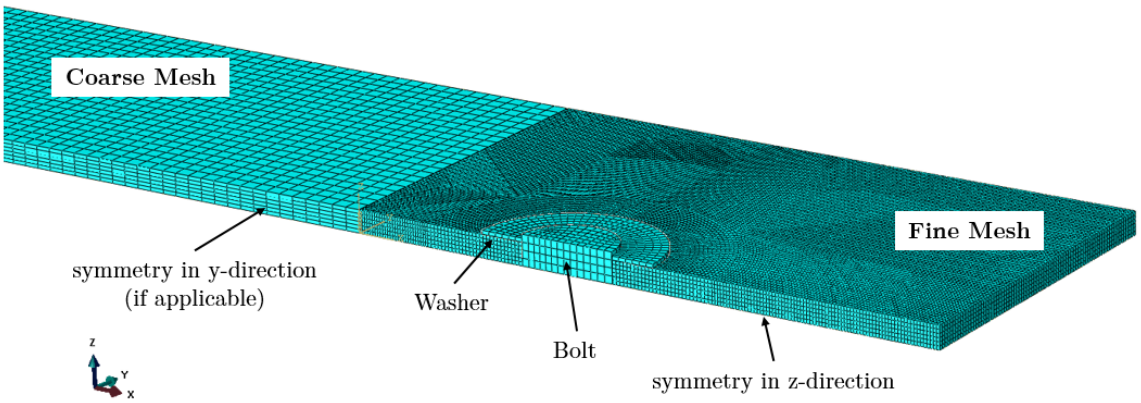

Figure 8.5: Finite Element model of the bearing specimens.

An initial step applying a clamping pressure, corresponding to the bolt torque, was first applied. The following step imposed a displacement on the bolt on the longitudinal axis.

Contact interactions between the bolt and the surface of the hole and the washer and the surface of the first ply were defined. Friction was modelled between the bolt and the laminate using a penalty approach and a coefficient of friction of 0.3.

To reduce the computational cost of the quasi-static analysis mass scaling was used and to assure that the finite element model produces a valid quasi-static response the energy balance was evaluated to guarantee that the kinetic energy of the model remains sufficiently small. As a general rule, for a quasi-static analysis, the kinetic energy of the deforming material should not exceed a small fraction (typically 5% to 10%) of its internal energy throughout most of the process [177].

8.2.3 Numerical Results and discussion

The bearing stress curve versus the hole displacement of the Reference, L6, L7 and L8 laminates obtained from the Abaqus built-in models were evaluated and compared with the solutions obtained from the full 3D numerical models using the VUMAT user subroutines. The bearing stresses for the hybrid laminates were also compared with the bearing stresses of the full CFRP Reference laminate and the impact of the hybridization technique on the bearing strength of the joints was assessed.

The bearing stress is defined as,

$$\boldsymbol{\sigma_b} = \frac{\boldsymbol{P}}{\boldsymbol{dt}}, \tag{8.2}$$

were $\boldsymbol{P}$ is the load, $\boldsymbol{d}$ the diameter of the hole and $\boldsymbol{t}$ the thickness of the laminate. The predicted bearing stress versus the bolt displacement for the built-in Abaqus models and the VUMAT models for all specimens analysed are given in Figure 8.6. A linear elastic region and a nonlinear region triggered by damage onset can be identified.

The consideration of 3D formulations in the finite element models has a significant impact on the bearing strength predictions of the joint for all the laminates tested. As can be seen from the bearing stress-hole displacement curves, greater divergences were obtained for the full CFRP laminate and closer solutions were obtained for the laminates with higher metal contents. The titanium plies are, irrespective of the models used, simulated with three dimensional continuum elements. Moreover, the titanium plies are oriented along the longitudinal direction (LD) and thus the solutions obtained from the von Mises and CPB06 models are not expected to differ significantly as the input data for the Abaqus built-in models is obtained from the experimental stress-strain values for this direction. Therefore, the higher the number of titanium plies in the laminate the closer the Abaqus models and VUMAT models predictions are and thus the differences are attributed mainly to the formulations used in the composite plies. For the 2D simulations using the Abaqus built-in models, the composite plies are modelled with continuum shell elements that, although are volumetric elements, can only predict the in-plane components of the stress tensor. The out-of-plane components of the stress tensor are therefore not taken into account. Furthermore, the Hashin built-in criteria does not take into account the effect of the shear stresses in the prediction of fibre kinking failure onset. However, as it is known, the in-plane shear stresses have an important role in fibre kinking as they reduce the compressive strength of a ply and their absence in the failure criteria results in an over prediction of the elastic limit of the joint [161].

The bearing stresses at the onset of the inelastic bearing response and the maximum bearing stresses obtained are resumed in Table 8.11.

Concerning the assessment of the impact of the hybridization technique on the bearing stresses, the values predicted by the full 3D models were analysed. The bearing stress-bolt displacement relations for all laminates are given in Figure 8.7. The predicted maximum bearing stresses and bearing stresses at the onset of non-linear response of the joint with the correspondent percentage increase relative to the reference laminate, for all the laminates analysed, are resumed in Table 8.12.

Table 8.11: Bearing strengths and bearing stresses at the onset of non linearity (ONL) obtained from Abaqus built-in models and VUMAT models.

	σ^b_{max} - Abaqus built-in models (MPa)	σ^b_{max} - VUMAT models (MPa)	Δ (%)
Reference	918	679	-26.0
L6	1140	940	-16.8
L7	1348	1144	-14.8
L8	1551	1322	-14.7
	σ^b_{ONL} - Abaqus built-in models (MPa)	σ^b_{ONL} - VUMAT models (MPa)	Δ (%)
Reference	740	590	-20.2
L6	850	728	-14.3
L7	853	775	-9.1
L8	978	907	-7.2

Table 8.12: Predicted bearing strength and bearing strength increase relative to the reference laminate value.

	Reference	L6	L7	L8
σ^b_{max} (MPa)	679	940	1144	1322
Δ (%)	NA	+38.4	+68.4	+94.6
σ^b_{ONL} (MPa)	590	728	775	907
Δ(%)	NA	+23.3	+31.3	+53.7

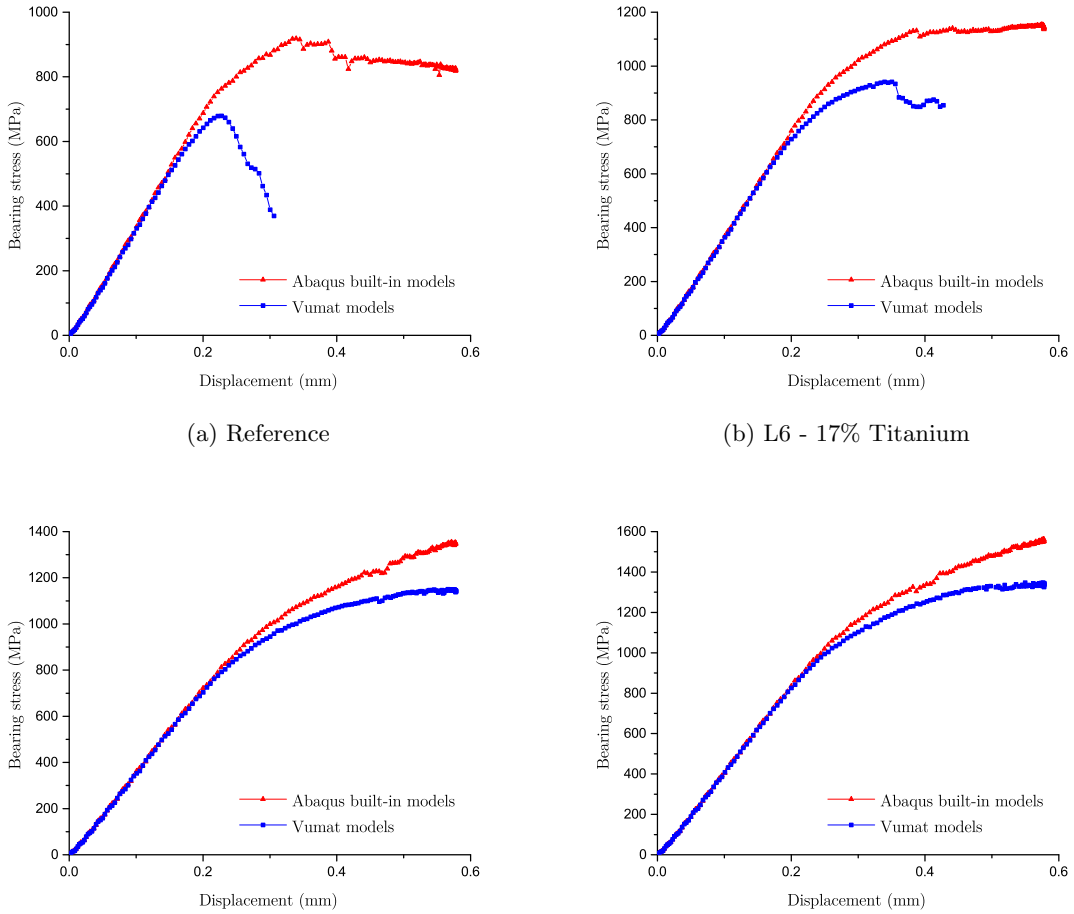

(a) Reference

(b) L6 - 17% Titanium

(c) L7 - 33%Titanium

(d) L8 - 50% Titanium

Figure 8.6: Bearing stress vs bolt displacement for built-in Abaqus models and VUMAT implemented models.

The results show that the bearing strength increases with increasing titanium content which is in accordance with the experimental evidence [5, 6, 15]. With the addition of one titanium ply (L6 laminate) a bearing strength increase of 38% can be achieved, further increased with the increasing value of titanium content up to 94% for 50% of titanium content. Relatively to the bearing stress at the onset of nonlinearity, the increase of titanium content on the laminate also contributed to an increase on the bearing stress when compared to the reference full CFRP laminate. With the addition of one titanium ply an increase of 23% was obtained and for the L8 laminate with a titanium content of 50% an increase of 62.7% was obtained. Comparing the bearing curves of the hybrid laminates with the reference laminate, a metal-like hardening effect is evidenced by the hybrid laminates with a steady increase of the load bearing capability within the plastic region. The full composite reference laminate shows a drastic drop of strength typical of laminated materials subjected to bolt bearing testing. The onset of the nonlinear bearing response for both the reference and hybrid laminates takes place at a bolt displacement of approximately 0.2mm. The maximum bearing stresses,

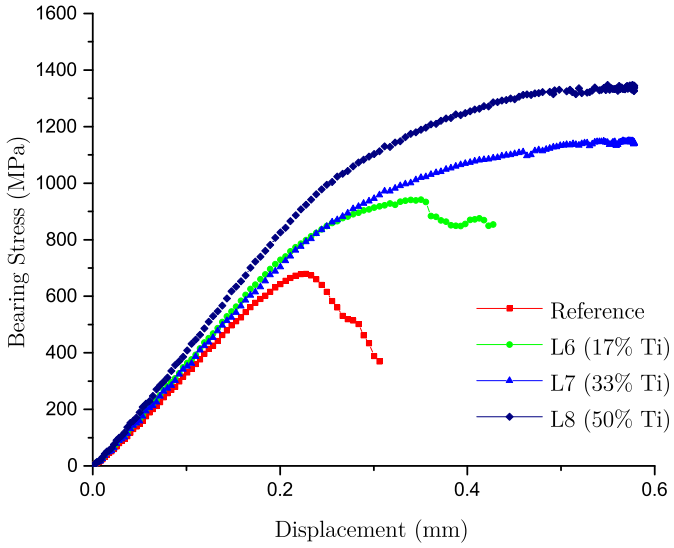

Figure 8.7: Bearing stress versus bolt displacement relations.

however, are reached at higher bolt displacements for the hybrid laminates when compared to the full composite laminate.

The bearing failure mode characterized by the progressive elongation of the hole and the compression of the laminate under the bolt-hole contact area was predicted for all laminates. The onset and evolution of damage for the 0^o ply at the onset of the nonlinear response and at the maximum bearing stress is depicted in Figure 8.8 for all laminates. Under bolt bearing loading the onset of nonlinearity is governed by the damage initiation and propagation at the 0^o plies with typical kink band formations at the bearing contact surface. At the maximum bearing stress damage had fully propagated within and beyond the washer supported area. The hybrid laminates are still capable of carrying increasing loads even with large degradation of the composite plies.

For the metal plies in the hybrid laminates, the damage onset is mainly related to the plastic zone at the notch root. At the onset of the inelastic bearing response of the joint, at the titanium plies, the level of the equivalent plastic strain is small and localized and significantly lower than the titanium's ultimate elongation (Figure 8.9). The impact of the strength of the metal sheets is therefore limited on the onset of damage as the composite plies start to deteriorate and trigger the nonlinear response. As the degradation of the composite plies develops there is an overloading of the titanium plies that start to develop high plastic strains. As was seen, higher metal contents on the hybrid laminates relieve the composite plies and allow larger stresses at the onset of damage.

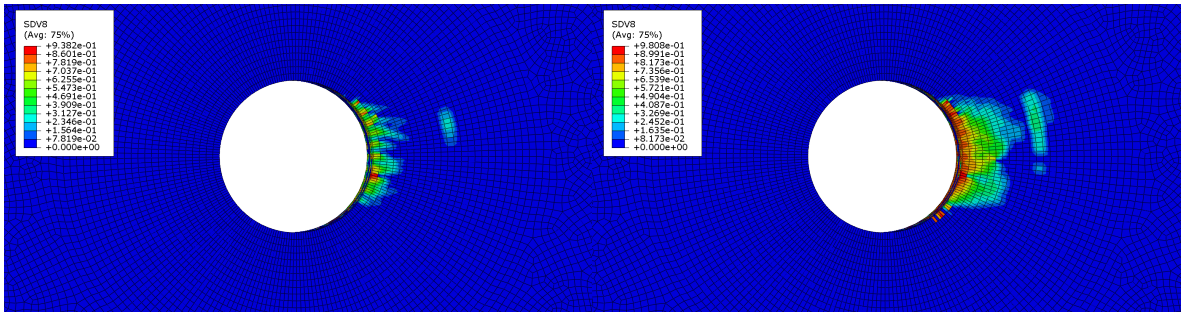

(a) Reference at the onset of nonlinear response. (b) Reference at maximum bearing stress.

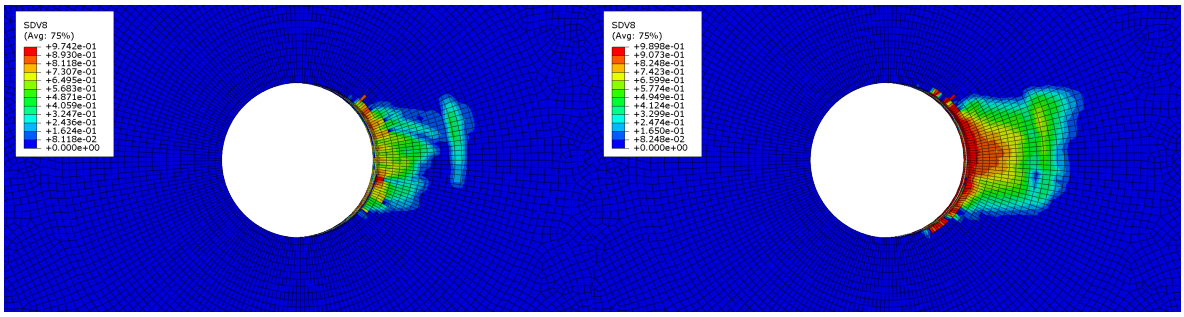

(c) L6 at the onset of nonlinear response. (d) L6 at maximum bearing stress.

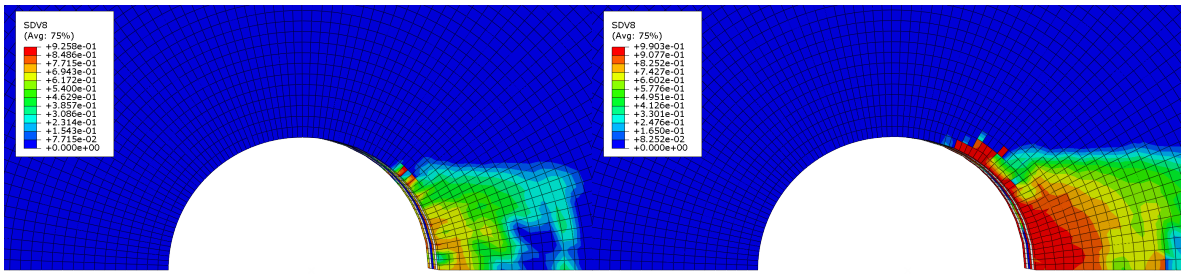

(e) L7 at at the onset of nonlinear response. (f) L7 at maximum bearing stress.

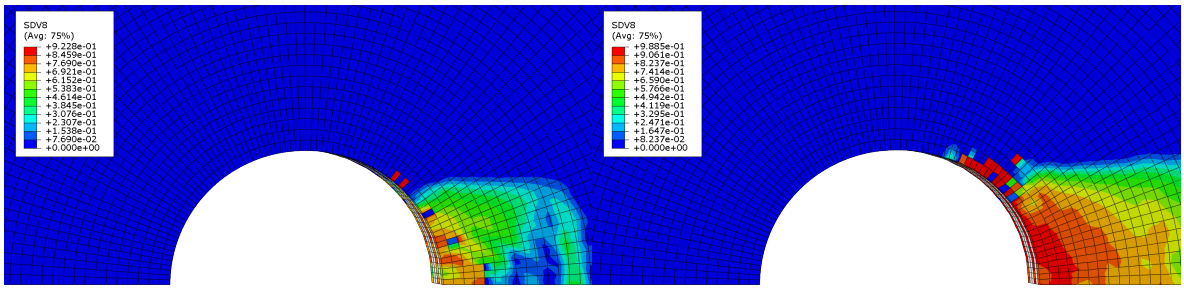

(g) L8 at the onset of nonlinear response. (h) L8 at maximum bearing stress.

Figure 8.8: Compressive damage for a 0^o ply at the onset of nonlinear response and at the maximum bearing stress.

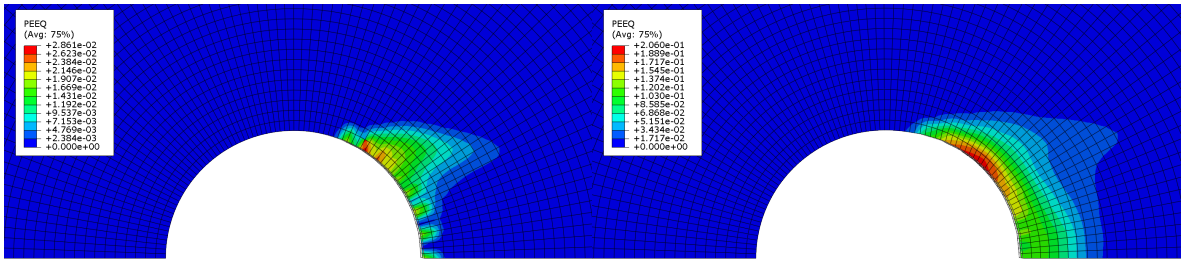

(a) Equivalent plastic strain at the onset of nonlinear response.

(b) Equivalent plastic strain at the maximum bearing stress.

Figure 8.9: Evolution of the equivalent plastic strain of a titanium ply.

Clamping Pressure

It is generally accepted that simulations based on two-dimensional finite element modelling give sufficiently accurate results for the majority of linear composite laminate analysis with a reasonable computational effort. However, in bearing analysis of bolted joints a three-dimensional approach is crucial in order to account for the through thickness stresses (clamping forces) which are known to have a significant impact on the initiation of bearing damage [178]. To evaluate the impact of the clamping forces on the simulations based on two and three-dimensional formulations, three different levels of clamping pressure were considered: 2.5, 22 and 40 MPa. For the finite element models based on the Abaqus built-in 2D formulations, the increase of the clamping pressure had no effect on the predicted bearing strengths or the bearing stresses at the onset of non linear response of the joint, as can be seen in Figure 8.10a for the L6 laminate. The VUMAT models on the other hand, are capable of capturing the clamping pressure effect by taking into account the through-thickness effects developed as shown in Figure 8.10b for the L6 laminate.

The effect of the clamping force on the maximum bearing stress and on the bearing stress at the onset of the non linear response of the joint was evaluated for all the laminates analysed. The results are shown in Figure 8.11 .

The increase of the clamping pressure caused a slight increase of the bearing stress at the onset of the non linear response of the joint for all laminates. Although small, this increase was more evident for the L7 and L8 laminates while for the full CFRP laminate and the L6 laminate the values remained almost constant. Therefore, the lateral constraint provided by the washer and the embedded titanium sheets had beneficial effect on the onset of damage. The lateral supports are known to offer constraints on the damage material under bearing failure. Concerning the maximum bearing stress both the full CFRP laminate as well as the L6 laminate had a slight increase of the bearing strength with increasing values of the clamping pressure while the L7 and L8 laminates evidenced slight decreases. The L7 and L8 laminates have higher number of titanium plies and the higher clamping pressures may cause excessive compression of the CFRP plies in between the metal plies.

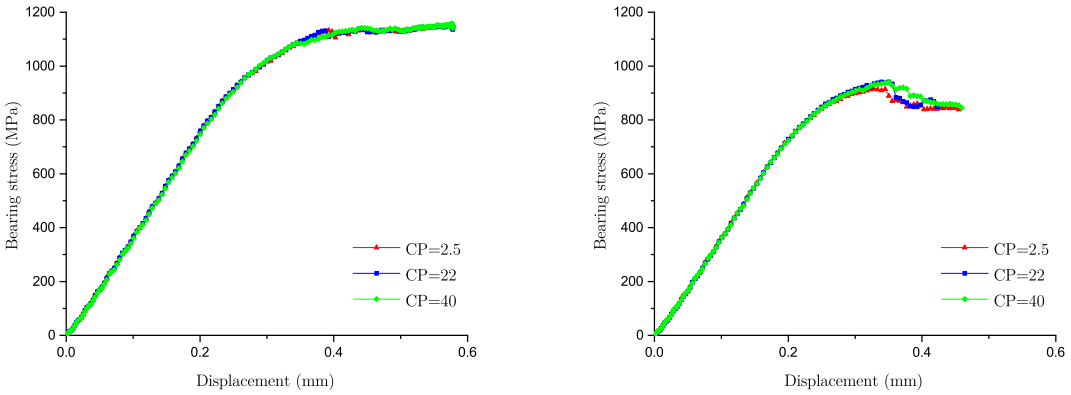

(a) L6 with Abaqus built-in models

(b) L6 with VUMAT models

Figure 8.10: Effect of clamping pressure on bearing stress vs bolt displacement for built-in Abaqus models and VUMAT implemented models.

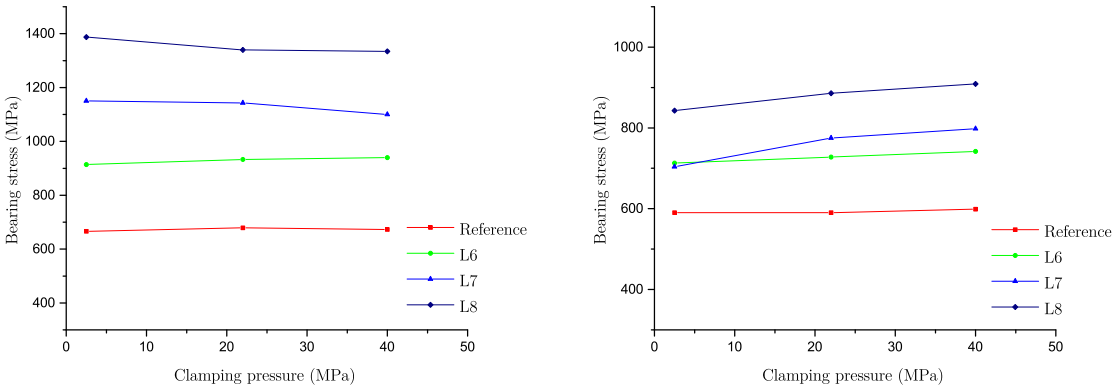

(a)

(b)

Figure 8.11: Effect of clamping pressure on: (a) the maximum bearing stress and (b) bearing stress at the onset of nonlinearity.

Orientation of Titanium plies

The different behaviour of the titanium alloy under tension and compression and the anisotropy can be correctly modelled with the CPB06 constitutive model implemented via VUMAT user subroutine in the simulations of the bolted joint. Therefore, the impact of considering different titanium orientations could be captured and simulations of the joint considering different orientations of the titanium plies were performed.

The impact of the orientation of the titanium ply on the bearing strength was evaluated. The predicted bearing strength of the joint using titanium plies oriented along LD was compared with the predicted bearing strength obtained with the titanium plies oriented along

TD. The results are shown in Figure 8.12. Note that this difference between the orientations of the titanium cannot be captured using the Abaqus built-in von Mises elastoplastic material model.

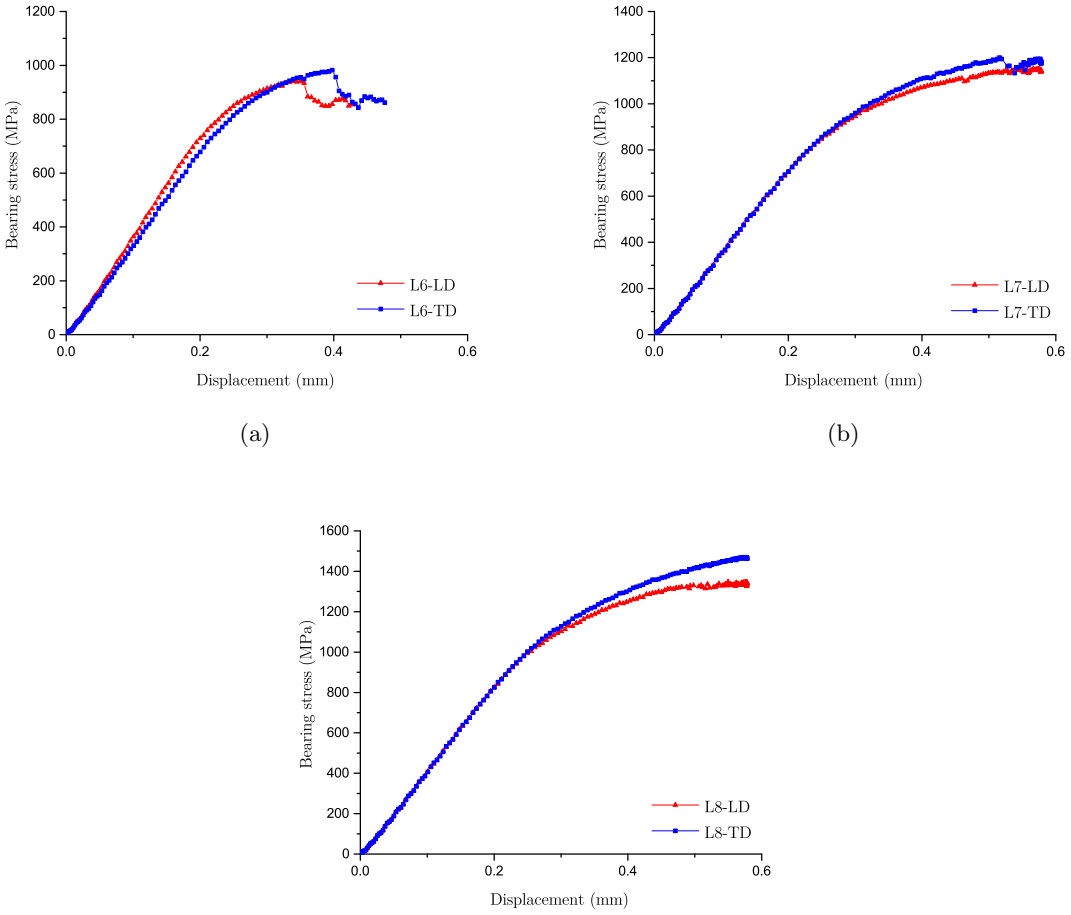

Figure 8.12: Predicted bearing stress-bolt displacement with titanium plies oriented along the LD and TD directions.

The bearing stress versus bolt displacement for the specimens analysed demonstrate a slightly higher bearing strength for the cases where the titanium plies are oriented in the TD direction. The strength differential behaviour found in titanium and titanium alloys reflects on the prediction of the bearing behaviour of the joint. Particularly in the case of the Ti6Al4V, higher strengths are found in the transverse direction when compared to the longitudinal direction especially for compressive states. These larger strengths of the reinforcing material result in a higher reinforcement effect. Also, the impact on the bearing strength of the joint is more noticeable in the specimens with higher titanium contents, L7 and L8, when compared to the L6 specimen.

The onset of the non linear behaviour is not significantly affected by the orientation

of the titanium plies as it is mainly governed by the deterioration of the composite plies. The effect of strength increase is therefore limited due to the damage accumulation on the composite plies that induce overstressing of the metal constituent. Thus, the damage onset on the hybrid laminate does not depend on the strength of the titanium. With the start of the deterioration of the composite, the resistance of the metal sheets against transversal deformation and buckling becomes the driving factor of the ultimate bearing capabilities.

Chapter 9

Conclusions and Future work

In this study, an extensive research concerning the state-of-the-art of a joint reinforcement method, by means of local hybridization techniques using titanium, was performed. Although promising results were obtained in space applications, extending this technology, particularly to the aircraft industry, requires better understanding and predictability of the mechanical behaviour of the titanium/CFRP hybrid joints. Advanced simulation methods as the ones presented in this work can contribute to the development and widespread use of advanced joining techniques increasing the use of composite materials in load carrying structures. In this chapter, the main conclusions and relevant results deriving from this work are presented. Following the promising perspectives regarding the utilization of hybrid joints, a set of research and development trends that will contribute to the progress of this reinforcing method are discussed.

9.1 Conclusions

The use of a local reinforcement technique using metal plies has proven to be an efficient way of improving the load capability of bolted joints. The main advantages of the use of this technique were demonstrated through aerospace applications where important weight savings, reduction of the number of bolts and design simplifications have been achieved. Experimental results evidenced the increase in the bearing strength for the hybrid joints with titanium and steel reinforcements in comparison to CFRP laminates. Additionally, an increase of the bearing strength of the hybrid joints with rising metal content was observed. The higher metal strengths also had a direct impact on the reinforcement effect although it is limited due to the damage onset of the composite plies. The largest improvements were registered with the use of steel as the reinforcing material. The mechanical response of the transition region is also crucial for the joint efficiency as it contains material discontinuities that may induce delaminations and are a source of stress concentrations. The superior strength of the transition region was demonstrated ensuring that this is not the week point of the reinforced joint and thus enables the full exploitation of the load capability of the bolted joint.

Accurate analysis methods for hybrid CFRP/metal joints enable a faster and more economic development of this reinforcement technique. Numerical studies of the inelastic re-

sponse of hybrid CFRP/titanium bolted joints were conducted and good predictions were obtained [15]. However, the use of the existing analysis methods implemented in finite element codes did not accounted for the through thickness effects nor the out-of-plane deformation of the plies. For the development of advanced simulation methods capable of accurately predicting the failure behaviour of hybrid laminate joints, proper damage models for the metal and composite plies have to be used.

A review of a continuum damage model for polymer composites that predicts the onset and evolution of intralaminar failure mechanisms was given. Additionally, new yield criteria capable of predicting the plastic deformation of titanium sheets, including the strength differential effect and the evolving anisotropy, were reviewed. The CPB06 proposed by Cazacu, Barlat and Plunkett [52] and the Nixon criteria [32] were selected and were implemented in Abaqus via a VUMAT subroutine. The reliability of these models is, however, strongly dependent on the identification of their parameters. More sophisticated material models tend to have larger number of parameters and thus more advanced identification techniques are required. A mixed optimization technique based on local and global search procedures was used for the identification of both the CPB06 and Nixon material parameters for the Ti6Al4V titanium alloy. The global search was performed using a genetic algorithm and it was demonstrated that only the neighbourhood of the optimum point could be achieved. On the other hand, local search methods like the Nelder-Mead algorithm are strongly dependent on the initial guess and, although simple, the solution tends to converge rapidly to a local minimum. The combination of the two algorithms allowed a more efficient optimization by performing a local search on the vicinity of the global minimum previously identified by the genetic algorithm. The yield locus for several levels of equivalent plastic strain were obtained for the Nixon and CPB06 model determined with the optimized yield function parameters. A good agreement between the predicted yield curves and the experimental data was found. Both models were able to predict the yield locus of the titanium alloy studied. A slightly distorted shape was observed which is compatible with the deformation behaviour of hexagonal closed packed metals.

The computational implementation of the elastoplastic constitutive model based on the yield criterion proposed by Cazacu, Plunket and Barlat (CPB06) and the criterion proposed by Nixon was performed. The models were firstly validated with single element simulations under uniaxial tension and compression along the longitudinal, transverse an small transverse directions and under simple shear. Next, compression and tension simulations were performed on elliptical and notched specimens, respectively. Both the anisotropy and the tension/compression asymmetry were evidenced on single element tension and compression tests. Also a good agreement was found between the predicted and experimental results in terms of the stress-strain response for the uniaxial tests and in terms of the load-displacement and final shapes for the tensile simulations of the axisymmetric notched specimens and the compression test on the elliptical specimen. A slightly higher deviation from the experimental curves was observed mostly for the Nixon model. It is noteworthy that, as previously mentioned, the accuracy of the models is highly dependent on the materials parameters that in turn depend on the experimental data used for its calibration. Thus, by using a greater number of input data the accuracy of the models could be increased particularly for the Nixon model that depends on considerably less material parameters than the CPB06.

Additionally to the plastic deformation behaviour the study was extended to the ductile

damage modelling of titanium and other hcp metals. The development of adequate macroscopic elastoplastic constitutive models capable of capturing the specifics of deformation behaviour of hcp materials has seen significant development with a number of yield criteria being proposed in the last decades. On the contrary, the comprehension of the damage processes in titanium and other hcp metals is still limited. The assessment of damage evolution and fracture in titanium and its alloys and also in other materials with tension/compression asymmetry was performed firstly following an uncoupled damage approach. Uncoupled damage models neglect the effects of damage on the yield surface of the materials, nevertheless, due to their simplicity they are widely used in the industry. A number of relevant uncoupled fracture criteria were implemented in a VUMAT subroutine and the fracture initiation site was predicted for a smooth and a notched axisymmetric specimen under uniaxial tensile loading. The results demonstrated that for the smooth specimen all fracture criteria predicted correctly the fracture initiation whereas for the notched specimen different results were obtained depending on the fracture indicator. It was seen that the notched specimen, due to presence of the notch, reaches a higher stress triaxiality in the centre which corresponds to the fracture initiation site. The influence of the stress triaxiality in the fracture prediction was only captured by the models proposed by Lemaitre and Vaz Jr. that demonstrated the correct prediction of the fracture initiation site. Notwithstanding the advantages of the uncoupled approach, uncoupled fracture criteria neglect the effects of damage on the yield surface of the material and estimate failure without considering the relevant physical background. Thus, a coupled approach based on the continuum ductile damage developed by Lemaitre was used. Lemaitre's damage model is however based on the assumption that the plastic behaviour is governed by the von Mises criterion which, as it is known, is inadequate for hcp materials. In this work, a fully coupled continuum damage model with elastoplastic CPB06 criterion has been proposed. The model was implemented on a VUMAT subroutine and finite element simulations of damage evolution and fracture initiation were performed for an axisymmetric smooth and notched Ti6Al4V specimen. The implemented model showed good results in the prediction of deformation and damage evolution. The numerical influence of the material's tension/compression asymmetry on damage distribution was also assessed. The analyses of the damage initiation and evolution of a notched axisymmetric tensile specimen for different strength differential parameters demonstrated that the finite element predictions of damage onset and evolution are strongly influenced by this parameter.

Finally, a numerical investigation on the mechanical response of bolted joints using local hybrid composite laminates was performed. The hybridization was based on the substitution of CFRP plies with titanium plies of Ti6Al4V alloy and three different laminates were tested with increasing titanium contents (17%, 33% and 50%). The simulation was firstly performed using the material models available in the Abaqus software, which included the von Mises yield criterion together with isotropic hardening for the titanium plies and a progressive damage model based on the Hashin failure criteria for the composite plies. The Abaqus built-in composite damage model is limited to plane stress formulations and therefore neglects the through-thickness effects on the prediction of the bearing behaviour of the hybrid joints. Thus, the bearing failure behaviour of hybrid joints requires the use of adequate full 3D material models for the composite plies and adequate constitutive models capable of capturing the specificity of the behaviour of the titanium plies. The implemented models were capable of capturing the out-of-plane stresses developed along the hole of the laminate that play an important role in the prediction of the failure behaviour of the joint. Concerning the

analysis of the titanium content, the comparison with the monolithic CFRP laminate showed an increase of the bearing strength of the hybrid laminates with the increasing titanium content. With the implemented models, the impact of different orientations of the titanium plies could be captured and bearing strength of the hybrid joints was assessed. It was seen that higher bearing strengths could be obtained with the transverse direction of the titanium plies oriented along the longitudinal direction of the laminate. This effect was more evident in the laminates with higher titanium contents. Furthermore, the impact of the clamping pressure on the bearing strength was assessed by simulating the hybrid joints for different bolt torques. The results showed slight increases for the bearing stresses at the onset on the non linear bearing behaviour showing a beneficial effect of the lateral constraint provided by the washer and the titanium sheets on the onset of damage.

9.2 Future work

Overall the present work aimed to be a contribution towards the development of innovative reinforcement techniques that can overcome the lower characteristics of composite joints enabling the continued integration of composites into aircraft structures. The development of advanced simulation methods that can contribute to a better understanding of the mechanical behaviour of the hybrid joints, including its failure behaviour is a key aspect once it enables virtual testing reducing the amount of expensive and time consuming physical testing. Nevertheless, a number of difficulties and challenges still need to be undertaken in order to advance this reinforcement solution into broader applications like highly loaded aircraft structures.

For application in aircraft structures an important issue concerns the long term requirements including impact damage, fatigue behaviour or the long term behaviour of the joints under consideration of environmental effects. Also the inspection and repair aspects need to be taken into account. Other important issues that need to be addressed concern the assessment of the adequacy of the different specific manufacturing processes to the production of hybrid laminates that can meet the aircraft industry production standards and volumes.

An important step in the continuity of the present work would be the implementation of the technology in real structures that would allow suitability and feasibility investigation regarding hybridization sequences, substitution strategies, material choices and the consideration of specific design solutions including the joint adjacent elements, the simplification of the joint design or the ability to transform a metal part to a more weight-efficient composite part.

Finally, a comprehensive experimental test program needs to be carried out to enable further validation of the numerical models presented in this work, comprising not only the elastoplastic behaviour and damage phenomenon on titanium alloys but also their accuracy and efficiency in the simulation of more complex structures.

Bibliography

[1] P. Camanho and S. Hallett, editors. *Composite Joints and Connections: Principles, Modelling and Testing*. Woodhead Publishing, October 2011.

[2] R. Li, D. Kelly, and A. Crosky. Strength improvement by fibre steering around a pin loaded hole. *Composite Structures*, 57(1–4):377 – 383, 2002.

[3] P.P. Camanho, C.M.L. Tavares, R. de Oliveira, A.T. Marques, and A.J.M. Ferreira. Increasing the efficiency of composite single–shear lap joints using bonded inserts. *Composites Part B: Engineering*, 36(5):372 – 383, 2005.

[4] B. Kolesnikov, L. Herbeck, and A. Fink. CFRP/Titanium hybrid material for improving composite bolted joints. *Composite Structures*, 83(4):368 – 380, 2008.

[5] A. Fink and B. Kolesnikov. Hybrid titanium composite material improving composite structure coupling. In *Spacecraft Structures, Materials and Mechanical Testing 2005*, volume 581, page 135, 2005.

[6] A. Fink, P.P. Camanho, J.M. Andrés, E. Pfeiffer, and A. Obst. Hybrid CFRP/Titanium bolted joints: Performance assessment and application to a spacecraft payload adaptor. *Composites Science and Technology*, 70(2):305–317, 2010.

[7] P. Maimí, P.P. Camanho, J.A. Mayugo, and C.G. Dávila. A continuum damage model for composite laminates: Part I–constitutive model. *Mechanics of Materials*, 39(10):897–908, 2007.

[8] M.A. Nadler, S.Y. Yoshino, and F.J. Jr. Darms. Boron/Epoxy suppot strut for non-integral cryogenic tankage. In *15th SAMPE symposium*, volume 15, pages 179–207, Jan 1969.

[9] W. Althof and J. Müller. Untersuchungen an geklebten und lösbaren verbindungen von faserverstärkten kunststoffen. *Kunststoffe*, (80):911–916, 1970.

[10] A. Vlot and J.W. Gunnink. *Fibre Metal Laminates: An Introduction*. Springer, 2001.

[11] R. Alderliesten. On the development of hybrid material concepts for aircraft structures. *Recent Patents on Engineering*, 3(1):25–38, 2009.

[12] J.J. Mazza, G.B. Gaskin, W.S.D. Piero, and K.Y. Blohowiak. Sol-gel technology for low-VOC, nonchromated adhesive bonding applications. Technical report, AFRL-MLWP-TR-2004-4063, 2004.

[13] A. Fink and B. DuMars. Development of an improved surface preparation for titanium bonding and titanium graphite laminates for aircraft and space vehicle applications. In *AIRTEC 5th International Conference, Frankfurt*, 2010.

[14] A. Fink. *Lokale Metall–Hybridisierung zur Effizienzsteigerung von Hochlastfügestellen in Faserverbundstrukturen–stoffen*. PhD thesis, DLR, Bibliotheks-und Informationswesen, 2010.

[15] P.P. Camanho, A. Fink, A. Obst, and S. Pimenta. Hybrid Titanium–CFRP laminates for high–performance bolted joints. *Composites Part A: Applied Science and Manufacturing*, 40(12):1826–1837, 2009.

[16] AITM 1-0009. Airbus test method: determination of bearing strength by either pin or bolt bearing configuration, 2003.

[17] A.P. Mouritz. *Introduction to aerospace materials*. Elsevier, 2012.

[18] I. Inagaki, T. Takechi, Y. Shirai, and N. Ariyasu. Application and features of titanium for aerospace industry. *Nippon Steel and Sumitomo Metal Technical Report*, (106), July 2014.

[19] M.J. Donachie. *Titanium: A technical guide*. ASM international, 2000.

[20] G. Lütjering and J.C. Williams. *Titanium*, volume 2. Springer, 2003.

[21] C. Leyens and M. Peters. *Titanium and titanium alloys*. Wiley Online Library, 2003.

[22] B.W. Plunkett. *Plastic anisotropy of hexagonal closed packed metals*. PhD thesis, University of Florida, 2005.

[23] R. von Mises. Mechanik der plastischen formänderung von kristallen. *ZAMM-Journal of Applied Mathematics and Mechanics/Zeitschrift für Angewandte Mathematik und Mechanik*, 8(3):161–185, 1928.

[24] S. Wu. *Continuum Modelling and Numerical Simulation of Hexagonal Close–Packed Materials*. PhD thesis, FEUP, 2014.

[25] P.S. Follansbee and G.T. Gray. An analysis of the low temperature, low and high strain-rate deformation of Ti–6Al–4V. *Metallurgical Transactions A*, 20(5):863–874, 1989.

[26] W. Lee and M. Lin. The effects of strain rate and temperature on the compressive deformation behaviour of Ti–6Al–4V alloy. *Journal of Materials Processing Technology*, 71(2):235–246, 1997.

[27] S. Nemat-Nasser, W. Guo, V.F. Nesterenko, S.S. Indrakanti, and Y. Gu. Dynamic response of conventional and hot isostatically pressed Ti–6Al–4V alloys: experiments and modeling. *Mechanics of Materials*, 33(8):425–439, 2001.

[28] A. Majorell, S. Srivatsa, and R.C. Picu. Mechanical behavior of Ti–6Al–4V at high and moderate temperatures–part I: Experimental results. *Materials Science and Engineering: A*, 326(2):297 – 305, 2002.

[29] A.S. Khan, Y.S. Suh, and R. Kazmi. Quasi–static and dynamic loading responses and constitutive modeling of titanium alloys. *International Journal of Plasticity*, 20(12):2233 – 2248, 2004.

[30] A.S. Khan, R. Kazmi, and B. Farrokh. Multiaxial and non–proportional loading responses, anisotropy and modeling of Ti–6Al–4V titanium alloy over wide ranges of strain rates and temperatures. *International Journal of Plasticity*, 23(6):931–950, 2007.

[31] A.S. Khan and S. Yu. Deformation induced anisotropic responses of Ti–6Al–4V alloy. part I: Experiments. *International Journal of Plasticity*, 38:1–13, 2012.

[32] M.E. Nixon, O. Cazacu, and R.A. Lebensohn. Anisotropic response of high-purity $\boldsymbol{\alpha}$–titanium: Experimental characterization and constitutive modeling. *International Journal of Plasticity*, 26(4):516–532, 2010.

[33] G. Gilles, W. Hammami, V. Libertiaux, O. Cazacu, J.H. Yoon, T. Kuwabara, A.M. Habraken, and L. Duchêne. Experimental characterization and elasto-plastic modeling of the quasi-static mechanical response of TA-6V at room temperature. *International Journal of Solids and Structures*, 48(9):1277 – 1289, 2011.

[34] V. Tuninetti, G. Gilles, O. Milis, T. Pardoen, and A. Habraken. Anisotropy and tension–compression asymmetry modeling of the room temperature plastic response of Ti–6Al–4V. *International Journal of Plasticity*, 67:53–68, 2015.

[35] M.A. Meyers, G. Subhash, B.K. Kad, and L. Prasad. Evolution of microstructure and shear–band formation in $\boldsymbol{\alpha}$–hcp titanium. *Mechanics of materials*, 17(2):175–193, 1994.

[36] S.G. Song and G.T. Gray. Structural interpretation of the nucleation and growth of deformation twins in Zr and Ti I. application of the coincidence site lattice (CSL) theory to twinning problems in hcp structures. *Acta metallurgica et materialia*, 43(6):2325 – 2337, 1995.

[37] D.R. Chichili, K.T. Ramesh, and K.J. Hemker. The high–strain–rate response of alpha–titanium: experiments, deformation mechanisms and modeling. *Acta materialia*, 46(3):1025–1043, 1998.

[38] A.A. Salem, S.R. Kalidindi, and R.D. Doherty. Strain hardening of titanium: role of deformation twinning. *Acta Materialia*, 51(14):4225–4237, 2003.

[39] Y.B. Chun, S.H. Yu, S.L. Semiatin, and S.K. Hwang. Effect of deformation twinning on microstructure and texture evolution during cold rolling of CP titanium. *Materials Science and Engineering: A*, 398(1):209–219, 2005.

[40] P. Flores, E. Rondia, and A. Habraken. Development of an experimental equipment for the identification of constitutive laws. *International Journal of Forming Processes*, (Special Issue), 2005.

[41] Surya R Kalidindi, Curt A Bronkhorst, and Lallit Anand. Crystallographic texture evolution in bulk deformation processing of fcc metals. *Journal of the Mechanics and Physics of Solids*, 40(3):537–569, 1992.

[42] RA Lebensohn and CN Tomé. A self-consistent anisotropic approach for the simulation of plastic deformation and texture development of polycrystals: application to zirconium alloys. *Acta metallurgica et materialia*, 41(9):2611–2624, 1993.

[43] M. Knezevic, R.A. Lebensohn, O. Cazacu, B. Revil-Baudard, G. Proust, S. C Vogel, and M.E. Nixon. Modeling bending of $\boldsymbol{\alpha}$–titanium with embedded polycrystal plasticity in implicit finite elements. *Materials Science and Engineering: A*, 564:116–126, 2013.

[44] F. Roters, P. Eisenlohr, L. Hantcherli, D.D. Tjahjanto, T.R. Bieler, and D. Raabe. Overview of constitutive laws, kinematics, homogenization and multiscale methods in crystal plasticity finite-element modeling: Theory, experiments, applications. *Acta Materialia*, 58(4):1152–1211, 2010.

[45] D. Banabic, F. Barlat, O. Cazacu, and T. Kuwabara. Advances in anisotropy and formability. *International journal of material forming*, 3(3):165–189, 2010.

[46] T. Kuwabara, C. Katami, M. Kikuchi, T. Shindo, and T. Ohwue. Cup drawing of pure titanium sheet–finite element analysis and experimental validation. In *Proc. 7th Int. Conf. Numerical Methods in Industrial Forming Processes*, pages 781–787, 2001.

[47] O. Cazacu and F. Barlat. A criterion for description of anisotropy and yield differential effects in pressure–insensitive metals. *International Journal of Plasticity*, 20(11):2027–2045, 2004.

[48] W.F. Hosford and T.J. Allen. Twinning and directional slip as a cause for a strength differential effect. *Metallurgical and Materials Transactions B*, 4(5):1424–1425, 1973.

[49] O. Cazacu and F. Barlat. Generalization of drucker's yield criterion to orthotropy. *Mathematics and Mechanics of Solids*, 6(6):613–630, 2001.

[50] O. Cazacu and F. Barlat. Application of the theory of representation to describe yielding of anisotropic aluminum alloys. *International Journal of Engineering Science*, 41(12):1367–1385, 2003.

[51] F. Barlat, J.W. Yoon, and O. Cazacu. On linear transformations of stress tensors for the description of plastic anisotropy. *International Journal of Plasticity*, 23(5):876–896, 2007.

[52] O. Cazacu, B. Plunkett, and F. Barlat. Orthotropic yield criterion for hexagonal closed packed metals. *International Journal of Plasticity*, 22(7):1171–1194, 2006.

[53] B. Plunkett, O. Cazacu, and F. Barlat. Orthotropic yield criteria for description of the anisotropy in tension and compression of sheet metals. *International Journal of Plasticity*, 24(5):847–866, 2008.

[54] B. Plunkett, R.A. Lebensohn, O. Cazacu, and F. Barlat. Anisotropic yield function of hexagonal materials taking into account texture development and anisotropic hardening. *Acta Materialia*, 54(16):4159–4169, 2006.

[55] R.M. Lewis, V. Torczon, and M.W. Trosset. Direct search methods: then and now. *Journal of computational and Applied Mathematics*, 124(1):191–207, 2000.

[56] T.G. Kolda, R.M. Lewis, and V. Torczon. Optimization by direct search: New perspectives on some classical and modern methods. *SIAM review*, 45(3):385–482, 2003.

[57] F.H. Walters and et al. *Sequential Simplex Optimization*. CRC Press LLC, 1999.

[58] E. Elbeltagi, T. Hegazy, and D. Grierson. Comparison among five evolutionary–based optimization algorithms. *Advanced engineering informatics*, 19(1):43–53, 2005.

[59] J.A. Nelder and R. Mead. A simplex method for function minimization. *The computer journal*, 7(4):308–313, 1965.

[60] J.C. Lagarias, J.A. Reeds, M.H. Wright, and P.E. Wright. Convergence properties of the nelder–mead simplex method in low dimensions. *SIAM Journal on optimization*, 9(1):112–147, 1998.

[61] J.H. Holland. *Adaptation in natural and artificial systems: an introductory analysis with applications to biology, control and artificial intelligence*. U Michigan Press, 1975.

[62] D.E. Goldberg. Genetic algorithms in search, optimization and machine learning, 1989.

[63] D.E. Goldberg and K. Deb. A comparative analysis of selection schemes used in genetic algorithms. *Foundations of genetic algorithms*, 1:69–93, 1991.

[64] T. Blickle and L. Thiele. A comparison of selection schemes used in genetic algorithms, 1995.

[65] N. M. Razali and J. Geraghty. Genetic algorithm performance with different selection strategies in solving tsp. In *Proceedings of the World Congress on Engineering*, volume 2, 2011.

[66] S.N. Sivanandam and S.N. Deepa. *Introduction to genetic algorithms*. Springer Science & Business Media, 2007.

[67] W Tirry, F Coghe, S Bouvier, M Gasperini, L Rabet, and D Schryvers. A multi-scale characterization of deformation twins in ti6al4v sheet material deformed by simple shear. *Materials Science and Engineering: A*, 527(16):4136–4145, 2010.

[68] R. Hill. *The mathematical theory of plasticity*, volume 11. Oxford university press, 1998.

[69] A. Anandarajah. *Computational methods in elasticity and plasticity: solids and porous media*. Springer Science & Business Media, 2011.

[70] M. Jirásek and Z.P. Bazant. *Inelastic analysis of structures*. John Wiley & Sons, 2002.

[71] E.A. de Souza Neto, D. Peric, and D.R.J. Owen. *Computational methods for plasticity: theory and applications*. John Wiley & Sons, 2011.

[72] E. Voce. A practical strain–hardening function. *Metallurgia*, 51(307):219–226, 1955.

[73] M.E. Nixon, R.A. Lebensohn, O. Cazacu, and C. Liu. Experimental and finite element analysis of the anisotropic response of high purity $\boldsymbol{\alpha}$–titanium in bending. *Acta Materialia*, 58(17):5759–5767, 2010.

[74] V. Tuninetti, G. Gilles, V. Péron-Lührs, and A. Habraken. Compression test for metal characterization using digital image correlation and inverse modeling. *Procedia IUTAM*, 4:206–214, 2012.

[75] V. T. Vásquez. *Experimental and numerical study of the quasi–static behaviour of Ti–6Al–4V*. PhD thesis, Université de Liège, 2014.

[76] O. Cazacu and J.B. Stewart. Analytic plastic potential for porous aggregates with matrix exhibiting tension–compression asymmetry. *Journal of the Mechanics and Physics of Solids*, 57(2):325–341, 2009.

[77] A.L. Gurson. Continuum theory of ductile rupture by void nucleation and growth: Part I–yield criteria and flow rules for porous ductile media. *Journal of engineering materials and technology*, 99(1):2–15, 1977.

[78] B. Revil-Baudard, J. Yoon, J.B. Stewart, and O. Cazacu. On the influence of damage evolution in an incompressible material with matrix displaying tension–compression asymmetry. *Procedia IUTAM*, 3:331–349, 2012.

[79] B. Revil-Baudard and O. Cazacu. On the effect of the matrix tension–compression asymmetry on damage evolution in porous plastic solids. *European Journal of Mechanics-A/Solids*, 37:35–44, 2013.

[80] C.F. Guzmán, V. Tuninetti, G. Gilles, and A. Habraken. Assessment of damage and anisotropic plasticity models to predict Ti-6Al-4V behavior. In *Key Engineering Materials*, volume 651, pages 575–580. Trans Tech Publ, 2015.

[81] R. Hill. A theory of the yielding and plastic flow of anisotropic metals. In *Proceedings of the Royal Society of London A: Mathematical, Physical and Engineering Sciences*, volume 193, pages 281–297. The Royal Society, 1948.

[82] N. Allahverdizadeh, A. Manes, and M. Giglio. Identification of damage parameters for Ti-6Al-4v titanium alloy using continuum damage mechanics. *Materialwissenschaft und Werkstofftechnik*, 43(5):435–440, 2012.

[83] J. Lemaitre. A continuous damage mechanics model for ductile fracture. *Journal of Engineering Materials and Technology*, 107(1):83–89, 1985.

[84] M. Giglio, A. Manes, and F. Vigano. Ductile fracture locus of Ti–6Al–4V titanium alloy. *International Journal of Mechanical Sciences*, 54(1):121–135, 2012.

[85] N. Allahverdizadeh, A. Gilioli, A. Manes, and M. Giglio. An experimental and numerical study for the damage characterization of a Ti–6Al–4V titanium alloy. *International Journal of Mechanical Sciences*, 93:32–47, 2015.

[86] Y. Bao and T. Wierzbicki. On fracture locus in the equivalent strain and stress triaxiality space. *International Journal of Mechanical Sciences*, 46(1):81–98, 2004.

[87] Y. Bai and T. Wierzbicki. Application of extended mohr–coulomb criterion to ductile fracture. *International Journal of Fracture*, 161(1):1–20, 2010.

[88] M. Giglio, A. Manes, and F. Viganò. Numerical simulation of the slant fracture of a helicopter's rotor hub with ductile damage failure criteria. *Fatigue & Fracture of Engineering Materials & Structures*, 35(4):317–327, 2012.

[89] S. Katani, F. Madadi, M. Atapour, and S.Z. Rad. Micromechanical modelling of damage behaviour of Ti–6Al–4V. *Materials & Design*, 49:1016–1021, 2013.

[90] C. Zheng, J.M.A. César de Sá, and F. Pires. A comparison of models for ductile fracture prediction in forging processes. *Computer Methods in Materials Science*, 7(4):389–396, 2007.

[91] Y. Bai and T. Wierzbicki. A new model of metal plasticity and fracture with pressure and lode dependence. *International journal of plasticity*, 24(6):1071–1096, 2008.

[92] X. Gao, G. Zhang, and C. Roe. A study on the effect of the stress state on ductile fracture. *International Journal of Damage Mechanics*, 2009.

[93] A. M. Freudenthal. *The inelastic behavior of engineering materials and structures.* Wiley, 1950.

[94] J. Datsko. *Material properties and manufacturing processes.* John Wiley & Sons Inc, 1966.

[95] F.A. McClintock. A criterion for ductile fracture by growth of holes. *J. Appl. Mech*, 35(2):363–371, 1968.

[96] J.R. Rice and D.M. Tracey. On the ductile enlargement of voids in triaxial stress fields. *Journal of the Mechanics and Physics of Solids*, 17(3):201–217, 1969.

[97] M.G. Cockcrof and D.J. Latham. Ductility and workability of metals. *Journal of the Institute of Metals*, 96:33, 1968.

[98] P. Brozzo, B. Deluca, and R. Rendina. A new method for the prediction of formability limits in metal sheets. In *Proc. 7th biennal Conf. IDDR*, 1972.

[99] D.M. Norris, J.E. Reaugh, B. Moran, and D.F. Quinones. A plastic–strain, mean–stress criterion for ductile fracture. *Journal of engineering materials and technology*, 100(3):279–286, 1978.

[100] A.G. Atkins. Possible explanation for unexpected departures in hydrostatic tension–fracture strain relations. *Metal Science*, 15(2):81–83, 1981.

[101] D. Francois. *Fracture and Damage, Elastic–Plastic Fracture Mechanics.* D. Reidel, 1985.

[102] S. Murakami. Role of continuum damage mechanics in fracture analysis. *Inelastic Solids and Structures*, pages 67–80, 1990.

[103] A. Benallal, R. Billardon, and I. Doghri. Numerical aspects of the damage and failure analysis of engineering structures. In *Computational Plasticity II: Models, Software and Applications*, pages 297–309. Pineridge Press Swansea, 1989.

[104] S. Cescotto and Y.Y. Zhu. Modelling of ductile fracture initiation during bulk forming. *Computational plasticity: fundamentals and applications*, 1995.

[105] J. Lemaitre. Local approach of fracture. *Engineering Fracture Mechanics*, 25(5-6):523–537, 1986.

[106] M. Vaz Jr. *Computational approaches to simulation of metal cutting process.* PhD thesis, PhD. Thesis, University College of Swansea, 1998.

[107] M. Vaz and D.R.J. Owen. Aspects of ductile fracture and adaptive mesh refinement in damaged elasto–plastic materials. *International Journal for Numerical Methods in Engineering*, 50(1):29–54, 2001.

[108] B.P.P.A. Gouveia, J.M.C. Rodrigues, and P.A.F. Martins. Fracture predicting in bulk metal forming. *International journal of mechanical sciences*, 38(4):361–372, 1996.

[109] F.M. Andrade Pires. Modelação por elementos finitos da iniciação da fractura dúctil nos processos de enformação plástica em massa. Master's thesis, Faculty of Engineering, University of Porto, Portugal, 2001.

[110] S.E. Clift, P. Hartley, C.E.N. Sturgess, and G.W. Rowe. Fracture prediction in plastic deformation processes. *International Journal of Mechanical Sciences*, 32(1):1–17, 1990.

[111] M.G. Cockcroft and D.J. Latham. Ductility and the workability of metals. *J Inst Metals*, 96(1):33–39, 1968.

[112] V. Tvergaard. Material failure by void coalescence in localized shear bands. *International journal of solids and structures*, 18(8):659–672, 1982.

[113] V. Tvergaard and A. Needleman. Analysis of the cup-cone fracture in a round tensile bar. *Acta metallurgica*, 32(1):157–169, 1984.

[114] J. Lemaitre. Coupled elasto-plasticity and damage constitutive equations. *Computer Methods in Applied Mechanics and Engineering*, 51(1-3):31–49, 1985.

[115] L. M. Kachanov. On the creep fracture time. *Izv Akad, Nauk USSR Otd, Tekh*, (8):26–31, 1958.

[116] Y. N. Rabotnov. On the equations of state for creep. *Progress in Applied Mechanics*, Prager Anniversary Volume, New York, MacMillan:307–315, 1963.

[117] D. Krajcinovic. *Damage mechanics*, volume 41. Elsevier, 1996.

[118] J. Lemaitre and J.L. Chaboche. *Mechanics of solid materials.* Cambridge university press, 1994.

[119] M. V. Junior, E. A. de Souza Neto, and P. A. Munoz-Rojas. *Advanced computational materials modeling: from classical to multi-scale techniques.* John Wiley & Sons, 2011.

[120] S. Murakami. Mechanical modeling of material damage. *Journal of Applied Mechanics*, 55(2):280–286, 1988.

[121] S. Murakami and K. Kamiya. Constitutive and damage evolution equations of elastic-brittle materials based on irreversible thermodynamics. *International Journal of Mechanical Sciences*, 39(4):473–486, 1997.

[122] D. Krajcinovic and G.U. Fonseka. The continuous damage theory of brittle materials, part 1: general theory. *Journal of applied Mechanics*, 48(4):809–815, 1981.

[123] D. Krajcinovic. Constitutive equations for damaging materials. *Journal of applied Mechanics*, 50(2):355–360, 1983.

[124] J. L. Chaboche. Continuum damage mechanics: Part i - general concepts. *Journal of Applied Mechanics, Transactions of the ASME*, 55(1):59–64, 1988.

[125] J. L. Chaboche. Continuum damage mechanics: Part ii - damage growth, crack initiation and crack growth. *Journal of Applies Mechanics, Transactions of the ASME*, 55(1):65–72, 1988.

[126] J. Janson. A continuous damage approach to the fatigue process. *Engineering Fracture Mechanics*, 10(3):651–657, 1978.

[127] J. Lemaitre. How to use damage mechanics. *Nuclear engineering and design*, 80(2):233–245, 1984.

[128] D. Marquis and J. Lemaitre. Constitutive equations for the coupling between elasto-plasticity damage and aging. *Revue de physique appliquée*, 23(4):615–624, 1988.

[129] J. Lemaitre, R. Desmorat, and M. Sauzay. Anisotropic damage law of evolution. *European Journal of Mechanics-A/Solids*, 19(2):187–208, 2000.

[130] J. P. Cordebois and F. Sidoroff. Endomagement anisotrope en élasticité et plasticité. *Journal de Mécanique Théorique et Appliquée*, (Numéro spécial):45–60, 1982.

[131] J. C. Simo and J. W. Ju. Strain and stress based continuum damage models - part i : Formulation. *International Journal of Solids and Structures*, 23:821–840, 1987.

[132] J. C. Simo and J. W. Ju. Strain and stress based continuum damage models part ii - computational aspects. *International Journal of Solids and Structures*, 23:841–869, 1987.

[133] J. Lemaitre. *A course on damage mechanics*. Springer Science & Business Media, 2012.

[134] Zdenek P Bazant and Milan Jirásek. Nonlocal integral formulations of plasticity and damage: survey of progress. *Journal of Engineering Mechanics*, 128(11):1119–1149, 2002.

[135] JMA César de Sá, PMA Areias, and Cai Zheng. Damage modelling in metal forming problems using an implicit non-local gradient model. *Computer methods in applied mechanics and engineering*, 195(48):6646–6660, 2006.

[136] F XC Andrade, JMA César de Sá, and FM Andrade Pires. A ductile damage nonlocal model of integral-type at finite strains: formulation and numerical issues. *International Journal of Damage Mechanics*, page 1056789510386850, 2011.

[137] A.C. Orifici, I. Herszberg, and R.S. Thomson. Review of methodologies for composite material modelling incorporating failure. *Composite Structures*, 86(1):194–210, 2008.

[138] P. Maimí, P.P. Camanho, J.A. Mayugo, and C.G. Dávila. A continuum damage model for composite laminates: Part II–computational implementation and validation. *Mechanics of Materials*, 39(10):909–919, 2007.

[139] C.G. Dávila, C.A. Rose, and E.V. Iarve. Modeling fracture and complex crack networks in laminated composites. *Mathematical methods and models in composites, Computational and experimental methods in structures*, 5:297–347, 2013.

[140] E. Totry, C. González, and J. LLorca. Prediction of the failure locus of C/PEEK composites under transverse compression and longitudinal shear through computational micromechanics. *Composites Science and Technology*, 68(15):3128–3136, 2008.

[141] C. González and Javier. Llorca. Mechanical behavior of unidirectional fiber-reinforced polymers under transverse compression: Microscopic mechanisms and modeling. *Composites Science and Technology*, 67(13):2795–2806, 2007.

[142] A.R. Melro, P.P. Camanho, and S.T. Pinho. Generation of random distribution of fibres in long–fibre reinforced composites. *Composites Science and Technology*, 68(9):2092–2102, 2008.

[143] P.P. Camanho and M. Lambert. A design methodology for mechanically fastened joints in laminated composite materials. *Composites Science and Technology*, 66(15):3004–3020, 2006.

[144] P.P. Camanho, G.H. Erçin, G. Catalanotti, S. Mahdi, and P. Linde. A finite fracture mechanics model for the prediction of the open–hole strength of composite laminates. *Composites Part A: Applied Science and Manufacturing*, 43(8):1219–1225, 2012.

[145] J.M. Whitney and R.J. Nuismer. Stress fracture criteria for laminated composites containing stress concentrations. *Journal of composite materials*, 8(3):253–265, 1974.

[146] T.E. Tay, S.H.N. Tan, V.B.C. Tan, and J.H. Gosse. Damage progression by the element–failure method (EFM) and strain invariant failure theory (SIFT). *Composites Science and Technology*, 65(6):935–944, 2005.

[147] E. Abisset, F. Daghia, and P. Ladevèze. On the validation of a damage mesomodel for laminated composites by means of open-hole tensile tests on quasi–isotropic laminates. *Composites Part A: Applied Science and Manufacturing*, 42(10):1515–1524, 2011.

[148] E.V. Iarve, M.R. Gurvich, D.H. Mollenhauer, C.A. Rose, and C.G. Dávila. Mesh–independent matrix cracking and delamination modeling in laminated composites. *International Journal for Numerical Methods in Engineering*, 88(8):749–773, 2011.

[149] F.P. Van der Meer, C. Oliver, and L.J. Sluys. Computational analysis of progressive failure in a notched laminate including shear nonlinearity and fiber failure. *Composites Science and Technology*, 70(4):692–700, 2010.

[150] D. Ling, Q. Yang, and B. Cox. An augmented finite element method for modeling arbitrary discontinuities in composite materials. *International journal of fracture*, 156(1):53–73, 2009.

[151] M.R. Wisnom. Modelling discrete failures in composites with interface elements. *Composites Part A: Applied Science and Manufacturing*, 41(7):795–805, 2010.

[152] C. Schuecker and H.E. Pettermann. A continuum damage model for fiber reinforced laminates based on ply failure mechanisms. *Composite structures*, 76(1):162–173, 2006.

[153] A. Turon, P.P. Camanho, J. Costa, and C.G. Dávila. A damage model for the simulation of delamination in advanced composites under variable–mode loading. *Mechanics of Materials*, 38(11):1072–1089, 2006.

[154] Y. Qiu, M.A. Crisfield, and G. Alfano. An interface element formulation for the simulation of delamination with buckling. *Engineering Fracture Mechanics*, 68(16):1755–1776, 2001.

[155] J.H.A. Schipperen and R. De Borst. A numerical analysis of mixed–mode delamination in carbon–epoxy prepregs. *Composite structures*, 54(4):445–451, 2001.

[156] Z. Hashin and A. Rotem. A fatigue failure criterion for fiber reinforced materials. *Journal of composite materials*, 7(4):448–464, 1973.

[157] Z. Hashin. Failure criteria for unidirectional fiber composites. *Journal of applied mechanics*, 47(2):329–334, 1980.

[158] C.G. Dávila and P.P. Camanho. Failure criteria for FRP laminates in plane stress. *NASA TM*, 212663(613), 2003.

[159] C.T Sun, B.J. Quinn, and D.W. Oplinger. Comparative evaluation of failure analysis methods for composite laminates. *DOT/FAA/AR-95/109*.

[160] A. Puck and H. Schürmann. Failure analysis of FRP laminates by means of physically based phenomenological models. *Composites Science and Technology*, 58(7):1045–1067, 1998.

[161] C.G. Dávila, P.P. Camanho, and C.A. Rose. Failure criteria for FRP laminates. *Journal of Composite materials*, 39(4):323–345, 2005.

[162] G.J. Dvorak and N. Laws. Analysis of progressive matrix cracking in composite laminates II. first ply failure. *Journal of Composite Materials*, 21(4):309–329, 1987.

[163] A.S. Argon. Fracture of composites. *Treatise on materials science and technology*, 1:79–114, 1972.

[164] S.T. Pinho, C.G. Dàvila, P.P. Camanho, L. Iannucci, and P. Robinson. Failure models and criteria for FRP under in–plane or three–dimensional stress states including shear non–linearity. 2005.

[165] A. Puck and H. Schürmann. Failure analysis of FRP laminates by means of physically based phenomenological models. *Composites Science and Technology*, 62(12):1633–1662, 2002.

[166] P. Ladeveze and E. LeDantec. Damage modelling of the elementary ply for laminated composites. *Composites science and technology*, 43(3):257–267, 1992.

[167] A.L.J.T.R. Matzenmiller, J. Lubliner, and R.L. Taylor. A constitutive model for anisotropic damage in fiber–composites. *Mechanics of materials*, 20(2):125–152, 1995.

[168] L. Kachanov. *Introduction to continuum damage mechanics.* Martinus Nijhoff, Dordrecht, NL, 1986.

[169] Zdeněk P Bažant and Byung H Oh. Crack band theory for fracture of concrete. *Matériaux et construction*, 16(3):155–177, 1983.

[170] P. Maimí, P.P. Camanho, J.A. Mayugo, and C.G. Dávila. A thermodynamically consistent damage model for advanced composites. 2006.

[171] P.P. Camanho, P. Maimí, and C.G. Dávila. Prediction of size effects in notched laminates using continuum damage mechanics. *Composites Science and Technology*, 67(13):2715–2727, 2007.

[172] M. Bessa. Meso–mechanical model of the structural integrity of advanced composite laminates. Master's thesis, Faculty of Engineering, University of Porto, 2010.

[173] C.S. Lopes, P.P. Camanho, Z. Gürdal, P. Maimí, and E.V. González. Low–velocity impact damage on dispersed stacking sequence laminates. part II: Numerical simulations. *Composites Science and Technology*, 69(7):937–947, 2009.

[174] E.V. González, P. Maimí, P.P. Camanho, A. Turon, and J.A. Mayugo. Simulation of drop-weight impact and compression after impact tests on composite laminates. *Composite Structures*, 94(11):3364–3378, 2012.

[175] M. Wiedemann and M. Sinapius. *Adaptive, tolerant and efficient composite structures.* Springer Science & Business Media, 2012.

[176] P.P. Camanho, C.G. Dávila, S.T. Pinho, L. Iannucci, and P. Robinson. Prediction of in situ strengths and matrix cracking in composites under transverse tension and in–plane shear. *Composites Part A: Applied Science and Manufacturing*, 37(2):165–176, 2006.

[177] Abaqus Inc., Pawtucket, RI, USA. *ABAQUS 6.14 "Getting Started with ABAQUS"*, 2014.

[178] H.J. Park. Effects of stacking sequence and clamping force on the bearing strengths of mechanically fastened joints in composite laminates. *Composite structures*, 53(2):213–221, 2001.

Appendix A

CPB06 yield function derivatives

According to the implementation procedure defined in Chapter 5 the yield function derivatives have to be determined. The yield function is given by,

$$\boldsymbol{f}\left(\boldsymbol{\sigma}, \bar{\boldsymbol{\varepsilon}}_{\boldsymbol{p}}\right) = \bar{\boldsymbol{\sigma}}\left(\boldsymbol{\sigma}, \bar{\boldsymbol{\varepsilon}}_{\boldsymbol{p}}\right) - \boldsymbol{Y}\left(\bar{\boldsymbol{\varepsilon}}_{\boldsymbol{p}}\right) \tag{A.1}$$

where $\bar{\boldsymbol{\sigma}}$ is the effective stress. Taking into account the anisotropic hardening approach used, the derivatives are evaluated as,

$$\frac{\boldsymbol{\partial f}}{\boldsymbol{\partial \sigma}} = \frac{\boldsymbol{\partial \bar{\sigma}}}{\boldsymbol{\partial \sigma}} = \boldsymbol{\xi}\left(\bar{\boldsymbol{\varepsilon}}_{\boldsymbol{p}}\right) \frac{\boldsymbol{\partial \bar{\sigma}}^{\boldsymbol{j}}}{\boldsymbol{\partial \sigma}} + \left(\mathbf{1} - \boldsymbol{\xi}(\bar{\boldsymbol{\varepsilon}}_{\boldsymbol{p}})\right) \frac{\boldsymbol{\partial \bar{\sigma}}^{\boldsymbol{j+1}}}{\boldsymbol{\partial \sigma}} \tag{A.2}$$

The derivatives of the effective stress, $\bar{\boldsymbol{\sigma}}$, are evaluated for the equivalent plastic strain values at $\boldsymbol{j}$ and $\boldsymbol{j+1}$ as,

$$\frac{\boldsymbol{\partial \bar{\sigma}}}{\boldsymbol{\partial \sigma}} = \frac{\boldsymbol{\partial \phi}}{\boldsymbol{\partial \sigma}} \tag{A.3}$$

where $\boldsymbol{\phi}$ defined the yield criterion proposed by Cazacu et al. [52].

To obtain the derivatives of $\boldsymbol{\phi}$ for a general three-dimensional problem it is necessary to develop an expression between the principal values of $\boldsymbol{\Sigma}$ and its components. This expression can be obtained through the use of the deviator of the transformed tensor $\boldsymbol{\Sigma}$, represented here by $\boldsymbol{\Sigma'}$,

$$\boldsymbol{\Sigma'} = \boldsymbol{\Sigma} - \frac{\boldsymbol{I_1}}{\mathbf{3}}\boldsymbol{I} \tag{A.4}$$

where $\boldsymbol{I_1}$ is the first invariant of $\boldsymbol{\Sigma}$ and $\boldsymbol{I}$ the identity tensor. By replacing $\boldsymbol{\Sigma}$ by $\boldsymbol{\Sigma'}$ in the characteristic equation of $\boldsymbol{\Sigma}$ (see equation 3.18 Chapter 3) the quadratic term disappears and

the following equation is obtained,

$$\boldsymbol{X^3 - H_2 X - H_3 = 0} \tag{A.5}$$

where $\boldsymbol{H_2}$ and $\boldsymbol{H_3}$ are the second and third invariants of $\boldsymbol{\Sigma'}$. To find the roots of equation A.5 the following quantities need to be computed,

$$\boldsymbol{Q = \frac{3H_2 - H_1}{9} = \frac{H_2}{3}} \tag{A.6}$$

$$\boldsymbol{R = \frac{2H_1^3 - 9H_1H_2 + 27H_3}{54} = \frac{H_3}{2}} \tag{A.7}$$

$$\boldsymbol{\theta = cos^{-}1\left(\frac{9}{2}\frac{H_3}{\sqrt{-3H_2^3}}\right)} \tag{A.8}$$

The principal values of $\boldsymbol{\Sigma}$ can then be obtained by adding the spherical portion of $\boldsymbol{\Sigma}$,

$$\boldsymbol{\Sigma_1 = 2\sqrt{-\frac{H_2}{3}}\cos\left(\frac{\theta}{3}\right) + \frac{I_1}{3}} \tag{A.9}$$

$$\boldsymbol{\Sigma_2 = 2\sqrt{-\frac{H_2}{3}}\cos\left(\frac{\theta + 4\pi}{3}\right) + \frac{I_1}{3}} \tag{A.10}$$

$$\boldsymbol{\Sigma_3 = 2\sqrt{-\frac{H_2}{3}}\cos\left(\frac{\theta + 2\pi}{3}\right) + \frac{I_1}{3}} \tag{A.11}$$

where $\boldsymbol{\Sigma_1 \geq \Sigma_2 \geq \Sigma_3}$. The first derivatives of the yield criterion are thus given by,

$$\begin{aligned}\boldsymbol{\frac{\partial\phi}{\partial\sigma_{ij}} = \frac{\partial\phi}{\partial\Sigma_q}\Bigg\{\Bigg[\frac{\partial\Sigma_q}{\partial\theta}\left(\frac{\partial\theta}{\partial H_2}\frac{\partial H_2}{\partial\Sigma_{kl}} + \frac{\partial\theta}{\partial H_3}\frac{\partial H_3}{\partial\Sigma_{kl}}\right)} \\ \boldsymbol{+ \frac{\partial\Sigma_q}{\partial H_2}\frac{\partial H_2}{\partial\Sigma_{kl}} + \frac{\partial\Sigma_q}{\partial H_3}\frac{\partial H_3}{\partial\Sigma_{kl}}\Bigg]\frac{\partial\Sigma_{kl}}{\partial S_{mn}}\frac{\partial S_{mn}}{\partial\sigma ij}\Bigg\}}\end{aligned} \tag{A.12}$$

Where the derivative of $\boldsymbol{\phi}$ in order of the principal values $\boldsymbol{\Sigma_q}$ are given by,

$$\boldsymbol{\frac{\partial\phi}{\partial\Sigma_q} = a\left(|\Sigma_q| - k\Sigma_q\right)^{a-1}\left(\frac{\Sigma_i}{|\Sigma_i|} - k\right)} \tag{A.13}$$

The derivative of the principal values in order of $\boldsymbol{\theta}$ are given by,

$$\frac{\partial \boldsymbol{\Sigma_1}}{\partial \boldsymbol{\theta}} = -\frac{\mathbf{2}}{\mathbf{3}}\sqrt{-\frac{\boldsymbol{H_2}}{\mathbf{3}}}\,\mathbf{sin}\left(\frac{\boldsymbol{\theta}}{\mathbf{3}}\right) \tag{A.14}$$

$$\frac{\partial \boldsymbol{\Sigma_2}}{\partial \boldsymbol{\theta}} = -\frac{\mathbf{2}}{\mathbf{3}}\sqrt{-\frac{\boldsymbol{H_2}}{\mathbf{3}}}\,\mathbf{sin}\left(\frac{\boldsymbol{\theta}+\mathbf{4\pi}}{\mathbf{3}}\right) \tag{A.15}$$

$$\frac{\partial \boldsymbol{\Sigma_3}}{\partial \boldsymbol{\theta}} = -\frac{\mathbf{2}}{\mathbf{3}}\sqrt{-\frac{\boldsymbol{H_2}}{\mathbf{3}}}\,\mathbf{sin}\left(\frac{\boldsymbol{\theta}+\mathbf{2\pi}}{\mathbf{3}}\right) \tag{A.16}$$

The derivatives of the principal values in order of $\boldsymbol{H_2}$ are given by,

$$\frac{\partial \boldsymbol{\Sigma_1}}{\partial \boldsymbol{H_2}} = -\frac{\mathbf{1}}{\mathbf{3}}\left(-\frac{\boldsymbol{H_2}}{\mathbf{3}}\right)^{-\frac{\mathbf{1}}{\mathbf{2}}}\mathbf{cos}\left(\frac{\boldsymbol{\theta}}{\mathbf{3}}\right) \tag{A.17}$$

$$\frac{\partial \boldsymbol{\Sigma_2}}{\partial \boldsymbol{H_2}} = -\frac{\mathbf{1}}{\mathbf{3}}\left(-\frac{\boldsymbol{H_2}}{\mathbf{3}}\right)^{-\frac{\mathbf{1}}{\mathbf{2}}}\mathbf{cos}\left(\frac{\boldsymbol{\theta}+\mathbf{4\pi}}{\mathbf{3}}\right) \tag{A.18}$$

$$\frac{\partial \boldsymbol{\Sigma_3}}{\partial \boldsymbol{H_2}} = -\frac{\mathbf{1}}{\mathbf{3}}\left(-\frac{\boldsymbol{H_2}}{\mathbf{3}}\right)^{-\frac{\mathbf{1}}{\mathbf{2}}}\mathbf{cos}\left(\frac{\boldsymbol{\theta}+\mathbf{2\pi}}{\mathbf{3}}\right) \tag{A.19}$$

The derivatives of the principal values in order of the first invariant are given by,

$$\frac{\partial \boldsymbol{\Sigma_1}}{\partial \boldsymbol{I_1}} = \frac{\partial \boldsymbol{\Sigma_2}}{\partial \boldsymbol{I_2}} = \frac{\partial \boldsymbol{\Sigma_3}}{\partial \boldsymbol{I_1}} = \frac{\mathbf{1}}{\mathbf{3}} \tag{A.20}$$

The derivatives of the first invariant in order of the components of $\boldsymbol{\Sigma}$ are given by,

$$\frac{\partial \boldsymbol{I_1}}{\partial \boldsymbol{\Sigma_{11}}} = \frac{\partial \boldsymbol{I_1}}{\partial \boldsymbol{\Sigma_{22}}} = \frac{\partial \boldsymbol{I_1}}{\partial \boldsymbol{\Sigma_{33}}} = \mathbf{1} \tag{A.21}$$

$$\frac{\partial \boldsymbol{I_1}}{\partial \boldsymbol{\Sigma_{12}}} = \frac{\partial \boldsymbol{I_1}}{\partial \boldsymbol{\Sigma_{23}}} = \frac{\partial \boldsymbol{I_1}}{\partial \boldsymbol{\Sigma_{13}}} = \mathbf{0} \tag{A.22}$$

The derivatives of $\boldsymbol{\theta}$ in order of $\boldsymbol{H_2}$ and $\boldsymbol{H_3}$ are given by,

$$\frac{\boldsymbol{\partial\theta}}{\boldsymbol{\partial H_2}} = -\frac{\boldsymbol{81}}{\boldsymbol{2}} \frac{\boldsymbol{H_3 H_2^2}}{\left(\boldsymbol{-3H_2^3}\right)^{\frac{3}{2}} \left(\boldsymbol{4 + \frac{27H_3^2}{H_2^3}}\right)} \tag{A.23}$$

$$\frac{\boldsymbol{\partial\theta}}{\boldsymbol{\partial H_3}} = -\frac{\boldsymbol{9}}{\left(\boldsymbol{-3H_2^3}\right)^{\frac{1}{2}} \left(\boldsymbol{4 + \frac{27H_3^2}{H_2^3}}\right)^{\frac{1}{2}}} \tag{A.24}$$

The derivatives of $\boldsymbol{H_2}$ in order of the components of $\boldsymbol{\Sigma}$ are given by,

$$\frac{\boldsymbol{\partial H_2}}{\boldsymbol{\partial \Sigma_{11}}} = \frac{\boldsymbol{1}}{\boldsymbol{3}} \left(\boldsymbol{-2\Sigma_{11} + \Sigma 22 + \Sigma_{33}}\right) \tag{A.25}$$

$$\frac{\boldsymbol{\partial H_2}}{\boldsymbol{\partial \Sigma_{22}}} = \frac{\boldsymbol{1}}{\boldsymbol{3}} \left(\boldsymbol{\Sigma_{11} - 2\Sigma 22 + \Sigma_{33}}\right) \tag{A.26}$$

$$\frac{\boldsymbol{\partial H_2}}{\boldsymbol{\partial \Sigma_{33}}} = \frac{\boldsymbol{1}}{\boldsymbol{3}} \left(\boldsymbol{\Sigma_{11} + \Sigma 22 - 2\Sigma_{33}}\right) \tag{A.27}$$

$$\frac{\boldsymbol{\partial H_2}}{\boldsymbol{\partial \Sigma_{12}}} = \boldsymbol{-2\Sigma_{12}} \tag{A.28}$$

$$\frac{\boldsymbol{\partial H_2}}{\boldsymbol{\partial \Sigma_{23}}} = \boldsymbol{-2\Sigma_{23}} \tag{A.29}$$

$$\frac{\boldsymbol{\partial H_2}}{\boldsymbol{\partial \Sigma_{13}}} = \boldsymbol{-2\Sigma_{13}} \tag{A.30}$$

The derivatives of $\boldsymbol{H_3}$ in order of the components of $\boldsymbol{\Sigma}$ are given by,

$$\begin{aligned}\frac{\partial H_3}{\partial \Sigma_{11}} = & \frac{2}{9}\left(-\Sigma_{11}+2\Sigma_{22}-\Sigma_{33}\right)\left(-\Sigma_{11}-\Sigma_{22}+2\Sigma_{33}\right) \\ & -\frac{1}{9}\left(2\Sigma_{11}-\Sigma_{22}-\Sigma_{33}\right)\left(-\Sigma_{11}-\Sigma_{22}+2\Sigma_{33}\right) \\ & -\frac{1}{9}\left(2\Sigma_{11}-\Sigma_{22}-\Sigma_{33}\right)\left(-\Sigma_{11}+2\Sigma_{22}-\Sigma_{33}\right) \\ & -\frac{2}{3}\Sigma_{23}^2+\frac{1}{3}\Sigma_{13}^2+\frac{1}{3}\Sigma_{12}^2\end{aligned} \tag{A.31}$$

$$\begin{aligned}\frac{\partial H_3}{\partial \Sigma_{22}} = & -\frac{1}{9}\left(-\Sigma_{11}+2\Sigma_{22}-\Sigma_{33}\right)\left(-\Sigma_{11}-\Sigma_{22}+2\Sigma_{33}\right) \\ & +\frac{2}{9}\left(2\Sigma_{11}-\Sigma_{22}-\Sigma_{33}\right)\left(-\Sigma_{11}-\Sigma_{22}+2\Sigma_{33}\right) \\ & -\frac{1}{9}\left(2\Sigma_{11}-\Sigma_{22}-\Sigma_{33}\right)\left(-\Sigma_{11}+2\Sigma_{22}-\Sigma_{33}\right) \\ & -\frac{2}{3}\Sigma_{13}^2+\frac{1}{3}\Sigma_{23}^2+\frac{1}{3}\Sigma_{12}^2\end{aligned} \tag{A.32}$$

$$\begin{aligned}\frac{\partial H_3}{\partial \Sigma_{33}} = & -\frac{1}{9}\left(-\Sigma_{11}+2\Sigma_{22}-\Sigma_{33}\right)\left(-\Sigma_{11}-\Sigma_{22}+2\Sigma_{33}\right) \\ & -\frac{1}{9}\left(2\Sigma_{11}-\Sigma_{22}-\Sigma_{33}\right)\left(-\Sigma_{11}-\Sigma_{22}+2\Sigma_{33}\right) \\ & +\frac{2}{9}\left(2\Sigma_{11}-\Sigma_{22}-\Sigma_{33}\right)\left(-\Sigma_{11}+2\Sigma_{22}-\Sigma_{33}\right) \\ & -\frac{2}{3}\Sigma_{12}^2+\frac{1}{3}\Sigma_{13}^2+\frac{1}{3}\Sigma_{23}^2\end{aligned} \tag{A.33}$$

$$\frac{\partial H_3}{\partial \Sigma_{12}} = -\frac{2}{3}\Sigma_{12}\left(-\Sigma_{11}-\Sigma_{22}-2\Sigma 33\right)+2\Sigma_{23}\Sigma_{13} \tag{A.34}$$

$$\frac{\partial H_3}{\partial \Sigma_{23}} = -\frac{2}{3}\Sigma_{23}\left(2\Sigma_{11}-\Sigma_{22}-\Sigma 33\right)+2\Sigma_{12}\Sigma_{13} \tag{A.35}$$

$$\frac{\partial H_3}{\partial \Sigma_{13}} = -\frac{2}{3}\Sigma_{13}\left(-\Sigma_{11}+2\Sigma_{22}-\Sigma 33\right)+2\Sigma_{12}\Sigma_{23} \tag{A.36}$$

Appendix B

Nixon yield function derivatives

For the yield criterion proposed by Nixon et al. [32] and considering the anisotropic hardening the derivative of the yield function is expressed as,

$$\frac{\partial f}{\partial \sigma} = \xi(\bar{\varepsilon}_p)\frac{\partial \bar{\sigma}^{j}}{\partial \sigma} + (1 - \xi(\bar{\varepsilon}_p))\,\frac{\partial \bar{\sigma}^{j+1}}{\partial \sigma} \tag{B.1}$$

The derivatives of the effective stress, $\bar{\sigma}$, for the Nixon yield criterion are evaluated for the equivalent plastic strain values at j and $j+1$ and can be expressed as,

$$\frac{\partial \bar{\sigma}}{\partial \sigma} = \begin{bmatrix} \frac{\partial \bar{\sigma}}{\partial \sigma_{11}} \\ \frac{\partial \bar{\sigma}}{\partial \sigma_{22}} \\ \frac{\partial \bar{\sigma}}{\partial \sigma_{33}} \\ \frac{\partial \bar{\sigma}}{\partial \sigma_{12}} \\ \frac{\partial \bar{\sigma}}{\partial \sigma_{23}} \\ \frac{\partial \bar{\sigma}}{\partial \sigma_{13}} \end{bmatrix} \tag{B.2}$$

Using the chain rule, the general expression for the derivatives of the effective stress is given by,

$$\frac{\partial \bar{\sigma}}{\partial \sigma_{ij}} = \frac{\partial \bar{\sigma}}{\partial J_2^0}\frac{\partial J_2^0}{\partial \sigma_{ij}} + \frac{\partial \bar{\sigma}}{\partial J_3^0}\frac{\partial J_3^0}{\partial \sigma_{ij}} \tag{B.3}$$

The derivatives of the effective stress in order of the invariants $\boldsymbol{J_2^0}$ and $\boldsymbol{J_3^0}$ are given by,

$$\frac{\partial \bar{\sigma}}{\partial J_2^0} = \frac{A {J_2^0}^{\frac{1}{2}}}{2\left({J_2^0}^{\frac{3}{2}} - cJ_3^0\right)^{\frac{2}{3}}} \tag{B.4}$$

$$\frac{\partial \bar{\sigma}}{\partial J_3^0} = -\frac{Ac}{3\left({J_2^0}^{\frac{3}{2}} - cJ_3^0\right)^{\frac{2}{3}}} \tag{B.5}$$

The derivatives of the invariant $\boldsymbol{J_2^0}$ in order of the components of the Cauchy stress tensor are given by,

$$\begin{aligned}\frac{\partial J_2^0}{\partial \sigma_{11}} =& \frac{1}{9}\left[2\left(a_2^2 + a_3^2 + a_2a_3\right)\sigma_{11} + \left(-2a_3^2 + a_1a_2 - a_1a_3 - a_2a_3\right)\sigma_{22}\right. \\ &\left. + \left(-2a_2^2 - a_1a_2 + a_1a_3 - a_2a_3\right)\sigma_{33}\right]\end{aligned} \tag{B.6}$$

$$\begin{aligned}\frac{\partial J_2^0}{\partial \sigma_{22}} =& \frac{1}{9}\left[2\left(a_1^2 + a_3^2 + a_1a_2\right)\sigma_{22} + \left(-2a_3^2 + a_1a_2 - a_1a_3 - a_2a_3\right)\sigma_{11}\right. \\ &\left. + \left(-2a_1^2 - a_1a_2 - a_1a_3 + a_2a_3\right)\sigma_{33}\right]\end{aligned} \tag{B.7}$$

$$\begin{aligned}\frac{\partial J_2^0}{\partial \sigma_{33}} =& \frac{1}{9}\left[2\left(a_1^2 + a_2^2 + a_1a_2\right)\sigma_{33} + \left(-2a_2^2 - a_1a_2 + a_1a_3 - a_2a_3\right)\sigma_{11}\right. \\ &\left. + \left(-2a_1^2 - a_1a_2 - a_1a_3 + a_2a_3\right)\sigma_{22}\right]\end{aligned} \tag{B.8}$$

$$\frac{\partial J_2^0}{\partial \sigma_{12}} = 2a_4^2\sigma_{12} \tag{B.9}$$

$$\frac{\partial J_2^0}{\partial \sigma_{23}} = 2a_5^2\sigma_{23} \tag{B.10}$$

$$\frac{\partial J_2^0}{\partial \sigma_{13}} = 2a_6^2\sigma_{13} \tag{B.11}$$

The derivatives of the invariant $\boldsymbol{J_3^0}$ in order of the components of the Cauchy stress tensor

are given by,

$$\begin{aligned}\frac{\partial J_3^0}{\partial \sigma_{11}} =& \frac{1}{27}\left[3\left(a_2^2a_3+a_2a_3^2\right)\sigma_{11}^2+2\left(-a_1a_2^2+a_1a_3^2-a_2^2a_3-2a_2a_3^2\right)\sigma_{11}\sigma_{22}\right.\\ &+2\left(a_1a_2^2-a_1a_3^2-2a_2^2a_3-a_2a_3^2\right)\sigma_{11}\sigma_{33}\\ &+\left(-a_1^2a_2-a_1^2a_3-2a_1a_3^2+a_2a_3^2\right)\sigma_{22}^2\\ &+2\left(a_1^2a_2+a_1^2a_3+a_2^2a_1+a_1a_3^2+a_2^2a_3+a_3^2a_2\right)\sigma_{22}\sigma_{33}\\ &\left.+\left(-a_1^2a_2-a_1^2a_3-2a_1a_2^2+a_2^2a_3\right)\sigma_{33}^2\right]\\ &+\frac{1}{3}\left[a_2a_4^2\sigma_{12}^2+a_3a_5^2\sigma_{13}^2+\left(-a_2a_6^2-a_3a_6^2\right)\sigma_{23}^2\right]\end{aligned} \tag{B.12}$$

$$\begin{aligned}\frac{\partial J_3^0}{\partial \sigma_{22}} =& \frac{1}{27}\left[3\left(a_1a_3^2+a_1^2a_3\right)\sigma_{22}^2+\left(-a_1a_2^2+a_1a_3^2-a_2^2a_3-2a_2a_3^2\right)\sigma_{11}^2\right.\\ &+2\left(-a_1^2a_2-a_1^2a_3-2a_1a_3^2+a_2a_3^2\right)\sigma_{11}\sigma_{22}\\ &+2\left(a_1^2a_2-2a_1^2a_3-a_1a_3^2-a_2a_3^2\right)\sigma_{22}\sigma_{33}\\ &+\left(-2a_1^2a_2+a_1^2a_3-a_1a_2^2-a_2^2a_3\right)\sigma_{33}^2\\ &\left.+2\left(a_1^2a_2+a_1^2a_3+a_1a_2^2+a_1a_3^2+a_2^2a_3+a_2a_3^2\right)\sigma_{11}\sigma_{33}\right]\\ &+\frac{1}{3}\left[a_1a_4^2\sigma_{12}^2-\left(a_1a_5^2+a_3a_5^2\right)\sigma_{13}^2+a_3a_6^2\sigma_{23}^2\right]\end{aligned} \tag{B.13}$$

$$\begin{aligned}\frac{\partial J_3^0}{\partial \sigma_{33}} =& \frac{1}{27}\left[3\left(a_1^2a_2+a_1a_2^2\right)\sigma_{33}^2+\left(a_1a_2^2-a_1a_3^2-2a_2^2a_3-a_2a_3^2\right)\sigma_{11}^2\right.\\ &+\left(a_1^2a_2-2a_1^2a_3-a_1a_3^2-a_2a_3^2\right)\sigma_{22}^2\\ &+2\left(-a_1^2a_2-a_1^2a_3-2a_1a_2^2+a_2^2a_3\right)\sigma_{33}\sigma_{11}\\ &+2\left(-2a_1^2a_2+a_1^2a_3-a_1a_2^2-a_2^2a_3\right)\sigma_{33}\sigma_{22}\\ &\left.+2\left(a_1^2a_2+a_1^2a_3+a_1a_2^2+a_1a_3^2+a_2^2a_3+a_2a_3^2\right)\sigma_{11}\sigma_{22}+\right]\\ &+\frac{1}{3}\left[-\left(a_2a_4^2+a_1a_4^2\right)\sigma_{12}^2+a_1a_5^2\sigma_{13}^2+a_2a_6^2\sigma_{23}^2\right]\end{aligned} \tag{B.14}$$

$$\begin{aligned}\frac{\partial J_3^0}{\partial \sigma_{12}} =& \frac{1}{3}\left[2\sigma_{12}\left(\sigma_{11}a_2a_4^2+\sigma_{22}a_1a_4^2-\sigma_{33}\left(a_2a_4^2+a_1a_4^2\right)\right)\right]\\ &+2a_4a_5a_6\sigma_{13}\sigma_{23}\end{aligned} \tag{B.15}$$

$$\begin{aligned}\frac{\partial J_3^0}{\partial \sigma_{23}} =& \frac{1}{3}\left[2\sigma_{23}\left(\sigma_{11}\left(-a_2a_6^2-a_3a_6^2\right)+a_3a_6^2\sigma_{22}+a_2a_6^2\sigma_{33}\right)\right]\\ &+2a_4a_5a_6\sigma_{12}\sigma_{13}\end{aligned} \tag{B.16}$$

$$\begin{aligned}\frac{\partial J_3^0}{\partial \sigma_{13}} =& \frac{1}{3}\left[2\sigma_{13}\left(a_3a_5^2\sigma_{11}-\left(a_1a_5^2+a_3a_5^2\right)\sigma_{22}+a_1a_5^2\sigma_{33}\right)\right]\\ &+2a_4a_5a_6\sigma_{12}\sigma_{23}\end{aligned} \tag{B.17}$$